UNIVERSITÀ
DI SIENA
1240

A thesis submitted in partial fulfilment of the requirements for the degree of Doctor of Philosophy

Non-Thermal Features
in TeV-Blazars and the Galactic Center Region
with MAGIC and Prospects for CTA

PhD Student:

Sofia VENTURA
University of Siena
Via Roma 56

Signature

Supervisor:

Dr. Giacomo BONNOLI
INAF - OA Brera

Signature

Tutor:

Prof. Dr. Riccardo PAOLETTI
University of Siena

Signature

Declaration of Authorship

I, Sofia Ventura, declare that this thesis titled, "Non-Thermal Features in TeV-Blazars and the Galactic Center Region with MAGIC and Prospects for CTA" and the work presented in it are my own. I confirm that:

- This work was done wholly or mainly while in candidature for a research degree at this University.

- Where any part of this thesis has previously been submitted for a degree or any other qualification at this University or any other institution, this has been clearly stated.

- Where I have consulted the published work of others, this is always clearly attributed.

- Where I have quoted from the work of others, the source is always given. With the exception of such quotations, this thesis is entirely my own work.

- I have acknowledged all main sources of help.

- Where the thesis is based on work done by myself jointly with others, I have made clear exactly what was done by others and what I have contributed myself.

Signed: *Sofia Ventura*

_____

Date: September 21, 2023

_____

*I remember
my friend Johnny von Neumann used to say,
with four parameters I can fit an elephant,
and with five I can make him wiggle his trunk.*

ENRICO FERMI

OUR Universe is known to be the venue where extreme, powerful and violent phenomena occur in the most compact objects, interstellar and intergalactic space. Its non-thermal behaviour can be seen with the "gamma eyes" of space-based and ground-based telescopes, and the observations performed with these innovative instruments represent the novel research field of the Gamma-ray Astronomy.

On the balance between the *life-and-death* in stars lies the presence of extremely energetic particles, the cosmic rays (CRs), which are accelerated in compact and massive astrophysical sources, and are responsible for the prominent part of the γ-ray emission detected at the Earth position. Several theories have been outlined for explaining how CRs are accelerated, and what are the mechanisms accountable for their diffusion and interaction with the interstellar environment of Our and external galaxies. Many questions are still open regarding the location at which the acceleration occurs, and the flavour's origin of the emission.

In the gamma-ray astronomy the sources under investigation are both galactic and extra-galactic, and the physical processes governing the observed emission are essentially the same, but what changes is the playground in which they work. Indeed, the channels that are responsible for energy losses in CR propagation (*dissipation* mechanisms), are invoked for describing the production of high energy photons (*seeding* mechanisms). With the current γ-ray telescopes many exciting studies on the non-thermal nature of the Universe can be done, including also exotic physics. Many new knowledges on the highest energetic face of the Universe have been achieved and many mysteries have been unveiled in the last two decades, when the gamma-ray astronomy has become increasingly important.

Accompanied to new discoveries there are always new mysteries and questions to answer. With the present date γ-ray telescopes many physical informations can be earned, and in the next generation instruments rely the expectation of finding the solutions to the nowadays unresolvable puzzles and questions, exposed by current operating telescopes.

In this context this project wants to contribute, by analyzing observational data and interpreting the measurements, in simulating synthetic data with the expectation of attaining explanations on the long-standing discussions and debates.

The physical processes and mechanisms responsible for the very high energy (VHE; $E > 100$ GeV) γ-ray emission from active galactic nuclei (AGNs) are still unclear and poor known. The characterization of the non-thermal features in these

sources is a vibrant research field, in which study the variability aspects in blazars, the cosmological origin of the Universe, the strength of the intergalactic magnetic field (IGMF) and its constraint, and the nature of the extragalactic background light (EBL). The extreme side of the Cosmos can further be used to test theories in fundamental physics and "unveil" new messengers of the novel multi-messenger astronomy.

The origin and transport mechanisms of relativistic CRs and their interplay with the interstellar environment of the Galaxy challenge the efforts of the astroparticle community in providing realistic modelling to describe the evolution of the CRs travel throughout the Milky Way, and the γ-ray production. Our Own Galaxy is known to be a strong source of γ-ray diffuse emission associated with the CR propagation within the galaxy. The implementation of increasingly realistic phenomenological models reproducing the γ-ray emission has a key role in the measurements of the γ-ray flux from astrophysical objects, since represents the only method providing the *background model* above which the sources appear.

This work has contributed as part of the multi-year observing campaign of the MAGIC experiment on the BL Lac prototype, BL Lacertae. In this context, the data measured by the MAGIC telescopes, and *Fermi*-LAT satellite have been analyzed and then have been compared with multi-wavelength observations and previous *flaring* activities in order to define the variability pattern of the source.

Moreover, in this project has been investigated the extreme behavior of 1RXS J081201.8 + 023735, an extragalactic source belonging to a peculiar class of blazars, the extreme high frequency peaked BL Lac objects (EBHL). Since the redshift of these objects is low, they represent ideal laboratories where studying the cosmological origin of the Universe, the interplay of γ rays with the IGMF, and testing emission mechanism models, both leptonic and hadronic in origin. In the key science project of the MAGIC collaboration the "hunting" and classification of promising candidates to include in the catalog of extreme blazars have a fundamental role. 1RXS J081201.8+023735 have been detected for the first time in the VHE regime at 5.21 σ significance level, its "discovery" has been presented at the COSPAR 2021 conference, and the source has been included in the TeVcat, the reference catalog of TeV sources, in January 2021.

The violent, powerful and extreme behavior is also a facet of Our Galaxy, and in this framework the Galactic Center region is an intriguing playground where the observed γ-ray emission could arise from several emission channels. Among the suggested scenarios, a definitive explanation seems not to be achievable with currently operating telescopes, and many expectations rely on the next generation imaging Cherenkov telescopes (IACTs), the Cherenkov Telescopes Array (CTA). In this project, the so-called Central Molecular Zone (CMZ) has been considered to test

four phenomenological models of the γ-ray diffuse emission in order to disentangle between the *PeVatron* and *inhomogeneous* diffusion scenarios.

The need to provide increasingly realistic models of the diffuse γ-ray emission has a crucial role in the definition of the *background* model used in the analysis chain of IACT data, and in particular for CTA it is represent a promising opportunity to disentangle among the scenarios. In this project, the unclassified source HESS J1741-302 has been considered to test the impact of different *background* models on the emission that will be measured with CTA. The simulated spectra advise that in the next future a definitive explanation on the Galactic Center intricate panorama could be reached. Moreover, a synthetic population of nowadays unresolved astrophysical particle accelerators residing in the inner parsecs of the Milky Way has been simulated in order to provide a realistic list of sources to include in the second Data γ rays of CTA.

In chapter 1 a short discussion on the novel gamma-ray astronomy is given, and in chapter 2 are described the major physical aspects in the astroparticle and high energy astrophysics research fields, namely a briefly description of non-thermal processes occurring in both the CR and γ-ray physics. In chapter 3 the major astrophysical sources of the galactic and extra-galactic sky have been briefly summarized, stressing the definition of *PeVatron*, diffuse γ-ray emission, and blazars, a subclass of active galaxies known as active galactic nuclei. In chapter 4 the description of the Cherenkov technique is provided, together with a summary review of the two telescopes used in this work, the two MAGIC telescopes located at Roque de Los Muchachos (La Palma island, Spain), the upcoming Cherenkov Telescopes Array, and their analysis chains. The detection and analysis of two BL Lac objects, the BL Lacertae and 1RXS J081201.8+023735 have been reported in chapter 5, while in chapter 6 is extensively studied the impact of the γ-ray diffuse emission in the present date observations, and its key role in the CTA analysis chain. The conclusions of the work and the future developments of the project are illustrated in chapter 7.

Contents

List of Figures

List of Tables

List of Abbreviations

AGN	Active Galactic Nucleus
AMC	Active Mirror Control
BH	Black Hole
BLR	Broad Line Region
CGRO	Compton Gamma Ray Observatory
CCSN	Core Collapse Super Nova
CMB	Cosmic Microwave Background
CMZ	Central Molecular Zone
CoG	Centre of Gravity
CR	Cosmic Ray
CTA	Cherenkov Telescope Array
CU	Crab Unit
DC	Direct Current
DT	Discrimination Threshold
DSA	Diffusive Shock Acceleration
EAS	Extended Air Shower
EBL	Extragalactic Background Light
ERC	External Radiation Compton
EHBL	Extreme High BL-Lac object
FoV	Field of View
FSRQ	Flat Spectrum Radio Quasar
GC	Galactic Center
GP	Galactic Plane
GR	General Relativity
GRB	Gamma Ray Burst
GW	Gravitational Wave
GZK	G Z K
HBL	High BL-Lac object
HE	High Energy
HEALPix	Hierarchical Equal Area isoLatitude Pixelation
H.E.S.S.	High Energy Stereoscopic System
IACT	Imaging Atmospheric Cherenkov Telescope
IBL	Intermediate BL-Lac object
IC	Inverse Compton
IGMF	Inter Galactic Magnetic Field
IR	Infra Red
IRFs	Instruemnt Response Functions
ISM	Inter Stellar Medium
ISRF	Inter Stellar Radiation Field
LAT	Large Area Telescope
LBL	Low BL-Lac object
LC	Light Curve

LSR	**L**ocal **S**tandard of **R**est
LST	**L**arge **S**ized **T**elescope
LUT	**L**ook **U**p **T**able
MAGIC	**M**ajor **A**tmospheric **G**amma-ray **I**maging **C**herenkov
MC	**M**onte **C**arlo
MF	**M**agnetic **F**ield
MHD	**M**agneto **H**ydro **D**ynamic
MM	**M**ulti- **M**essenger
MST	**M**edium **S**ized **T**elescope
MWL	**M**ulti- **W**ave **L**ength
NIR	**N**ear **I**ngra **R**ed
NLR	**N**arrow **L**ine **R**egion
NS	**N**eutron **S**tar
NSG	**N**ight **S**ky **B**ackground
NSBH	**N**eutron **S**tar **B**lack **H**ole
PSF	**P**oint **S**pread **F**unction
PMT	**P**hoto **M**ul**T**iplier
PSR	**P**ul **S**a **R**
PWN	**P**ulsar **W**ind **N**ebula
QE	**Q**uantum **E**fficiency
QLT	**Q**uasi **L**inear **T**heory
RF	**R**andom **F**orest
RoI	**R**egion **o**f **I**nterest
SB	**S**uper **B**ubble
SBG	**S**tar **B**urst **G**alaxy
SC	**S**tellar **C**luster
SED	**S**pectral **E**nergy **D**istribution
SF	**S**tar **F**ormation
SFR	**S**tar **F**ormaton **R**ate
Sgr A*	**S**a **gg**ita **r**ius **A***
SGRB	**S**hort **G**amma **R**ay **B**urst
SiPMT	**S**ilicon **P**hoto **M**ult **T**iplier
SMBH	**S**uper **M**assive **B**lack **H**ole
SMBHB	**S**uper **M**assive **B**lack **H**ole **B**inary
SN	**S**uper **N**ova
SNOB	**S**uper **N**ova **OB** association
SNR	**S**uper **N**ova **R**emnant
SSC	**S**ynchrotron **Self**- **C**ompton
SST	**S**mall **S**ized **T**elescope
SW	**S**tellar **W**ind
TL	**T**rigger **L**evel
UV	**U**ltra **V**iolet
VERITAS	**V**ery **E**nergetic **R**adiation **I**maging **T**elescope **A**rray **S**hower
VHE	**V**ery **H**igh **E**nergy
UHE	**U**ltra **H**igh **E**nergy
UHECR	**U**ltra **H**igh **E**nergy **C**osmic **R**ay
WIMP	**W**eakly **I**nteractive **M**assive **P**article
WR	**W**olf- **R**ailey
YSC	**Y**oung **S**tellar **C**luster

To my baby Abram Giovanni…

Part I

The High Energy Flavor of the Universe

1 Gamma-ray Astronomy

SINCE long-time the scientific community learnt that extreme events occur in Our Universe, characterized by γ-ray emission associated with the violent collision of cosmic rays (CRs) with the interstellar gas, supernova (SN) explosions, or relativistic electrons interacting with magnetic fields (MFs). Only in 1960s, the γ-ray sky became accessible for scientific (unfortunately not only) investigations, dating back the dawn of gamma-ray astronomy when the first balloon satellites were launched, and the very first gamma-ray telescope was carried aboard the US satellite Explorer 11 in 1961. This experiment picked up fewer than 100 cosmic γ-ray photons which appeared to come from all directions in the sky implying a sort of *uniform gamma-ray background* expected to be due to the CR interactions with the interstellar gas. In 1967, the OSO-3 satellite detected the first γ-ray source outside the Milky Way, while only in the 1970s, significant improvements were achieved with the SAS-2 (1972) and the COS-B (1975-1982) satellites, confirming the γ-ray background emission, but the poor angular resolution did not allow to single out point sources. Moreover in the same decade, the defence satellites Vela 5b, Soviet Venera spacecraft and the Pioneer Venus Orbiter, designed to detect γ rays from nuclear bomb blasts, discovered that γ-ray flashes came from outside the Earth and probably from external galaxies. Only at the end of the 20$^{\text{th}}$ century these fast flashes were associated with gamma-ray bursts (GRBs) coming from distant galaxies.

The gamma-ray astronomy became an integral part of astronomical research, when 3 innovative satellites SIGMA, Compton Gamma-Ray Observatory, and Beppo-Sax, provided the astrophysics community with a completely new picture of our Universe, in the 1990s. The Compton Gamma Ray Observatory (CGRO), launched in 1991, provided the first survey of γ-ray sources, and showed that the mysterious bursts are uniformly distributed across the sky implying their extra-galactic origin. One of the 4 detectors onboard of CGRO, was EGRET that provided the very first view of the galactic γ-ray diffuse emission (Hunter et al., 1997). In 2004, NASA launched the Swift satellite (now renamed as Neil Gehrels Swift Observatory) aiming to "catch" GRBs, and the next generation instrument, *Fermi* Gamma-ray Space Telescope, launched in 2008, discovered a lot of new sources emitting only in γ rays, including some pulsars.

The most energetic part of the electromagnetic radiation gives in form of γ rays which are absorbed by the Earth atmosphere, and for directly detecting high energy photons satellite experiments represent the unique possibility. The satellite telescopes have their best sensitivity ranging in the MeVs, and can reach with acceptable systematics few GeVs. The main obstacle to detect higher energies γ rays is given by the mechanical and structural limitations related with size and weight of an instrument to launch to geostationary orbits. Indeed, in this case the calorimeter, which converts photons in pairs later reconstructed as events, cannot be large enough to reconstruct the energy of events originated by primary γ rays with energies above a few hundreds of GeV. On the other hand, the very high energy (VHE; $E > 100$ GeV) photons are accessible from the ground exploiting the Earth atmosphere as a giant natural calorimeter in which γ rays generate electromagnetic cascades characterized by Cherenkov light emission which can be detected by the telescopes' *eyes* sensitive to the blue-UV Cherenkov light (see chapter 4).

The ground-based γ-ray astronomy began its journey in 1989 when Whipple telescope detected TeV γ rays from the Crab nebula, a pulsar wind nebula in Our Galaxy. Exciting new results have been delivered in the last two decades of this century thanks to technological improvements that allowed to provide a deeper insight into a large number of questions in high energy astrophysics and astroparticle physics, with the detection of hundreds new TeV emitters (see chapter 3). In the Whipple era, to detect the Crab nebula at $5\,\sigma$ significance level 25 h of data-taking was required, while current generation imaging atmospheric Cherenkov telescopes (IACTs), like H.E.S.S. (Bolmont et al., 2014; Bernlöhr et al., 2003), MAGIC (Aleksić et al., 2016b; Aleksić et al., 2016a) and VERITAS (Park and VERITAS Collaboration, 2015) need a few minutes of exposure to detect Crab nebula at $5\,\sigma$ significance level. With the next generation array, the Cherenkov Telescopes Array (CTA; Gueta, 2022), the Crab nebula would be detected with $5\,\sigma$ significance in less than a minute, thanks to an order of magnitude improvement in sensitivity compared to present generation telescopes. Moreover, it is expected that the number of detected TeV sources could be around one thousand at the end of the current decade.

The space-based γ-ray telescopes are characterized by large field of view (FoV) allowing to perform *all*-sky survey and mapping the sky. On the other hand, with ground-based γ-ray telescopes, due to the restricted field of view (FoV), only limited region of the sky can be studied with increased angular resolution and the benefit of a large ($\sim 10^{5 \div 6}$ m^2) effective area, partly compensating the photon-starved fluxes at the hundreds of GeV and beyond.(see chapter 3; Aharonian et al., 1997a; Aharonian et al., 1997b.

With "gamma eyes" the aspect of the sky looks strange and unfamiliar. Instead of the constantly shining stars and galaxies observable in the optical band, the gamma-ray sky is replaced by something ever-changing associated with gamma-flashes due to solar flares, supernova explosions, neutron stars merging, black holes'

accretion disk generating jets, jets of active galaxies, and the collisions of CRs with the gas locked in Our Galaxy plane. In this context, gamma-ray astronomy presents unique opportunities to explore the exotic and extreme face of the cosmos, allowing to search for new physics, test theories and perform experiments which are not possible in earth-bound laboratories.

1.1 Gamma-ray Detectors

As said earlier, the gamma-sky can be accessible to our observations with innovative *eyes* installed on space-based satellites and ground-based telescopes. In this section the γ-ray detectors, which data have been used in this work, are briefly introduced. In particular the MAGIC telescopes and CTA are described with deeper details in chapter 4.

The High Energy Stereoscopic System (H.E.S.S.; see fig. 1.1; Bolmont et al., 2014; Bernlöhr et al., 2003) is a system of five imaging atmospheric Cherenkov telescopes, located in Namibia, which operates in the $50\,\mathrm{GeV} \div 100\,\mathrm{TeV}$ energy range, reaching energies well beyond those accessible to satellite-based detectors, typically operating between tens of MeVs up to hundreds GeVs. The stereoscopic system is guaranteed when multiple telescopes view the same air shower. The first 4 telescopes with $12\,\mathrm{m}$ diameter (Phase I) were arranged to form a square with $120\,\mathrm{m}$ side and the diagonal oriented north-south. While for the Phase II a huge telescopes with a primary dish of 28 meters in diameter was added in the centre of the square, increasing the sensitivity and angular resolution of the whole array. This layout allows to cover a great portion of the Cherenkov light pool (chapter 4), with an overall angular resolution of $0.1°$. The $12\,\mathrm{m}$ telescopes have a camera with 980-pixel photomultipliers (PMTs) with a total FoV of $5°$, while the $28\,\mathrm{m}$ telescope has 2048-pixel PMTs encompassing a FoV of $3.2°$.

The Very Energetic Radiation Imaging Telescope Array System (VERITAS; see fig. 1.2; Park and VERITAS Collaboration, 2015) is an array of 4 IACTs operating since 2007 at the Fred Lawrence Whipple Observatory in southern Arizona, and is designed to measure γ rays with energies from ~ 85 GeV up to 30 TeV. Each telescope has a primary dish of $12\,\mathrm{m}$ in diameter and a camera of 499-pixel photo multipliers (PMT), reaching a FoV of $3.5°$. The angular resolution is $\sim 0.06°$ at higher energies, and $\sim 0.16°$ at lower energies. In chapter 5 the analysis of data from BL Lac and 1RXS J081201.8+023735 observed with the MAGIC telescopes, have been combined with *Fermi*-LAT data at lower energies. Even in chapter 6 the VHE γ-ray observations of the Galactic Center (GC) region have been combined with *Fermi*-LAT data of the same region. In this case the analysis chain has been implemented with original personally written codes for analyzing data (a complete description of the

FIGURE 1.1: The High Energy Stereoscopic System (H.E.S.S.) Phase II
array. *Credit: Observatoire de Paris webpage..*

FIGURE 1.2: The Very Energetic Radiation Imaging Telescope Array
System (VERITAS) array. *Credit: VERITAS webpage..*

method is reported in chapter 4 of Ventura, 2018), while in the case of BL Lac and
1RXS J081201.8+023735 the standard analysis has been performed.

The *Fermi* Gamma-ray Space Telescope (*Fermi*; fig. 1.3) is a space-based satel-
lite with two major instruments, the Gamma-ray Burst Monitoring (GBM), and the
Large Area Telescope (LAT), and the data from the latter are used in this work. *Fermi*-
LAT is a pair-conversion instrument sensitive to γ-rays with energies from 20 MeV
to greater than 300 GeV (Ajello et al., 2021).Since August 2008, it has operated con-
tinuously, primarily in an *all*-sky survey mode. Its wide field of view of ~ 2.4 sr pro-
vides coverage of the entire γ-ray sky every three hours. The event reconstruction
is divided in reconstruction event classes – the most used are 128 for point-source
analysis, and 256 for extended source analysis – which are partitioned in two conver-
sion event types, FRONT and BACK, depending on the location of the tracker layer

where the photon-to-pair conversion occurs. Starting from the top of the instrument, the tracker consists of 12 layers of 3% radiation length tungsten converters (FRONT or thin section), followed by 4 layers of 18% radiation length tungsten converters (BACK or thick section). Photons that convert in the FRONT section have intrinsically better angular resolution than those converted in the BACK section[1]. The event type used in this work is FRONT+BACK (`event_type==3`), The *Fermi*-LAT instrumental response function (IRF) is evaluated with a dedicated Monte Carlo (MC) simulation. A large number of incident γ-ray events are simulated in order to cover all possible photon inclination angles and energies. The comparison between the properties of the simulated events within a given event class and the input photons gives the IRFs. The *Fermi*-LAT angular resolution increases with energies, reaching almost $0.1°$ (Atwood et al., 2009; Ackermann et al., 2012b).

FIGURE 1.3: The *Fermi* Gamma-ray Observatory satellite. *Credit: NASA webpage.*.

---

[1]This is due to the fact that multiple-scattering is more likely to occur in thicker material.

2 Astroparticles

$\mathcal{T}$HE origin of cosmic rays (CRs) is of crucial interest in the astroparticle physics since represents a still open question to answer. Primary CRs are accelerated in astrophysical sources and their interaction with the surrounding medium produce secondary γ rays. Cosmic rays and gamma rays reveal the non-thermal and extreme behaviour of Our Universe, featured by explosions and violent collisions, in combination with other cosmic messengers. This chapter is devoted to describe the mechanisms and the physics behind the most important messengers of the very-high energy Sky.

2.1 Cosmic Rays

Energetic elementary particles and nuclei, coming from both the Solar System and interstellar space, hit continuously the top of terrestrial atmosphere. This population of elements are the so-called Cosmic Rays (CRs) featured by a steeply falling, nearly power-law spectrum extending from a few MeV to PeV (Compton, 1933). Primary CRs can be measured directly by spacecraft experiments or on balloons, and in 1912, the first balloon experiments provided the extraterrestrial origin of CRs (Hess, 1912).

Primary CRs interacting with the Earth atmosphere produce fluxes of secondary elementary particles which can be detected at ground level, and underground. Primaries are composed by all stable charged particles and nuclei with lifetimes of order 10^6 years or longer, and the origin of primary CRs is associated with astrophysical sites of particle acceleration. At high energies, even a single primary generates an air shower of secondaries when travels in the Earth's atmosphere, and the cascade can be detected by ground based air-shower detector arrays. These showers can be reconstructed to determine the energy, direction, and composition of the incident particle.

Associated with CRs there are even γ rays and neutrinos. Gamma-ray photons are observed both as diffuse fluxes (steady-state) and transient emission from galactic and extragalactic sources. Energetic neutrinos are thus generated by charged

pions decay cascade produced by CR protons and nuclei that are accelerated in astrophysical sources and interacting with the medium in which diffuse.

CRs are believed to pervade the entire Galaxy as testified by the synchrotron radiation and interstellar γ-ray diffuse emission produced by CR diffusing in the Galaxy (sections 2.1.2 and 3.1.4), and interacting with the galactic magnetic field (MF), interstellar radiation field (ISRF), and the gaseous matter forming the interstellar medium (ISM) (sections 3.1.4 and 6.1.2).

Direct measurements provide informations on the CR composition, energy spectra and arrival directions. The majority of cosmic radiation comes from outside the Solar System[1]. The incoming charged particles are *modulated* by the presence of the Sun and its solar wind generating expanding magnetized plasma that decelerates and partially excludes the lower energy extrasolar CR components, especially the GeV part. This mechanism is known as *Solar Modulation*. Indeed, CRs with rigidity (eq. (2.1)) $R \sim 10$ GV have a Larmor radius (r_{L}) larger than the characteristic dimensions of the Solar System magnetic field structures, and are swept out along the magnetic field lines (Parker, 1965). Solar Modulation can explain the low density of low-energy CRs at the Earth position with respect to that observed in the interstellar space (Stone et al., 2013; Cummings et al., 2016). Moreover, the solar modulation depends on the phase of the solar cycle (an alternating 11-year cycle), showing anti-correlation with the solar activity (Forbush, 1954). Even solar flare eruptions produce energetic particles (*solar energetic particles*) which can reach energies of ~ 100 MeV (electrons), and up to GeVs (ions).

The overall spectrum of CR components can be described in four different ways

1. by particles per unit rigidity, in which propagation and acceleration through cosmic magnetic fields depends on the gyroradius (Larmor radius) or magnetic rigidity R

$$R = \frac{pc}{Ze} = r_{\mathrm{L}} B c \tag{2.1}$$

where r_{L} is the Larmor radius, and B is the magnetic field strength

2. by particles per energy-per-nucleon, where fragmentation of nuclei propagating through the ISM depends on the energy per nucleon, since that quantity is conserved when a nucleus breaks up on interaction with the gaseous matter

3. by nucleons per energy-per-nucleon, in which the production of secondary CRs in the atmosphere depends on the intensity of nucleons per energy-per-nucleon, independently of whether the incident nucleons are free protons or bound in nuclei

---

[1]Apart from particles associated with solar flares.

4. by particles per energy-per-nucleus, where the CR spectrum measurement is related to total energy per particle; air shower experiments that use the atmosphere as a calorimeter measure this quantity (section 4.3).

The units of differential intensity I are $[\mathrm{m}^{-2}\mathrm{s}^{-1}\mathrm{sr}^{-1}\mathcal{E}^{-1}]$, where $\mathcal{E}$ represents the units of one of the four variables listed above (Workman et al., 2022). The intensity of primary nucleons in the energy range from several GeV to ~ 100 TeV is given by

$$I_{\mathrm{N}}(E) \approx 1.8 \times 10^4 \left(\frac{E}{1 \text{ GeV}} \right)^{-\alpha} \frac{\text{nucleons}}{\mathrm{m}^2 \text{ s srGeV}} \tag{2.2}$$

where E is the energy-per-nucleon (including rest mass energy), $\alpha \equiv \gamma + 1 \approx 2.7$ is the differential spectral index of the CRs flux, and γ is the integral spectral index. The differential spectral index variation with energy has been established independently by several experiments above $\sim 10^{15}$ eV to $\sim 10^{18}$ eV, where the slope slightly steepens to $\alpha \sim 3.1$.

The well-know *propagation models* (sections 2.1.2 and 2.1.5) describe the composition and energy spectrum of CRs, in which the sources of the primary cosmic radiation are located within the Galaxy (section 2.1.4; Haungs, Rebel, and Roth, 2003). The ratio of secondary to primary nuclei is observed to decrease with increasing energy, since the lifetime of CRs in the Galaxy decreases with energy (~ 15 Myr).
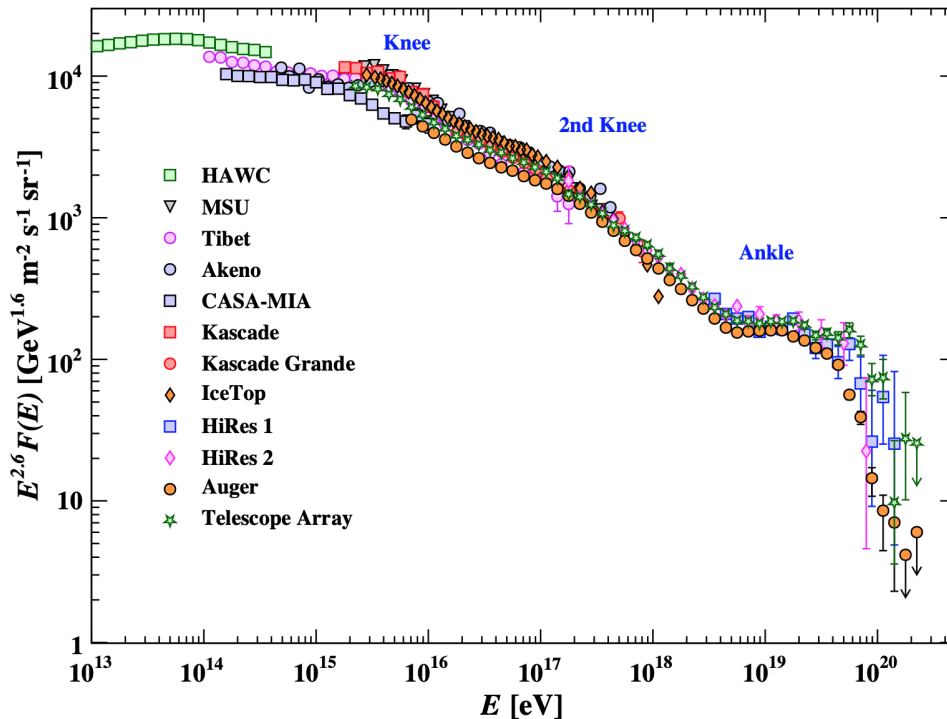
FIGURE 2.1: The all-particle CR spectrum as a function of E (energy-per-nucleus) from air shower measurements (see section 4.1). *Credit: fig. 30.9 in Workman et al., 2022.*

From eq. (2.2) the spectrum of primary CRs is described by a power-law characterized by some peculiar features, the *knee* and *ankle* (fig. 2.1). Assuming the CR spectrum below 10^{18} eV is of galactic origin, the *knee* could reflect the fact that most cosmic accelerators in the Galaxy have reached their maximum energy. As an example, some types of expanding supernova remnants (SNRs) are estimated not to be able to accelerate protons up to energies of 10^{15} eV (CasA; Ahnen et al., 2017a). Thus, propagation and confinement effects active in the Galaxy are claimed to explain the measured spectrum. The KASCADE-GRANDE experiment (Apel et al., 2011) has reported observation of a second steepening of the spectrum near 8×10^{16} eV, with evidence that the structure is accompanied a transition to heavy primaries (nuclei).

On the other hand, concerning the *ankle*, one explanation is the result of a dominant higher energy particles population of extragalactic origin overtaking a lower energy galactic CR flux (Bird et al., 1994). In a different interpretation, this dip structure of the *ankle* region is due to $p + \gamma \rightarrow e^+ + e^-$ energy losses of extragalactic protons on the 2.7 K cosmic microwave radiation (CMB; Berezinsky, Gazizov, and Grigorieva, 2006). The dip structure has been considered as a robust signature of both the protonic and extragalactic origin of the highest energy CRs (Berezinskii and Grigor'eva, 1988). Moreover, it predicts the galactic CRs do not contribute significantly to the flux above 10^{18} eV, which is consistent with the maximum expected range of acceleration by SNRs. Another explanation for the *ankle* region has been advanced by the HiRes and Auger experiments in which the particles above 10^{18} eV are lighter nuclei (mainly protons and helium), implying that the extragalactic CRs have a mixed composition similar to the GeV galactic CRs (Abbasi et al., 2005; Unger et al., 2007; The Pierre Auger Collaboration et al., 2009). On the other hand, if the CR flux at the highest energies is cosmological in origin, the spectrum should be steepen since the Universe is not transparent at energies above 5×10^{19} eV, causing a cutoff energy known as *GZK cutoff*. This cutoff is the result of the onset of inelastic interactions of ultra-high-energy (UHE) CRs[2] with the photons of the CMB (Greisen, 1966; Zatsepin and Kuz'min, 1966).

About 74% of the primary CRs are free protons, and about 70% of the rest are nucleons bound in helium nuclei, and the fractions of the primary nuclei are nearly constant over the whole energy range. Secondaries contribute to increased abundances of rare elements and reduced *even-odd effect* (Workman et al., 2022). Around $10^8 \div 10^{10}$ eV the hadronic component is given by $\sim 87\%$ of protons, 12% of He and $\sim 1\%$ of heavier nuclei (Schlickeiser, 2002). Moreover the measured composition of CRs is different with respect to the Solar System elements abundance, indeed the carbon, hydrogen and helium are *under*-abundant, while nuclei of the Li, Be, B and sub-Fe groups are *over*-abundant by several orders of magnitude (fig. 2.2). The

---

[2]At these energies, CRs lie above the threshold for photopion production.

presence of *antiparticles* (mainly antiprotons and positrons) is another observed discrepancy, which is expected to be due to the *spallation processes* occurring both during propagation in the interstellar space and around sources.
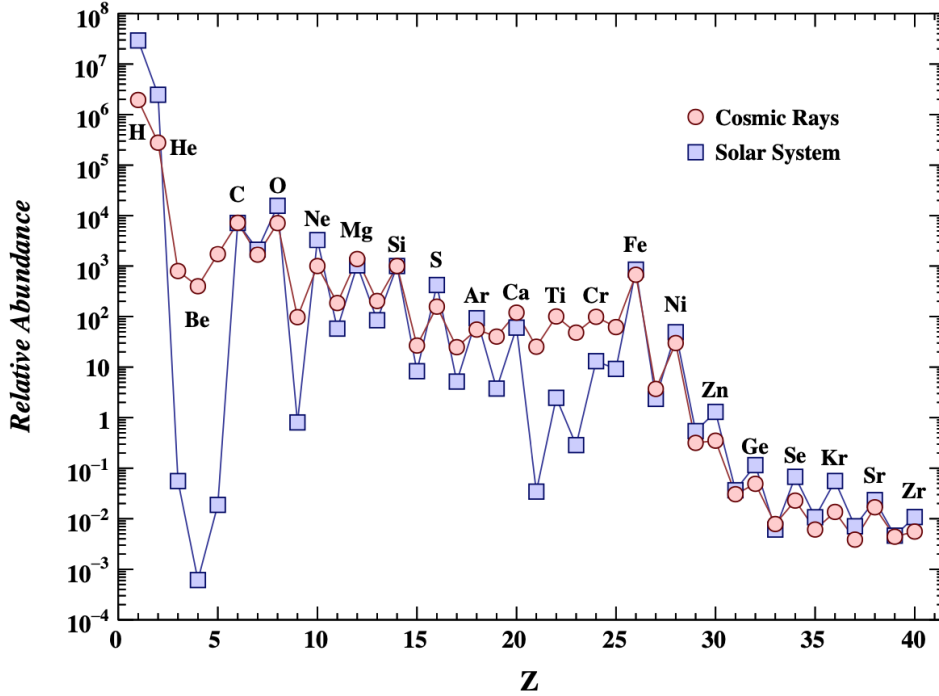
FIGURE 2.2: Cosmic ray elemental abundances compared to abundances in present-day Solar System material. Abundances are normalized to $Si \equiv 10$. CR abundances are from AMS-02 (H, He), ACE/CRIS (Li-Ni), and TIGER/SuperTIGER (Cu-Zr). Solar System abundances are from tab. 6 in (Lodders, Palme, and Gail, 2009). *Credit: fig. 30.2 in Workman et al., 2022 for major details.*

The angular distribution of CRs are nearly isotropic at most energies due to diffusive propagation in the Galactic magnetic field, causing the charged particles trajectories to be tangled by the interstellar magnetic field (section 2.1.3). An upper limit of the order of 10^{-3} on the level of anisotropy in the energy range $10^{12} \div 10^{14}$ eV has been observed by several collaborations (Ambrosio et al., 2003; Abdo et al., 2009; Amenomori et al., 2010; Aartsen et al., 2016; Amenomori et al., 2017; Abeysekara et al., 2019a). This anisotropy could be due to the direction of local galactic MFs, motion of the Solar System in the Galaxy, and the distribution of astrophysical particle accelerators (Greisen, 1966). Moreover at lower energies the angular distribution is strongly affected by the solar modulation, providing anisotropy levels at most of a few percents (Amenomori et al., 2005). Above a few EeV a possible association with nearby active galactic nuclei (AGNs) has been observed by the Auger observatory (Pierre Auger Collaboration et al., 2007).

Recent measurements of the combined electron+positron spectrum at higher energy reveal a relatively smooth spectrum to ~ 1 TeV (Aharonian et al., 2008; DAMPE Collaboration et al., 2017; Archer et al., 2018). Generally the $e^+ + e^-$ spectrum is expected to steepen by a power of E above 5 GeV because of the radiative energy loss effects occurring during the CRs' travel within the Galaxy. Instead, the positron to electron ratio has been measured to increase above 10 GeV (Moskalenko and Strong, 1998) as shown by PAMELA (Adriani et al., 2009a; Adriani et al., 2009b) and AMS-02 (Aguilar et al., 2013; Accardo et al., 2014). Several scenarios are claimed to interpret the electron spectrum structure and the increase in the positron fraction. In the first, individual nearby sources (SNRs or pulsars section 3.1) *pumps* particles above a background suppressed at high energy by synchrotron losses (Nishimura et al., 1997). Other explanations are mechanisms related with propagation effects (Gaggero et al., 2013) or dark matter decay/annihilation processes (Ibarra, Tran, and Weniger, 2013). On the other hand, the significant disagreement in the ratio below ~ 10 GeV is attributable to solar modulation effects near the Earth at the times of measurement.

The measured ratio of antiprotons to protons ($\sim 2 \times 10^{-4}$ at $\sim 10 - 20$ GeV) is related with the kinematic suppression at lower energies of secondary antiprotons (Beach et al., 2001; Yamamoto et al., 2008). Also in this case, the $\overline{p}/p$ ratio is strongly dependent to the solar modulation and solar cycle in the opposite sense to that of the positron fraction (Asaoka et al., 2002). Nowadays, there is no evidence for a significant primary component of antiprotons, as well as no antihelium or antideuteron has been found in the cosmic radiation (Fuke et al., 2005; Abe et al., 2012).

2.1.1 Acceleration Mechanisms

The understanding of the origin of galactic CRs and their diffusion mechanisms throughout the Milky Way are an intriguing research field in high energy astrophysics and in astroparticle physics. The Diffuse Shock Acceleration (DSA) occurring in strong shocks associated with supernova (SN) explosion and represents the only theory capable to fulfill many observational constraints (Berezinskii et al., 1990). This approach can reproduce the power required to maintain the Galactic CR population that is estimated to be a fraction of the energy input in the Milky Way by SN explosions (Ginzburg and Syrovatskii, 1964). The SN explosion itself suffers from adiabatic energy losses, hence the acceleration site must be located in the subsequent SNR phase characterized by particle acceleration through collisionless shock against magnetic turbulences rather than against other particles (Drury et al., 2001).

The very first connection with CRs and SNRs date back to 1930s. Considering appropriate parameters to describe the SN explosion, $\sim 3\% \div 30\%$ of the SNR mechanical energy is transferred to CRs (energetic argument). While the very first mathematical description of the CR spectral shape and the CR density was proposed

by Fermi, 1949, and known as *second order Fermi mechanism*. This theory consists in stochastic scattering of CRs in random moving magnetized cloud ($E_{\text{gain}} \propto v_{\text{cloud}}^2 \rightarrow$), but this approximation explains only the CRs acceleration till few GeVs.

In 1970s the DSA theory was developed to explain the energy transfer from SNe to CRs. In this case, the *Fermi mechanism* is applied to shock wave as the reference frame of the velocity of magnetic turbulence in which particles gain energy through *head-on scattering* with shock front and remain confined around the shock until their Larmor radius is smaller then shock front itself. Consequently, the energy gain is

$$\frac{\Delta E}{E} \sim \frac{4}{3}\beta_{\text{rel}} \tag{2.3}$$

where $\beta_{\text{rel}} = \frac{u_{\text{rel}}}{c} = u_1 - u_2$, $u_1 = u_{\text{shock}}$ is the upstream velocity, and u_2 is the down stream velocity (see fig. 2.3).
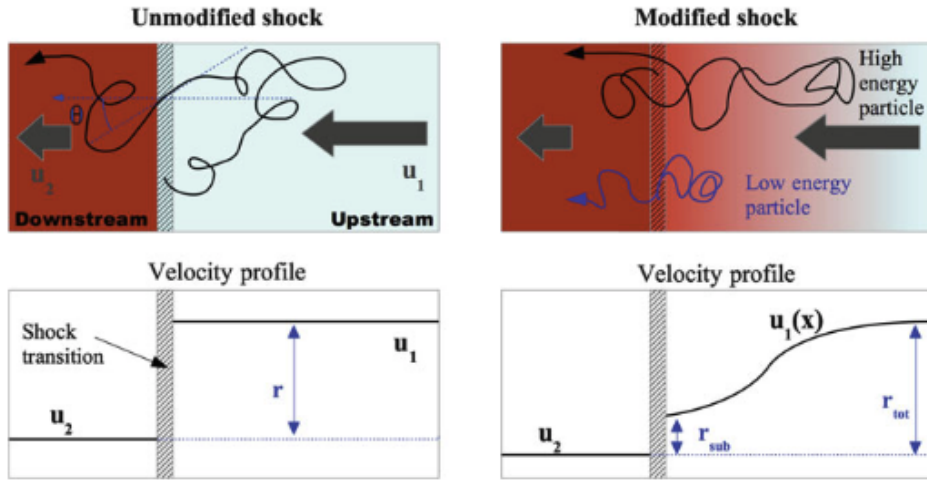
FIGURE 2.3: Cartoon representation of DSA mechanism.
Credit: Giovanni Morlino.

The DSA mechanism provides a power-law spectrum of accelerated CRs as a result of the balance between energy gain ($\frac{\Delta E}{E}$) and escape probability from the source like

$$P_{\text{escape}} = \frac{J_\infty}{J_+} \sim \frac{4u_2}{c} \tag{2.4}$$

and after CRs passed through the front for $k = \frac{\ln(E/E_0)}{\ln(1+\Delta E/E)}$ cycles, the resulting spectrum has the form of

$$N(> E) = \frac{1}{P_{\text{escape}}} \left(\frac{E}{E_0} \right)^{-\delta} \Rightarrow f(E) = \frac{dN}{dE} \propto E^{-\alpha} \tag{2.5}$$

where $\alpha = \frac{r+2}{r-1}$ and $r = \frac{(\gamma_g+1)M^2}{(\gamma_g-1)M^2+2}$. For $M \gg 1$ and monoatomic gas the resulting spectral shape is $f(E) \propto E^{-2}$.

The energy injected by shock acceleration mechanism is thus able sustaining the population of energetic CRs since such population of super-thermal[3] charged particles – with a power-law momentum spectrum – results from properties of a plasma shock wave traveling through a medium in which energetic particles diffuse (Axford, Leer, and Skadron, 1977; Krymskii, 1977; Bell, 1978b; Bell, 1978a; Blandford and Ostriker, 1978). As a consequence, the steady-state power-law spectrum resulting from DSA is independent from the injection spectrum, the details of the interaction processes and the geometry of the shock.

Recent developments of the DSA scenario account for the (non-linear) back-reaction of the accelerated CR on turbulent magnetic field and successfully reproduce a large number of observations, such as the CR spectrum up to the *knee* (Blasi, Amato, and Caprioli, 2007). Indeed, for reaching larger energy ($E_{\max} = 100$ TeV) the presence of magnetic amplification upstream and downstream is invoked. In this framework, shock and accelerated particles become a symbiotic self-organizing system in which CRs exert pressure on plasma (shock rest frame) slowing down thier motion (*precursor*). As a consequence, CRs at right and left side of the shock front feel different compression factor and when most energetic CRs escape the shock, it becomes radiative. This mechanism leads to increase the compression factor curving the spectrum (*harder*). Moreover multi-wavelength observations of SNRs show that more than 50% of the post-shock pressure is produced by CRs suggesting they can significantly affect the properties of the ISM in the shock region (Helder et al., 2009). The presence of non-thermal emission from several SNRs is further observed as *filament* in X-rays[4]. The thickness of $\sim 10 \div 20$ pc in SNR shells is consistent with the idea of synchrotron-limited structure formation in strong magnetic fields (of the order of $100\ \mu$G), which suggests also the acceleration of hadrons up to PeV energies[5]. Non-linear DSA can reproduce Chandra observations of the precursor upstream of the shock in SN 1006, indicating amplifications of the magnetic field by a factor of ~ 10 at the shock level (Morlino et al., 2010).

SNRs hence represent the favourite candidate to be the source class active in the very high-energy (VHE) γ-ray astronomy (section 3.1.1). They can accelerate galactic particle up to energies close to the *knee* of CR energy spectrum (Funk, 2008). A further evidence of CR acceleration by SNRs – especially of its hadron component – may come from the observations of the γ-ray emission from molecular clouds close to active SNR (section 3.1.3; Aharonian, 2004).

Among the sites of non-thermal particle acceleration there are the so-called Super-Bubbles (SB), associations of SNRs and OB-WR stars – that coexist in the same region. In these associations of massive stars, featured by strong stellar winds, tens

---

[3]The plasma velocity is major of the sound speed.

[4]For instance, J1713.7-3946, Cas A.

[5]For instance, the presence of high magnetic fields have been confirmed by the strong-variability observed in J1713.7-3946.

of SN explosions can take place in a few million years. This results in a collective expansion, powered by both the SN explosions and the strong winds of Wolf-Rayet (WR) stars, which produces a bubble of hot tenuous plasma[6] (Mac Low and Mc-Cray, 1988; Binns et al., 2007). The observation of coincidences between SB γ-ray sources, SNRs and OB associations, lead to the SN-OB scenario, where ions are first injected by strong stellar winds and then accelerated at higher energies by the nearby SNR shocks (Ackermann et al., 2011a; Aharonian, Yang, and de Oña Wilhelmi, 2019; Abeysekara et al., 2021; Amenomori et al., 2021b; Morlino, 2021).

Nowadays a few number of galactic source have been found accelerate CRs till PeV energies (Abeysekara et al., 2019b; Amenomori et al., 2019; Cao et al., 2021). In this context the presence of a *PeVatron* in the center of the Milky Way represents a breakthrough in understanding the origin of high-energetic CRs which are accelerated in the vicinity of a supermassive black hole (SMBH), that is Sgr A* in our Galaxy.

2.1.2 Transport Mechanisms

As said earlier, CR spectrum from few GeV/nucleon to the *knee* (~ 10 PeV/nucleon) is well described in the context of DSA and galactic diffusion scenario. DSA predicts a power law (PL) spectrum, with a spectral index close to $\Gamma = 2$, while at Earth position, the observed CR spectral index is $\Gamma \sim 2.7$ (eq. (2.2)). This discrepancy can be explained in terms of energy dependent CR escape time from the Galaxy as expected from diffusion theory. Abdo et al., 2010a, found the signature of proton acceleration in the γ-ray spectrum of some galactic SNRs (section 2.1.1). CRs from 1 GeV to the *knee* (fig. 2.1) have a galactic origin and they are likely accelerated in SNRs, but not only. Propagating throughout the Galaxy, the flux of CRs becomes isotropic because they undergo a random walk due to the turbulent component of the galactic MF hence their motion can be described in terms of the diffusion equation. The CR spectrum is thus the combination of acceleration (section 2.1.1), diffusion (section 2.1.5) and energy-losses mechanisms (section 2.1.6). Despite the strong anisotropy distribution of high-energy sources[7], through to the diffusion mechanism the CR spatial profile shows an high level of isotropy. Then, the discrepancy observed in light elements (namely Li, Be, B) find an explanation in the process of *spallation* occurring during CR travel throughout the Galaxy[8].

In order to explain the observed abundances of the elements, a CR should go through a column density of ~ 5 g cm^{-2} before reaching the Earth. This value, compared to the average column density along a line-of-sight in the Galaxy ($\sim 10^{-3}$

---

[6]The energy contained in the SB magnetohydrodynamic (MHD) turbulence is thought to be converted into nuclei non-thermal energy via Fermi second order acceleration with an efficiency of $\sim 20\%$.

[7]SNRs lie mainly along the galactic plane.

[8]The interaction of heavy CRs with interstellar gas creates lighter nuclei.

g cm^{-2}), leads to the conclusion that CR propagation cannot occur along straight lines. The requirement of some mechanism to confine the particles within the Galaxy is thus required. A simple method to describe CR confinement is the so called *leaky box* model. The CRs are assumed to propagate freely within a cylindrical box and reflected at the boundaries, the loss of particles is defined by a non-zero probability of escape for each hit with the boundary. The spectra of primary and secondary CRs is probed by the leaky box model although the necessity of a more realistic description of the general confinement mechanism. The presence of magnetic field in the Galaxy – with regular and a random component – leads to diffusive propagation explaining the increasing in the escape time. The diffusion equation can reproduce all these processes.

2.1.3   The Confinement Condition

The *isotropization* of CR arrival direction is actuate because of the confinement of CRs within the Galaxy by the magnetic fields, from large to small length scales. The presence of ionized gas in the ISM is the probe of co-living magnetic fields (MFs) in the galaxies structure[9].In Our Galaxy, the energy density of interstellar MFs is comparable to the energy density of diffuse starlight, CRs, and kinetic energy density of ISM, playing a key role among all these components.

The *Faraday rotation of linearly polarized radiation* is invoked to probe the large scale structure of the galactic MF. Pulsars and extragalactic sources – mainly external galaxies – emit linearly polarized radiation which rotates as it passes through regions filled with free electrons, and an embedded magnetic field. Measuring the galaxy rotation is possible to estimate the magnetic field component along the line-of-sight, relying on a model for the electron density distribution (Cordes and Lazio, 2002). The galactic magnetic field consists of a regular part and a turbulent component. The regular field is itself divided into a large-scale disk field – similar to nearby galaxies (Sun et al., 2008) – and a halo field. The regular field follows the spiral pattern of Milky Way, while the halo field is poorly known.

Besides the regular magnetic field coexists the MF random component. Indeed, the particles interaction with this component forces the CRs to undergo a random walk, diverging from the simply spiral propagation along the regular field lines. The equations of Magneto-hydrodynamics (MHD) imply that – for very low resistivity – the field lines are *frozen* in the plasma and follow its motion, namely the *Alfvén theorem of flux Freezing*. In this sense, the random component of the MF is related to the turbulent motion in the ISM, which is observed over a wide range of scales at different wavelengths, from ~ 100 pc down to $\sim 10 \div 6$ pc or less (Berezinskii et al., 1990). A fluid model for turbulence was developed by Kolmogorov, 1991,

---

[9]MFs are active in star forming regions, providing the pressure balance that prevents gravitational collapse of the Galaxy and play a key role in the galaxies as well as galaxy clusters formation.

where some kind of driving energy is injected at large scales and then generates a cascade to smaller scales by interactions between eddies of different size. Each eddy provides energy only to smaller scale, and cascade proceeds at a rate independent with scale[10], until the smallest one in which energy is dissipated by viscosity. This model predicts a power spectrum of the type

$$E(k) = C\epsilon^{2/3}k^{-5/3} \tag{2.6}$$

where ϵ is the energy transfer rate, and k is the inverse of the length scale. The eq. (2.6) describes generally how turbulent kinetic energy is distributed as a function of the assumed scale. Conversely, in Kraichnan, 1965, is developed a different model for the turbulence energy spectrum including the effect of magnetic field. The energy spectrum for Kraichnan MHD turbulence is

$$E(k) \propto k^{-3/2} \tag{2.7}$$

In summary, the driving energy is injected into the ISM at large scale by supernova explosions, for instance, and transported over all the length scales to the smallest one via turbulent energy distribution, through Kolmogorov-like or Kraichnan-like spectrum, which connect large scales to small ones (Armstrong, Rickett, and Spangler, 1995).

2.1.4 The Source Term

The most important aspect in understanding the origin of CRs is the site in which charged particles are accelerated to high, very-high and ultra-high energies (section 2.1.1). An extended description of galactic sources responsible for the acceleration processes is presented in chapter 3.As mentioned above SNRs are the privileged candidates with other different astrophysical sites of particle acceleration, such as pulsars, pulsar wind nebulae, OB associations and stellar clusters (section 3.1). The exigence to include many other types of sources is based on the evidence that the SNRs spatial distribution is uncertain, while different astrophysical environments are better know and easily observed.

On the other hand, another important research field in the astroparticle community is the study of the origin of the highest energetic CRs (UHECRs) above 10^{18} eV. These particles are thought to be produced in relativistic jets of powerful active galactic nuclei (AGNs; section 3.2). The dub *"espresso"* mechanism is responsible for such acceleration. Galactic CRs (*seed*) penetrate the jet sideways receiving a *boost* of a factor of Γ^2 in energy, where Γ is the Lorentz factor of the relativistic flow. Powerful blazars (section 3.2.1.1) with $\Gamma \sim 30$ may accelerate UHE CRs up to more than 10^{20} eV. In agreement with recent Pierre Auger Observatory measurements (Aab et

---

[10]That because cascade is local in the Fourier space.

al., 2014), the chemical composition of *espresso-accelerated* UHE CRs is the same of the galactic CR*knee* proton-dominated at 10^{18} eV, and increasingly heavy at higher energies (Caprioli, 2015).

2.1.5   The Diffusion Equation

As understood so far, CRs are charged particle accelerated in astrophysical sites and traveling throughout a magnetized plasma extremely collisionless. in the *quasi-linear theory* (QLT), the *diffusion equation* is the standard way to describe how CRs moving and propagating within the Galaxy, starting from the Vlasov equation (Berezinskii et al., 1990). This is an approximation based on the separation between electric and magnetic field into their average values of both, and the random fluctuations corresponding to an ensemble of waves with random phases. In this context, CR diffusion can be described in terms of scattering process onto the magnetohydrodynamical fluctuations of the interstellar plasma, where the scattering is a *resonant* process between particle and the magnetic wave that occurs when wavelength and Larmor radius of the particle are of the same order.

The most relevant modes are *Alfvén wave*, in which are only involved oscillations of the magnetic and velocity field. In particular, a perturbation in the plasma velocity perpendicular to the external field B_{average} *bends* the magnetic field lines like a violin string, and the magnetic tension provides the restoring force. CR scattering is thus efficient only under resonant condition in which the outgoing oscillations propagate with wave vector k parallel to the external MF lines, as shown by

$$\omega(\mathbf{k}) = \pm k_{\parallel} c_{\mathrm{A}} \tag{2.8}$$

where $\mathbf{k}$ is the wave vector and c_A is Alfvén velocity

$$c_{\mathrm{A}} = \frac{B_{\mathrm{average}}}{\sqrt{4\pi\rho}} \tag{2.9}$$

where ρ is the mass density of the charged particle in the plasma. The Alfvén waves propagate in the direction of the MF, while magnetosonic waves propagate in the perpendicular direction, and the restoring force is the magnetic pressure which is itself directed perpendicularly to the field. Hence, the waves with k parallel to the average component of B_{average} propagate as sound waves driving the interaction of CR particles with Alfvén waves. From that follows the first form of CR diffusion equation

$$\frac{\partial f}{\partial t} = \frac{\partial}{\partial z} D_{xx} \frac{\partial f}{\partial z} + \frac{1}{p^2} \frac{\partial}{\partial p} p^2 D_{pp} \frac{\partial f}{\partial p} + Q \tag{2.10}$$

where f is the probability distribution function of particles in an average volume, D_{xx} is the spatial diffusion coefficient and D_{pp} is the diffusion coefficient in the momenta space. D_{pp} is dependent on rigidity and *re*-acceleration, and so on c_{A}, while

D_{xx} yields a rigidity dependence, but its definition is still under discussion since it is strongly dependent on the model used to describe the turbulence in the ISM. In the QLT , the relation between D_{pp} and D_{xx} is

$$D_{pp} \sim \frac{p^2 c_{\mathrm{A}}^2}{D_{xx}} \tag{2.11}$$

The Q term in eq. (2.10) is the source function, which includes primaries injected by sources into the interstellar space (sections 2.1.4 and 3.1), and secondaries from spallation or decay.

Since the CR escape is predominantly along the perpendicular direction of the galactic disk and regular magnetic field component, the eq. (2.10) can be written in terms of parallel and perpendicular diffusion coefficients (for major details see chapter 2 in Ventura, 2018).

For small fluctuation of the regular magnetic field, the perpendicular diffusion coefficient is related to the parallel one as follow

$$D_\perp = D_\parallel \left(\frac{\delta B}{B} \right)^4 \tag{2.12}$$

where δB is the amplitude of the random field at the resonant wave number $k = r_g^{-1}$, and $r_g = pc/ZeB$ is the particle gyroradius. The spectral energy density of interstellar turbulence has a power-law profile $w(k)dk \approx k^{-2+\delta}dk$, where $\delta = 1/3$ over a wide range of wave numbers (Elmegreen and Scalo, 2004). This provides a diffusion coefficient in term of

$$D_{xx} = D_0 \beta \left(\frac{R}{R_0} \right)^\delta \tag{2.13}$$

where R_0 is the rigidity scale and $D_{xx} \approx 2 \times 10^{27}$ cm^{-2} s^{-1} for CRs with a rigidity $R < 10^8$ GV. The D_{xx} value is the result of the B/C measurements.

The Kolmogorov-like spectrum ($\delta = 1/3$) may refer only to some part of the MHD turbulence, indeed an exponent $\delta = 1/2$, typical for the Kraichnan-type turbulence, may also apply to the ISM (Yan and Lazarian, 2004), and returns $D_{xx} \propto R^{1/2}$. However, if the CR data are consistent with $\delta = 1/3$ or $\delta = 1/2$ is still an open question. Moreover, the scattering of CR particles on randomly moving MHD waves leads also to stochastic *re*-acceleration. The presence of galactic winds in many external galaxies may suggest that convective (advective) transport may play a role determining the propagated CR spectrum. However, for reasonable choices of the wind velocity this effect has a negligible role for energies larger than 10 GeV.

2.1.6   Energy Losses

Moving throughout the Galaxy, CRs interact with the interstellar gas leading to several energy-losses channels. The leptonic (electrons and positrons) component undergoes to *non-thermal bremsstrahlung* (*free-free* process), *Inverse Compton* (IC), and *Synchrotron Emission*. On the other hand, for CR nucleons energy losses are mainly due to *ionization*, *Coulomb scattering*, *fragmentation* and *radioactive decay*. Generally, leptonic and hadronic interaction processes lead to the production of secondaries[11]. Studying these mechanisms permit to understand the properties of CR transport (section 3.1.4).

CR electrons produce synchrotron radiation (mostly in the radio band) and IC emission from their interaction with the magnetic field and interstellar radiation field respectively. They also give rise to bremsstrahlung emission (in the γ-ray domain) via interactions with the gaseous matter of the ISM. While the nucleon-nucleon interactions are of great interest because they lead to the production of secondaries like nucleons (both stable and unstable), antinucleons and mesons, with final products like γ rays, $e^{\pm}$ and neutrinos.

The stable secondaries to primary ratios bring information on the number of interactions which primaries underwent during their propagation, giving the opportunity to study the propagation mechanism. The reference ratio is always B/C because boron is entirely of secondary origin, the systematic errors are low up to high energies, and the cross sections for its production from C, N and O are well known. The B/C ratio is used to constrain the diffusion coefficient D_0 and the power-law dependence on rigidity (eq. (2.13)), *re*-acceleration affects as well the energy dependence of the B/C ratio, especially below few tens of GeV/nucleon.

The unstable secondaries to primary ratios are used as radioactive clock since providing information about the CR spent time in the Galaxy. ^{10}Be is the longest lived and best measured unstable secondary. The ^{10}Be/^{9}Be ratio indicates residence times of the order $10^7 \div 10^8$ years. This ratio and the B/C ratio provide an estimate on the half-height of the propagation halo ($\sim 4 \div 20$ kpc) in some diffusive-halo-models (Strong and Moskalenko, 1998)[12]. Moreover, some isotopes are produced in explosive nucleosynthesis by SNe, such as ^{59}Ni (decay time 7.5×10^4 years), ^{57}Co (decay time 0.74 years) and ^{56}Ni (decay time 6 days). These elements decay only by electron capture. If acceleration occurs before their decay, it is then suppressed, for instance, ^{59}Ni is not observed (Wiedenbeck et al., 2000). A reasonable conclusion is that CRs do not come from SN ejecta during the explosion, but from sub-sequent acceleration of matter in the SNR expansion, which may be even a probe in support of the Super Bubble scenario (sections 2.1.1 and 6.4).

---

[11]Secondaries are either CRs or electromagnetic radiation.

[12]The Local Bubble can influence this determination, since secondaries might be underproduced in the gas-depleted region around the Sun leading to an overestimation of the propagation volume (Donato, Maurin, and Taillet, 2002).

Even most of the antiprotons are of secondary origin (Mitchell et al., 1996), and produced by nucleon-nucleon interactions in the ISM (Adriani et al., 2010). But the measurements of $e^+/(e^+ + e^-)$ show a rise above 10 GeV which is difficult to interpret as secondary in origin. Several scenarios have been proposed to explain the observed feature, for instance, the presence freshly accelerated dark matter particles from nearby sources like SNRs or pulsars interacting with nearby interstellar clouds (Grasso et al., 2009).

2.2   Gamma Rays

This section is devoted to the description of the processes leading to gamma-ray production. As seen in previous section, CRs accelerated in astrophysical sites, either galactic or extragalactic, are responsible for the observed γ-ray emission (sections 3.1 and 3.2). The fundamental difference between CRs and γ rays is the information on the source location carried by photons, since they are neutral and their trajectory is not untangled by galactic and extragalactic magnetic fields. At the Earth position, the *isotropization* of CR arrival direction, due to propagation effects within the Galaxy, losses every kind of informations on the position of sources accelerating such particles. In contrast, photons travel "almost" linearly from the emitter to us, bringing a precious information on the origin of particles producing the measured γ rays.

Here, are summarized the principal non-thermal mechanisms involved in gamma-ray production. Note that such channels that are responsible for energy losses in CR propagation (*dissipation* mechanisms), in contrast the same are invoked for describing the production of high energy photons (*seeding* mechanisms).

Relativistic Bremsstrahlung Radiation

When a charged particle (usually electron) passes in the vicinity of the proton (or ion) electric field the Coulomb force of the second deflects the particle, and due to energy conservation, the lost *braked* energy is emitted as a high-energy photons in hard X-rays and soft γ rays till ~ 2 MeV. That is a *free-free* process since the electrons are free after and before the braking, and the resulting spectral shape is continuous. One example of Bremsstrahlung radiation is the diffuse light emitted by the hot intracluster gas of galaxy clusters, like Coma cluster (fig. 2.4).

Synchrotron Radiation

High-energy (relativistic[13]) electrons moving in a magnetic field, with velocity perpendicular to its lines, produce synchrotron radiation since they are accelerated by the MF itself, spiralling around its lines (Carr, Desch, and Alexander,

---

[13]The radiation emitted by nonrelativistic electrons is referred to as cyclotron radiation.
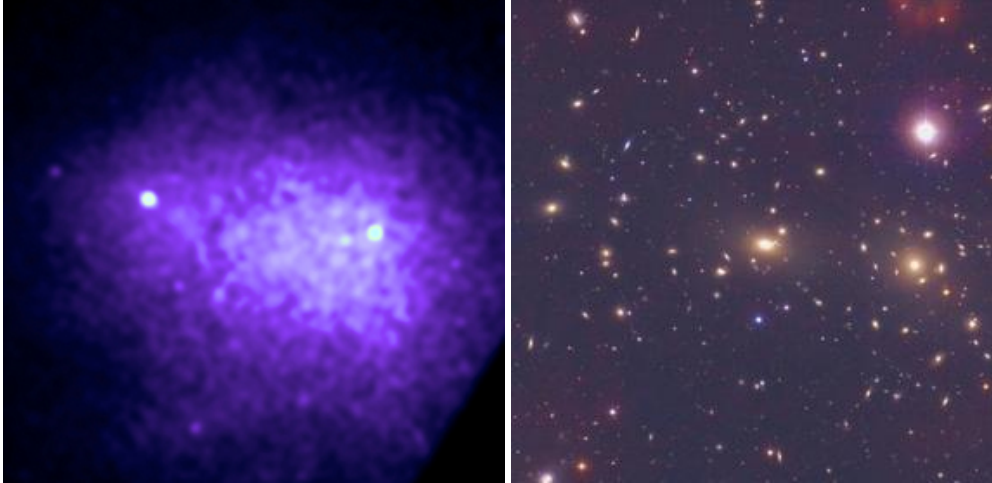
FIGURE 2.4: *On the left*:Chandra X-ray image of Coma cluster. *Credit: NASA/CXC/SAO/A.Vikhlinin et al. On the right: Hubble view of Coma cluster. Credit: Omar Lopez-Cruz & Ian Shelton, NOAO/AURA/NSF.*

1983). The emitted photons have the frequencies determined by the speed of the electron at that instant, and the resulting synchrotron emission spectrum is the sum of the emission spectra of individual electrons. As the electron spirals around the magnetic field, it emits radiation over a range of frequencies peaking at the critical frequency ν_0, and longer electron travels around the magnetic field, more energy it loses, narrower the spiral it makes, and longer is the wavelength of ν_0. The emitted radiation is *beamed* since it is confined to a narrow cone pointing in the direction of the motion of the particle, and it is also polarised in the plane perpendicular to the MF. The degree and orientation of the polarisation providing information about the magnetic field of the source, and the characteristic of the spectrum of synchrotron radiation is the flux steadily declines with frequency as

$$F \sim \nu^{\alpha} \tag{2.14}$$

where α is the spectral index for the emitting object (between -3 and 2.5). The synchrotron radiation lies in a broad energy range of the electromagnetic spectrum, from radio to visible, ultraviolet and X-ray wavelengths, depending on the energy of the electron and the strength of the MF. Typical astrophysical sources are radio galaxies (section 3.2.2), pulsars (section 3.1.2), and active galactic nuclei (AGN; section 3.2.1)

Inverse Compton Scattering

The scattering of ultra-relativistic electrons on low energy photons which are up-scattered to higher energies, since the energy is transferred by the electron (losses energy) to the photon (gains energy). In Blumenthal and Gould, 1970 was first derived the energy spectrum of IC scattering. Since the frequency of

the scattered photons is $\nu \approx \gamma^2 \nu_0$, in astrophysical environments, electrons has a Lorentz factor $\Gamma \, 100 \div 1000$, and consequently they scatter any low energy photons to very much higher energies.

Waveband	Frequency (Hz) ν_0	Scattered Frequency (Hz) & Waveband
Radio	10^9	$10^{15} = \text{UV}$
Far infrared	3×10^{12}	$3 \times 10^{18} = \text{X-rays}$
Optical	4×10^{14}	$4 \times 10^{21} \equiv 1.6\,\text{MeV} = \gamma\text{-rays}$

TABLE 2.1: For astrophysical in origin electrons with $\gamma \sim 1000$.

The resulting intensity spectrum of scattered photons by power-law energy spectrum of electrons is

$$I(\nu) \propto \nu^{\frac{p-1}{2}} \tag{2.15}$$

Every astrophysical sites of particle acceleration are good candidate to be responsible for IC scattering, especially when ultra-relativistic particles scatter on CMB photons.

Neutral Pion Decay

It is decay of neutral pions created in collisions between relativistic protons and nuclei of atoms and ions of the interstellar gas.

$$p + p \rightarrow \pi^+, \pi^-, \pi^0 \tag{2.16}$$

Charged pions decay in muons and neutrinos, while neutral pions decay into pairs of γ rays in only 1.78×10^{-16} s

$$\pi^0 \rightarrow \gamma + \gamma \tag{2.17}$$

The cross-section for the production of neutral pion is $\sigma_{pp \rightarrow \gamma\gamma} \approx 10 \div 30$ fm^2 and the emitted γ rays have an energy of ~ 70 MeV in the π^0 reference frame (see sect. 20.1 in Longair, 2011). This is the process responsible for the continuum (diffuse) emission of the interstellar gas at energies above 100 MeV (cfr. section 3.1.4 and chapter 6). If the mean number density of the ISM is $N \sim 10^6$ m^{-3}, and the average energy density of CR protons – with $E > 1\,\text{GeV}$ – is $\sim 10^6\,\text{eV}\,\text{m}^{-3}$, the γ-ray luminosity of the disc of our Galaxy (galactic plane) is $\sim 10^{32}$ W, as observed.

Electron-Positron Annihilation

This process is responsible for the 0.511 MeV line observed in the spectra.

$$e^+ + e^- \rightarrow 2\gamma \tag{2.18}$$

Positrons are created in the decay of positively charged pions (π^+) which are created in collisions between CR protons and nuclei of the interstellar gas. Since the production of all pions is roughly equal in number, the flux of positron can be estimated from the γ-ray luminosity of the galactic plane.

A second process is the decay of long-lived radioactive isotopes created by nucleosynthesis in supernova explosions. As an example, the $\beta+$ decay of ^{26}Al formed in SN explosions and then ejected into the ISM where the decay results in a flux of interstellar positrons.

A third process is the creation of electron-positron pairs through photon-photon collisions.

$$\gamma\gamma \rightarrow e^+ + e^- \tag{2.19}$$

This process is of considerable importance in compact γ-ray emitters, and results an important source of opacity for very-high-energy (VHE) γ rays, that are absorbed when passing in a strong radiation field at lower energies[14]. Moreover large fluxes of positrons could be generated through $\gamma\gamma$ collision in the vicinity of AGNs.

2.2.1   The Signature of non-thermal processes

This section is organized to be an overview of the main mechanisms active in the astrophysical environments also at the very high energies in gamma rays[15].

Synchrotron Self-Compton (SSC) and External Radiation Compton (ERC)

The first signature of a non-thermal process responsible for the entire spectral energy distribution (SED) of sources, such as AGNs, especially BL-Lac objects (sections 3.2.1 and 3.2.1.1), or Gamma Ray Bursts (GRB; section 3.2.2), observed at all wavelengths, from radio up to VHE γ rays, is the so-called *Synchrotron Self-Compton* (SSC, *leptonic* model). The presence of polarized emission from these sources is a probe in favour the existence of synchrotron processes. SSC is the combination of two mechanisms, the synchrotron radiation and Inverse Compton, where the same relativistic electrons that radiate synchrotron

---

[14]Such as CMB, starlight and infrared emission of dust, as in the Galactic Centre region.
[15]Sikora, 1997, for a review.

photons (*cooling* process) scatter these synchrotron seed photons to high energies (*heating* process, Comptonization of the lower energy photons), forming a distinct spectral shape (Meszaros, Rees, and Papathanassiou, 1994; Ghisellini, Haardt, and Svensson, 1998). The low-energy component, from radio to X-rays, is ascribed to synchrotron radiation (*synchrotron peak*), and the high-energy component, from X-rays to gamma rays ($\sim$ MeVs up to TeVs), arises from the Inverse Compton process (*IC peak*). In fig. 2.5 the SED of various types of blazars, a subclass of AGNs, is shown (section 3.2.1). It is referred to as the so-called *blazar sequence* which is a unified theory to explain the spectral features of these sources at different energies.
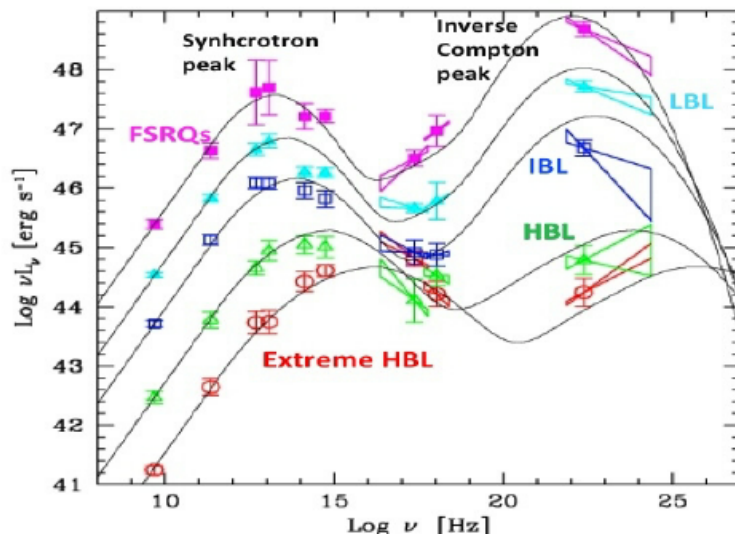
FIGURE 2.5: Overall SED of blazars, AGN type objects described in section 3.2.1. Note the differences of the relative intensities and frequencies of the two emission peaks for various types of objects. This behavior is referred to as *blazar sequence* (see section 3.2.1.1). *Credit: Fossati et al., 1998.*

In the SSC model the connection of both the low-energy and high-energy components is in the location of the emitting region considered as a *single zone* filled by a single population of relativistic electrons accelerated in a blob of plasma which itself moves relativistically outwards from the core of the source (Ghisellini and Maraschi, 1996; Mastichiadis and Kirk, 1997; Tavecchio, Maraschi, and Ghisellini, 1998).

Since the nature of the IC-scattered seed photons is still not clear, several models are proposed to explain the observed γ-ray emission from AGNs. In particular, the Comptonization of the lower energy photons could also arise from those in external regions to the jet, like UV radiation from the accretion disk or from the emission-line region (Sikora, Begelman, and Rees, 1994), or IR radiation from torus dust (Błażejowski et al., 2000). The External Radiation Compton (ERC) model is more applicable for describing the SED of Flat Spectrum

Radio-Quasars (FSRQs), a subclass of AGN (section 3.2.1), in which the presence of strong optical-UV radiation fields provide sufficient seed photons.

Hadronic and Lepto-Hadronic Scenarios

Production of γ rays is also predicted by the so-called *hadronic* models, where ultrarelativistic electrons/positrons are injected by UHE protons since in acceleration processes both particles are released by shocks in jet of extragalactic source (Mannheim and Biermann, 1992; Mannheim, 1993). The high energy radiation arises from several mechanisms of primary particle energy conversion, such as direct synchrotron radiation of protons, proton-photon and photomeson production, and nuclear collisions. The first three processes are known to be very inefficient because they become important only for protons with energy of $\sim 10^5 \div 10^7$ TeV, strong magnetic fields of $\sim 10 \div 100$ G – for the proton-synchrotron process – and small electron density to avoid overprediction of the low energy SED hump.

In the hadronic scenario the high-energy SED component is due to the proton-synchrotron radiation (Aharonian, 2000; Mücke and Protheroe, 2001), while the low energy component is the result of the electron-synchrotron described above. In this scenario the proton density has to be high enough in order to get efficient the photohadronic production of secondary particles that can then contribute to the VHE γ-ray component (Cerruti et al., 2015). The main photohadronic processes are photon-meson and Bethe–Heitler pair production:

$$
p + \gamma \rightarrow
\begin{cases}
p' + n^0\pi^0 + n^-\pi^- + n^+\pi^+ \ldots \\
n + n^0\pi^0 + n^-\pi^- + n^+\pi^+ \ldots
\end{cases}
, \quad \text{photomeson production}
$$

$$
p + \gamma \rightarrow p' + e^+ + e^- \qquad , \quad \mathrm{Bethe - Heitler pair}
$$

$$
\begin{cases}
\pi^0 \rightarrow \gamma\gamma \\
\pi^\pm \rightarrow \nu_\mu \mu^\pm \\
\mu^\pm \rightarrow \nu_\mu + \nu_e + e^\pm \\
e^+ + e^- \rightarrow \gamma\gamma \\
\gamma\gamma \rightarrow e^+ + e^-
\end{cases}
, \quad \text{cascade}
$$

$$\tag{2.20}$$

For the photomeson production, the radiation targets are the near/mid-IR and the synchrotron radiation fields. The first is associated with the hot dust close to the core, and the second is produced by accelerated primary electrons in the jet of a source[16]. After the collision of ultrarelativistic protons[16] with these soft photons, the main product are pions. They take about 30% of the proton energy and convert it to photons, neutrinos, and through muons, into electrons, positrons and other neutrinos. The injected photons are absorbed by

---

[16]These protons have sufficient energy above the threshold for the secondary particle production.

the same soft photons producing pairs, which have with electrons/positrons – injected by muons – Lorentz factors $\Gamma \sim 10^{11}$, and for such energies, Compton scattering with the ambient radiation field takes place in the Klein-Nishina regime. Therefore, the synchrotron radiation represents the main energy losses channel for these ultrarelativistic particles. The subsequent radiation is still energetic enough to produce two more generations of photons and pairs. The final outputs of this synchrotron-supported pair cascade are γ-ray photons at VHEs, featured by the cutoff due to the absorption of $\gamma\gamma$-pair production process (*opacity* effect)[17].

The weakness of the photomeson model is the requirement of fine tuning in order to predict the luminosity peak above MeV energies. That because, after 3 pair generations, the location of the peak depends on the 6th power of the maximum proton energy. This model can reproduce the higher energy component, but is not able to explain how to obtain the hard X-ray spectral component after three generations of the pair cascade process (Svensson, 1987).

Several tentative explanation are proposed, as the transition from softer γ rays to harder X-rays resulting from a break in the pair production function (Mannheim, 1993). But, the external UV and IR radiation fields cut the γ rays spectrum at GeV-TeV energies. Furthermore, another critical point for the photomeson production is the evidence that the observed IR radiation density in low luminosity extragalactic sources[18] is to low to support the proton energy losses in measured short time scales ($< 1\,\text{h}$) (Protheroe and Biermann, 1997). In contrast, different theoretical approaches invoke the collision of less energetic protons with ambient gas. The output of this channel is the same of photomeson production: electrons/positrons, photons and neutrinos, but to be efficient the gas column density has to be of order $n_{\text{H}} \sim 10^{26}\,\text{cm}^{-2}$, for instance when the jet crosses clouds, or atmosphere of bloated stars, or stellar winds (section 5.2.1; Bednarek, 1993; Dar and Laor, 1997). The weakness of these interpretations is that relativistic protons, before colliding with the nuclei, may easily suffer deflections by strong magnetic fields resulting in a lack of collimation of the produced radiation after pp collisions[19].

On the other hand, in the lepto-hadronic models the SSC component due to the primary electrons can also contribute to the high-energy spectrum of extragalactic sources (Cerruti et al., 2015). The weakness of these models is that a very high luminosity of the proton population is required to reproduce the

---

[17]The cutoff energy is ~ 30 GeV in FSRQs, as determined by external UV radiation, and ~ 1 TeV in low luminosity BL Lac objects, as determined by IR radiation of dust (Protheroe and Biermann, 1997).

[18]*e.g.* BL Lacs, see section 3.2.1.1.

[19]The observed VHE γ-ray emission is extremely collimated to small solid angle in blazars, for instance (section 3.2.1.1).

observed SED. Such higher luminosity is guaranteed by super-Eddington accretion rate by the central engineer of a bright extragalactic source[20] (Zdziarski and Bottcher, 2015). In fig. 2.6 a comparison of the lepto-hadronic and purely leptonic model interpretations for the bright nearby AGN Markarian 421 (Mrk 421) is displayed. Both models can naturally reproduced the observed SED.
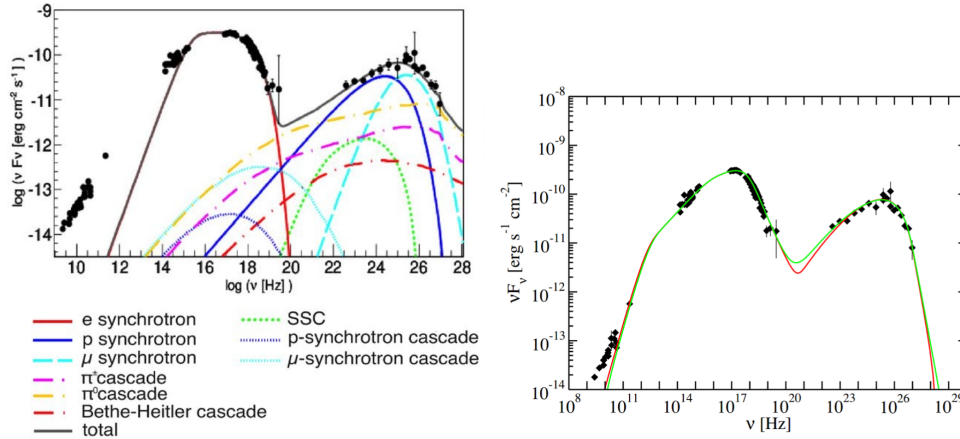
FIGURE 2.6: Lepto-hadronic model vs Leptonic model interpretation of the Mrk 421 SED in its quiescent state. Black points represent the observed data in both plots. *On the left* the black continuous line is the total lepto-hadronic model, while other lines represent the contribution from several emission channel labeled in the caption. On the right red and green lines represent the single zone SSC model compute at different values of timescale variability, one day and one hour respectively. *Credit: On the left, fig. 1 in Cerruti et al., 2015. On the right, fig 11 in Abdo et al., 2011a.*

2.3 The Multi-Messenger Era

Nowadays, in the gamma-ray astronomy other *messengers* bring informations about the nature of galactic and extragalactic sources, the origin of violent and powerful phenomena, and nonetheless on the story of Our Universe. This is the time of the dubbed *MultiMessenger Era*. In this section are summarized the most important research fields of this new branch in astroparticle observation of the Universe.

Neutrinos

Astrophysical neutrinos are important *cosmic messenger* strictly related and associated with CRs, γ rays and the extreme non-thermal Universe. They are associated with supernova explosions (Ando and Beacom, 2005), the decay of secondary CRs (section 2.1.6), DM annihilation, the accretion mechanisms

---

[20]As an example, FSRQs and LBLs are among this class of sources. For major details see section 3.2.1.

in AGNs (Stecker et al., 1991), processes featuring Star Burst Galaxies (Ambrosone et al., 2022), and finally even with extended sources, such as the Galactic Centre region (Gaggero et al., 2015b) and the Fermi Bubbles (Lunardini and Razzaque, 2012). The decay of secondary CRs and the presence of strong and very strong magnetic fields are among the mechanisms responsible for the *oscillation* of neutrino flavours. The measurements of such ratio at the Earth position with neutrino experiments can give informations on the production processes and the environments releasing them. Moreover, for energies above 100 GeV the Universe starts to become *opaque* to gamma rays ($\gamma\gamma$-absorption; section 2.2), and neutrinos represent the unique chance to study phenomena in the PeV and EeV regime.

Like for gamma rays, neutrinos travel through the cosmos unmodified (except for redshift energy losses and flavour oscillations) and without significant deflections by MFs. Since they are very tiny interacting with matter, a cross-check with informations coming from other cosmic messengers, as CRs, γ rays and gravitational waves is required. The first detection of extra-solar neutrinos is associated with the explosion of SN1987A, but only in 2013 the IceCube experiment reported the first detection of extraterrestrial neutrinos in the energy range 10 TeV $\div 2$ PeV (IceCube Collaboration, 2013). Additional observations have shown that these events had angular and energy distribution consistent with extragalactic origin (Kopper and IceCube Collaboration, 2017). Nowadays, the neutrino astronomy is possible and the combination of the informations bring by different messengers have been started to the MultiMessenger Astronomy. For a review see Pisanti, 2019. Moreover the detection of neutrinos in coincidence with a blazars (Ansoldi et al., 2018) promoted the hadronic or mixed processes to be responsible for the VHE non-thermal emission in blazars (section 5.3 and fig. 5.20).

Very recently high-energy neutrinos from the galactic plane of Our Galaxy, associated with extended sources, have been observed by the IceCube experiment (Icecube Collaboration et al., 2023). The presence within the Milky Way of these energetic messengers is evidence that Our Galaxy is the place where PeV particle accelerators lie.

Gravitational Waves

The first multimessenger observation of a source was independently detected in gamma rays by *Fermi*-GBM and INTEGRAL SPI-ACS satellites, and gravitational waves by Advanced LIGO and Advanced Virgo. (LIGO Scientific Collaboration, Abbott, et al., 2017) This event is known as *kilonova*, associated with the merging of two neutron stars (NSs).

Gravitational waves (GWs) are emitted from systems with accelerating quadrupole

moments, and detectable sources are expected to be compact objects. Generally, the astrophysical sources emitting in γ rays are associated with distant compact objects, and the joint detection of GWs and γ rays ushered in a new era of multimessenger astronomy (Abbott et al., 2017).

NS mergers are considered the canonical multimessenger source, but they are not the only expected sources of GWs. Binary NS and some neutron-star-black-hole (NSBH) mergers are referred to as NS mergers producing short gamma-ray bursts (SGRBs; section 3.2.2) as well as kilonovae. Other plausible candidates for the simultaneous detection of GWs and gamma rays are core collapse Supernovae (CCSN) in the Milky Way that may produce detectable GW burst emission and long GRBs (Kobayashi and Mészáros, 2003; Liu, Gu, and Zhang, 2017). Neutrinos from collapse events are also associated, and joint GW, neutrino, and γ-ray detections would constrain both the understanding of the supernova engine and the physics behind it (Fryer et al., 2019). Moreover, gamma-ray monitoring of pulsars (PSRs) enable searches for continuous GWs. Indeed, PSRs emit pulsed electromagnetic emission because they are NSs in rapid rotation with strong magnetic fields, and any non-axisymmetric deformation in the object cause it to emit continuous GWs (Glampedakis and Gualtieri, 2018). Other promising sources are accreting NSs because they are expected to emit intermediate duration GWs, and γ-ay observations can measure the frequency change and inform on the accretion rate (Watts et al., 2008). Even the constrain on the glitch time of γ-ray pulsars to minutes-scale can enable follow-up searches for intermediate-duration GWs, as has been recently done for a Vela pulsar glitch (Kerr, 2019). Pulsar Glitches are sudden changes in the rotation period of the pulsar, and they are thought to be caused by interactions at the core-crust interface which could produce GWs during the recovery period. Another interesting class of sources are the Giant Magnetar Flares that are short, bright flashes of γ-rays resulting from non-axisymmetric deformations of the magnetar through crust-cracking or magnetic field-induced structural changes (Kerr, 2019), that produce GWs emission (Watts and Strohmayer, 2007).

As said earlier, AGNs represent peculiar extragalactic sources in the multimessenger astronomy. In that context, long timescale observations can reveal periodicity that may be related to GW sources, such as the super massive black hole binaries (SMBHBs). An example is the BL Lac object PG 1553+113. It has an apparent 2.2 year cycle that has been firstly observed in γ-rays by the *Fermi*-LAT satellite (Ventura, 2015; Ackermann et al., 2015). Observations of blazars (section 3.2.1.1) would allow for multimessenger constraints on the formation of SMBHBs. While among the unexpected candidates of multimessenger sources there are short GRBs following stellar mass binary black holes mergers (Connaughton et al., 2016).

In conclusion, all-sky γ-ray monitoring can provide useful informations on the sources expected to emit GWs.

Gravitational waves were first conceptualized by Poincaré (Poincaré, 1905) and first predicted in the context of General Relativity (GR) in 1916 (Einstein, 1916). Their existence was indirectly confirmed by measuring the orbital frequency evolution of the Hulse-Taylor pulsar (Taylor and Weisberg, 1982). GWs were directly observed only a few years ago (LIGO Scientific Collaboration and Virgo Collaboration, Abbott, et al., 2016), and now the third GW catalog is available (The LIGO Scientific Collaboration and the Virgo Collaboration and the KAGRA Collaboration, Abbott, et al., 2021). It describes signals detected with Advanced LIGO and Advanced Virgo up to the end of their third observing run.

Dark Matter

Another intriguing research field for the astroparticle community is the field of the Dark Matter nature and origin that are still unknown. The first evidences arise from kinematic arguments related with the motion of galaxies in clusters (Zwicky, 1933; Zwicky, 1937) and of stars (Roberts, 1966; Rubin and Ford, 1970). while the idea of non-luminous matter may be traced back further (see the review in Bertone and Hooper, 2018). The velocity dispersion of galaxies in clusters is higher than expected by luminous matter, and the rotation curves of galaxies are observed to flatten beyond the edges of visible matter[21]. Additional evidence for dark matter include stellar velocities perpendicular to the galactic plane (Oort, 1932; Bahcall, Flynn, and Gould, 1992), the CMB fluctuation (Hinshaw et al., 2013; Planck Collaboration et al., 2020), and the observations of large scale structure (Tegmark et al., 2004) and gravitational lensing (Massey, Kitching, and Richard, 2010). Lensing observations of merging galaxy clusters, such as the Bullet Cluster, reveal the evidence that baryonic and dark matter are spatially separated (Clowe, Gonzalez, and Markevitch, 2004; Clowe et al., 2006; Bradač et al., 2008).

The most plausible model describing Our Universe considers the so-called cold (not relativistic) dark matter component is made up of elementary particles beyond the Standard Model (Feng, 2010), and represents $\sim 84\%$ of the total mass, five times larger the baryonic component (Reeves et al., 1973; Fukugita, Hogan, and Peebles, 1998). Indeed, not detectable low luminous stars, planets, interstellar gas and compact objects are not sufficient to explain such required amount of mass.

A promising candidate is the Weakly Interacting Massive Particle (WIMP; Steigman and Turner, 1985; Roszkowski, Sessolo, and Trojanowski, 2018), and it may

---

[21]It is possible to explain this feature including a significant amount of dark matter beyond these edges.

be any non-baryonic massive particle that interacts through the weak nuclear force and has masses around 1 GeV to 100 TeV[22] (Bottaro et al., 2022). WIMPs that form the lightest supersymmetric particle, known as *neutralino*, could be a good candidate (Ellis et al., 1984). The assumption is that the thermal freeze-out in the early Universe leaves a relic density of DM particles in the current Universe because of the primordial condition prevent the DM particles to annihilate and preserve the density. An appealing WIMP candidate has a mass around 100 GeV and an annihilation cross section typical of weak interactions in thermal equilibrium at present days, known as "WIMP miracle" (Feng and Kumar, 2008). Non-WIMP candidates also exist, as *axions*, *axino* and *gravitino* (see Arcadi et al., 2018 for a review)

Many experiments are devoted to explore the annihilation processes in the mass-energy range covered by the WIMPs. Under theoretical assumptions, they are expected to annihilate in standard model particles, and then in γ rays and CRs. In particular regions of the Universe with high dark matter densities, as the centers of galaxies and clusters of galaxies, have enhanced probabilities that DM particles encounter each other and annihilate, for instance in γ rays which energies related to the rest mass of DM particles. In that framework, gamma rays can bring informations on the annihilation region because they are not deflected by magnetic fields, and for that reason it is possible to point back to the progenitor source (*smocking gun*).
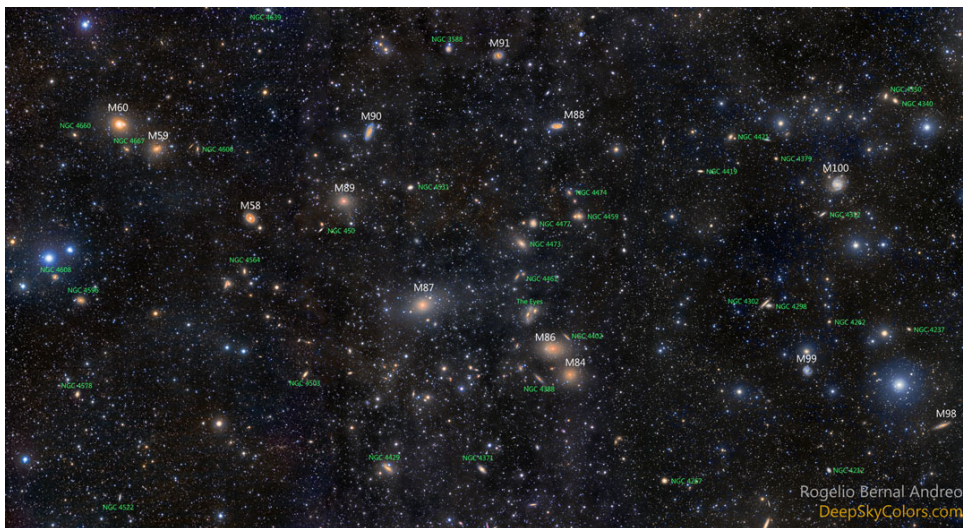
FIGURE 2.7: Virgo cluster galaxies. *Credit: Copyright Rogelio Bernal Andreo – APOD August 4, 2015.*

[22]The lower and upper mass limits come from cosmological constraints (Leane et al., 2018) and unitarity arguments (Smirnov and Beacom, 2019), respectively.

The γ-ray detectability of any particular region in the Universe strongly depends on the density distribution along the line-of-sight of the DM particles, the so-called *J-factor*. It is computed through cold DM N-body simulations, and the choice of a specific J-factor is fundamental in DM studies with γ rays. As mentioned in above, promising candidates for the detection of gamma rays from DM are satellite dwarf spheroidal galaxies, galaxy cluster (such as Virgo or Coma, see fig. 2.7) and the Galactic Centre with the observed excess diffuse emission (section 3.1.4 and chapter 6), and its halo. For a review on indirect method to detect dark matter see Funk, 2015b.

3 GeV and TeV Sky

O̧UR Universe reveals its extreme behaviour through several cosmic messengers as seen in section 2.3. Among them the high and very-high energy γ rays represent the novel facet of the future in astronomy. With them, the sources accelerating very-high cosmic rays (CRs) are unveiled because of gamma rays are neutral and travel in a straight line without deflection due to galactic and extragalactic magnetic fields (MFs). The accelerated CRs interact with the gaseous matter surrounding the origin sites producing secondary γ rays that can also bring informations on both astrophysical sources and their environments.

The very first detection of γ rays date back to the 1960s, when the Vela defense satellites – designed to detect γ rays from clandestine nuclear testing – serendipitously discovered enigmatic γ-ray bursts coming from deep space (chapter 1). While the first γ-ray emitter associated with a galactic point source was *Geminga* detected by SAS-2 and COS-B satellites in the 1970s (Fichtel et al., 1975), later identify as a nearby pulsar (Bignami, Caraveo, and Lamb, 1983; Halpern and Holt, 1992). The Crab nebula was the first source detected at very-high energy (VHE) γ rays by the Whipple imaging atmospheric Cherenkov telescope (IACT, see section 4.2) in 1989 (Weekes et al., 1989). At the beginning of 21$^{\text{th}}$ century, the total number of sources detected by ground-based telescopes, were only eight. Thanks to the improvements in the IACTs sensitivity and resolution, in the second decades of the new millennium the number of detected sources increased, and at present days more than 250 VHE sources are listed in the TeV Catalog[1]. With the next generation IACTs (see section 4.3) it is expected that the improvement in sensitivity leads to the detection of new emitters also at very-high energies. The skymap of the sources measured so far is shown in the fig. 3.1. The source positions are plotted above the *all*-sky map of the high energy (HE) γ-ray emission detected by the *Fermi*-LAT satellite. The last plot in the figure shows the class pie chart of the current TeVCat.

The most efficient way to detect new sources is the sky survey mode. Orbital satellites are the best telescopes for this scope thanks to the large field of view and to the acquisition method that consists in scanning the sky at each orbit[2]. Rarely

---

[1]TeVcat webpage.
[2]*Fermi*-LAT scans the entire sky every 3 hours (two orbits).
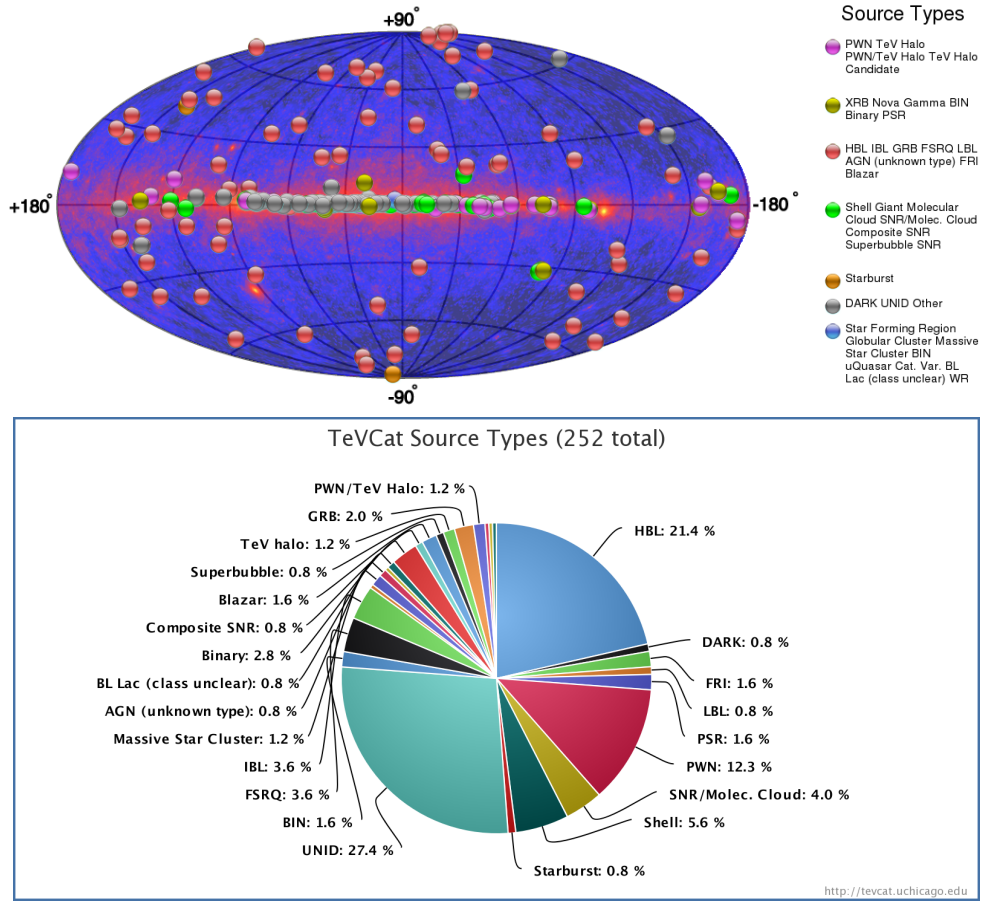
FIGURE 3.1: Skymap of the sources listed in the TeVCat plotted above the γ-ray *all*-sky map as observed by the *Fermi*-LAT satellite (*Fermi* NASA web page) . *On the bottom* the class pie chart. *Credit: http://tevcat.uchicago.edu*

these satellites point to a specific source, as done, instead, by ground-based IACTs. The first gamma-ray survey above $E > 20$ MeV was performed by EGRET aboard the Compton Gamma Ray Observatory (third released catalog, Hartman et al., 1999), and later by the Fermi Gamma-ray Space Telescope (fourth released catalog by *Fermi*-LAT Abdollahi et al., 2020a and *Fermi*-GMB von Kienlin et al., 2020). At VHE γ rays the first catalog was released by Whipple and HEGRA (Aharonian et al., 2001; Aharonian et al., 2002), but only with the present generation IACTs, as MAGIC, VERITAS (Patel et al., 2022) and H.E.S.S. (galactic plane survey; H. E. S. S. Collaboration et al., 2018d;see also section 1.1) many sources have been detected in the energy range $0.2 \div 100$ TeV (in fig. 3.2 are illustrated the source positions of the galactic plane survey). A sky survey has also been carried out using the water Cherenkov observatory HAWC above several TeVs (Albert et al., 2020a). Very recently also the Large High Altitude Air Shower Observatory (LHAASO) released its first catalog of very-high and ultra-high energy γ rays (Cao et al., 2023b).

Comparing the source positions of the objects listed in the catalogs seems that

a correlation likely exist between HE and VHE sources, but for more realistic conclusions some factors have to be take into account as the source distances, the possibility of source confusion, the differences in the diffuse Galactic background (see section 3.1.4 and chapter 6) and several other ones.
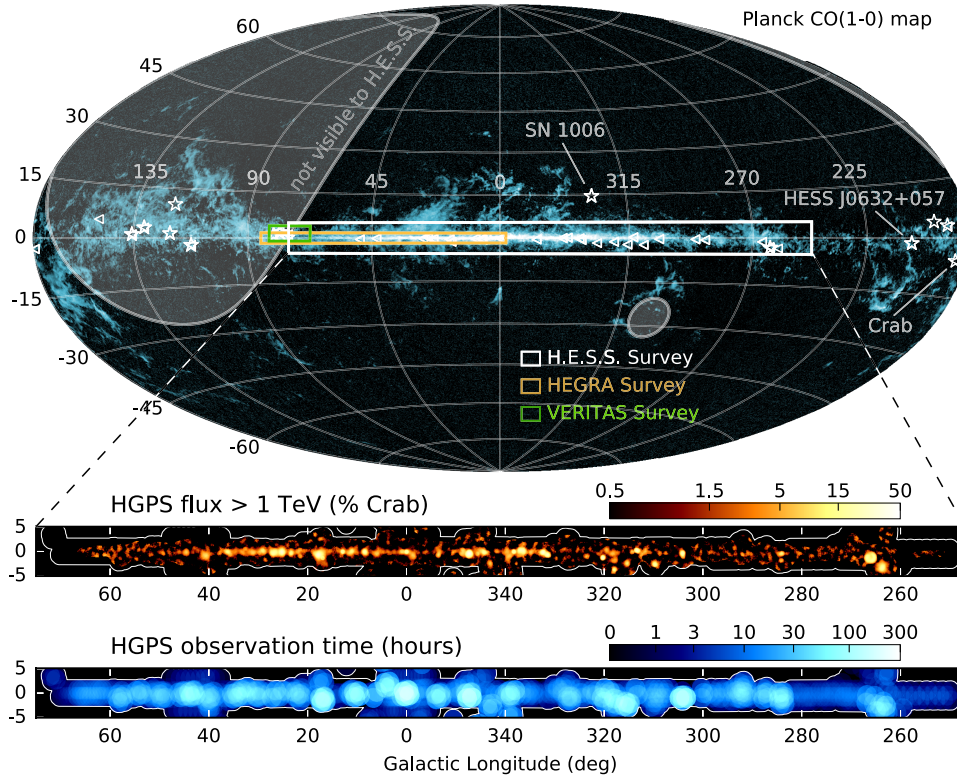
FIGURE 3.2: H.E.S.S. galactic plane survey region superimposed on the *all*-sky image of Planck CO(1-0) data (Planck Collaboration et al., 2016) in galactic coordinates. HEGRA Galactic plane survey (Aharonian et al., 2002) and VERITAS Cygnus survey (Weinstein, 2009) footprints are overlayed for comparison. Lower panels show γ-ray flux above 1 TeV as detected by H.E.S.S.. *Credit: fig.1 in H. E. S. S. Collaboration et al., 2018d*

This chapter is an attempt to enumerate the most important galactic and extragalactic sources of GeV and TeV Sky, with major remarks on the galactic diffuse emission and blazars, the source classes studied in this work.

3.1 Galactic Sky Sources and Diffuse Emission

In Our Own Galaxy, among the astrophysical sources detected at HE and VHE γ rays there are supernova remnants (SNRs), pulsars (PSRs), pulsar wind nebulae (PWNe), X-ray Binaries, and many more. There are also many unidentified sources, the majority of which are located along the galactic plane, yet to be confirmed from observations at other wavelengths. The importance of studying galactic sources is the improvement on the knowledge of emission mechanisms, the nature of objects, and CR physics. Another important motivation to study VHE γ-ray emission from

these emitters is to find sites for particle acceleration, since the measured CR spectrum at the Earth position has a break, the *knee*, at 10^{15} eV (fig. 2.1). It is believed that CRs with energies below the *knee* could be accelerated by galactic sources (see section 2.1).

In this section are illustrated the most important emitters, and the role of the γ-ray diffuse emission in the present days studies of the non-thermal galactic sky.

3.1.1   Supernova Remnants (SNRs)

The end of the life of massive stars leads to supernova (SN) explosions which have as latest state neutron stars or black holes. These explosions blow off the outer layers of the precursor stars into interstellar medium (ISM) forming supernova remnants (SNRs). Thus the sites where a lot of gas in different phases is present and Star Formation (SF) occurs – in Giant Molecular Clouds – are often associated with the surroundings of astrophysical sources, like pulsars and SNRs that are crucial components in CR physics (section 2.1.1).

SNRs are thought to be the best candidates for the origin of galactic CRs, because they are accelerated in shock waves resulting the SN explosion. This mechanism is described by the diffusive shock acceleration (DSA) theory (section 2.1.2). About 10% of the energy released by the explosion is converted to CRs, and SNRs could be also able to maintain the flux of galactic CRs at the observation level. SNRs are bright radio, X-rays and γ-ray emitters, and two main classes of them are thought to be potential sites of CR acceleration. In the first there are the so-called composite SNRs with an energetic pulsar at the center; while in the second there are the shell-type SNRs that are considered the most abundant in the GeV sky, and the younger ones contribute to populate the TeV sky. As an example, in the northern hemisphere a lot of SNRs are detected by MAGIC (see section 4.3.1) and VERITAS, like Cas A (Albert et al., 2007c; Acciari et al., 2010), and by H.E.S.S. in the southern emisphere, like RX J0852.04622 (also known as Vela Junior; Aharonian et al., 2005a),

The observed gamma-ray spectrum – both in the GeV and TeV band – is reproduced by two main scenarios:

- *leptonic model* in which γ rays are emitted by accelerated electrons/positrons via Inverse Compton emission

- *hadronic model* where γ rays are emitted by accelerated protons and nuclei that interact with the surrounding gas, producing pions, and eventually gamma rays via π^0 decay.

The leptonic scenario can explain the γ-ray emission from some type of sources, as for example Cas A or RX J1713.7-3946, a shell-type SNR interacting with the surrounding molecular cloud, first discovered by CANGAROO. But the measurements

of its morphology, firstly made by H.E.S.S., showed that an hadronic component is required to explain the observed spectrum. Later, observations above TeV energies performed with moon filters by the MAGIC telescopes measured the cutoff showing that Cas A is not a *PeVatron* (see section 3.1.3; Ahnen et al., 2017a).

On the other hand, an example of observed spectrum described by hadronic scenario is that of IC443, also known as Jellyfish nebula, firstly observed by both MAGIC (Albert et al., 2007b) and VERITAS (Acciari et al., 2009a), and later by AGILE and *Fermi*-LAT (Abdo et al., 2010b) at high energies. It is a a shell-type SNRs with a complex morphology, and the TeV centroid is associated with the molecular cloud (MC) close to the remnant. To explain the observed spectrum a *pion bump* is required promoting SNRs like proton accelerators (Ackermann et al., 2013). Consequently SNRs are considered the first candidate sites where the bulk acceleration of CR protons takes place.

Another class of SNR is the core-collapse type, slightly older than the class which Cas A belongs. An example is γ-Cygni, located in the heart of the Cygnus region. It was observed by both MAGIC (MAGIC Collaboration et al., 2023) and VERITAS (Aliu et al., 2013) telescopes, and *Fermi*-LAT (Fraija and Araya, 2016). Detailed investigations and modeling of the region revealed that CRs are escaping the shock of the SNR upstream into the ISM, while less energetic CRs are confined within the SNR shock. A definitively proof of the hadronic interpretation would be the observation of neutrino emission because in this scenario also charged pions are released, and their decay produces neutrinos.

3.1.2 Pulsars (PSRs), Pulsar Wind Nebulae (PWNe) and X-ray Binaries

Pulsars are highly magnetised rapidly rotating neutron stars formed in supernova explosions. Because of the fast rotation, charged particles are ripped away from the surface of the neutron star and accelerated along the magnetic field lines producing electromagnetic radiation. At the Earth position, the emission coming from a pulsar is observed pulsating because the magnetic axis and rotation axis are not aligned. The beam of radiation originating from a specific region in magnetosphere is then swept through the line-of-sight and pulsations are detected. Pulsed emission from these objects is observed from radio to γ rays.

The primary radiation mechanism is thought to be the synchrotron-curvature radiation due to relativistic electrons trapped in extremely strong MFs or close to the neutron star surface (polar cap scenario) or at various heights in the magnetosphere (slot gap and outer gap scenarios; see Bose et al., 2022 and references therein). All these models provide different γ rays spectra hence the observations at hight and very high energies, in particular the detection of a cutoff, are crucial to discriminate among pulsar emission models.

The spectral cutoff energy depends on the maximum energy of electrons and absorption of emitted γ rays in the pulsar magnetosphere. The first detection of pulsations was from Crab pulsar (period ~ 33 ms) at energies above 25 GeV performed by the MAGIC telescope (Aliu et al., 2008). The detection of γ rays above 100 GeV rules out curvature radiation as a possible production mechanism for these VHE emission considering a balance between acceleration gains and radiative losses by curvature radiation (Aleksić et al., 2011b). But later combined observations at high and very high energies indicate that the VHE emission could be an additional component produced by IC scattering of secondary and tertiary electron-positron pairs on IR-UV photons (Aleksić et al., 2012). The presence of pulsations at TeV energies indicates the parent population of electrons with a Lorentz factor above 5×10^6, suggesting IC scattering as the emission mechanism and γ-ray production region in the vicinity of the light cylinder. As a consequence the observed spectrum is characterized by the curvature due to curvature radiation, and at higher energies may correspond to the transition from curvature radiation to the IC scattering of particles accelerated in the northern outer gap.

Pulsar Wind Neubulae are isolated pulsar in which the rotational energy of the pulsar is converted into particle acceleration forcing pulsar to spin down. This mechanism gives rise to a relativistic magnetised plasma (*wind*) beyond the shock in the pulsar magnetosphere. The *wind* is an ultra-relativistic cold plasma of electrons, positrons and possibly ions interacting with the surrounding ISM forming termination shocks (for a review see Gaensler and Slane, 2006 and references therein).

PWNe are believed to be the source of galactic leptonic cosmic rays. The observed emission is the combination of the the power and spectrum of particles injected by the pulsar and those present in the environment in which the pulsar expands. The electrons/positrons injected into the nebula can produce synchrotron emission because of the magnetic field of the nebula itself. The radiation emitted by the relativistic electrons peaks at optical to X-ray energies, and TeV γ rays are produced by IC scattering of low energy photons – from the CMB or IR emission of dust – by electrons. In order to study the nature of PWNe, the combined observation of X-rays and γ rays are fundamental because the particle densities is derived by γ-ray measurements, and the MF strength is deduced by X-ray data.

Also for PWNe, the Crab nebula represents the best example and it is an extensively studied source from radio to VHE γ rays. The size of the nebula shrinks with increasing energy, giving information on the cooling processes since high-energy particles injected into the nebula at the wind shock undergo both synchrotron and adiabatic energy losses. Thus the HE component of the Crab Nebula spectrum is due to synchrotron emission, while that one at VHE

γ rays is related with IC scattering. Recently LHAASO (Cao et al., 2021), Tibet ASγ (Amenomori et al., 2019) and HAWC (Abeysekara et al., 2019b) provided data at energies above 100 TeV making the Crab Nebula a fascinating object to study, indicating the presence of extremely high energy particles.

Several associations of pulsar/PWNe were detected by H.E.S.S. and listed in the HGPS showing that the majority of the PWNe are located towards the inner galaxy, and only young energetic pulsars are able to produce TeV pulsar winds which can be detected by the present generation IACTs (H. E. S. S. Collaboration et al., 2018e). An example is HSS J1825-137 (Aharonian et al., 2006c), and very recently LHAASO observations have reported the evidence of photons above 100 TeV from this PWN making the source to be a possible *PeVatron* (see section 3.1.3 and Cao et al., 2021).

X-ray Binaries consist of a compact object, either a neutron star or a black hole accreting matter from a companion star. Transfer of matter could be due to Roche lobe overflow forming an accretion disk around the compact object, in case of low mass companion, and through the stellar wind in case high mass companion like OB stars. Eventually, the companion is a Be star with non-isotropic stellar wind forming an equatorial disk around the star. When relativistic outflows or jets have been observed from compact objects, they are called microquasars.

A small fraction of X-ray binaries are found to emit VHE γ rays. If one companion is a neutron stars, ultra-relativistic particles are accelerated in the pulsar wind and interact with the high-density UV-photon field of the companion, if it is a massive star. This interaction produces VHE γ rays though IC scattering. On the other hand if the companion is a Be star, pulsar wind particles interact with ions in the Be star disk and produce γ rays. In the case of microquasars, instead, with a massive star featured by strong UV field as a companion, γ rays can be produced by electron-proton or electron-photon interactions (Mirabel, 2012). The first microquasar discovered to be a VHE γ-ray emitter is LS 5039. The extreme emission from this source was first detected by H.E.S.S. (Aharonian et al., 2005b). Other interesting objects are LMC P3, which is the first γ-ray binary detected outside the Galaxy (H. E. S. S. Collaboration et al., 2018b) and Eta Carina, which is a colliding wind binary system, consisting of two massive stars orbiting each other (H. E. S. S. Collaboration et al., 2020a). Recently VHE γ-ray emission due to relativistic jet originating from the black hole was detected from SS 433 by HAWC (Abeysekara et al., 2018b).

3.1.3 *PeVatrons*

Some of the sources described above, such as SNRs and PWNe are thought to be capable of accelerating CR protons, heavier nuclei and electrons to PeV energies.

Several theoretical models try to explain how astronomical sources can accelerate particle up to PeV energies (Berezinskii et al., 1990; Malkov and Drury, 2001). If a source is found to accelerate particles at PeV energies is called *PeVatron* (Aloisio, Coccia, and Vissani, 2018). Subsequently accelerated CRs interact with the surrounding matter or photon fields producing VHE γ rays that are expected to have $\sim 10\%$ lower energy compared to parent CRs, then approximately around 100 TeV. Current IACTs have not detected any *PeVatrons* because of their limited sensitivity above a few tens of TeV. While air shower experiments are suitable for the detection of *PeVatrons*, because of their wide field of view, better sensitivities above 100 TeV and longer duty cycle. Recently, LHAASO collaboration (Cao et al., 2021) has reported detection of γ rays above 100 TeV from 12 galactic sources, including Crab nebula (Lhaaso Collaboration et al., 2021) with an event at 1.12 PeV establishing Crab as a possible *PeVatron* (fig. 3.3).
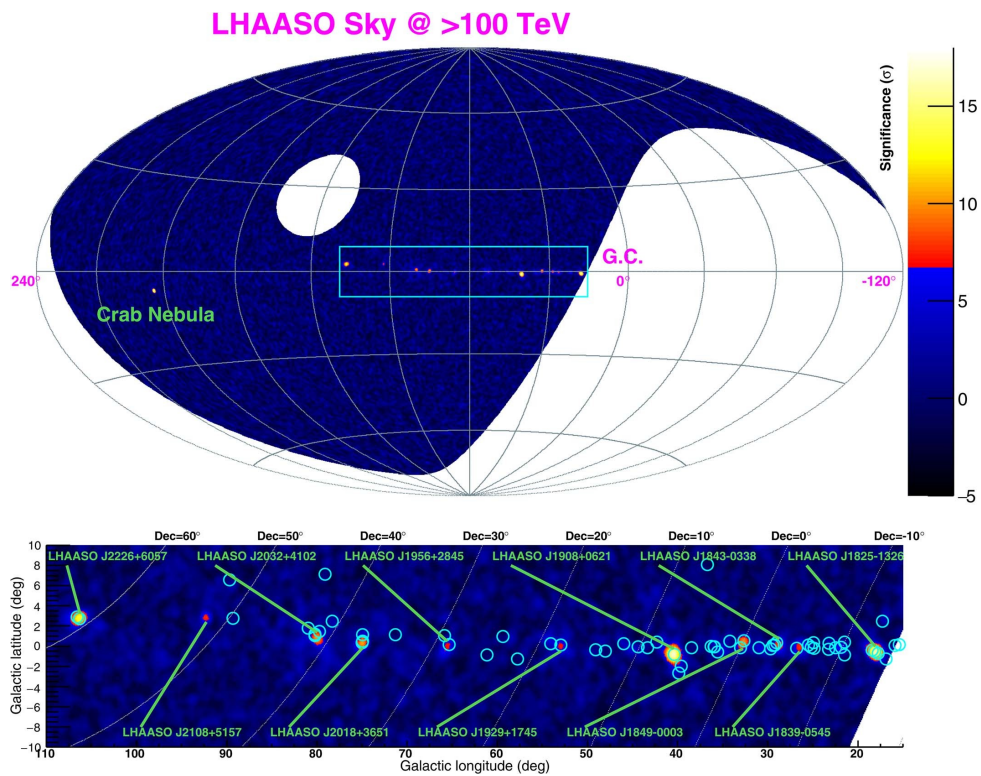
FIGURE 3.3: The circles represent the position of known γ-ray sources. Apart the Crab nebula, the sources are along the galactic plane. *Credit: fig.4 of extended data in Cao et al., 2021.*

The measured spectrum is fitted by a single-zone (leptonic) model in which the low energy component is due to synchrotron radiation, and the second one by IC scattering on low energy photons. Above 100 TeV the IC scattering occurs mainly on the 2.7 K CMB photons. But the observed spectrum seems to harden around 1 PeV, and a pure leptonic model is not able to reproduce this feature. The most plausible explanation of the *hardening* is then given by hadronic origin in which PeV protons and heavier nuclei interact with the ambient photon fields and/or gas/plasmas in

the vicinity of the source producing secondary charged and neutral pions. π^0s decay in VHE γ rays, and also neutrinos are produced via charged pion decay.

Except for Crab nebula, all other sources detected by LHAASO, are in the galactic plane. PWNe are thought to be also electron PeV accelerator, but to reach this limit a very strong MF is required, but under this condition the γ-ray spectrum is suppressed by Klein-Nishina effects. For that reason, it is believed that hadronic interactions might play a dominant role in PeV emissions.

In summary, the most favoured candidates able to accelerate CRs at PeV energies are SNRs and young massive star clusters, in which strong winds of massive stars interact with SNR shocks. An example of this second class is the source LHAASO J2032+4102 from which an event at 1.4 PeV was detected. This object is believed to be associated with a massive young star cluster Cygnus OB2.

However, even leptonic models are taken into account: electrons can also be accelerated to PeVs by reverse shock to very high energies at the SNR shell and produce γ rays via IC scattering. An example is G106.3+2.7 observed by VERITAS and HAWC Albert et al., 2020b, which hosts the Boomerang pulsar, and nebula, also detected in radio, X-rays, HE and VHE γ rays. Joint analysis of this object have promoted it to a plausible *PeVatron*.

It is argued that γ rays produced by a *PeVatron* could have both leptonic and hadronic origin. In that sense, it is possible to use the peak position of synchrotron emission in X-ray regime to distinguish between leptonic and hadronic scenario, because in order to produce 100 TeV γ rays via IC of CMB photons, electrons need to have energy around few hundreds of TeV and corresponding synchrotron peak will be at 10 keV.

3.1.3.1 An hidden *PeVatron* in the centre of the Milky Way?

One of the most appealing context of Our Own Galaxy is the Galactic Centre (GC) region that represents an intriguing playground in the astroparticle research field because the nature of its emission is still unknown, and it could be a potential site of multimessenger phenomena, including with DM and neutrino emission. This complex environment is extensively studied in chapter 6 of this work.

The GC region hosts numerous potential sites of particle acceleration, including the supermassive ($M \sim 2.6 \times 10^6 M_\odot$) black hole Sagittarius A* (Sgr A*; Schödel et al., 2002), SNRs, and PWNe. The GC also contains dense molecular clouds, forming the so-called Central Molecular Zone (CMZ, Morris and Serabyn, 1996). Gamma-ray emission above 100 GeV has been detected from the direction of the GC with IACTs, firstly by Whipple (Kosack et al., 2004), CANGAROO-II (Kosack et al., 2004), one MAGIC telescope (Albert et al., 2006), and by H.E.S.S. with the experimental set-up of 4 telescopes (Aharonian et al., 2006b). Later observations are performed also by

VERITAS (Archer et al., 2014; Archer et al., 2016; Adams et al., 2021), two MAGIC telescopes (Ahnen et al., 2017b; MAGIC Collaboration et al., 2020b; Abe et al., 2023), and the upgraded configuration of H.E.S.S. (HESS Collaboration et al., 2016; H. E. S. S. Collaboration et al., 2018a), leading to important discoveries in high-energy astrophysics and even constraints on models for particle dark matter (for a review see van Eldik, 2015).

In the GC region a sources of VHE γ rays include the strong central source HESS J1745-290 or VER J1745-290, spatially coincident with both Sgr A* (Atoyan and Dermer, 2004; Aharonian and Neronov, 2005; Fujita, Murase, and Kimura, 2017) or PWN G359.95-0.04 (Wang, Lu, and Gotthelf, 2006; Acero et al., 2010). Even the composite SNR G0.9+0.1 (Aharonian et al., 2005c), and an unidentified source identified as VER 1746-289 (Archer et al., 2014; Ahnen et al., 2017b) or HESS J1746-285 (H. E. S. S. Collaboration et al., 2018a) are located in the vicinity of the centre.

The H.E.S.S. collaboration reported for the first time the presence of diffuse γ-ray emission associated with the central region (Aharonian et al., 2006b; HESS Collaboration et al., 2016; H. E. S. S. Collaboration et al., 2018a), observed also with both MAGIC (Ahnen et al., 2017b; MAGIC Collaboration et al., 2020b; Abe et al., 2023) and VERITAS (Archer et al., 2014; Archer et al., 2016; Adams et al., 2021). The VHE emission is found to approximately trace the column density of the dense molecular clouds traced by CO and CS molecular emission lines, and extended over about 2 degrees in galactic longitude along the Galactic Plane (GP) corresponding to the dubbed central *Galactic Ridge* region. The spectrum of central source HESS/VER J1745-290 has a photon index $\Gamma \sim 2.2$, and a break at ~ 10 TeV, while the diffuse emission spectrum has $\Gamma \sim 2.3$ with no break or cutoff up to tens of TeV.

The origin of the GC VHE emission is still unknown, because of source confusion and the limitations of current IACTs. It may be the central source associated with Sgr A*, or the annihilation of dark matter particles (Horns, 2005; Gammaldi et al., 2016), a population of millisecond pulsars (Bednarek and Sobczak, 2013; Guépin et al., 2018), especially contributing at the GeV excess (Bartels, Krishnamurthy, and Weniger, 2016). Another explanation invokes radiative-inefficient accretion flow Sgr A* as a CR accelerator assuming acceleration by turbulent magnetic reconnection. Under some assumptions, the numerical general relativistic magnetohydrodynamic together with leptonic radiative transfer simulation performed by Rodríguez-Ramírez, de Gouveia Dal Pino, and Alves Batista, 2019, reproduces the observed VHE γ-ray emission from the region surrounding Sgr A*.

Above TeV energies the CR leptonic component is believed to be negligible because of the radiation losses afflicting synchrotron and Inverse Compton mechanisms, caused by strong MFs – as strong as $\sim 100 \, \mu G$ (Crocker et al., 2010) – and dense IR radiation field in the inner Galaxy respectively. Hence the observed emission is primarily originated by the interactions of high and very-high energy CR

hadrons (mostly protons) with the dense gaseous mater enclosed in the molecular clouds filling the GC region. As shown in section 2.1, the *pp* interaction produces pions, and the neutral pion rapidly decay in γ rays (Aharonian and Neronov, 2005). A probe in favour of the hadronic scenario is the morphology of the central source at TeVs. Indeed ultra-relativistic CR hadrons interact with the dense gas locked in the inner pc of the Milky Way, producing an extended emission with the same morphology of the CMZ. Moreover the lack of the cutoff in the diffuse emission is another ingredient supporting the hadronic scenario (Linden, Lovegrove, and Profumo, 2012; HESS Collaboration et al., 2016; Gaggero et al., 2017a; Ventura, 2018; Ventura, Grasso, and Marinelli, 2019; Ventura, 2022).

Several attempts, instead, trying to explain the observed high and very-high γ-ray emission with leptonic scenario invoking the IC scattering as main channel for the GeV and also TeV emission produced by ultra-relativistic electrons associated with PWNe or eventually DM decay (Hinton and Aharonian, 2007; Kusunose and Takahara, 2012; Lacroix et al., 2016). A combination of processes (hybrid scenario) has also be suggested to explain the measured flux, where leptons produce high-energy, but not VHE, γ rays. In the GC region both leptonic and hadronic component were accelerated during the previous activity of the central source and diffused out the accelerator. The interaction of hadronic CRs with the surrounding gas are responsible for the TeV emission, while the electrons contribute to the GeV emission because of the strong cooling due to IC scattering of ultra-relativistic leptons with the dense soft photon field (Guo et al., 2013).

Sgr A* is considered a viable *PeVatron* candidate, although it is relatively quiet today and unable to provide the required acceleration power (HESS Collaboration et al., 2016). Several arguments suggests that during the last $10^6 - 10^7$ years it could have been more active when its accretion may have powered strong relativistic jets able to accelerate particles up to the PeVs. In fact, nowadays it is known that this object had experienced an active phase in the past as demonstrated by X-ray outbursts (Clavel et al., 2013) and an outflow from the GC (Su, Slatyer, and Finkbeiner, 2010). Another important aspect to take into account is the variability of the central source that could give informations about the particle acceleration during weak accretion of Sgr A* in its quiescent phase, and the size of the central object (Ballantyne, Schumann, and Ford, 2011; Chernyakova et al., 2011; Fatuzzo and Melia, 2012; Viana et al., 2019).

Other plausible sites of proton acceleration in the GC are the ultra-compact stellar cluster (Crocker et al., 2011), where the mechanical power released by strong stellar winds (SWs) of massive stars can provide adequate conditions for particle acceleration, and could be sufficient to explain the required total energy of CRs in the CMZ. Some authors advanced the idea that young stellar cluster could act as *PeVatrons* and partially contribute to the galactic CRs (Aharonian, Yang, and de Oña Wilhelmi, 2019; Jouvin, Lemière, and Terrier, 2017). This proton acceleration power

could only exit in a stellar cluster because of the presence of both massive stars and very young supernova shocks[3] (Bykov, 2014). Hence, in this framework, supernova shocks supply the power to accelerate protons, reducing the requirement of a single *PeVatron*. But, the acceleration of PeV particles by shocks, either in an individual SNR or in a stellar cluster, cannot be longer than 100 years (Bell et al., 2013). Hence more than 10 supernova events are required to maintain a continuous injection of CRs in the central 10 pc region, but this high supernova rate could be unlikely. Recent works showed that in some peculiar young stellar cluster is plausible to reach PeV energies (Morlino et al., 2021; Morlino, 2021; Blasi and Morlino, 2023). The authors developed a diffusive shock acceleration theory in which the particle acceleration occurs at the termination shock developed in the bubble excavated by star clusters' winds in the ISM.

An alternative interpretation invokes the role of the diffuse γ-ray emission due to CRs **propagation within the Galaxy. Considering an appropriate set of parameters, including the linear dependence of diffusion coefficient with galactocentric distance and rigidity** (Gaggero et al., 2015c). The authors tuned their phenomenological model – computed with DRAGON[4] (Evoli et al., 2008; Gaggero et al., 2013) and GAMMASKY codes (Di Bernardo et al., 2013; Evoli et al., 2012) – on high energy γ-ray emission from *all*-sky maps built with *Fermi*-LAT data. This model is able to reproduce the observed hardening of the CR spectral index in the inner galaxy (Acero et al., 2016), in contrast with the homogeneous diffusion computed with GALPROP code (Vladimirov et al., 2011). Later works included upgrading of PASS8 *Fermi*-LAT analysis, and model parameters in order to reproduce PAMELA (Adriani et al., 2011), AMS-02 (Aguilar et al., 2015) and CREAM (Ahn et al., 2010) local data and the MILAGRO anomaly[5] (Gaggero et al., 2015b; Gaggero et al., 2017a). In this framework are considered not the whole GP but smaller region, associated with the GC, Sagittarius B, Bania Clumps and HESS J1741- regions (see chapter 6 and Gaggero et al., 2017a; Gaggero et al., 2017c; Gaggero et al., 2017b; Marinelli et al., 2017; Ventura, 2018; Ventura, Grasso, and Marinelli, 2019; Ventura, 2022). **The main results of this interpretation is related with the evidence that γ-ray diffuse emission featured by inhomogeneous diffusion –** *harder* **CR-*sea*– is able to reproduce the observed VHE γ-ray *excess* by H.E.S.S., MAGIC and VERITAS.** In these works are also performed a customized analysis of *Fermi*-LAT data aiming to compare HE and VHE measurements (see fig. 6.17, and for major details see chapter 4 in Ventura, 2018). Nevertheless, considering the luminosity profile computed in the CMZ with the *hard* CR-*sea*, the contribution of a local source corresponding to the central object Sgr A* is required to fit the measured luminosity by H.E.S.S. (for major details on this analysis see chapters 5, and 6 for discussions in Ventura, 2018).

---

[3]To accelerate protons up to PeV energies is required a bulk motion in excess of 10.000 km s^{-1} compatible with young SNRs.

[4]DRAGON project webpage.

[5]This anomaly consists in an excess of the diffuse emission in the inner GP at 15 TeV that is not explained by the predictions of conventional models (Abdo et al., 2008).
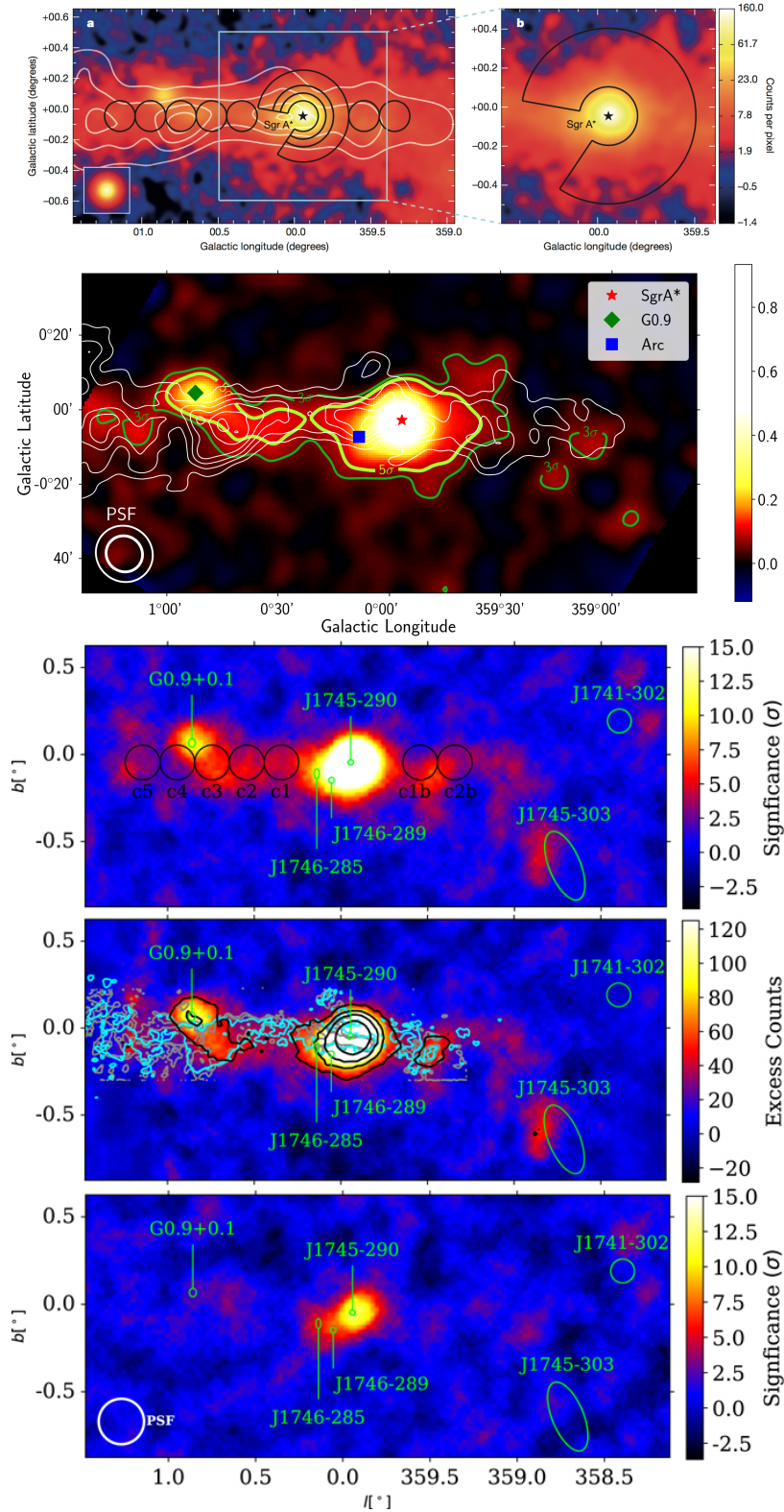
FIGURE 3.4: *On the top.* The map of the CMZ as observed by H.E.S.S.. The black lines on the left map outline the regions used to calculate the CR energy density throughout the CMZ. White contour lines indicate the density distribution of molecular gas, as traced by CS line emission (Tsuboi, Handa, and Ukita, 1999). The Black star is the location of Sgr A*. At the bottom left, a simulation of a point-like source. A zoomed view of the inner ∼ 70 pc and the contour of the region used to extract the spectrum of the diffuse emission on the right. *Credit: fig.1 in HESS Collaboration et al., 2016. In the middle.* Sky map of the GC region as seen by MAGIC telescopes at $E > 1$ TeV. *Credit: fig. 1 in MAGIC Collaboration et al., 2020b. On the bottom.* Maps of the statistical significance for γ-ray-like events detected by VERITAS above 2 TeV (top) and 10 TeV (bottom), the map of excess counts above 2 TeV (middle). *Credit: fig.1 in Adams et al., 2021.*

In conclusion, **the galactic *hard* CR-*sea* could naturally reproduce the observed energy spectrum in the GC region, but it is not the unique contributor to the measured flux: a local source that in some way *freshly* and continuously accelerate CRs in the region is required to have the $1/r$ CR density profile deduced by H.E.S.S. and MAGIC observations (fig. 6.12). Under the *PeVatron* scenario, in which the CRs are continuously injected in the surrounding environment, the derived CR density profile is strongly dependent on the mass of the gaseous target, and hence on the not negligible uncertainties related with the measurements of gas distribution in the inner Galaxy.**

In HESS Collaboration et al., 2016, the derived CR density was fitted with a $1/r$ profile, signature of the presence of a *PeVatron*, as

$$\omega_{\mathrm{CR}}(E, r) = \frac{Q_{\mathrm{source}}(E)}{4\pi D(E)} \frac{1}{r} \propto E^{-(\Gamma_{\mathrm{source}} + \delta)} \tag{3.1}$$

where Q_{source} is the source term (section 2.1.4), $D(E)$ is the diffusion coefficient (eq. (2.13)) proportional to E^{δ}.

For all these reasons, **the GC region represents a peculiar target for the next generation IACTs, such as the Cherenkov Telescope Array (CTA; see section 4.3.2). Thanks to the improvement in sensitivity and angular resolution will be possible to study with major details the VHE γ-ray emission, the morphology of the region, and hopefully the variability of the central source** (Viana et al., 2019). In fig. 3.4 are shown the sky maps of the GC region as observed by H.E.S.S. (HESS Collaboration et al., 2016), MAGIC (MAGIC Collaboration et al., 2020b) and VERITAS (Adams et al., 2021).

3.1.4   Diffuse Emission

As said in section 2.1, primary CRs of all flavours produce γ rays as the results of several decay channels.

The Milky Way has long been known to be a strong source of diffuse γ-ray emission. As for the search of new sources, the unique method to obtain *all*-sky diffuse γ-ray emission under 1 TeV is the measurements performed by space detectors, firstly by OSO-3 (Clark, Garmire, and Kraushaar, 1968), SAS-2 (Fichtel et al., 1975), COS-B (Mayer-Hasselwander et al., 1982), EGRET (Hunter et al., 1997) , and recently by *Fermi*-LAT (Ackermann et al., 2012a), with increased angular resolution and sensitivity (above 100 GeV; see fig. 3.5). While at higher energies, the detection of the diffuse emission is performed by ground-based IACTs, but only in selected regions of the Galactic plane because of the limited field-of-view, as done by MILAGRO (Abdo et al., 2007; Abdo et al., 2008), ARGO-YBJ (Bartoli et al., 2015), H.E.S.S. (H. E. S. S. Collaboration et al., 2018a), Tibet As-γ (Amenomori et al., 2021a), HAWC (Abeysekara et al., 2021), and LHAASO (Cao et al., 2023a).
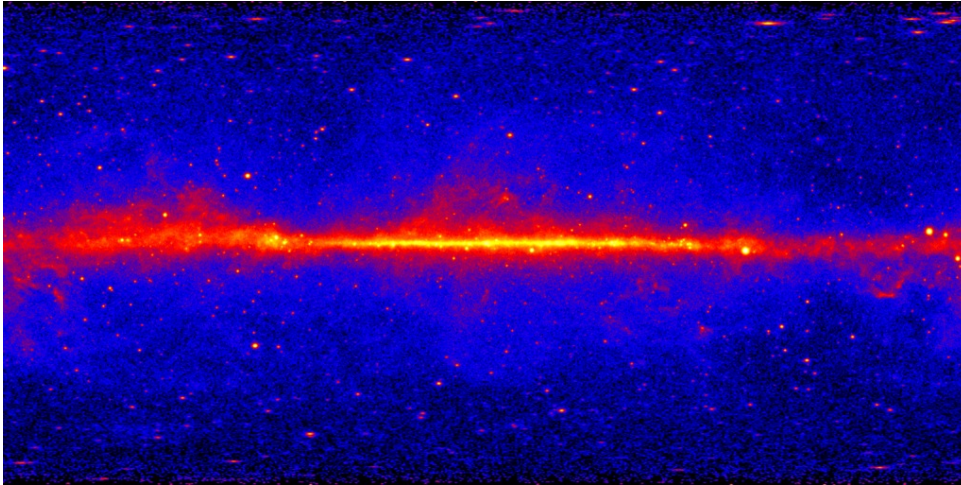
FIGURE 3.5: The *Fermi*-LAT 5-years all-sky image related to γ rays with energies greater than 1 GeV. The most prominent feature is the bright band of diffuse glow along the Galactic Plane, which marks the central plane of our Milky Way galaxy. The gamma rays are mostly produced when energetic particles accelerated in the shock waves of SNRs collide with gas atoms and even photons between the stars.
Credit: Fermi-LAT diffuse emission webpage.

One of the most important research field in the astroparticle community is the study and characterization of such emission, because it represents the only method to provide the background models, fundamental ingredients in the analysis chain of the current and next generation γ-ray experiments and observatories. These templates assume a key role in the analysis of complex regions, such as the astrophysical environments associated to extended sources – like the galactic ones – and diffuse excesses, like that observed in the GC region. A detailed study of phenomenological models for the dubbed *Cosmic-Ray sea* (CR-*sea*) is illustrated in chapter 6.

Along the Galactic Plane (GP) the most significant component of the diffuse emission, especially at very-high energies, arises from the **decay of neutral pions (π^0)** (section 2.1) produced by the collisions of the hadronic component of the galactic CRs with the gaseous component of the ISM (Stecker, 1970; Dermer, 1986). Therefore, the angular distribution of the pionic component of the galactic diffuse γ-ray emission traces the column density of the interstellar matter, but the derivation of that quantity is quite difficult from an observational point of view. Indeed, although the ISM is composed mainly of hydrogen, this element can appear in three different forms: molecular (H_2), atomic (HI) and ionized (HII) with different spatial distributions. Only H_2 and HI – detected and studied via the 21-cm line – have significant density along the GP.

The π^0 emissivity[6] is a function of

$$Q_{\pi^0}(E_{\pi^0}) = cn_{\mathrm{ISM}} \int_{E_{\mathrm{treshold,RC}}(E_{\pi^0})}^{\infty} dE_{\mathrm{RC}} \frac{dn_{\mathrm{RC}}}{dE} E_{\mathrm{RC}} \frac{d\sigma_{pp}}{dE_{\pi^0}} \qquad (3.2)$$

where $\frac{d\sigma_{pp}}{dE_{\pi^0}}$ is the differential cross-section of π^0 production from pp collisions. Assuming a power-law with index α for the spectral dependence of CR, above few GeV, the cross section can be approximated with

$$\frac{d\sigma_{pp}}{dE_{\pi^0}} = \frac{\sigma_0}{E_{\pi^0}} f_{\pi^0}(x) \qquad (3.3)$$

where $\sigma_0 \approx 3 \times 10^{-26} \ \mathrm{cm}^{-2}$, and the π^0 emissivity is given by (Grasso and Maccione, 2005; Cavasinni, Grasso, and Maccione, 2006)

$$Q_{\pi^0}(E_{\pi^0}) = \frac{2}{\alpha} cn_{\mathrm{ISM}} \sigma_0 \frac{dn_{\mathrm{RC}}}{dE} E_{\pi^0} Y_\gamma(\alpha) \qquad (3.4)$$

Hence, the related *photon emissivity* is

$$Q_\gamma(E_\gamma) = \frac{2}{\alpha} cn_{\mathrm{ISM}} \sigma_0 \frac{dn_{\mathrm{CR}}}{dE} E_\gamma Y_\gamma(\alpha) \qquad (3.5)$$

where Y (the Y_{ield}) is a function of the spectral index of the CRs.

As a result, the gamma photons emitted through this mechanism have, above some GeVs, a power-law spectrum with the same index as the primary CR protons (and nuclei). The shape of the γ-ray energy spectrum is thus someway related to the kinematics of the boosted hadrons by SNRs, for instance, the subsequently pion decays, and the galactic gas distribution. This shape is symmetrical – when plotted as $\log dN/dE$ vs $\log E$ – around the *pion bump* peak at $m_{\pi^0}/2 \sim 0.07$ GeV, with long power-law tails to higher and lower energies (Stecker, 1971). For energy above the pion bump the γ-rays have a slope follows the hadronic CR component (Strong, Moskalenko, and Reimer, 2004). While, the continuum emission at energies below the bump is associated with the leptonic component, and IC scattering and bremsstrahlung (section 2.1.2).

The **Inverse Compton scattering** between *ultra*-relativistic CR electrons and ambient photons – mainly in the radio, microwave, IR, optical and UV domain – results in a loss of energy for the CRs and a gain for the photons, which are then converted into X-rays or γ rays. This process traces the spatial distribution of CR electrons and the interstellar radiation field (ISRF). On the other hand, the **bremsstrahlung** radiation is emitted in γ rays when galactic CRs electrons interact with the gaseous component of the ISM, hence tracing the distribution of the leptonic CR component and the gas morphology.

---

[6]The emissivity is the number of particles (neutral pions in this case) emitted per unit of volume, time, energy.

Finally, the γ-ray diffuse emission traces the large scale distribution of CR protons and electrons in the Galaxy, allowing to probe the CR properties throughout the Galaxy, which may be rather different from those measured at the Solar System position. Moreover, many questions are still open and many problems are still unresolved, such as the various effects contributing to that emission, and the difficulty to disentangle the effective diffuse component from unresolved point sources. But what makes the modelling of the *background* γ-ray emission a serious issue to further investigate, is the huge number of free parameters involved in the phenomenological models reproducing the γ-ray diffuse emission (see sections 6.1.1 and 6.2).

In conclusion, understanding the galactic diffuse γ-ray emission is essential not only to determine the background for point-like and extended sources analysis, but also to study the properties of CR transport, energy spectrum and spatial distribution in the Galaxy.

3.2 Extragalactic Sky Sources

High and very-high energy γ rays are also observed in the extragalactic sky produced by ultra-relativistic particles in jets of active galactic nuclei (AGNs), star formation at exceptional rate in starburst galaxies (SBGs), and as afterglow emission from gamma-ray bursts (GRBs). Another component of extragalactic origin are CRs with energy above 10^{15} eV that have Larmor radius greater than the size of the Milky Way and cannot remain confined within the galaxy. UHE CRs are thought to be produced inside the jets of AGNs, GRBs or SBGs. Extragalactic objects are the majority of the sources detected by ground-based instruments and they are located mostly away from the GP.

3.2.1 Active Galactic Nuclei (AGNs)

This section is devoted to the description of AGNs and the peculiar subclass of blazars. An active galactic nucleus is a compact central region of a galaxy extremely bright, brighter than can be explained by the stellar population alone. This nuclear region outshines the emission from the rest of the galaxy, and AGNs have nearly a stellar shape on photographic plates. Furthermore, AGNs are the most luminous objects in the extragalactic sky, emitting persistent radiation in the entire electromagnetic spectrum, and they are believed to be powered by the accretion of matter from the host galaxy onto the supermassive black hole (SMBH; $M_{\mathrm{SMBH}} \sim 10^6 \div 10^9 \ M_\odot$) at the centre. For this reason AGNs are experiencing an active phase, and the central SMBH emits bright jets, a prodigious amount of energy, from radio to γ rays, and winds that shape the galaxy. Only 1% of the observed galaxies have an active SMBH in the center, and it is estimated AGNs remain active for up to $\sim 10^7$ years, consuming an enormous amount of matter to maintain their luminosity. AGNs are

extremely variable sources, featured by fast increasing of luminosity – the so-called *flares* – which can last from minutes to days or weeks in the entire or in a part of the electromagnetic spectrum. They are among the fundamental sources, together with GRBs, for understanding the origin and evolution of the Universe and studying distant objects thanks to their persistent luminosity in the entire energy spectrum.

The accreting matter forms an accretion disk spiralling around the central BH, and rotates with different velocities – correlated with temperature – which increase approaching the event horizon. Thermal radiation is thus emitted as a superposition of black-bodies at different temperatures, spanning from UV to optical bands (*blue bump*). An extreme hot population of electrons surround the accretion disk forming the *corona*, and emitting X-rays through the IC-scattering of these electrons with the UV photons. Beyond the accretion disk, at $\sim 0.1 \div 1$ pc from the center, a cloudy gas shell of ionized matter is present. In some types of AGNs like quasars the reprocessed UV photons of the disk photo-ionize the gas leading to an optical spectrum featured by broad components with Doppler widths in the range $\sim 10^3 - -10^4$ km/s. This region is the so-called *Broad Line Region* (BLR). Moving away from the BH, at $\sim 1 \div 10$pc from the center and surrounding the BLR is located the compact dusty torus with toroidal shape emitting mainly in the IR wavelengths. Those AGNs having the orientation of this structure crossing the line-of-sight do not present broad emission lines due to the strong absorption properties of the dusty torus. Farther again, at ~ 100 pc from the BH is located the *Narrow Line Region* (NLR) responsible for the narrow lines in the optical spectrum due to ionized gas moves slowly. In case of radio-loud AGNs, like blazars (see section 3.2.1.1 and fig. 3.6), a pair of twin jets pointing in opposite directions (bipolar jets) and perpendicular to the disk plane is present. These large structures extend from the nucleus up to large distance greater than 100 kpc. The jets are filled by ultra-relativistic particle populations especially close to the BH, and they are responsible for the γ rays production (Blandford and Znajek, 1977; Blandford and Payne, 1982).

The AGN classification is based on their radio emission and spectral differences. At the first two classes belong the so-called *radio-loud* and *radio-quiet* AGNs. The *radio-loudness* parameter R is used to distinguish between the two classes. It is defined as

$$R = \frac{F_5}{F_B} \tag{3.6}$$

where F_5 is the flux at 5 GHz, and F_B is the optical one in the B band, and the R parameter is distributed with bimodal profile (Kellermann et al., 1989). For $R \sim 1$ corresponds radio-loud galaxy, while radio-quiet galaxies are associated with $R \sim 100$. The next divisions come from the apparent morphology of the galaxies, then on the flux, and finally on the characteristic of the optical spectrum (see fig. 3.6).

The radio-quiet galaxies are subdivided depending on the optical spectral line widths. Blazars – the source class considered in this work (see chapter 5) – are
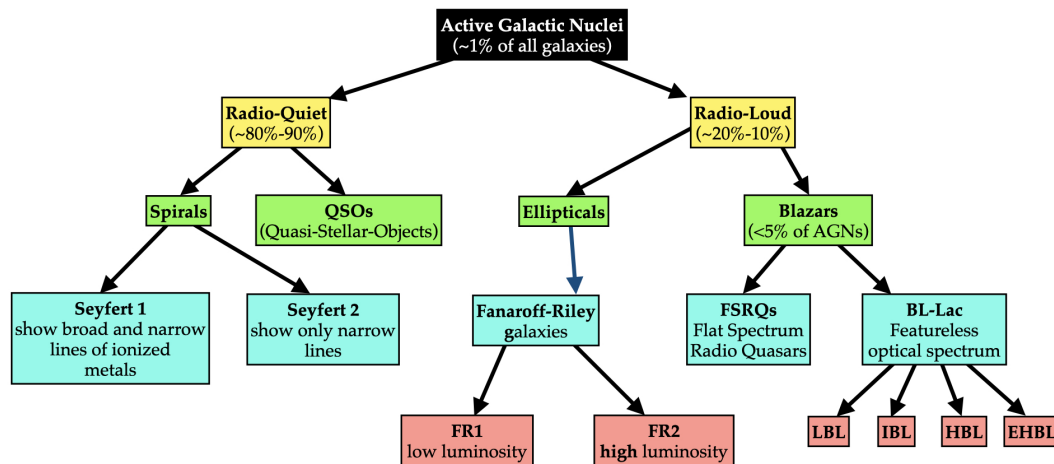
FIGURE 3.6: AGNs classification. The acronyms LBL, IBL, HBL and EHBL correspond to Low-frequency peaked, Intermediate-frequency peaked, high-frequency peaked and extreme-high-frequency peaked BL Lac objects.
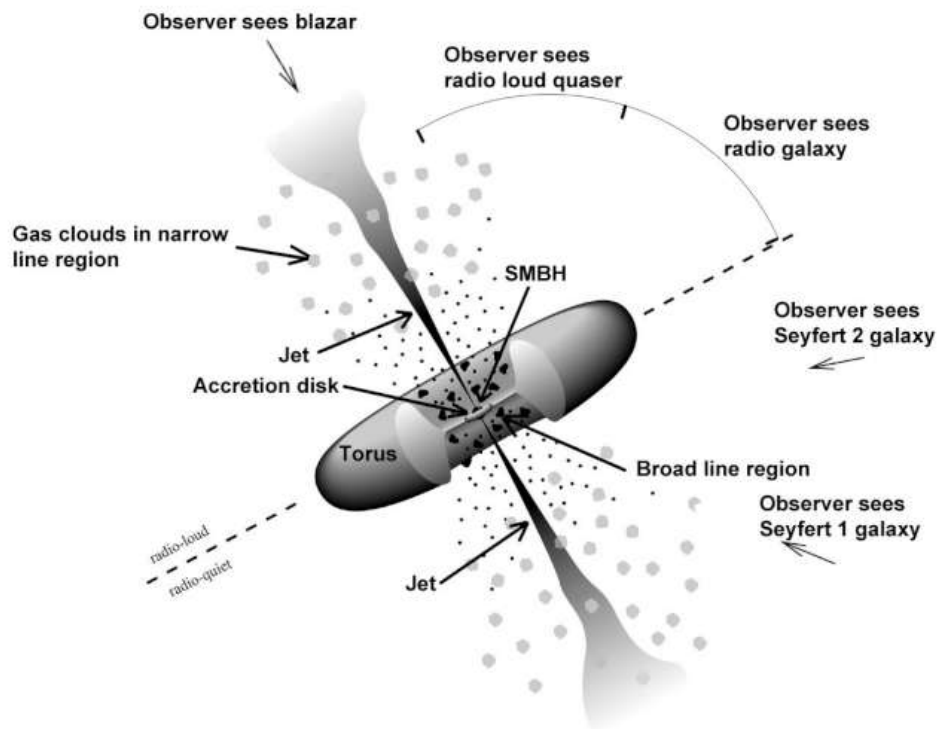
FIGURE 3.7: The *zoo* of AGNs with different names can be thought of as variations on a basic theme: the central power comes from accretion onto a SMBH, but what can be seen depends on the orientation of the observer with respect to the accretion disk, the dusty torus, and the jet. *Credit:* https://fermi.gsfc.nasa.gov/science/eteu/agn/

very compact objects emitting throughout the whole electromagnetic spectrum with highly variable fluxes. They are further divided into Flat Spectrum Radio Quasars (FSRQs), with clear emission lines in the optical spectrum, and BLLac objects which typically display weak lines (if any) and are dominated by continuum emission in the optical range. The Spectral Energy Distribution (SED) of blazars is featured by two bumps: one at low energies (UV to X-ray) and the second at high energies (X-ray to γ-ray). According to the peak frequency of the synchrotron part, BL Lacs can be further divided into Extreme-High, High, Intermediate and Low-peaked (EHBL, HBL, IBL and LBL) BL Lac objects (see section 2.2.1 and fig. 2.5). This interpretation is know as the *Unified Model* (Antonucci, 1993; Urry and Padovani, 1995). According to this model and despite of the classes' variety, it is believed that the underlying physics of AGNs is the same, and the observed differences among various classes are due to different source orientation with respect to the line-of-sight, the SMBH mass, the accretion rate, and the interstellar environment too (fig. 3.7).

3.2.1.1   Blazar Family

VHE γ-ray emission has been detected mostly from blazars and few radio galaxies. In according with the *Unified Model*, the blazar jet points toward the Earth under a small angle with the line-of-sight, and the observed emission is Doppler boosted. According to relativistic beaming models, the matter locked into the jet is relativistic with an intrinsic velocity close to the speed of light with a Lorentz factor Γ. Under the ballistic model assumptions, in which all jets have the same Lorentz factor, the effect of Doppler boosting increases the probability of observing sources close to the line-of-sight. Moreover the ultra-relativistic motion of the jet close to the line-of-sight produces a compression of the time frame resulting in apparent superluminal motion (Kellermann et al., 2003).

Blazars are known to be variable sources, showing variability in all wavebands on time scales from minutes to years. As said in section 2.2.1, the broad-band SED of blazars shows two peaks of non-thermal radiation (fig. 2.5). The low-energy hump lying between radio to X-rays and it is generally attributed to synchrotron emission from relativistic electrons filling the emitting zone within the jet. On the other hand, **the origin of γ-ray radiation forming the second hump of SED is still a matter of debate**.

As seen also for galactic sources, the emission mechanism could be of *leptonic, hadronic or lepto-hadronic (hybrid)* origin. In the *leptonic scenario* accelerated electrons/positrons produce the observed emission through IC scattering of low energy photons, either from jet or from external regions (Sikora, Begelman, and Rees, 1994). In contrast, in the *hadronic scenario* the accelerated protons/ions produce neutral and charged pions which decay into secondary γ rays, electron-positron pairs, and neutrinos or protons producing additional synchrotron emission, or mixed (Mannheim

and Biermann, 1989; Mannheim, 1998; Aharonian, 2000; Mücke et al., 2003). Moreover, the association of observed high-energy neutrinos with blazars (IceCube Collaboration et al., 2018b) is a probe in favour of the hadronic mechanism active in the jet, and promote blazars to be also plausible sites for UHE CR acceleration.

As seen in fig. 3.6 and fig. 2.5 and depending on the equivalent line width of emission lines in the optical spectra, blazars are further subdivided in FSRQ (> 5 Å) and BL Lac (< 5 Å) objects (Urry and Padovani, 1995). Instead, a different approach to distinguish between the two classes is based on physical properties of the sources (Ghisellini et al., 2011). The method consists in measuring the luminosity (L_{BLR}) of all broad lines in units of the Eddington luminosity (L_{Edd}). FSRQs are the sources whose $L_{\mathrm{BLR}} \gtrsim 10^{-3} L_{\mathrm{Edd}}$, and BL Lacs are the others. The physical mechanism on the basis of this approach is supposing the change of the regime of accretion occurring at disc luminosities $L_{\mathrm{disc}}/L_{\mathrm{Edd}} \sim 10^{-2}$, and also the evidence that in average $L_{\mathrm{BLR}} \approx 0.1\, L_{\mathrm{disc}}$ (Calderone et al., 2013). Below this value, the disc is thought to become radiatively inefficient, and its UV-ionizing luminosity is a minor fraction of its bolometric output being inadequate to photoionize the broad-line clouds (Sbarrato, Padovani, and Ghisellini, 2014).

BL Lacs are further sub-divided in other 4 classes depending on the position of the synchrotron peak in the SEDs (figs. 2.5 and 3.8), in LBL, IBL, HBL and EHBL objects. An anti-correlation is seen between the location of the first peak and the source luminosity. The first peak moves from higher to lower frequency passing from EHBL to LBL, and finally to FSRQ, whereas the source luminosity increases. The observed broad-band SED of all blazar classes show a *sequence* behaviour that is firstly described and parametrized in terms of bolometric luminosity (L_{bol}) by Fossati et al., 1998. The evidence arising from this sequence are

- blazars become *redder* with increasing L_{bol}, and the peak frequencies become smaller (especially moving toward FSRQs)

- the ratio CD of the luminosity of the high-energy hump – due to IC scattering – over the low-energy hump – due to synchrotron radiation – increases for FSRQs and decreases for BL Lacs

- the γ-ray slope becomes softer with increasing L_{bol}

- the X-ray slope becomes harder with increasing L_{bol}.

These properties was interpreted in terms of radiative cooling suffered by the emitting electrons in different sources, assuming that the heating mechanism, was similar for all blazars (Ghisellini et al., 1998). In FSRQs the IC luminosity of the second hump is higher with respect that of BL Lacs because in the first sources the photon seed is denser and consist also of external components. Indeed the photons emitted by the disk are re-isotropized by the BLR and dusty torus in IR radiation causing a large CD value and then high luminosity (Sikora, Begelman, and Rees,

1994)- In contrast, the electrons in the jet suffer strong radiative losses reaching lower energies, and the spectrum of FSRQs is redder. In BL Lac objects, instead, the lines and the torus are absent (Chiaberge, Capetti, and Celotti, 1999), whereas the photon seed is represented only by the internal synchrotron radiation, and the electrons suffer less radiative cooling, reaching higher energies. As a consequence, BL Lacs are less luminous and with a bluish spectrum. At the low-luminosity extreme, the bluest BL Lacs should not be strong MeV or GeV emitters. For that reason, satellite instruments, as *Fermi*-LAT sensitive in the MeV-GeV range (section 1.1), could not detect these extreme sources (Bonnoli et al., 2015).

Ghisellini et al., 2017 updated the original blazar sequence using *Fermi*-LAT observations. Also in this study, a sequence is clearly depicted by data, even if the differences are mainly due to the sampling mode since *Fermi*-LAT is more sensitive with respect to the previous instrument EGRET. A substantial difference between the new and old sequence is the evidence that FSRQs do not redder when increasing the luminosity, in contrast the BL Lacs do it. FSRQs form a sequence only in the CD and in the X-ray slope. Moreover at high redshift the signature of the accretion disk become evident in the SED of FSRQs (fig. 3.8).
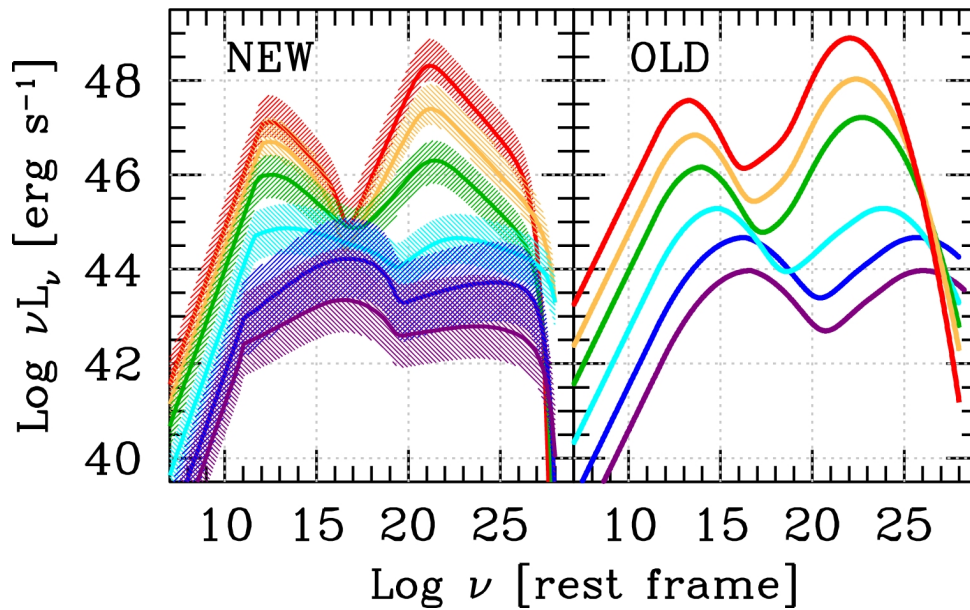
FIGURE 3.8: Comparison between the new and the original blazar sequence for all blazar types. The original blazar sequence considered five radio luminosity bins, while the new one considers bins in the γ-ray band. *Credit: fig.9 in Ghisellini et al., 2017.*

3.2.1.2   Temporal, Spectral and Multimessenger Signatures in Blazars

As said earlier, the jets of blazars are ideal laboratories for studying the origin of high energy emission and the role of particle acceleration. **Among the open questions to answer there are the understanding of mechanisms which launch the jet and how**

it is collimated, the mechanisms for particle acceleration in a jet, whether it is stochastic or diffusive shock acceleration or magnetic reconnection, or something else. Also, as mentioned earlier, it is unclear whether the high energy emission mechanism is leptonic, hadronic, or hybrid. Using VHE γ-ray observations is possible to obtain useful informations on the nature of the source and the physics underlying the object from temporal and spectral data.

Most of AGNs detected at high – currently by *Fermi*-LAT – and very-high energies are blazars. The first observed blazar at VHE γ rays was Markarian 421 (Mrk 421, Punch et al., 1992 and later Mrk 501 (Quinn et al., 1996) measured by Whipple. Currently, in the TeVCat (fig. 3.1) more than 67% of blazars belong to the HBL class. But only with the present generation IACTs has been possible to detect blazars of other classes such as IBL, LBL, and FSRQs. FSRQs are among the most distant objects, as 3C 279 was the first one detected by the MAGIC telescopes (MAGIC Collaboration et al., 2008), and the farthest FSRQs detected so far are S3 0218+35 with $z = 0.954$ by MAGIC (Mirzoyan, 2014) and PKS 0346-27 with $z = 0.991$ by H.E.S.S. (Wagner, Rani, and H. E. S. S. Collaboration, 2021).

Temporal Signatures

All types of blazars are found to show flux variability on various time scales, and during the brightest flare, the flux increases/changes by almost an order of magnitude. The Doppler boosting causes this strong enhancement of flux variation because – as seen in section 2.2.1 – the blazar emission is dominated by non-thermal radiation arising from ultra-relativistic particle populations in the jet pointing towards the Earth. This phenomenon is due to the ultra-relativistic motion of the plasma that boosts the non-thermal jet emission into a forward cone, hence enhancing the emitted flux (by $\propto \delta^3$) and the variability timescales are shortened (by $\propto 1/\delta$)[7] in the observer's frame. As a result the lux from blazars varies over several time scales from years to minutes.

One of the most studied object is Mrk 421 by various IACTs for last almost 30 years. It has shown a flux variation ranging from ~ 0.3 to ~ 27 Crab units[8]. In fig. 3.9 is shown the VHE light curve of Mrk 421 during 1992-2008, obtained by combining count rate measurements from various telescopes like Whipple, CAT, HEGRA, H.E.S.S., MAGIC and VERITAS (Tluczykont et al., 2010).

Another interesting source is the blazar 1ES 1959+650 which has shown an *orphan* γ-ray flare detected on 2002 by Whipple telescope (Krawczynski et al., 2004). It was not accompanied by X-ray flare, as usually is the case for HBLs, and after this bright flare, the source has not shown much activity until 2016,

---

[7]δ is the beaming factor expressed in terms of Γ Lorentz factor and viewing angle θ_V by $\delta = \frac{1}{\Gamma(1-\beta\cos\theta_V)}$.

[8]In VHE γ-ray astronomy the flux is often mentioned in units of the Crab nebula flux, which is a steady source considered as a standard candle.

when an exceptionally high flare measuring up to ~ 3 Crab units was detected by the MAGIC telescopes (MAGIC Collaboration et al., 2020a).
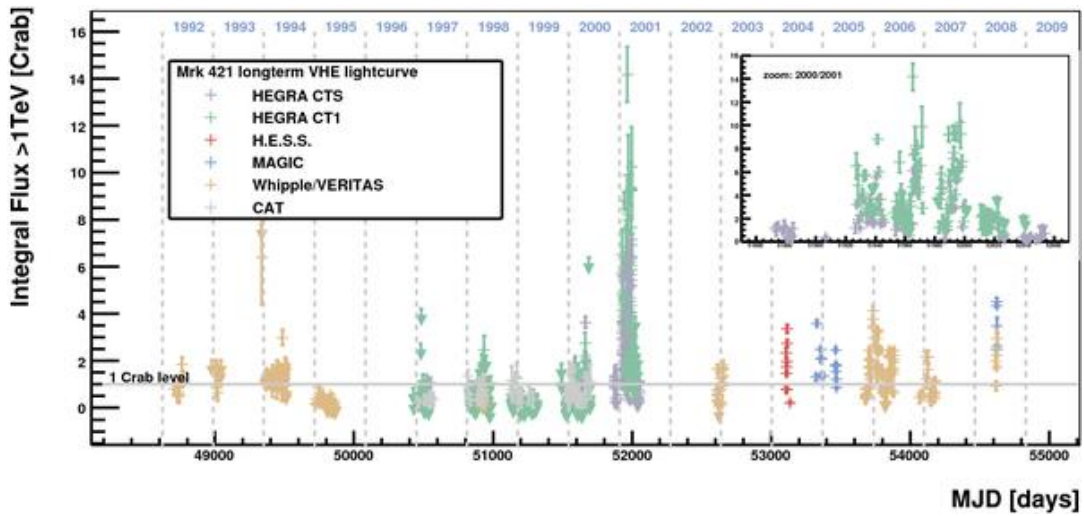
FIGURE 3.9: Long-term light curve of Mrk 421 (day-wise integral flux). Data from the major γ-ray telescopes were combined and normalized to the same energy threshold (1 TeV) and converted to Crab units. A zoom into the period of strong activity (2000/2001) is also shown. *Credit: fig.1 in Tluczykont et al., 2010 .*

The detection of blazars during their moderate and high state is quite common, but the measurements of the low state is a capability of present day and particularly for the next generation IACTs, as the Cherenkov Telescope Array (see section 4.3.2). Most of the blazars show moderate flux variations on daily time scales , while, hour and sub-hour scale flux variations are less common and only detected during the high flaring states. Among these blazars there is also the BL Lac object prototype, the IBL BLLacertae (Neshpor et al., 2001), that is extensively studied during its flaring state in 2019/2020. For major details see section 5.2.

The substructures in the flaring state light curve suggests that the burst is composed of a few rapid flares of the order of a few minutes, and the flux changes from some percents to several times the Crab units. The observed day-scale to hour-scale variability from blazars at VHE is supposed to be correlated with the size of the emitting region, that may be the scale of the size of the SMBH event horizon or passing/standing shock wave in the jet. In the *shock-in-jet* model different parts of the jet moving at different speeds, may collide and give rise to the internal shock front. This shock front may accelerate particles to high and very-high energies, and subsequently dissipate energy in the form of non-thermal radiation. It is assumed that front shock size is compatible with the diameter of the entire jet. In this framework the sub-hour-scale variability is associated with shock acceleration scenario, even because the size of the event horizon of a SMBH of 10^9 $M_\odot$ is tipically around 80 minutes, hence

the observed short variability cannot be originated directly from the central engine.

However the general picture could be more complex. Indeed the detection of fast flaring state in γ rays of FSRQs (Aleksić et al., 2011a) has opened up new interpretative scenarios, as turbulence, multi-zone emission (see section 2.2.1), or magnetic reconnection, emission from the magnetosphere of black holes (Begelman, Fabian, and Rees, 2008; Lefa, Aharonian, and Rieger, 2011; Subramanian, Shukla, and Becker, 2012; Shukla and Mannheim, 2020). That because for γ rays with energy above $20\,\mathrm{GeV}/(1+z)$ are absorbed by $\gamma - \gamma$ interaction taking place within the BLR – ~ 0.1 pc from the central engine – with the UV photons emitted by H-Lyα and continuum emission of a quasar characterized by an accretion disk luminosity above 10^{45} erg/s (Liu and Bai, 2006).

Another method to get insight into emission mechanisms is the multi-wavelengths light curves obtained with observations from radio to VHE γ rays. In this way it is possible to search correlated variability in different wavebands during flaring, moderate and low states, and perform studies using the informations given by the Discrete Correlation Function (DCF), for instance. Some examples are the correlated variability in X-ray and VHE γ rays observed in HBLs that indicates a similar origin of both these photons (MAGIC Collaboration et al., 2020a), and correlation with optical band and γ rays have shown evidence for an optical lag of $\sim 25 \div 55$ minutes indicating lower cooling of less energetic electrons in a *single*-zone SCC scenario (Abeysekara et al., 2020)

Another type of study carried out with multi-waveband temporal data is the wavelength dependence of variability. The flux variability F_{var} is quantified in terms of flux variance intrinsic to the source, normalized to mean flux, and is given by

$$F_{\mathrm{var}} = \sqrt{\frac{S^2 - \langle \sigma_{\mathrm{err}}^2 \rangle}{\langle x \rangle^2}} \tag{3.7}$$

where S is the standard deviation of the measured flux, $\langle \sigma_{\mathrm{err}}^2 \rangle$ is the mean squared error, and $\langle x \rangle^2$ is the square of the average photon flux (Vaughan et al., 2003). The general trend of F_{var} is proportional to the energy.

An ulterior important tool is the Power Spectral Density (PSD) used for characterizing the variability, since it provides an estimation of the power present at different timescales in a light curve. However, this method is not extensively used in VHE γ rays because of the gaps in the data due to the observations associated essentially to high flaring states. An example is PKS 2155-304 studied by H.E.S.S. during ~ 9 years observations (H. E. S. S. Collaboration et al., 2017). On the other hand, PSD is a useful tool in continuous observations performed in optical and X-ray bands.

Finally, an interesting algorithm to study quasi-periodic variability in astronomical sources, featured by observations performed sparsely leading to unevenly sampled time-series, is the Lomb-Scargle Periodogram. This method has been used for the first in the study of quasi-periodicity in the γ-ray blazar PG 1553+113 (Ventura, 2015; Ackermann et al., 2015).

Spectral Signatures

As already said **the origin of γ-ray radiation from blazars is still under debate for both the open questions related to the emission mechanisms and the location of the emitting region within the jet. The observed SED could be the result of leptonic, hadronic or hybrid scenarios. The detection of high energy neutrinos associated with blazars requires that hadronic processes are active in the emission region. In summary, all these processes reflect the physical conditions of the plasma where the particles get accelerated, and the location of the region in the jet in which it moves toward the observer with a bulk Lorentz factor.**

Most of the TeV blazars show the γ-ray peak at high energy, and the observed spectrum is fitted by a power-law with spectral index $3 \div 4$. However in some occasions the spectral index is harder, around ~ 2.2 (Mrk 421; Albert et al., 2007d) and ~ 2.7 (Mrk 501; Acciari et al., 2011), or steeper ~ 4.8 (PG 1553+113; Abramowski et al., 2015) and ~ 4.1 (3C66A; Acciari et al., 2009b). The leptonic scenario alone is able to reproduce the multi-wavelength double-peaked SED (see section 2.2.1 and fig. 2.5) and the correlated variability in X-rays and γ rays. As said in section 2.2.1 the physical mechanism invoked in this interpretation is the Synchrotron Self-Compton (SSC) of ultra-relativistic electrons locked in a spherical blob moving in the jet. The emission is Doppler boosted and the size of the emitting zone is related to variability time scale by light-travel time argument. Sometimes the *single*-zone SSC model is not enough to reproduce the observed SED. In these case *multiple*-zones are responsible for the emission: the inner region produces the VHE γ rays, while the outer one the HE part (Shukla et al., 2015).

Building the MWL SED is useful also to study the observed *harder-with-brighter* trend of the spectrum emitted by BLLac objects. It is the hardening or flattening of the spectrum with an increase in flux measured at X-ray and VHE γ rays, and the first and/or second peak of the SED shifts to higher energies as the source brightens. Sometimes the X-ray peak is found to shift at higher energies, but the second peak, at VHE γ rays, varied little, possibly due to the Klein-Nishima suppression. However in some case HBLs behave as extreme-high-frequency peaked EHBL, shifting the VHE γ-ray peak and showing also an hardening of the X-ray and γ-ray spectral index < 2 (an example is Mrk

501; Acciari et al., 2011). Even IBLs are found to behave like HBLs, shifting the X-ray peak, like 1ES 1215+303 (Valverde et al., 2020).

Moving at lower frequency toward IBLs, LBLs and FSRQs to explain the observed SED a combination of SSC and *external* Compton (EC) is used, because different sources for seed photons available for Inverse Comptonization are required to explain the observed SED[9]. These seeds, external to the jet, are photons provided by the UV radiation associated with the accretion disk onto the SMBH, or from the BLR (Sikora, Begelman, and Rees, 1994), or from farther region, like the IR diffuse radiation of the dusty torus (Sikora et al., 2002).

Multimessenger Signatures

Since AGNs are thought to accelerate UHE CRs, together with leptons also hadrons are accelerated. In the hadronic scenario the injected protons in the emission region produce synchrotron radiation and contribute to the second peak of the SED (MAGIC Collaboration et al., 2020a). Moreover these ultra-relativistic protons interact with low-energy synchrotron photon emitting in γ rays (photo-meson interaction $p\gamma$). In this scenario to account for observed variability, for instance hour-scale, the strength of the MF is required to be of the order of 100 G, while in leptonic model a fraction of a Gauss is sufficient (Aharonian, 2000). In some cases, lepto-hadronic models are also used to explain the second peak of SED as a combination of SSC and photo-meson interaction.

The most direct probe in favor to hadronic mechanisms is the detection of neutrinos, because in hadronic processes neutrinos of all flavors are produced. An example is the high-energy neutrino detected by IceCube in coincidence with the blazar TXS 0506+056, detected in flaring state (IceCube Collaboration et al., 2018a). This detection promotes the blazar TXS 0506+056 to be the third astrophysical source to be identified, after the Sun and a nearby SN 1987A, as a neutrino emitter. Consequently Multimessenger observations can provide crucial informations about emission mechanisms in blazars as well as CR acceleration processes.

3.2.2   Radio galaxies, Starburst galaxies and Gamma-Ray Bursts

Radio Galaxies

Radio galaxies provide crucial informations on the γ-ray emitting region that could be either close or far from the SMBH accretion disk. The MAGIC telescopes observed very fast variability in IC 310 arising from a small region not compatible with the size of event horizon, but could be associated with a pulsar-like particle acceleration in the electric field across a magnetospheric

---

[9]The EC is used also to explain the SED of some HBLs, like 1ES 1440+122 (Archambault et al., 2016).

gap situated at the base of the radio jet (Aleksić et al., 2014). Instead the H.E.S.S. telescopes observed large-scale structure in the jet at TeV energies from Centaurus A, suggesting the γ-ray emission is due to the central engine (H. E. S. S. Collaboration et al., 2020b). Another example of radio galaxy is M87 that not always has shown increasing in the radio regime associated with VHE γ-ray flares (Aharonian et al., 2006d), but when it happens the association of enhanced flux in both radio band and γ rays suggests the origin site of the emission close to the central SMBH (Abramowski et al., 2012).

Starburst galaxies (SBGs)

In a starburst galaxy the star formation of massive stars occurs with exceptionally high rate, almost 10^3 times greater than that in a normal galaxy like the Milky Way. High concentration of gas and radiation is observed in optical and IR regime and it is associated with the regions in which young stars are located. These young and massive stars have relatively short lifetime and at the end of their life they explode as supernovae. Hence an high rate of supernova explosion is associated with high star formation making of the SBGs ideal laboratories for CRs acceleration. Indeed the CR density is order of magnitudes higher than that in a normal galaxy. The most plausible channel for HE and VHE γ-ray emission is the neutral pion decay due to CR collisions with the gaseous matter of the ISM, whereas the charged pions decay in neutrinos. Even electrons are supposed to produce γ rays via bremsstrahlung or by upscattering low energy photons from ambient radiation fields via IC scattering (Völk, Aharonian, and Breitschwerdt, 1996; Paglione et al., 1996; Aharonian et al., 2004). NGC 253 and M82 are examples of sources detected by IACTs. These sources are experiencing a starburst phase because they are merging/colliding with nearby galaxies, this mechanism enriches of fresh gas the galactic environment, thus triggering the star formation.

Gamma-Ray Burst (GRBs)

GRBs are the most violent and catastrophic explosions in the Universe relising a huge amount of energy ($10^{51} \div 10^{54}$ erg) in a very short time (Gehrels and Mészáros, 2012; Kumar and Zhang, 2015). After the detection of a GRB, the initial light curve is characterized by a very short variability pattern from milliseconds to thousands of seconds. To milliseconds/seconds time scale (the prompt phase) it is associated the emission of photons in the keV-MeV range, while later there are emitted photons of the afterglow spanning from radio to HE and VHE γ rays.

GRBs are supposed to be of stellar origin because of the huge amount of energy released and because of the very rapid flux variability. Moreover they are distributed isotropically in the sky showing GRBs are of extragalactic origin.

GRBs are classified in two classes: in the first there are the *short* GRBs with duration of the prompt emission < 1 s, whereas in the second there are *long* GRBs with duration of prompt emission > 2 s. With the first class are associated merging of two compact objects (NS-NS or NS-BH). On the other hand at second class are associated the death of a massive star or a core-collapse supernova. In both cases, a BH is formed and a relativistic jet emerges from the central engine. In this picture, the prompt emission arises from internal shocks occurring in a very compact region. The radiation pressure overcomes gravity and heats up matter into a fireball, which then expands relativistically by this radiation pressure. Subsequently the matter (leptons, hadrons and photons) is ejected in shells moving with different speeds, producing internal shocks when slow-moving shells collide with fast-moving ones. After some time, the fireball becomes transparent and the electrons escaping at this phase emit synchrotron radiation giving origin to the observed prompt emission. The following long afterglow is associated with relativistic jet interacting with the ambient medium (see fig. 3.10 and Zhang, 2019).
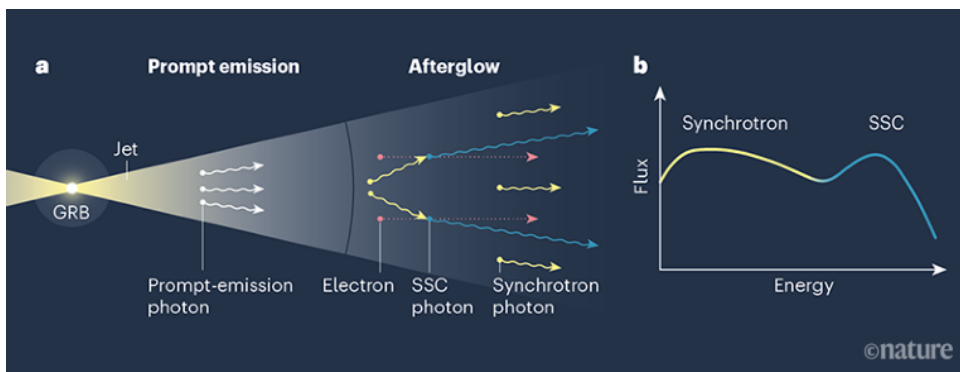
FIGURE 3.10: Emission from a γ-ray burst. The explosive energy from a GRB is thought to be channeled into two narrow jets. Photon emission occurs in two stages: the prompt-emission phase and the afterglow phase. In the afterglow phase, low-energy photons are thought to be generated by synchrotron radiation. High-energy photons are thought to be mainly produced through the SSC process, whereby the scattering of synchrotron photons on energetic electrons gives the photons a boost in energy. One key prediction of the SSC mechanism is the presence of two "humps" in the spectral energy distribution of the afterglow spectrum: one corresponding to synchrotron photons and the other to SSC photons. *Credit: fig.1 in Zhang, 2019*.

As said above, VHE γ rays are expected from the afterglow and several theoretical models try to explain the mechanisms (Mészáros, Razzaque, and Zhang, 2004; Fan and Piran, 2008; Inoue et al., 2013). Under the leptonic scenario the afterglow could be the result of the synchrotron emission of electrons on local MF, but in this case electrons have to be accelerated at PeV energies corresponding to a Lorentz factor larger than that observed. On the other hand, if the emission mechanism is the SSC, the electrons responsible for the emission have to be accelerated at GeV energies then with a smaller Lorentz factor. VHE

γ rays can also be produced by hadronic processes (proton synchrotron or via proton-proton or proton-photon interactions), but these processes are believed to be less efficient compared to leptonic processes.

The space satellite are the best instruments to detect GRBs, and several ones are devoted to this job, as *Fermi*-GBM or BAT, onboard of Swift. When a burst occurs, an alert to ground-based telescopes is sent. The first GRB detected at VHE γ rays was GRB 190114C by the MAGIC telescopes after a bunch of seconds later the alert (Abdalla et al., 2019; Abdalla et al., 2019). During the same period the H.E.S.S. collaboration released the analysis of GRB 180702B detected 10 hours later the alert (Abdalla et al., 2019). In both cases the afterglow emission was measured by the IACTs. After these first two observations, several other GRBs are detected, including the most distant with $z = 1.1$ by the MAGIC telescopes (Blanch, 2020b; Fukami et al., 2022).

3.2.3   Extragalactic Background Light (EBL)

An important ingredient to take into account when analyzing γ-ray data is the presence of the Extragalactic Background Light. The EBL is the diffuse radiation consisting of the sum of the starlight emitted by galaxies through the history of the Universe, and it has the second-highest energy density after the CMB. From a cosmology point of view, the first stars formed before the beginning of galaxy formation contribute to "build" the EBL. VHE γ-ray photons originating from distant sources, like AGNs and GRBs, interact with EBL approaching to the Earth.

The SED of EBL consists of two bumps: the cosmic optical background and the cosmic IR background. The first bump corresponds to stellar emission from optical to near infrared (NIR), whereas the second one corresponds to UV/optical light absorbed and reprocessed in the IR domain by dust (Hauser and Dwek, 2001). From an observational point of view, the EBL is overestimated because of the foreground contamination due to the zodiacal light, for instance; anyway strict lower limits are obtained from integrated galaxy counts (Madau and Pozzetti, 2000; Qin et al., 2023). In this context several models have been developed to describe the EBL SED; some examples are Franceschini, Rodighiero, and Vaccari, 2008; Finke, Razzaque, and Dermer, 2010; Domínguez et al., 2011; Gilmore et al., 2012; Stecker, Scully, and Malkan, 2016.

In the gamma-ray astronomy and observations, the knowledge of EBL assumes a key role because VHE γ rays coming from astronomical sources interact with EBL photons producing electron-positron pairs. This leads to modification of the original spectrum and flux attenuation. Hence the observed flux from a source is given by

$$F_{\mathrm{obs}} = F_{\mathrm{int}}(E) \cdot e^{-\tau(E)} \tag{3.8}$$

where $F_{\text{int}}(E)$ is the intrinsic spectrum and $\tau(E)$ is the optical depth of EBL. As a consequence, the power-law spectrum of high energy photons interacting with EBL is modified, and the flux is attenuated depending on the energy as well as the distance traveled. Hence the subsequent absorption gives rise to the cosmic γ-ray horizon that is the energy-dependent distance beyond which the optical depth due to this interaction becomes large (greater than one). At lower redshift, the Universe is more transparent and only the highest energy γ rays are absorbed, in contrast, at higher redshift, Universe is opaque to γ rays of even lower energies.

The cosmic γ-ray horizon is also used as a cosmological probe, and to give an estimation of source distance. In general to estimate the EBL is used the distorted incident spectrum caused by EBL itself.

3.3   InterGalactic Magnetic Field (IGMF)

Magnetic fields are present on all scales, from small objects like planets to clusters of galaxies. Galaxies have fields of $B \sim 1\,\mu$ G, which drive the magnetisation of the circumgalactic medium via winds. Active galaxies can eject jets of magnetized material into galaxy clusters and cosmic voids. Clusters of galaxies are connected to each other through filaments with $B \sim 0.1 \div 10\,\nu$ G, constituting the cosmic web, whose magnetic properties are poorly known.

Due to the intrinsic difficulties in measuring MFs at scales larger than clusters of galaxies, the scarcity of observational data makes of γ rays one of the most promising messenger to probe the nature and strength of the IGMFs. They are produced in electromagnetic cascades initiated by high-energy γ rays or CRs in the intergalactic space since the charged component of the cascade is sensitive to magnetic fields and γ-ray observations of distant objects such as blazars can be used to constrain IGMF properties. The measurements obtained with ground-based and space-borne γ-ray telescopes provide useful informations on the spectral, temporal, and angular information of γ-ray sources, which carry imprints of the intervening MFs and allow to get insights into the nature of the processes that led to the creation of the first MFs and into the phenomena that impacted their evolution.

The large-scale component of the MFs are investigable through several techniques which exploit the X-rays and radio emission of the magnetized ridge connecting galaxy clusters. In contrast, in cosmic voids where the low density of these regions make difficult to measure quantities, the HE γ rays from electromagnetic cascades provide tomographic informations of the MF structure of the regions themselves. Since the MFs in voids are virtually unaffected by structure formation, they provide a direct window into the early Universe and the magnetogenesis process.

The absence of such fields would indicate that seed MFs are originated in astrophysical objects, where they were subsequently amplified through dynamo processes until they reached present-day levels of $\sim 1\,\mu$ G in galaxies.

On the other hand, if IGMFs have been generated in the early Universe – called primordial magnetic fields – they represent an additional component of the total energy of the Universe and they have thus an impact on its evolution – which results in manifold imprints onto the CMB – and they may even be able to reduce the tension on the Hubble constant value[10]. Moreover, depending on their strength, primordial MFs created at the electroweak phase transition may prevent the electroweak baryogenesis, even if recently observations has been shown that Inflation-generated helical MFs could create the necessary baryon asymmetry. Finally, strong MFs have an impact on the neutron-proton conversion rate, therefore affecting the rates of the weak reactions which are responsible for the chemical equilibrium of neutrons and protons before Big Bang nucleosynthesis, hence modifying it. For a review see Alves Batista and Saveliev, 2021 and reference therein.

---

[10]Indeed the value obtained through type Ia Supernovae observations is different from Planck measurements of the CMB.

4 Cherenkov Technique and Detectors

G AMMA-RAYS are the shortest waves (~ 0.1 Å or less) and therefore have the highest energy in the electromagnetic spectrum. Due to the high-energy of γ rays, they pass right through the mirror of a standard optical telescope, instead, γ rays are detected by the optical flashes they produce when interacting with the material in a specially designed instrument such as a scintillation detector. Earth "blocks" most of the γ rays reaching the top of the atmosphere, for that reason many gamma-ray telescopes are carried on satellites and balloons. While to observe the very-high energy part of these γ rays, ground-based telescopes represent the best instruments to observe the Cherenkov radiation produced when a γ-ray strikes the Earth's upper atmosphere.

4.1 Extensive Air Showers

The Earth is continuously bombarded by high energy particles from deep space with a rate of about one particle per square centimetre per second. When an energetic cosmic ray (CR; $E > 100$ TeV), during its travel through the Galaxy, interacts with the Earth's atmosphere produces a cascade of secondary newly created particles detectable at the ground level. This cascade is known as *hadronic air shower*, and later the initial interactions in the upper atmosphere produce large numbers of charged and neutral pions. The charged pions decay into muons and muons in neutrinos, whereas the neutral pions decay into pairs of high energy photons which become the starting points of large cascades of electrons, positrons and then γ rays. Hence the hadronic core of the initial cascade acts as a collimated source of electromagnetic sub-showers, the *secondary electromagnetic air shower*. An hadronic air shower is more penetrating in the atmosphere with respect to an electromagnetic air shower started by a primary γ-ray. At ground level the resulting flux of particles consists mainly of muons and electrons/positrons in the ratio of roughly 75 to 25 percent, and neutrinos. The cascade is thus strongly dependent to the primary progenitor particle.

In summary, the primary particles interact with air molecules and atoms producing secondary particles, which in turn interact with air molecules and atoms and so on (see fig. 4.1). Thus the shower growing until the secondary particles have energy enough to divide into different particles.
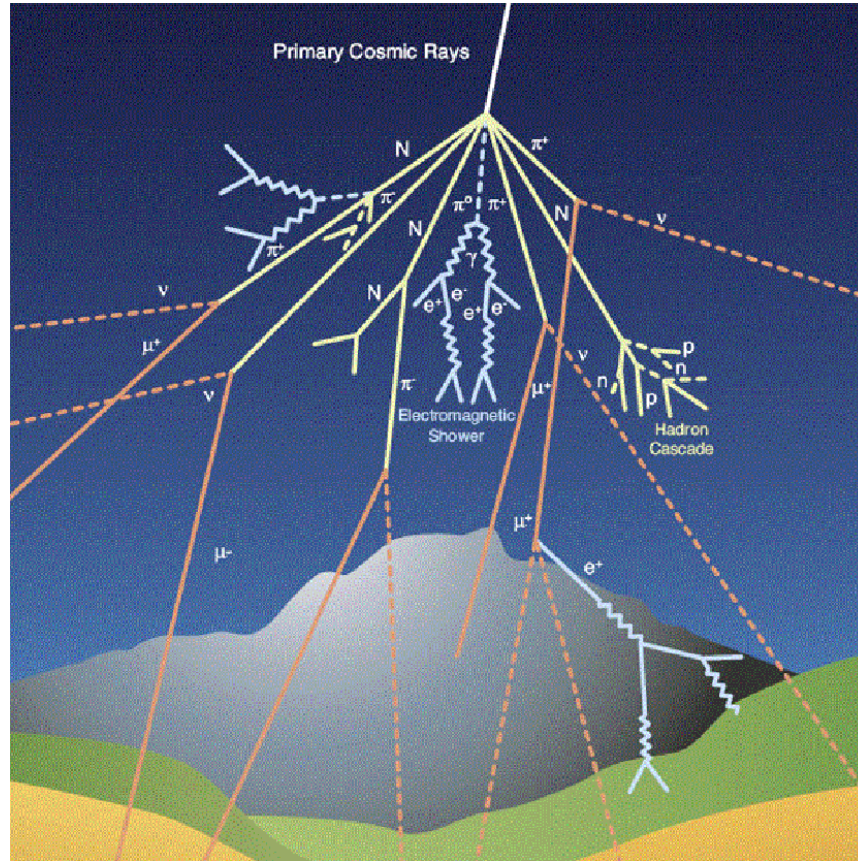
FIGURE 4.1: Formation of air shower in atmosphere. *Credit: fig.1 in Pushkin and Villani, 2021*.

When the maximum is reached, the shower starts to decrease because of radiation losses due to ionization and Compton scattering. As a result, the cascade goes on until the threshold at critical energy is reached, and the associated height of the maximum depends on the energy of the primary CR.

As a consequence of this multi-generation production, the lateral development of air showers spread over a large area on the ground, and to collect the largest part of the showers, arrays of detectors represent the best telescopes to detect the low flux of primary multi-TeV CR hitting the upper atmosphere. Air shower detectors are of 3 types (Workman et al., 2022)

- *shower array* that measures the shower size, muon number, and the lateral distribution of the shower on the ground

- *optical Cherenkov* and *radio* detectors that detect forward-beamed emission by the charged particles of the shower

- *fluorescence* detectors that measure nitrogen scintillation excited by the charged particles in the shower.

For establishing the primary energy spectrum from air-shower experiments, cross-calibrations between different types of detectors and detailed simulations of the shower are required[1]. In the energy range above 10^{17} eV, the fluorescence technique is useful because it can establish the primary energy in a model-independent way, even if the result depends strongly on the light absorption in the atmosphere, and on the effective area of the detector (Bird et al., 1994).

The air showers are mainly produced in the troposphere, because that layer – between the ground until $10 \div 12$ km above sea level – contains almost 99% of the atmospheric mass. Moreover the hadronic component of CRs generate the so-called *hadronic showers*, whereas primary electrons and γ rays give rise to the *electromagnetic cascade*. The method to distinguish γ rays from nucleons is based on the differences between hadronic and electromagnetic showers. This procedure is known as *gamma-hadron separation* (section 4.3.1.1), and assumes a key role in the low level analysis chain of data measured with IACTs.

Electromagnetic Air Shower (EAS)

In the case of a primary γ-ray hits the top of the Earth's atmosphere an electromagnetic air shower is generated. When this γ-ray passes close to the nucleus of an atom it converts into an electron-positron pair (e^+e^-) because of the interaction of the photon with the strong electric field of the nucleus. Then the e^+e^- pair undergoes bremsstrahlung while moving in the atmosphere and additionals secondary γ rays are generated in this process. These secondary γ rays convert in turn into electron-positron pairs that in turn produces additional secondaries γ rays leading to an exponential growth of the number of particles as the shower develop. The multiplication of the charged particles continue till the energy of the γ rays exceed the pair production threshold ~ 1 MeV. The bremsstrahlung process is relevant for electrons/positrons energies above $sim81$ MeV, below which energy loss occurs mainly by ionization. The *critical energy* of the charged particles is defined as the energy in which the energy loss by bremsstrahlung equals the energy loss by ionization. The exponential growth of the shower terminates essentially wWhen the electrons/positrons reach this energy.

The longitudinal evolution of the air shower depends on the energy of the incident particle and on the traveled path in the atmosphere. The *Rossi's Approximation B* is widely used to parametrize the vertical development (Rossi,

---

[1] Specialized simulation codes such as CORSIKA () include both the relevant physics – mainly studied at particle accelerators – and methods for dealing with the large number of particles in high energy air showers.

1952) of the shower. The showers generated by low energy γ rays die out before reach the ground. In the case of the two MAGIC telescopes which are located at a height of 2200 m above sea level, the shower multiplicity decays for photons with energies ~ 200 GeV.

Air showers are characterized also by the transverse development that is due to the multiple scattering affecting electrons and positrons translating away from the cascade central axis. The *Molière* radius R_{M} is used to parametrize the size of the shower. Indeed it is defined as a cylinder containing 90% of the cascade, and 99% of the particles are in a cylinder with a radius of 3.5 R_{M}.

The lateral evolution of the shower is instead parametrized by the Nishimura-Kamata-Greisen (NKG) function that gives an estimation of the density of electrons/positrons as a function of the distance to the shower axis and of the time in terms of radiation lengths, and of the energy of the primary γ-ray. The extension at ground level of an electromagnetic cascade is more compact and symmetric with respect to the hadronic one (see fig. 4.2).

Gamma shower   Hadronic shower
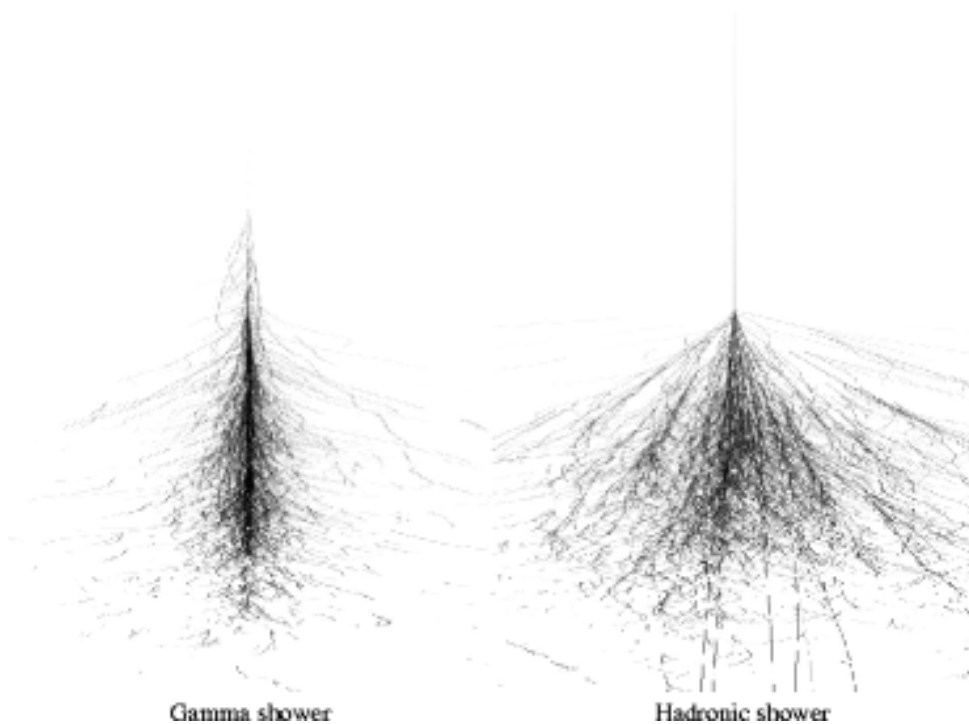
FIGURE 4.2: The gamma shower is slender and axially symmetric with respect to the direction of the primary. The hadronic shower is irregular and may contain electromagnetic subshowers as a result of the π^0 with large transverse momenta generated in hadronic interactions that decays in γ γ. *Credit: fig.2 in (Völk and Bernlöhr, 2009)*

.

As said earlier, also hadronic shower initiates secondary electromagnetic cascade, either from neutral pion decay or from the Cherenkov light (see fig. 4.2) emitted by muons. In this case, the γ rays due π^0s decay could be confused with γ rays due to pure electromagnetic shower, and they represent the background component that cannot be subtracted by measurements performed by IACTs. Whilst the Cherenkov light due to muons has a ring shape on the camera plane of the detector, for that reason can be distinguished and removed (fig. 4.3). The on average statistically different shapes of images from hadronic and electromagnetic cascades are thus used by IACTs to discriminate among the progenitor. These images are reduced to statistical parameters, known as *Hillas parameters* (Hillas, 1984; Hillas, 1985) that are used to remove more than 99% of the hadronic background fig. 4.3.
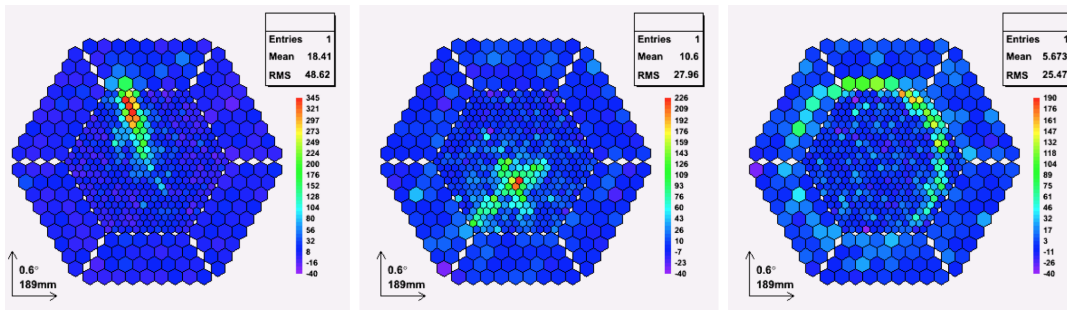
FIGURE 4.3: Example of the three different types of shower images recorded by the MAGIC camera. From left to right, gamma-like shower, hadronic shower, and muon ring. *Credit: fig. 38 in Gaug, 2006.*

The main emission channel of an air shoer are the fluorescence and the Cherenkov radiation, that represent that type of emission exploited by IACTs to collect information on the VHE γ-ray photons reaching the Earth, and used in this work.

The most energetic CRs hitting the top of the atmosphere, moving downwards to the ground, ionize and excite atoms and molecules. The excitation to meta-stable electron levels, with short mean lifetime, and subsequently decay at ground level causing UV fluorescence peaked at wavelengths from 300 nm up to 430 nm. This emission is isotropic and depends on the shower size, hence it can be used for indirect measurements of CRs, but, since the energy threshold for fluorescence emission is $\sim 10^{18}$ eV, this technique can only be used for UHE CR studies. Fluorescence light comes mainly from Nitrogen atoms because it is the most abbundant component of the Earth's atmosphere, (Abraham et al., 2010).

4.1.1 Atmospheric Cherenkov Light

The discovery and the interpretation of the Cherenkov effect (Čerenkov, 1937; Frank and Tamm, 1937) have assumed a key role in the astroparticle physics, especially in

the progress on CR physics knowledge, the establishment of γ-ray astronomy, the discovery of neutrino oscillations, and the detection of high-energy cosmic neutrinos.

The majority of the particles in the shower moves down with relativistic velocity exceding the speed of light in the atmosphere provoking emission of Cherenkov radiation. Briefly, the atoms and molecules of the atmosphere, which are close to the trajectory of a relativistic particle, are temporarily polarized by the electric field of the impinging particle. When the impinging particle moves away they turn back intto their initial configuration and they emit radiation. If the velocity of the impinging particle exceeds the speed of light in the medium then the contributions to the radiation field of all the atoms and molecules add up coherently leading to a shock wave in the electro magnetic field that is called Cherenkov radiation.

The Cherenkov effect is a threshold mechanism that occurs when the particle energy is above the energy threshold, that is itself strongly related with the refraction index of the atmosphere, which changes with the altitude. Hence the energy threshold changes during along the trajectory of the particle.

The maximum development of the shower is at ~ 10 km in altitude that correspond to the maximum production of Cherenkov light. The geometry of the emitted radiation assumes the shape of a small cone which axis is coincident with the particle trajectory, and the aperture of the cone is the so-called *Cherenkov angle* θ_C, itself dependent of the refraction index of the medium. θ_C has an amplitude of $\sim 1°$, and
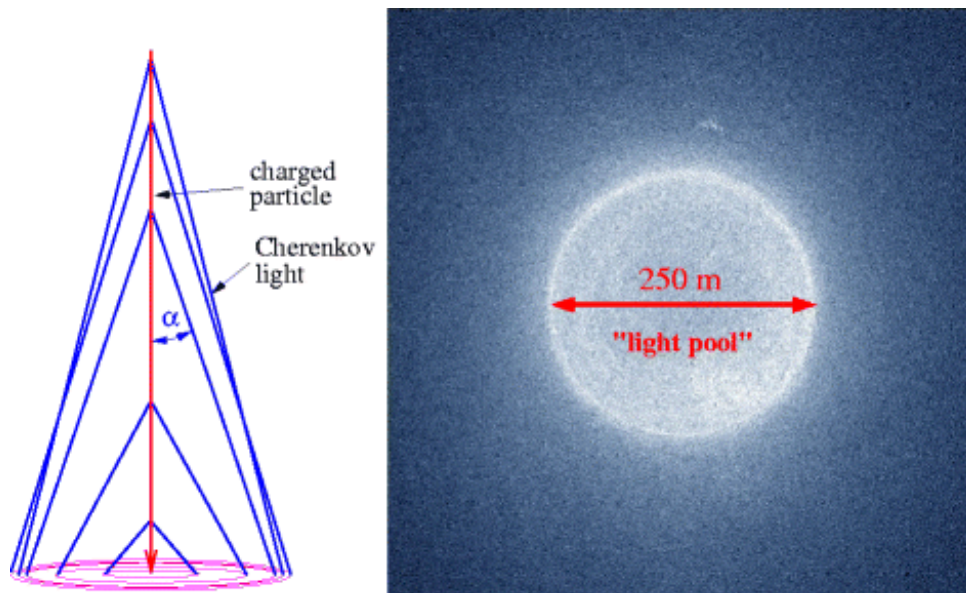
FIGURE 4.4: *On the left*: Atmospheric Cherenkov emission from a downward-moving single particle. *On the right*: The *Cherenkov light pool* at an observation level (~ 1800 m above sea level) from a γ-ray shower with a primary energy of 1 TeV. *Credit: fig.3 in Völk and Bernlöhr, 2009.*

increases with the air density increasing. During the development of the air shower, several particles emit at the same time, and the resulting emission spectrum is thus a superposition of the emitting cones, known as *Cherenkov light pool* (see fig. 4.4). The integrated path length of all $e^\pm$ in the cascade and therefore the overall Cherenkov light yield is to a good approximation proportional to the initial γ-ray energy E_γ.

At the ground the illuminated surface has the shape of an ellipse with a radius of ~ 120 m, depending on the observer zenith angle, and covering an area of 1.6×10^5 m^2. The characteristics of the Cherenkov radiation are therefore its emission angle with respect to the particle's direction of flight θ_C, its intensity dN_γ/dx, given by the Frank-Tamm formula, and its spectrum

$$\cos \theta_C = \frac{1}{n\beta} \tag{4.1}$$

$$\frac{dN_\gamma}{dx} = 2\pi\alpha \left(1 - \frac{1}{n^2\beta^2}\right) \cdot \left(\frac{1}{\lambda_{\min}} - \frac{1}{\lambda_{\max}}\right) \tag{4.2}$$

$$\frac{d^2N_\gamma}{dEdx} \approx 370 \sin^2 \theta_C(E) \ \text{eV}^{-1}\text{cm}^{-1} \tag{4.3}$$

where n is the refraction index, $\beta = v/c$ the particle velocity, λ the emitted wavelength, that roughly corresponds to the sensitivity range of typical light sensors, and finally α is the fine structure constant. The duration of the Cherenkov light is comparable to that of a *flash* of $\sim 3 \div 10$ ns for an electromagnetic air shower, or longer for hadronic cascade (see fig. 4.5).
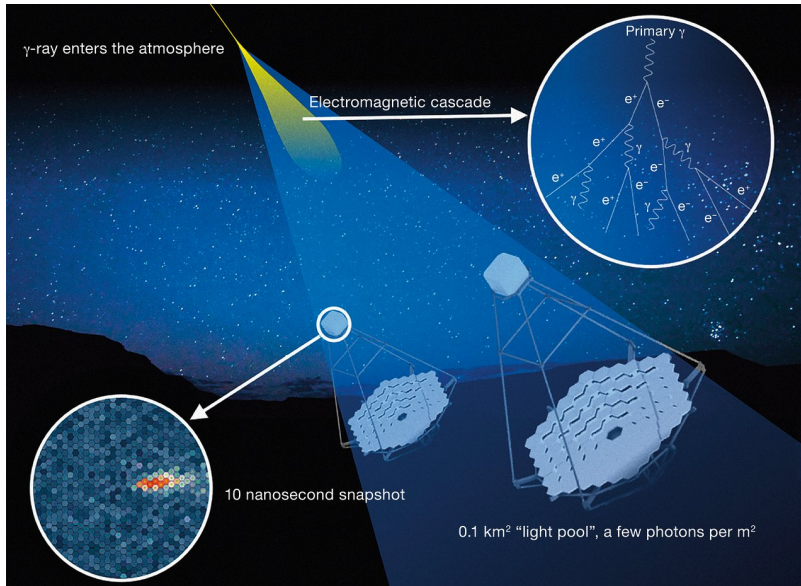
FIGURE 4.5: A picture of the Cherenkov light, the blue flash of light resulting from γ rays interacting with the Earth's atmosphere. IACTs, as the MAGIC telescopes and CTA indirectly detect γ rays through the Cherenkov effect, and exploiting the atmosphere as a calorimeter of ~ 30 radiation length. *Credit: www.eso.org*.

Cherenkov photons are measured with good spatial and time resolution allowing to be separated from background light, and the geometry ot the emission enable to reconstruct the primary incident particle trajectory. The recorded Cherenkov intensity is furthermore related with particle energy. Usually, the detectors are shielded from ambient light, and the photo-sensors are sensitive to single photons with nanosecond time resolution (Katz, 2020). The standard used sensors are photomultiplier tubes (PMTs) and, more recently, silicon photomultipliers (SiPMs) (Barbato et al., 2016; Vinogradov and Popova, 2020).

Each GeV of energy coming from the progenitor γ-ray photons generates 500 Cherenkov photons, and its spectrum is emitted in the UV-optical range with less than 300 nm down to the radio wavelength. Not all the Cherenkov photons, especially the less energetic, reach the detector because of the multiple interactions with the atoms and molecules of the atmosphere that scatter or absorb them. These effects are strongly dependent with the zenith angle of the observer, and then the altitude at which the detector is located. The Rayleigh scattering, that is dependent to λ^{-1}, represents the main mechanism of photon privation during good weather condition. In contrast, during not optimal conditions, as in presence of clouds or calima[2], the dominant process is is the Mie scattering occurring with atmospheric particles bigger than the photon wavelengths, such as water drops, dusty grains, or small ice crystals. It depends on λ^{-a} where $1 < a < 1.5$. Particles undergoing multiple scattering move away from the cone axis, and they emit radiation outer the Cherenkov light pool, forming an halo around it. Even in this case this phenomenon depends on the observer zenith angle.

4.2   Imaging Atmospheric Cherenkov Telescopes (IACTs)

Our atmosphere is transparent to electromagnetic radiation in the radio and in the optical bands, by contrast, it is opaque for X-rays and γ rays. Gamma rays below 20 GeV are measured by satellite experiments, while those at higher energies by ground-based detector. That because satellite instruments rapidly loose sensitivity to the steeply decreasing γ-ray flux due to their limited collection area (Funk, 2015a). On the other hand, ground-based observatories, as Imaging Air Cherenkov Telescopes (IACTs), can detect VHE γ rays through their "Cherenkov behavior" in atmosphere. They operate preferentially under moon-less nights, and they are located in sites with negligible light pollution and an elevation of typically 2 km. As said in chapter 3, they are pointing instruments with a field of view of a few degrees in diameter. Other type of instruments able to collect air showers are timing arrays at higher altitude. They cover a significant fraction of the sky – for that reason

---

[2]The Calima is a meteorological phenomenon consisting of the presence of very small particles of Saharian dust, ash, clay or sand in suspension in the atmosphere.

can provide survey – albeit with a higher energy threshold than IACTs and inferior sensitivity at energies below ~ 50 TeV.

Since all particles in the air shower propagate with a speed close to that of light, at ground the Cherenkov radiation is a flash of few nanoseconds of duration and can thus be separated from the night-sky background. IACTs have a camera made of photomultipliers or SiPM detectors in their focal plane making possible to collect the *blue flashes* of Cherenkov light. The field of view of some degrees, featuring IACTs, is estimated on the extension of the camera since each camera pixel corresponds to a certain solid angle of the light arrival direction. When a telescope points to a γ-ray source, sees the start of the cascade close to its centre, from where it propagates outward.

For achieving a better reconstruction of γ-ray direction and energy, several camera, of different telescopes builded in the area covered by the Cherenkov light pool, are used in stereoscopic mode. This technique achieves a resolution of $\sim 0.1°$ and $\sim 20\%$ in energy. The implementation of SiPM in the camera, as done by FACT (Anderhub et al., 2013) operating since 2011, has demonstrated that SiPMs can take very high rates, enabling observations even in full-moon nights. A large reflector focuses Cherenkov light on a camera made by several PMTs or SiPMs, that samples its angular distribution (fig. 4.6).
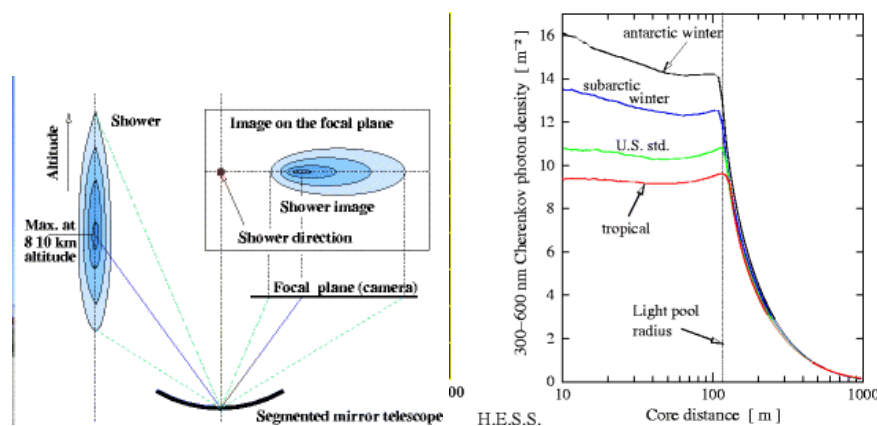
FIGURE 4.6: *On the left*.Despite some asymmetry, the shower image in the camera has the shape of an ellipse (see also fig. 4.3). The shower direction is a point somewhere on the extension of its major axis. For γ-ray primaries the image intensity gives the primary energy. *On the right*. Lateral distribution per unit area of the blue Cherenkov emission from a shower with primary energy of 100 GeV, for various atmospheric profiles. *Credit: fig.6 and fig.5 in Völk and Bernlöhr, 2009*.

As said earlier, the Cherenkov angle θ_C at higher altitudes is smaller than that at lower ones. As a result, the higher section of the shower is reflected closer to its axis than the lower sections are, and the cascade maximum lyes somewhere in between the images. The signal in the sensors is used to reconstruct the elliptically-shaped Cherenkov image of the shower. Hillas parameters are then used to describe the measured images that have different sets of the parameters allowing to perform the gamma/hadron separation (fig. 4.7).
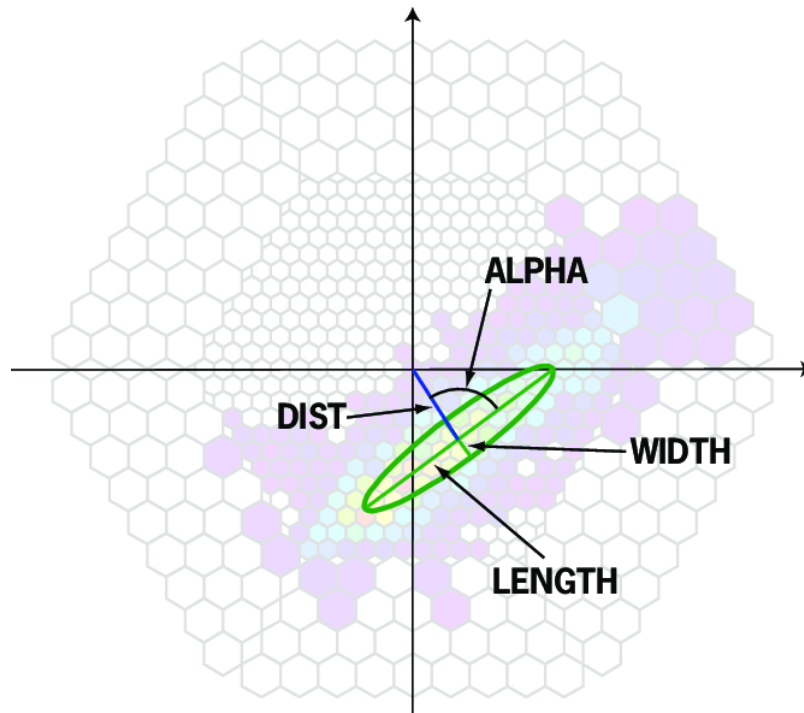
FIGURE 4.7: Example of Hillas parameters. The shower image is parametrized with few geometrical parameters derived from its zero, first and second moments. They are WIDTH, LENGTH, DIST and AL-PHA. WIDTH and LENGTH are the eigenvalues of the covariance matrix. ALPHA is the angle between the major shower axis and the vector from the center of gravity of the shower to the center of the camera. DIST is the distance between the center of gravity of the shower to the center of the camera. ALPHA is related to the arrival direction of the recorded shower and it is used to extract the γ-ray signal. *Credit: fig. 5.4 in Otte, 2007.*

Additionally, informations about the shower orientations – and hence the primary γ-ray direction – are achieved by directing towards the impact point the major axis of the ellipse. Operating in stereoscopic mode, with multiple telescopes and camera in the same observational site (fig. 4.8), enables to perform triangulation to better reconstruct the direction of the primary γ rays, the impact point and the height of the shower maximum (Völk and Bernlöhr, 2009; Hinton and Hofmann, 2009). The background is furthermore suppressed more efficiently thanks to coincidence triggering. In the case of two telescopes, such as the MAGIC telescopes, no triangulation is possible when the projection of the shower axis on the ground is parallel to the line

linking the two telescopes, because the effective baseline separation between the two becomes zero.
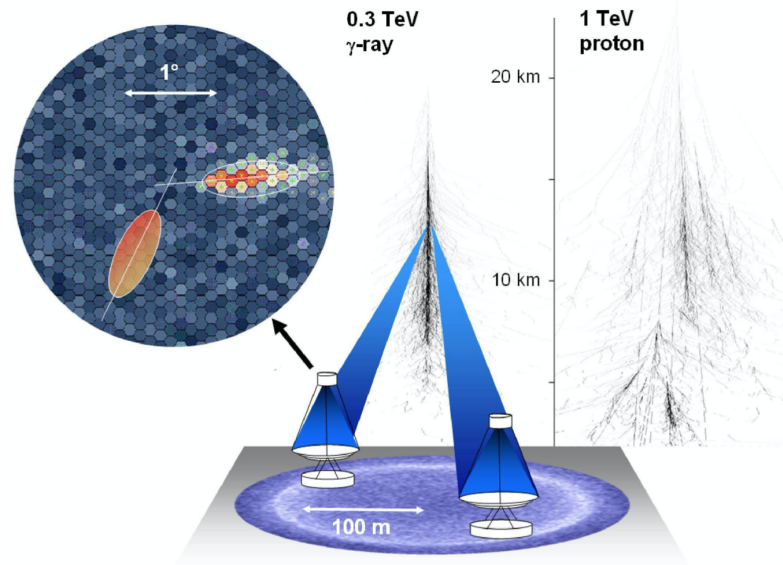
FIGURE 4.8: Sketch of the imaging atmospheric Cherenkov technique showing the formation of an electromagnetic cascade for a 300 GeV primary γ-ray, the production of Cherenkov light, and the formation of an image in the camera of a Cherenkov telescope. Cherenkov light production for a proton initiated cascade is shown for comparison. *Credit: fig. 5 in Hinton and Hofmann, 2009.*

The advent of Imaging Atmospheric Cherenkov Technique has opened the era of γ-ray astronomy at very-high energy, allowing to study the powerful and extreme phenomena of the Universe[3].

4.3 Detectors

The aim of this section is to briefly describe the principal characteristics of the two IACTs used in this project. The observations performed by the MAGIC telescopes, regarding the BLLac flare in the period 2019/2020, and the detection at VHE of the EHBL 1RXS J081201.8+023735 are discussed in chapter 5. Moreover, the simulations performed in view of the next generation Cherenkov Telescope Array (CTA) regarding the peculiar Galactic Center region, are discussed in chapter 6.

4.3.1 Major Atmospheric Gamma Imaging Cherenkov telescopes (MAGIC)

The MAGIC Florian Goebel Telescopes consist in two $17\,\mathrm{m}$ diameter imaging atmospheric Cherenkov telescopes separated by ~ 85 m, located at the Observatorio del

---

[3]For an historical review of the early days of Cherenkov technique see Weekes, 2003; Lorenz and Wagner, 2012.

Roque de Los Muchachos (ORM) on the Canary Island, La Palma (Spain), at an altitude of 2200 m above the sea level (fig. 4.9). The MAGIC telescopes were designed in 1997 to cover the then-uncharted energy region between 20 GeV and 300 GeV (Lorenz and MAGIC Telescope Design Group, 1997). For reaching this energy sensitivity, the energy threshold has been lowered by building extremely large mirrors with an area of $236\,\mathrm{m}^2$, and exploiting PMTs with enhanced quantum efficiency to collect the faint light of Cherenkov light. Moreover the large mirror surface and the high sampling speed of the data readout allow to lower the analysis energy threshold and enhance the sensitivity, reaching a value of ~ 30 GeV. Many elements in the structure are made in aluminium and reinforced carbon fibre, and the readout electronics is separated from the camera, making both IACTs very light-weight telescopes. This innovative design has made possible the detection of the first GRB – that is a γ-ray flash of few seconds – later a bunch of seconds the alert sent by a satellite monitoring (see section 3.2.2), and in general of transient phenomena that require a fast repositioning of the telescopes.

The MAGIC observations allow to bridge the gap with satellite γ-ray measurements, which sensitivity is limited to few tens of GeV by low statistic. The possibility to observe the gamma-sky from ground level at energies below 100 GeV is crucial for many studies, such as the detection of steep spectra of pulsars or GRBs. Moreover low energy thresholds allow to extend the horizon of the Universe detectable through γ rays, because above this energy the emission from high-redshift sources is suppressed by the interaction with the EBL section 3.2.3. The MAGIC telescopes are located in the northern hemisphere that represent the ideal position on the Earth to observe the extragalactic sky, which sources mainly lie outside the *luminous* galactic plane, better observable from the southern hemisphere.

FIGURE 4.9: The MAGIC telescopes (center and right) at the Roque de los Muchachos observatory in July 2020, with comet NEOWISE in the background. On the left the first prototype Large Sized Telescope (LST) of CTA. *Credit: Urs Leutenegger.*

Telescopes Architecture

The MAGIC-I (M1) telescope was finished to build in 2003, and the MAGIC-II (M2) in 2009, allowing to operate in stereoscopic mode and to trigger in coincidence. In 2011 after an upgrade the readout of both telescopes was unified in a single architecture[4]. During the upgrade the M1 camera and the trigger system were also renewed. Software and hardware improvements made possible to stabilize the overall system performance and to achieve a sensitivity of $0.66 \pm 0.03\%$ of the Crab nebula flux above 220 GeV for 50 hours of integration time (Aleksić et al., 2016b). The telescope structure supporting the mirrors is a frame of octagonal shape, with 7 m side length, of carbon fibre-epoxy tubes, with altitude-azimuth mount.

The camera is sustained by an aluminium arch, stabilized by 10 pairs of steel cables tied to the main frame. The arch continues over the back of the dish becoming a rail of circular shape, for the altitude drive and a support for the counterweights. The whole structure is connected to six bogeys resting on a circular rail, and the total weight of a single telescope is ~ 60 metric ton. Three electrical servo-motors move the telescope, two in azimuth and one in elevation, covering a range of $\sim 10°$ to $160°$ in elevation and $\sim 90°$ to $318°$ in azimuth. The telescopes can track a source with a precision of the order of $0.02°$ thanks to the starguider camera mounted in the centre of the dish, which compares the position of the telescope camera with that of the background stars. The telescope can rotate by $180°$ in less than 20 s allowing to fast pointing GRB allerts. The diameter D of the parabolic reflector dishes is 17 m as well as its focal length f is close to 17 m leading to $f/D = 1.03$. Moreover the reflector is tessellated and each of the facets has an area of about 1 m ^{2}, and the whole mirrors are coated with a protective layer of quartz. In both telescopes all mirror facets are spherically shaped with a curvature radius varying from 34 m to 36.7 m, depending on their position in the dish. This configuration achieves a Point Spread Function (PSF)[5] of less than 10 mm wide, hence most of the reflected light is contained inside a single PMT, and the 104 aluminium coated facet mirrors of M2 reach a PSF less than 10 nm. The paraboloid shape of the mirror surfaces allow to further reduce the night sky contamination since the arrival time of photons are conserved on the camera plane, and in a second moment are used in the analysis to reach good image cleaning, angular resolution and energy estimation. But, "life is not a bowl of cherries", and the parabolic reflectors suffer to several aberrations[6]. As a consequence the PSF of the instrument gets larger, and the Active Mirror Control (AMC)[7] plays against

---

[4]It is based on DRS version 4 (Ritt, 2008; Sitarek et al., 2013).

[5]Here the PSF is defined as the 39% containment radius of the reflected spot of a point-like source on the focal plane of the mirror.

[6]The main onew are spherical aberration, curvature of the field, astigmatism, finite quality aberration, tessellation aberration and coma aberration.

[7]The AMC is a motorized mirror alignment system.

somewhat mitigating the effect. Moreover the AMC automatically corrects the position of each facet while MAGIC is operating in order to maintain the optics of the telescope stable and focus the whole reflector continuously (Biland et al., 2008).

The camera of the telescopes are stabilized in temperature, and the PMTs – often called *pixels* – are organized in hexagonal shape of 114×104 cm in size, covered by a plexiglass window and movable lids in order to protect the PMTs from atmospheric agents and light. The photo-conversion efficiency is further enhanced by the Winston cones, which are light concentrators, favouring double photo-cathode crossings (Ostankov et al., 2000). The camera of MAGIC-II and the new camera of MAGIC-I, installed in 2012, have 1039 pixels all of the same size with a field of View (FoV) of $0.1°$[8] and a quantum efficiency (QE) of $\sim 32\%$ in the blue band. The overall camera FoV is $\sim 3.5°$ for both telescopes. The PMTs gain is of the order of $3 \cdot 10^4$ allowing for observation under moderate moonlight, hence extending the duty cycle of $\sim 60\%$. The signal produced in the PMTs[9] is converted by a low-noise pre-amplifier (VCSEL) into optical signal and transmitted to the readout electronics via optical fibres. The central pixel of both the camera is a modified PMT designed to detect slow variations of the optical flux of selected sources, such as pulsars and blazars (Lucarelli et al., 2008), hence allowing for optical monitoring of the Crab pulsar, for instance, during regular data-taking.

From Telescopes till Images

The signals from the camera arrive via optical fibres to the *counting house* , where the trigger and the readout electronics are located. At trigger level-0 (TL0) the signal is converted back into electronic pulse and digitalized. At this stage the signals from both the camera are discriminate in amplitude adopting *discriminator thresholds* (DTs; usually set to 4.25 phe for extragalactic observation in dark time[10]) for each pixel. At this level the total FoV reached by both the telescope is $\sim 2.5°$ since the trigger region comprises the 547 inner pixels. The digitalized signals are then sent to TL1, in which the nightsky background (NSB) events are rejected by exploiting the fact that Cherenkov flashes of air showers display tight spatial and temporal correlations. Hence in this case groups of neighbouring pixels collect the signal at the same time in coincidence window belonging to air shower, while signals from the NSB are not correlated in time. The two TL1 – one for each telescope – are then sent to the Global Trigger System (GTS; the TL3) which generates the coincidence (stereo) trigger signal – performing ON operation and founding the coincidences – later transferred to the readout at the correct time (Paoletti et al., 2008).

---

[8]FoV of $0.07°$ at 300 GeV.

[9]During dark conditions the typical PMT direct current is around $1\,\mu A$.

[10]During the night the DTs are continuously monitored to maintain constant rate in case of bright stars or moon condition.

At the edge of MAGIC-I reflector is installed a pyrometer with the aim to evaluate the temperature of the nightsky in terms of the **cloudiness** parameter which provides a roughly estimation of the sky quality. Indeed if there are clouds they act as blanckets keeping the atmosphere at higher temperature. A weather station is further placed on the top of the counting house and provides informations about the local temperature, wind speed, and air humidity. Atmospheric calibrations are also performed with the **LIDAR** system, located on top of the roof of the counting house. Its goal is to measure the aerosols and the height of clouds causing the attenuation [11] of air showers' Cherenkov light and to correct the reconstructed events. The solid-angle-corrected signal is described by a barometric altitude profile as

$$S(h) = C \cdot \exp \frac{h}{h_S} \tag{4.4}$$

where h_S is a scaling constant of the height. For each layer of aerosols in the atmosphere is computed the attenuation factor as function of the altitude of the layer as

$$\alpha_{\text{att}}(h) = \tau_{\text{att}} \cdot \frac{ex(h)}{\int_{h_2}^{h_1} ex(h)dh} \tag{4.5}$$

where τ_{att} is the total transmission of the layer, $ex(h)$ is the excess over $S(h)$ related to the layer density, and $h_1 - h_2$ are the lower and upper altitude of the layer. The total absorption at 9 km ($\boldsymbol{T_{9\text{km}}}$)[12] is used as data quality proxy since at that height the air shower reach its maximum development.

A strong atmospheric absorption leads to events reconstructed with lower energy than the true one[13]. The estimated energy is then corrected as

$$E_{\text{est, corr}} = \frac{E_{\text{est}}}{\tau} \tag{4.6}$$

where τ is a scaling factor proportional to the integrated transmission factor from ground to h (obtained by $\alpha_{\text{att}}(h)$), and the distribution of the emitted Cherenkov light in the shower as function of the altitude. approximated to a Gaussian profile centred at the shower maximum (for major details see Fruck et al., 2011; Fruck et al., 2014; Fruck, 2015).

During the night, when the observations occur, a software, the GRB monitoring program, checks the GRB Coordinate Network (GCN) for valid alerts with predefined observability criteria, as the zenith angle, position uncertainty of the candidate GRB, and its distance from the Sun and the Moon. If an alert is

---

[11]The attenuation is mainly due to scattering effects; during good weather conditions the main scattering source is the Rayleigh scattering.

[12]In general, for T_9km $= 0.7$ the data quality is good; for $0.5 < T_9$km<0.7 the data are still exploitable.

[13]This reduction in energy is due to the attenuation effect that reduces the *size Hillas parameter* that is proportional to the energy of the event.

considered positive, both telescopes are pointed to the GRB coordinates in few seconds from the allert.

As already mentioned, the MAGIC telescopes operate during the night and also under moonlight conditions. Around 1600 hours of **dark time** observations are allocated during the year, and ~ 600 are the additional hours reserved for **moon time** observations[14]. For six days per month, coincident with the full moon, the telescopes do not operate.

The trigger TL1 is set in **stereoscopic mode**, and works with 3NN multiplicity logic under *standard* observations[15]. The stereoscopic mode implies that both telescopes point to the same position in the sky contemporary, and two main pointing strategy are used. In the first, during the observations of extragalactic objects, for instance, the source of interest, **on-source**, is pointed with the center of the camera for maximizing the effective area. This procedure however requires to collect additional time, observing different objects, the **off-sources**, located in a region of the sky where there are no known γ-ray sources and with the same star background and zenith angle of the on-source region. As a result, the background estimation is possible and it can be subtracted during the analysis chain of the on-source. While in the second strategy, the telescopes operate in *false-source tracking* mode, also known as **wooble** mode, which consists in pointing the telescopes at a certain position with an angular offset of $d = 0.04°$ from the source location in the sky (Fomin et al., 1994). At each acquisition run[16] the telescopes rotates around the source of $90°$ leading to a total of 4 pointing position. The source therefore occupies different regions on the camera plane during the observation. With this procedure the background (OFF) and the source (ON) are in the same data sample, acquired with the same exposure. The wooble mode further enables to average out systematics due to the PMT response inhomogeneities across the camera plane or due to the asymmetry in the acceptance of the telescopes.

4.3.1.1 The Analysis Chain

Once the data are collected the low and high level analysis can start in order to obtain the final physical informations about the source under investigation. The output of the analysis chain are skymap, spectrum and light curve. MARS is the software used by the collaboration for the analysis and for the event reconstruction (Moralejo et al., 2009; Zanin et al., 2013), it is written in C++ on top of the ROOT data analysis framework (Brun and Rademakers, 1997). The analysis flow consists in:

---

[14]Almost $40 \div 60\%$ of the hours are lost because of bad weather or technical problems.

[15]x next-neighbouring (xNN) pixels illuminated in coincidence inside 19 macro-cells composed by 36 pixels; $2 \leq x \leq 5$.

[16]The duration of an acquisition run is usually 20 minutes.

1. reconstruction and calibration of the Cherenkov pulses contained in raw data,

2. image cleaning and calculation of stereo parameters,

3. training and application of a machine-learning algorithm to discriminate γ-ray against hadrons, and look-up-tables (LUT) to estimate the energy of each event,

4. gamma/hadron separation,

5. determination of the source significance, spectrum, skymap and light curve.

The first 3 points represent the low level analysis, and the last two the high level one.

A large part of the analysis relies on Monte Carlo (MC) simulations. As said earlier, the air showers are simulated with CORSIKA (Heck et al., 1998) software[17], whilst the simulation of the propagation of the Cherenkov light, of the MAGIC mirrors optics and of the detector response [18] is performed with the software described in Majumdar et al., 2005. MC simulations allow also to obtain the instrumental response for events with known nature, and their zenith and azimuth angle ranges are the same of the telescopes since the size of the shower is affected by the zenith[19], and azimuth[20] angles.

The signal reconstruction and calibration are performed extracting from the raw data the arrival time and the intensity of the signal aiming to convert it into high level quantities (Gaug, 2006). The signal waveforms from the pixels are digitized by several DRS4 chips, and calibrated using the F-factor method (for major details see Mirzoyan, 1997).

The PSF of the instruments can be measured with two main strategies. In the first it is used the radius, width and charge distribution of ring-like images produced by the Cherenkov light of a 5 GeV muon (Saito, 2011). While in the second a white diffusor disk is placed in front of the camera and a high resolution and sensitivity CCD is placed near the optical axis. The telescope is pointed to a relatively bright star so that the CCD can capture both the direct image of the star and its image reflected by the MAGIC mirror and focused on the white disk. The PSF and the light collection efficiency can be estimated by comparing the two images of the star (Kellermann et al., 2012).

The previous step is followed by the **image cleaning**, in which the pixels containing noise are rejected (Shayduk et al., 2005).The cleaning consists in selecting the pixels which contain the photons of the Cherenkov light, deleting those which signals is due to NSB light. Practically, the cleaning algorithm selects a compact group

---

[17]CORSIKA webpage.

[18]In particular, the absorption and scattering of Cherenkov photons in the atmosphere, reflection of Cherenkov light on the MAGIC mirrors, response of the MAGIC camera and readout.

[19]At higher zenith angles the Cherenkov light travels a longer path in the atmosphere leading to a stronger absorption as well as a smaller Cherenkov photon density on ground.

[20]The geomagnetic field modifies the overall shape of the air shower.

of neighbouring pixels that simultaneously contains a signal, corresponding to the elliptical shape of the projected Cherenkov photon on the camera (fig. 4.3). Consequently, the obtained ellipses, representing the Cherenkov light, is parametrized using the **Hillas parameters** (Hillas, 1984; Hillas, 1985). The parameters representing the image of each telescope that are independent to the source position are

- **size**, that is the total charge contained in the image, in photoelectrons (phe), which is proportional to the total number of Cherenkov photons and, in first approximation, proportional to the energy of the incident γ-ray[21]

- **Centre of Gravity** (CoG), that is the position on the camera of the weighted mean number of phe, expressed in (X, Y) coordinates

- **width**, that is the spread of the light along the minor axis of the ellipse (half width)

- **length**, that is the spread of the light along the major axis of the ellipse (half length)

- **conc-n**, for *concentration* or *compactness*, that is the fraction of phe (image size) contained in the n-brightest pixels; it is related with the compactness of the image useful to discriminate γ rays and hadrons since the image of the first is more compact (conc-1 & conc-2 generally used)

- **leakage_1/2**, that is the fraction of the image size (phe) contained in the outermost rings of pixels of the camera (Leakage_1) and in the two outermost rings (Leakage_2)

- **M3Long**, that is the third moment of the image along its major axis, with positive sign if directed towards the camera centre; it relates to the asymmetry of the image along the major axis

- **asymmetry**, that is the distance between the image CoG and the pixel with the largest charge, positive if directed towards the camera centre

- **number of islands**, that is the number of isolated groups of pixels which survive the image cleaning; hadrons show a larger amount of islands – since the development is more fragmented – than γ-ray showers.

Whilst the source dependent parameters are

- **time RMS**, that is the RMS of the arrival times of the Cherenkov photons in the pixels surviving the cleaning

- **time gradient** or **time profile**, that is the linear coefficient (slope) of the fitted arrival time projection along the major axis of the ellipse

---

[21]For discriminating gammas and hadrons the cut applied to size parameter is > 50 for dark time.

- **dist**, that is the angular distance between the CoG of the image and the source position

- α, that is the absolute value of the angle between the major axis of the image and the direction from the CoG to the nominal source position on the camera plane

This set of parameters describe one image (monoscopic), and thus by combing the images of the same shower from the two telescopes (stereoscopic) it is possible to reconstruct the 3D extension of the shower, since the telescopes observe the shower from two different point-of-view (Kohnle et al., 1996). As said earlier in section 4.2, the **shower direction** is get by intersecting the major axes of the two elliptical images on the camera, while the **core impact point** on the ground is determined by the intersection of the major axes of both ellipses taking into account the telescopes positions (fig. 4.10).
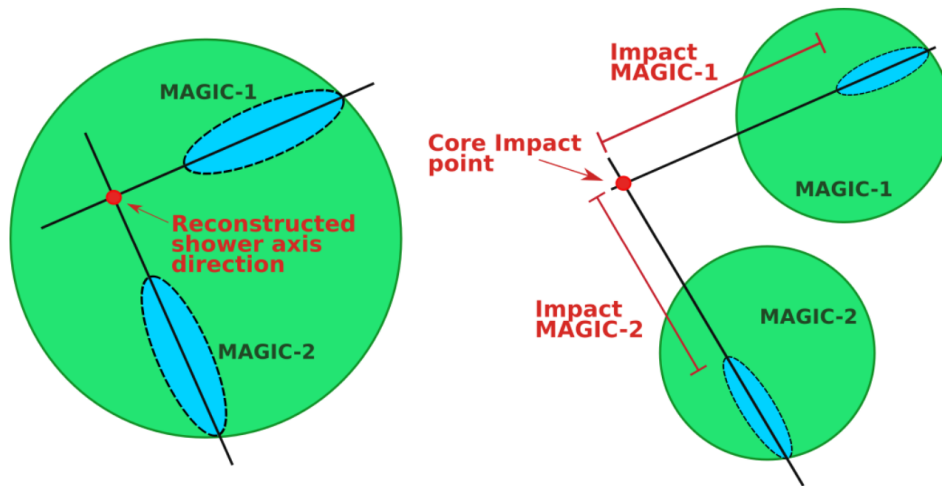
FIGURE 4.10: Stereoscopic parameters for direction reconstruction. *On the left* the overlay of the MAGIC-1 and MAGIC-2 air shower images is shown. From the crossing points of the two ellipses major axes, the direction of the shower axis is calculated. *On the right* the same event as seen in the telescopes separately is shown. From the crossing point of the two prolongated major axes of the ellipses, the core impact point is computed.. *Credit: MAGIC software school*.

The shower axis and the telescope axis is called **impact parameter** (p), and the **maximum height** ($h_{\max}$) is the reconstructed altitude at which the air shower reaches its maximum number of particles. It is determined from the intersection of the shower axis and the line between the telescope position and the direction in the sky given by the ellipse CoG. $h_{\max}$ is energy dependent and its value is between 7 and 9 km. The **Cherenkov light pool radius** (r_{Cher}) represents the radius of the Cherenkov light pool at the ground level computed by assuming the Cherenkov light produced by a single electron with critical energy of 86 MeV at the shower maximum height

(corresponding to the maximum growth of the shower). The light pool radius depends on the local atmospheric density. With the same approach is estimated the **Cherenkov photon density** (ρ_{Cher}).

At this stage the 3D shower development is reconstructed, and the angular distance between the reconstructed shower direction and the expected position of the source is called **θ parameter**. For reconstructing the **direction** of the shower is used the crossing point of the major axis of the ellipses in both telescopes, but if the angle between the ellipses is small then a small error in one of the reconstructed major axes leads to a large misreconstruction of the direction. The **DISP** method is then used to avoid this error, and DISP represents the distance between the ellipse CoG and the nominal source position on the ellipse major axis, and it is reconstructed through the Random Forest algorith (see below). The training is based on MC-simulated γ rays where the DISP is known, and the decision trees grow in a similar approach as for the γ/hadron separation (section 4.3.1.1), with $N = 100$ trained trees. The tree stops growing when there are less than 5 events in the final branch. At this stage, there are two pair of parameters – one for each telescope – because the DISP only gives the source distance from the CoG on the main axis, hence two source positions on either side of the ellipse are possible. The reconstructed source position is obtained from the mean value of the closest position pair. For stereoscopic observations the DISP parameter is useful to improve the performace of both telescopes (Aleksić, J. et al., 2010; Aleksić, J. et al., 2012).

Gamma/hadron Separation and Energy Estimation

Within the camera the γ-ray events, associated with air showers, represent at most 0.05% (~ 1 out of 10^3 events), in contrast the vast majority are of hadronic origin (*background* events). For discriminating between the two, a multi-variate classification algorithm, called Random Forest (RF) is used by the MAGIC collaboration in the analysis chain (Albert et al., 2008). Since RF is a machine learning algorithm, the first step of the process is represented by the *training* performed with event samples of known nature. In particular, the γ rays are produced with MC simulation, while the hadrons come from real off-events[22], hence at each stage of the method the nature of the events is known. In order to avoid artefacts, the distribution in size and in zenith angle of both MC and off-data has to be the same or at least compatible with those of on(source)-data.

During the training are built a large number ($N = 100$) of *decision tree* applying sets of consecutive cuts[23] on the Hillas parameters listed above. Two branches are generated at each cut (node), and the loop ends when the number of events

---

[22]The off-events are associated with the events coming from the observation of undetected or faint sources, in which there are no γ-ray events, hence all off-events are supposed to be hadronic in origin.

[23]The first parameter is chosen randomly, and the cut value is obtained from the minimisation of the Gini index $4G = 4N_\gamma N_{\mathrm{hadron}}/(N_\gamma + N_{\mathrm{hadron}})^2$, where N_γ and N_{hadron} are the number of γ rays and hadrons after applying the cut. $G = 0$ corresponds to a perfect separation, while $G = 1$ indicates an equal distribution of events for both classes (Gini, 1921).

in the left and right branch splitting is small (usually $= 3$) or one of the two branches (left and right) contains only events of one nature. As a consequence, to each ending branch, called *leaf*, is assigned the **hadroness** h parameter, that is defined as the portion of hadrons in the leaf, $h = N_{\text{hadrons}}/(N_{\text{hadrons}} + N_\gamma)$. The trained decision tree is then applied to on-events, performing the **γ/hadron** separation. At each event is assigned a value of h_i, corresponding to the hadronness of the leaf it reaches in the tree i. The final hadroness is $H = \frac{1}{100}\Sigma h_i$ and lies between 0 and 1, provides informations on the probability for an event to be a gamma or an hadron, since γ-ray-like events are identified with H close to 0. Even electrons have H close to 0 and it is difficult to discriminate them and γ rays.

On the other hand, the **energy estimation** is performed using the look-up table (LUT), one for each telescope. The LUTs are binned in size and in p/r_{Cher}, the ratio between impact parameter and the Cherenkov radius. The values of the table are the average and RMS of the true energy distribution (E_{true}) of MC-simulated γ-ray events inside each bin. The estimated energy E_{est} of each event is the RMS value over the average E_{true} value of the LUT bin at which the event corresponds. An empirical correction factor is then applied to the events, and it is proportional to the cosine of the zenith angle, in order to take into account the absorption effect of the atmosphere. The resolution of the energy reconstruction ($\frac{E_{\text{est}}-E_{\text{true}}}{E_{\text{true}}}$ for stereo analysis is as good as 15% in the range 200 GeV $\div 1$ TeV. Finally, the energy threshold (E_{th}) of the analysis – higher than the energy threshold of the trigger – is defined as the peak of the E_{true} distribution of γ-ray MC-simulated events after applying all the cuts. As said earlier, the energy of the primary γ-ray is proportional to the number of Cherenkov photons in the shower, hence the energy is proportional to the size parameter. Other Hillas parameters affecting the number of Cherenkov photons are the impact parameter, the maximum height[24], and the already mentioned, zenith angle.

Significance of the Signal

For stereoscopic observations the square of θ parameter (θ^2)[25] is used to validate the detection of the source under investigation, since its distribution is peaked toward small values in the case of γ-ray, while for hadronic events is flat. The signal region is then determined by an upper cut on θ^2. All those events pass the previous cut and the hadroness one, belong to N_{ON} counts. Whilst the corresponding background events N_{OFF} is estimated on the basis of analogous θ^2 cuts calculated through the positions of one or more *false-sources*, in the case of *wooble* data, or those of *off-sources*, in the case of *on-source* data. In

---

[24]Even in this case, the energy is proportional to h_{max} because it is obtained by the ratio of the two parameters size and ρ_{Cher}.

[25]θ^2 is the angular size of the ON and OFF regions.

Li and Ma, 1983, is defined the **significance σ** as

$$\sigma = \sqrt{2\left\{N_{\text{ON}} \ln\left[\frac{1+\alpha}{\alpha}\left(\frac{N_{\text{ON}}}{N_{\text{ON}} + N_{\text{OFF}}}\right)\right] + N_{\text{OFF}} \ln\left[\alpha\left(\frac{N_{\text{OFF}}}{N_{\text{ON}} + N_{\text{OFF}}}\right)\right]\right\}}$$

(4.7)

where α is the ON/OFF normalization parameter. The choice of hadroness and θ^2 cuts to use in the analysis of the *on-source* is based on the same optimized parameters used to analyze the Crab nebula. Indeed, the Crab nebula represents the reference source – even the flux of a γ-ray source is expressed in terms of Crab units (CU) – and whenever a source is analyzed, a set of Crab nebula data, obtained more or less in the same period and under the same weather, zenith and dark/moon time conditions is analyzed, as reference. This process is repeated for different energy thresholds, namely *Low Energy* (LE), *High Energy* (HE) and *Full Range* (FR).

The θ^2 plot represents the visualization of the significance of the signal and it is computed with the ODIE toll in MARS. ODIE computes Theta-Square Plots for any sky coordinate in the FoV and It can be used also to study source extension.

Flux reconstruction and differential energy Spectrum

The flux reconstruction happens once the hadroness, energy and direction are estimated for each event. It is defined as the excess of gamma rays in an energy range per unit time and area expressed in unit of $[\text{cm}^{-2}\,\text{s}^{-1}]$ as

$$F(E_1 < E < E_2) = \frac{N(E_1 < E < E_2)}{A_{\text{eff}}(E_1 < E < E_2, Zd, Az)T_{\text{eff}}}$$

(4.8)

where A_{eff} is the effective area, T_{eff} is the effective time, and $N(E_1 < E < E_2)$ is the number of excess events.

The effective area is calculated using a MC sample (test sample) that is totally independent from the sample used to build the RF and the LUTs, and the RF and LUTs are then applied to the test sample. It is defined as

$$A_{\text{eff}} = A_{\text{sim}}\epsilon_\gamma = A_{\text{sim}}\frac{N_{\gamma,\text{sel}}}{N_{\gamma,\text{tot}}}$$

(4.9)

where A_{sim} is a disk of radius 450 m representing the area above the telescope in which the γ rays are uniformly produced, and ϵ_γ is the γ-ray efficiency, defined as the ratio between the number of simulated γ-ray events after cuts ($N_{\gamma,\text{sel}}$) and the total number of simulated events ($N_{\gamma,\text{tot}}$). A_{eff} depends on the energy, zenith and azimuth of the observation. The dependence to the zenith angle is related to the fact that at higher zenith the light pool of higher energetic γ rays at ground is larger leading to an increment of the effective area. On the other hand, the A_{eff} decreases for the less energetic γ rays which are instead absorbed due to the long distance travelled in the atmosphere and do not pass

the trigger level. Whilst the effect related to the azimuth is due to the geomagnetic field that modifies the trajectories of the charged particles in the shower, which thus distorts the shape of the light pool on the ground (Commichau, 2007).

T_{eff}, instead, is the effective time of the observation defined as the time difference (dT) among successive events. Under the assumption that the events are Poisson-distributed, dT has distributed as an exponential function

$$dT \sim A \exp^{-\frac{dT}{\tau}} \qquad (4.10)$$

where τ is the mean arrival time difference, resulting by the fit, and t_{eff} is calculated multiplying τ by the total number of triggers N_{all}.

The **differential energy spectrum** represent an important information about the source together with the θ^2 distribution and its significance. The energy spectrum is defined in unit of $[\text{TeV}^{-1}\,\text{cm}^{-2}\,\text{s}^{-1}]$ as

$$\frac{dF(E)}{dE} = \frac{dN_\gamma(E)}{dE\, dA_{\text{eff}}(E)\, dT_{\text{eff}}} \qquad (4.11)$$

It is estimated in energy bins, and for each bin is computed the number of the excess events dn_γ and A_{eff}. All these quantities and the cuts are expressed in terms of the *true* energy of the simulated γ-ray event. Hence the effective area depends on energy increasing rapidly at low energies until reaches a plateau corresponding to the value at which the telescopes are triggered.

In order to obtain physical informations by the spectrum is computed the **unfolded spectrum** converting binned energy into true energy (for major details see Albert et al., 2007e).

The **systematic uncertainties** on the measured spectrum affecting the energy scale are $< 15\%$, the flux normalization (F_{N}) are $11 - 18\%$, and ± 0.15 for the energy spectrum power-law slope (Aleksić et al., 2016b).

For obtaining the energy spectrum and the light curve of a gamma-ray source by the MAGIC collaboration FLUTE is used (FLUx vs. Time and Energy) is a MARS program. Moreover, the FOLD program is used to obtain spectra via forward-folding Poissonian Likelihood maximization.

Skymap and Light Curves

Additional physical informations about the source under investigation are obtained with the skymap, that reproduce the source position in the sky (R.A., Dec), and eventually its extension if larger than the instrumental PSF. The light curves also represent the temporal evolution of the source flux, and they are

fundamental tool to study the flaring pattern of a source, especially in a multi-wavelength context, to achieve details on the size of the emitting zone, for example (see section 3.2.1.1).

Skymaps are 2D histograms of event arrival directions in sky coordinates. The arrival direction is usually reconstructed by means of the *disp* parameter. It is also required the background event distribution in order to estimate the number of excess (N_{excess}). The background is obtained through the camera exposure models that are the distribution of the camera efficiency to Cherenkov light in the camera plane, builded starting from the exposure map with only background events. As a result, *on-map* and *off-map* are achieved and then smeared with a Gaussian kernel with σ equal to the MAGIC PSF. The skymap significance is estimated by the eq. (4.7) as well.

CASPAR represents the tool to build skymaps.

Light curves (LCs), instead, show integral γ-ray fluxes above a certain energy as a function of time. For obtaining LCs, the differential spectrum (eq. (4.11)) is calculated for each bin in time, and then integrated above $E_{\text{min}} \rightarrow F(E > E_{\text{min}})$. E_{min} is chosen to lay at the beginning of the A_{eff} in order to reduce the errors.

Moon data analysis

As said earlier, the presence of the moon increases the photon flux of the NSB leading to adapt the cuts in order to obtain an acceptable image cleaning (Ahnen et al., 2017c).In this case the accidental events are higher and to remove them at TL0 the DTs are increased leading to a higher energy threshold of the analysis. Moreover the higher NSB increases the random fluctuation leading to an higher *number of islands* (fake islands) surviving the cleaning procedure. An efficient tool to evaluate the NSB level is the mean direct current (DC) absorbed by the PMTs in the camera, since the mean DC grows proportionally with the NSB level (table 4.1). It is also applied an higher cut in size parameter (> 60), since this size cut is essential to ensure a good data-MC matching.

TABLE 4.1: Mean DC level in presence of the Moon.

NSB level	$\langle \text{DC} \rangle$
Dark Time	$\sim 1 \, \mu\text{A}$
Weak Moon	$< 2 \, \mu\text{A}$
Moderate Moon	$2 \div 4 \, \mu\text{A}$
Bright Moon	$4 \div 8 \, \mu\text{A}$

The MC simulations are essential for the event reconstruction, hence additional noise from the increased NSB flux needs to be add to the MC events, especially under moderate moon and bright moon levels observations. The NSB noise is artificially injected at level of calibrated raw data in order to reproduce the observed charge in each pixel. The MC events are then processed similarly to the real (on) data with the same cleaning levels. A similar approach is further applied to off-data in order to perform the γ/hadron separation. Even the energy threshold of the observations increseases because of the increase of DTs, DC, image cleaning levels and size cuts. As already mentioned, it also dependent to the zenith angle, and increases with high zenith angle[26].

4.3.2 Cherenkov Telescope Array (CTA)

The future of the VHE γ-ray astronomy falls in the next generation IACT, the Cherenkov Telescope Array (CTA) which is expected to provide improvements in accuracy and sensitivity with respect to existing instruments thanks to a increase in the number of telescopes and their innovative design[27]. Detailed MC simulation are used to compute the instrumental performance, in which are considered the optimised number of telescopes for the final layout, and the impact of different atmospheric conditions that could decrease the telescope sensitivity leading to misreconstructed energies and spectra (Pecimotika et al., 2022).

The array will be composed of more than 50 IACTs, and will be built at two sites located on the island of La Palma (Spain), at an altitude of 2200 m close to the MAGIC telescopes, and near Paranal (Chile), even in this case at an altitude of 2200 m above the sea level. The innovative design of CTA is based on the use of 3 types of telescopes of varying sizes – namely Large Sized Telescopes (LSTs), Medium Sized Telescopes (MSTs) and Small Sized Telescopes (SSTs) – which provide achieving a sensitivity in the γ-ray range $20\,\text{GeV} < \text{E} < 300\,\text{TeV}$ (fig. 4.11).

The increment in sensitivity is expected to be about a factor of five to ten better than current instruments – such as MAGIC and VERITAS in the northern emisphere – in the entire energy range, allowing, for instance, deep surveys of various sky regions. Moreover the short-term sensitivity of CTA (fig. 4.12 *left*) is expected to be a few orders of magnitude better than that of *Fermi*-LAT giving the opportunity to detect and study short-timescale transient phenomena, as GRBs or BH merging, or very fast AGN variability, like in blazars (section 3.2.1.1 and chapter 5). On short time scales ($< 1\,\text{h}$) is expected that CTA will be 10^3 times (at 25 GeV) to 10^6 times (at 250 GeV) more sensitive than *Fermi*-LAT.

The angular resolution (fig. 4.12 *right*) is then expected to be of about one arcminute at high energies for the southern site enabling detailed imaging of extend

---

[26]For dark conditions, $E_{\text{th}} \sim 70$ GeV with low zenith, and $E_{\text{th}} > 400$ GeV with high zenith.
[27]CTA observatory webpage..

- **2-mirror Schwarzschild-Couder optical design**
- **4.3 m ⌀ primary reflective surface**
- **SiPM camera: 2048 pixels (0.16°)**
- **8.8° FoV**
- **17.5 tonne**

- **Davies-Cotton optical design**
- **12 m ⌀ reflective surface**
- **PMT camera – 2 designs:**
  - **NectarCam: 1855 pixels**
  - **FlashCam: 1764 pixels**
- **~7° FoV**
- **82 tonne**

- **Parabolic optical design**
- **23 m ⌀ reflective surface**
- **PMT camera: 1855 pixels (0.1°)**
- **4.3° FoV**
- **100 tonne**

Small-Sized Telescope
SST

Medium-Sized Telescope
MST

Large-Sized Telescope
LST

300 TeV   5 TeV   200 GeV   20 GeV
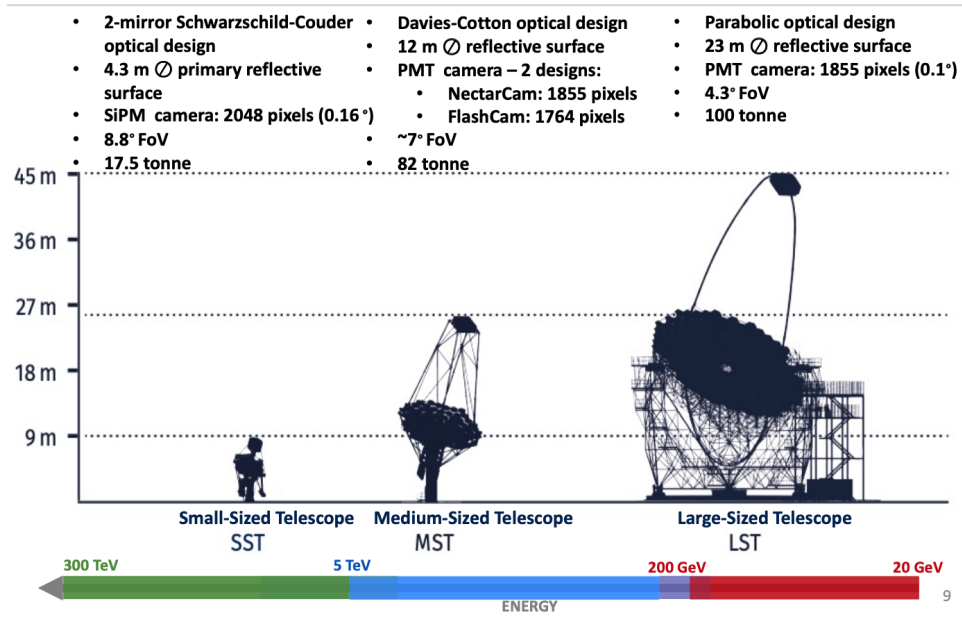
ENERGY

FIGURE 4.11: CTA telescopes design. *Credit: Roberta Zanin - CTAO Project Scientist*
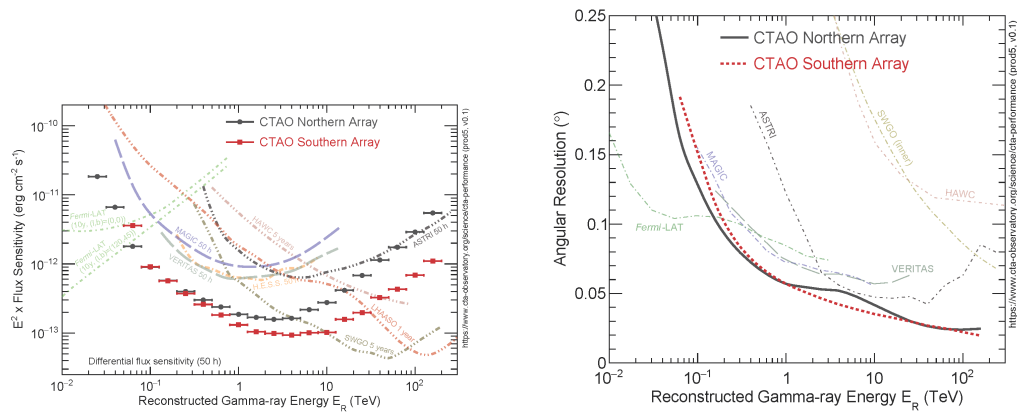

FIGURE 4.12:
Alpha configuration sensitivity compared with other instruments (*left*), and angular resolution (*right*). The performance are considered for `Prod5 v.01` IRFs. *Credit: CTA performance webpage* .

sources, also thanks to the large FoV ($4.5° \div 8.5°$), with respect to the present day H.E.S.S. telescopes. Together with the improvement in angular resolution, the energy resolution is also expected to reach 5% at 1 TeV, making possible to measure spectral cutoffs, *i.e* in the search of *PeVatrons* (section 3.1.3 and chapter 6), and detect spectral features, such as those associated with DM annihilation.

As said earlier, the MC simulation models reproducing the optimised telescope layout are used to estimate the performance of CTA (Maier, 2019). The process starts with CORSIKA (Heck et al., 1998) simulations of EAS and Cherenkov photons, which are then propagated through the telescopes using SIM_TELARRAY simulation

package (Bernlöhr, 2008). In order to obtain realistic simulations of the photons observed by the telescopes, within SIM_TELARRAY are included detailed models of

- updated atmospheric templates for La Palma and geomagnetic field values for both sites

- detailed ray-tracing simulations of optical elements to model the shadowing on the camera as a function of *off-axis angle* due to various telescope components

- collecting lab and on-site prototype measurements of various telescope simulated components

- appropriate trigger threshold levels

- the expected night-sky background light level in each pixel.

Currently, the simulations are performed for 3 zenith angle ($20°$, $40°$, $60°$) and both northern and southern sites, considering the telescopes pointing parallel to each other. A previous optimised layout configurations provided more telescopes (Acharyya et al., 2019) than the current version, called *Alpha configuration*[28]. In this configuration, the northern array is provided of 4 LSTs and 9 MSTs, covering a total area of $\sim 0.25 \text{ km}^2$. On the other hemisphere, the southern array is composed by 14 MSTs, and 37 SSTs, for a total area of $\sim 3 \text{ km}^2$.
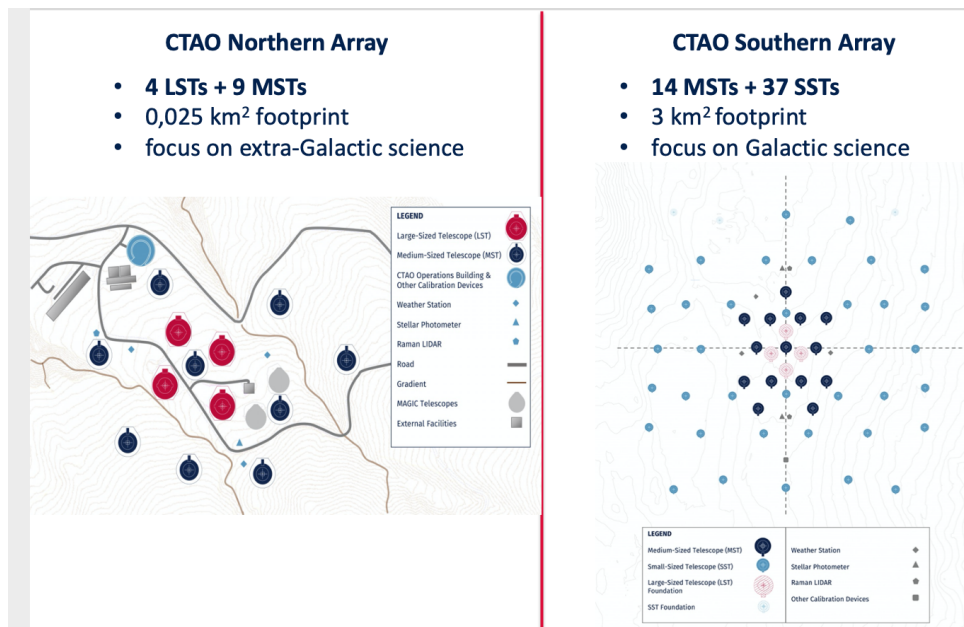

FIGURE 4.13: Alpha configuration for the two initial CTA arrays.
Credit: Roberta Zanin - CTAO Project Scientist.

---

[28]In the *Alpha configuration* are not included the 4 LSTs of the northern site shown in fig. 4.13, but in the future they are included.

The reconstruction and analysis of the simulation output is performed with the EVENTDISPLAY analysis software (Maier and Holder, 2017), which computes waveform integration, image cleaning, stereoscopic reconstruction and cut optimisation (for major details see Bernlöhr et al., 2013).

The **performance** of an IACT, in this case of CTA[29], are based on the evaluation of few criteria, and the main are the effective collection area, angular resolution, energy resolution, residual background rate and differential sensitivity. The optimization of these criteria, especially the differential sensitivity[30], is used to discriminate among telescope layouts. For calculating the sensitivity at least 10 detected γ rays and a minimal signal to background ratio of $1/20$ in each energy bin are required, and the analysis cuts – dependent on the observation time – in each energy bin are optimised for best flux sensitivity.
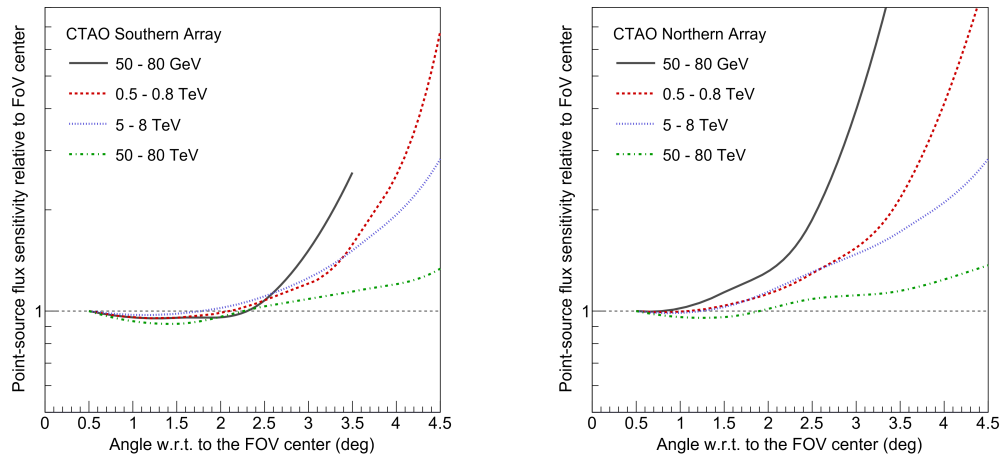

FIGURE 4.14: The differential sensitivity curves for a point-like source at increasing angular distances from the centre of the CTA FoV. *Credit: CTA performance webpage.*

In the *on-axis* observations the source is pointed in the center of the camera, while in the *off-axis* it is at $3° \div 4°$ from the camera center, and this type of observations are possible thanks to the large FoV of CTA camera (fig. 4.14). Moreover *off*-axis observations causing angular and energy resolution also degrade approaching the edge of the CTA camera.

The effective collection area[31] is calculated assuming 30 minutes observation time and optimising the cuts for best sensitivity (Gueta, 2022).

The current IACTs performances are expected to be outperformed of a factor of 5 by the CTA performance, expanding the energy coverage at VHE above 100 TeV, in

---

[29]CTA performance webpage.

[30]The differential sensitivity is the minimal flux required to detect a point-like source ($\sigma > 5$)

[31]The effective collection area is the ratio of the differential γ-ray detection rate over the differential flux of incident γ rays.

contrast with the current sensitivity around 10 TeV. However, nowadays air shower detectors, as LHAASO, HAWC and SWGO, are more sensitive above $10 \div 20$ TeV with respect to CTA, but their angular resolution is worse[32] (Abeysekara et al., 2017; Aharonian et al., 2021; Barres de Almeida, 2022). The angular resolution[33] of the southern site is expected to be less than $0.01°$, providing a significant improvement compared to current instruments, ranging between $0.02°$ to $0.2°$. A better angular resolution could be further obtained, in future, with appropriately optimised cuts in case of morphology studies of bright sources, such as the reference source Crab nebula.

The outputs of current simulations show that the northern site is a few orders of magnitude more sensitive than *Fermi*-LAT for short-time observations, promoting CTA to be the best instrument to potentially discover short-transient phenomena that could reach its FoV. In any case, the discovery potential of satellite instruments is expected to be higher because of the larger FoV, such as that of 2.4 sr of *Fermi*-LAT. The CTA telescopes are however designed with fast repointing capabilities, as in case of the MAGIC telescopes, allowing to catch the signal of short-time events 20 s later the alert, and then incrementing the discovery potential of CTA.

Simulated Data Analysis

The simulation and high level analysis of γ-ray data can be done with two softwares based on different working packages, CTOOLS[34] and GAMMAPY[35] (fig. 4.15). Both softwares are a set of tools for the analysis of data from existing and future IACTs, including H.E.S.S., VERITAS, MAGIC and CTA.

FIGURE 4.15: Logos of the software used by CTA collaboration.

[32]The HAWC and LHAASO angular resolution is $0.1°$ and $0.2°$ respectively.
[33]The angular resolution in each energy bin represents the angle containing 68% of the reconstructed simulated γ-ray events' direction.
[34]CTOOLS webpage.
[35]GAMMAPY webpage.

CTOOLS support also the analysis of data from CGRO/COMPTEL, *Fermi*/LAT and INTEGRAL/SPI, enabling the exploration of the gamma sky from hundreds of keV to hundreds of TeV. The data analysis performed by CTOOLS are observations and event selection, binning, sky map creation, source detection, model fitting, spectra, phase curve and light curve generation, and observation simulations. They can be used as command-line executables, alike FTOOLS and FERMITOOLS, or through PYTHON modules and provided tutorials in JUPYTER NOTEBOOKS. CTOOLS are based on GAMMALIB, a toolbox for the scientific analysis of astronomical γ-ray data.

GAMMAPY is an open-source PYTHON package built on NUMPY, SCIPY and ASTROPY. It is used as core library for the science analysis tools of the CTA, recommended by the H.E.S.S. collaboration to be used for science publications, and is also used in the analysis of existing air shower detectors, such as MAGIC, VERITAS and HAWC.

Part II

IACTs as Pillars for the Understanding of the TeV Sky

5 MAGIC Observations
of TeV Blazars

THE chapter is devoted to the description of the analysis of BL Lacearte, the BL Lac objects prototype, which is one of the most observed source across the whole electromagnetic spectrum, and 1RXS J081201.8+023735, which is one of the new cataloged sources in the VHE reference catalog TeVCat (chapter 3 and figs. 3.1 and 5.26). The two sources have been analyzed using both MAGIC and *Fermi*-LAT data, and for both the sources the multi-wavelength coverage has been reported and exploited in the interpretation.

5.1 Context

The gamma-ray astronomy allows us to access to the extreme and catastrophic face of the Universe, in which powerful and violent explosions of stellar and compact objects occur, and ultra-relativistic particles are accelerated by either single sources or nuclei of active galaxies. With gamma-ray detectors the highest component of the energy spectrum is investigable, as well as physical mechanisms occurring at such higher energies, which are still matter of debate.

In this context, blazars represent ideal laboratories to study the powerful phenomena associated with their jets arising from the vicinity of the black hole in the center of active galaxies. Blazars are a subclass of active galactic nuclei (AGNs) featured by persistent and extremely variable emission associated with still unclear processes happening in ultra-relativistic jets pointing toward our line-of-sight (section 3.2.1.1). Their spectral energy distribution (SED) is characterized by two emission components, associated with synchrotron emission, the first, and with IC-scattering, the second (sections 2.2.1 and 3.2.1.1). The low-energy component peaks in optical to X-ray energies and the high-energy hump peaks in the γ-ray band (fig. 2.5). The physical origin of the synchrotron component is widely embraced to be associated with leptons relativistically moving in the jet. On the other hand, the nature of the IC component is still unclear, and it could be of both leptonic and hadronic in origin, or a mixing of the two (*hybrid*; see Böttcher, 2007, and discussion in section 2.2.1).

The broadband SED of blazars is commonly reproduced by *leptonic* models, even for the high energy component that is due to processes occurring in the same place of those responsible for the synchrotron emission, or in a different location within the jet, or externally. Recently, *hadronic* scenarios are becoming increasingly important in the astroparticle community mainly thanks to the detection of high energy neutrinos in coincidence with γ-ray emission from blazars (Ansoldi et al., 2018), even if several criticisms are associated with this kind of modelling (Neronov, Semikoz, and Ptitsyna, 2017).

Furthermore, the mechanisms producing fast variability (down to the scale of minutes) of the γ-ray emission in AGNs are not clear and under debate. The attempts to model the rapid enhancement of the source flux (*flare*) are still not able to properly reproduce the observations. *Hadronic* models, for instance, where protons in the jet are responsible for the observed emission, cannot be ruled out at the present state of measurements (Mannheim, 1993; Mücke et al., 2003). On the other hand, many *leptonic* models have been suggested, in which VHE γ rays could to be originated close to the central black hole magnetosphere (Aleksić et al., 2014; Hirotani and Pu, 2016) , or due to magnetic reconnection promoting emission in mini-jets (Giannios, Uzdensky, and Begelman, 2009; Morris, Potter, and Cotter, 2019) , or even caused by star/cloud-jet interactions (Barkov, Aharonian, and Bosch-Ramon, 2010) or originating by small blobs traveling with large Doppler factor in the jet and possibly interacting with larger emission regions (Tavecchio et al., 2011; Begelman, Fabian, and Rees, 2008, and see discussion in section 5.2.1).

Another critical point associated with blazar studies at VHE γ rays, is the research of a classification method *free* from observational biases, essentially related with the capabilities of the instruments that observe the gamma-sky at each epoch. Blazars are usually classified following two main criteria: the position of the SED synchrotron peak frequency ($\nu F(\nu)$), and the radio morphology at large scale. The first criterion leads to further classify the blazars in Extreme, High, Intermediate and Low frequency peaked BL Lac objects (EHBLs, HBLs, IBLs, and LBLs), and Flat Spectrum Radio Quasars (FSRQs). With the second criteria, instead, the blazars are subdivided in FR I and FR II (see section 3.2.1 and fig. 3.6). However this classification is not able to characterize the huge diversity of properties observed in blazars. Several other methods are proposed by the community, such as the study of the kinematic features of the radio jets which returns a good overlap with the standard spectral classification (see discussion in section 5.2.1 for major details)

Among the sources observed by the VHE γ rays eyes of IACTs, the Extreme High-frequency-peaked BL Lac objects (EHBLs) are of particular interest because they represent powerful tools to study particle acceleration mechanisms, and can be used as cosmological probe. EHBLs are the most energetic persistent sources in

the γ-sky showing the most extreme properties, challenging current standard models for the emission and the acceleration mechanisms (Biteau et al., 2020; Kaufmann et al., 2011). In the past decades, X-ray observations have revealed the existence of this blazar population (Costamante et al., 2001; Biteau et al., 2020; Costamante, 2017), characterized by the SED synchrotron peak usually located at energy above 1 keV, sometimes associated with hard spectral index ($\Gamma \leq 2$) at very high energies ($E > 100$ GeV) leading to locate the IC-peak above 1 TeV (*hard-TeV blazars*). EHBLs display their behavior persistently, but recent observations unveiled that some sources display only *temporarily* their EHBL behavior, associated with high states (see also section 3.2.1.2, Pian et al., 1998; Giommi, Padovani, and Perlman, 2000 and the discussion in section 5.3).

With the hard-TeV blazars cosmological studies can be carried out, such as setting the limit on the intensity of the intergalactic magnetic field (IGMF) by constraining the production of the electromagnetic cascade triggered by $\sim 1\,\mathrm{TeV}$ photons propagating through the Universe (see sections 3.2.3 and 3.3 and H. E. S. S. Collaboration et al., 2014; Archambault et al., 2017; Silvestri, 2020; Ventura et al., 2022). Other studies carried out with hard-TeV EHBLs aim to constrain the density of the extra galactic background light (EBL; Aharonian et al., 2006a.

In order to perform cosmological and physical studies with EBHLs, the knowledge on their redshift is crucial to quantify the effect on the γ-ray absorption due to EBL photons and intrinsic absorption, and to study γ-ray emission processes (Becerra González et al., 2021). EHBLs have their emission budget dominated by VHE γ rays while the synchrotron component is relatively dim, as a consequence their host galaxies are observable in the optical regime thus allowing to characterize the optical spectrum and to derive many informations including the redshift value and the capability to constrain the emitting region within the relativistic jets (Becerra González et al., 2021).

Moreover the EBHL SED is well fitted by *hadronic* models that are able to reproduce the observed flux and that predict the presence of a third SED peak due to neutrinos together with its location (see section 2.2.1 and fig. 5.20). Hence, these sources represent also exceptional laboratories where studying and testing multi-messenger (MM) phenomena.

5.2 BL Lac flaring activity in 2019/2020

In this context, the study of fast variability of the BL Lac objects prototype (sections 3.2.1.1 and 3.2.1.2), the BL Lacertae (in short BL Lac) is fundamental since the source is one of the most observed object in the entire electromagnetic spectrum,

including optical polarimetry measurements. In this section it is illustrated the analysis of data collected with the MAGIC telescopes during the BL Lac flaring state in May, July, December 2019, and January 2020.

On 2019 May the 3rd the MAGIC telescopes observed an increase in the VHE ($E > 100$ GeV) γ-ray flux from a position compatible with the blazar BL Lacertae (R.A. $22^{\mathrm{h}}2^{\mathrm{m}}43.3^{\mathrm{s}}$, Dec. $42°16'40''$; J2000.0). The flux was larger than 10% of the Crab nebula flux above 200 GeV, and the detection significance over 6 σ in 0.76 h of observation under dark-time condition (Mirzoyan, 2019). The MAGIC observations were triggered by the flaring activity at HE γ rays reported by *Fermi*-LAT (Garrappa and Buson, 2019), and optical observations by the Astronomical Observatory of the University of Siena (Marchini et al., 2019).

BL Lac is extensively observed by several telescopes, even by IACTs, as MAGIC and VERITAS. In the MAGIC observing campaign, the source is included in the Target of Opportunity (ToO) observations. When the source is in quiescent-state, its flux is under the instrumental sensitivity leading to VHE γ-ray observations only during its flaring-state. Long term observation of BL Lac optical polarization are also performed by several telescopes around the world providing valuable information on the physics of the source.

5.2.1   About the source

The redshift of BL Lac is $z = 0.069$ (Miller, French, and Hawley, 1978), and according to its synchrotron peak frequency is classified as a LBL (Nilsson et al., 2018) or IBL (Ackermann et al., 2011b) object (section 3.2.1 and fig. 3.6). Recently, BL Lac has been classified as an intermediate source on the basis of its kinematic features of the radio jets, observed by VLBI (Hervet, Boisson, and Sol, 2016). In this classification, BL Lac shows quasi-stationary knots close to the jet base ($\min(\beta_{\mathrm{app}}) \leq 1c$) and they are in apparent relativistic motion downstream ($\max(\beta_{\mathrm{app}}) \geq 2c$). Moreover it is characterized by *transient knots* that quickly appear and disappear due to a complex jet structure of turbulences and recollimation shocks.

The prominent variability, especially in optical and radio bands, has promoted BL Lac to be a target of many MWL campaigns (Hagen-Thorn et al., 2002; Marscher et al., 2008; Raiteri et al., 2009; Abdo et al., 2011b; Raiteri et al., 2013; Wehrle et al., 2016). The optical and HE γ-ray light curves of BL Lac display a complex long term behavior that some authors interpret as quasi-periodic variability, with a period of ~ 680 days, found in coincidence for both optical and γ-ray bands, supposed to be of a physical relevance but uncertain in origin (Sandrinelli et al., 2017).

The first detection in the VHE γ-ray band was claimed in 1998, when the Crimean Observatory measured its flux above 1 TeV with a significance of 7.2 σ (Neshpor et al., 2001), while, in the same period, the HEGRA experiment obtained only an upper

limit (Kranich, 2003). The next generation instrument of that time, the MAGIC-I, observed the source for 22.2 h in 2005 and 26 h in 2006, finding its integral flux above 200 GeV higher than 3% of that of Crab nebula, in August 2005 during its flaring state (Albert et al., 2007a). On June 2011, the source was detected by VERITAS in an exceptional flaring state reaching above 200 GeV a flux of $F = (3.4\pm0.6)\times10^{-6}$ ph m^{-2} s^{-1}, roughly 125% of the Crab nebula, in 34.6 minute exposure (Arlen et al., 2013). This flare had a rapid exponential decay of $\tau = 13 \pm 4$ min and was associated with the appearance of a superluminal radio knot[1]. Two smaller flares at the level of $\sim 16\%$ Crab and $\sim 9\%$ Crab were recorded on June and on November 2015, respectively, by VERITAS (Abeysekara and VERITAS Collaboration, 2017). On October 2016, the source was detected again by VERITAS during an exceptional flaring-state which led to a strong detection of $\sim 71\,\sigma$ in 2.6 h of good-quality data. The light curve was characterized by a slow rise of $\tau \sim 140 \pm 25$ min followed by a more rapid decay of $\tau \sim 36 \pm 8$ min explained, even in this case, with the appearance of a candidate superluminal radio knot (Abeysekara et al., 2018a). In particular, the superluminal knot is associated with a brightening in radio band – that can be observed by radio telescopes, as VLBA – which is supposed to be due to a conical shock, in which turbulent shells of plasma passing through that conical shock accelerating electrons. In this model the size of the shells is small and thus it can explain the fast VHE γ-ray flares (Marscher, 2014).

The MAGIC telescopes observed the source during a fast flare on June 2015, and the observations were triggered by a high state in HE γ-ray ($F(E > 100$ MeV$) > 0.5 \times 10^{-6}$ [ph cm^{-2} s^{-1}]), detected by *Fermi*-LAT, and in the optical R band ($F_R > 20$ mJy), in the framework of the *Tuorla blazar monitoring program*[2] (MAGIC Collaboration et al., 2019). The MAGIC observations were performed in *wobble* mode and in ~ 8.6 h the source reached a significance of $16.4\,\sigma$, an averaged integral flux above 200 GeV of $F_{\mathrm{VHE}} = (1.5 \pm 0.2) \times 10^{-11}$ ph cm^{-2} s^{-1}, and a variability timescale of $\tau = 26 \pm 8$ min. The best fit to the observed spectrum was given by a logparabola (LP) even after the EBL correction (see section 3.2.3 and Domínguez et al., 2011).

$$\frac{dN}{dE} = (3.7 \pm 0.3) \times 10^{-10} \cdot \left(\frac{E}{200 \text{ GeV}}\right)^{-(3.0\pm0.2)-(0.8\pm0.4)\cdot\log\left(\frac{E}{200 \text{ GeV}}\right)} \tag{5.1}$$

In this case the MWL behavior of BL Lac during the flaring-state was compatible to previous similar events, in which the optical and γ-ray emission correlate, while

---

[1] Small morphological structures of blazar jets, including the closest region to the emission site, are investigable through radio observations, which can reach arcsec resolution. In this case, jets present bright knots with origin and properties still poorly understood. Some of these knots are observed to have relativistic motions in the jet, which are identifiable by their superluminal apparent velocities. Moreover knot properties (size, apparent velocity, luminosity) are used to constrain the Doppler factor of the non-thermal emission zone, its Lorentz factor and angle to the line-of-sight (Lähteenmäki and Valtaoja, 1999; Jorstad et al., 2005; Hovatta et al., 2009).

[2] *Tuorla blazar monitoring program* webpage.

X-ray variability is less prominent. The fast VHE flares have been preceded by enhanced flux in optical and HE γ-ray regime, and also by the drop of optical polarization degree, few day before the flare, and the electric vector position angle (EVPA) during the flare. These observable features are still unclear mainly because of poor statistics, nevertheless the model of Marscher, 2014, seems to be the most plausible explanation for the phenomenon. An important aspect to take into account is that the VHE observations, usually, are triggered by high state in HE γ-ray and optical bands leading to a significant observational bias.

The MWL SED was early modeled by *single-zone* SSC (Ghisellini et al., 1998; Ravasio et al., 2002), but since the EGRET era, the need to include external target photons for IC-scattering has been invoked to reproduce the observed spectra (Sambruna et al., 1999; Madejski et al., 1999; Böttcher and Bloom, 2000). More commonly this external photon source is associated with the BLR, in both leptonic and hadronic scenarios[3] (Böttcher et al., 2013). The first attempt to model the MWL SED of BL Lac, including VHE γ rays flares, was suggested by Morris, Potter, and Cotter, 2019, which considers the time evolution of a reconnecting plasmoid whose radius and velocity evolve as it travels through the reconnection layer. The model can produce the profile of the fast flare, but overproduces the optical to X-ray part of the SED.
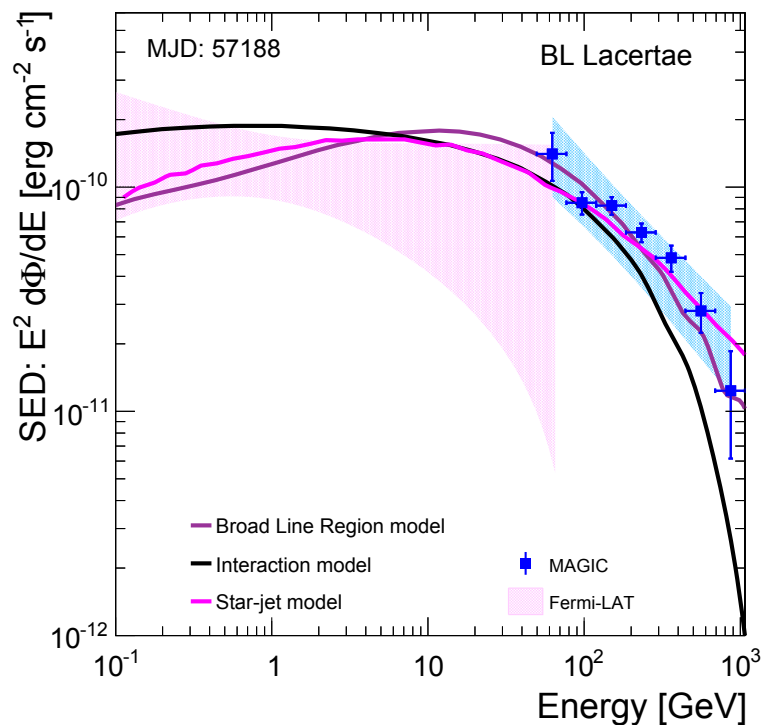
FIGURE 5.1: Gamma-ray SED of MJD 57188 compared to the three models scrutinized in MAGIC Collaboration et al., 2019. The light blue band shows the systematic uncertainty of the MAGIC data. *Credit:* fig.12 in MAGIC Collaboration et al., 2019.

---

[3]However, in this case the required strength of the MF is around 10 G, while the usually observed one by radio measurements is around 0.1 G.

In MAGIC Collaboration et al., 2019, for achieving consistent explanations, three different models were used to reproduce the observed MWL SED (fig. 5.1), namely a fast blob inside the BLR, a fast blob interacting with a larger component and star-jet interaction (Aleksić et al., 2014). The first two are based on a *two-zone* leptonic model similar to that suggested by Tavecchio et al., 2011, which assumes two emission components: a small blob, emitting the rapidly variable VHE emission, and a larger jet responsible for the slower variability in the other bands. The location of both the smaller and the larger emitting regions could be different, or they could be co-spatial. In the first version (*model A* in Tavecchio et al., 2011), the small blob is at the outer edge of the BLR to avoid the $\gamma\gamma$-absorption, even if the observed BLR in BL Lac is faint. On the other hand, in the second version (*model B*), the two emitting zones interact with each other, and an external photon seed is not required since it is provided by the photons emitted by the larger component. The location of the larger blob is not deducible by the MWL light curve, but it is unlikely located beyond the BLR, for instance in the dusty torus like in FSRQs (Sikora, Moderski, and Madejski, 2008), since there is no observational evidence for the existence of such structure in the lower luminosity BL Lacs. The third model tested in the paper is the *star-jet interaction*, which is an alternative explanation of the fast variability. The interactions of ultra-relativistic particles, inside the jet, with compact objects entering the jet, such as stars or clouds could represent a viable explanation, especially in the case of orphan or nearly-orphan flares [4](Bednarek and Protheroe, 1997; Barkov, Aharonian, and Bosch-Ramon, 2010; Bosch-Ramon, Perucho, and Barkov, 2012; Araudo, Bosch-Ramon, and Romero, 2013; Bosch-Ramon, 2015; MAGIC Collaboration et al., 2019; Reimer, Böttcher, and Buson, 2019; Bednarek and Sitarek, 2021; Wang and Xue, 2021). In this scenario, the blob is filled by electrons interacting with the radiation field of a star, and HE and VHE γ rays are produced via IC-scattering on the stellar photons and via pair production – resulting from the interactions of the leptons with the star core – which triggers an electromagnetic cascade (Banasiński, Bednarek, and Sitarek, 2016).

All the proposed models have several drawbacks and are not able to properly reproduce the MWL SED, and then settle on preferred one. In *model A* the estimated position of the smaller blob is outside the BLR, even if the size of the BLR is very uncertain. On the other hand, *model B* overproduces the *Fermi*-LAT observed flux, and to obtain reasonable results the strength of the magnetic field, used as parameter in the model, is set 50% lower than that obtained by VLBA observations. Finally, the last suggested scenario seems unlikely since several fast VHE γ-ray flares have been observed during last decade by different telescopes. Under this complex scenario, MWL observations in coincidence with VHE γ-ray flares are crucial since repeating MWL patterns could play a key role in constraining the location and the physical

---

[4]An orphan flare is defined as an increase of the VHE flux without any associated enhancement of the optical flux; while with a sudden increase of VHE emission during a higher optical state without a simultaneous enhancement of the optical flux is called a nearly-orphan flare.

mechanisms leading to fast γ-ray flares (for major details see MAGIC Collaboration et al., 2019).

The MAGIC telescopes observed other flares, on May-July-December 2019/January 2020 extensively described in section 5.2.2, and in August-September 2020 (Blanch, 2020c; Blanch, 2020a). Broadband studies in optical-UV and X-ray during high state underline the evidence of an observed spectral change leading to shifts in the location of the synchrotron peak towards higher energy, suggesting an emergence of a new HBL component (Prince, 2021). More recently, BL Lac has been detected by the first prototype of CTA Large Sized Telescopes LST-1 during its commissioning phase (in prep. Nozaky et al., ICRC 2023).

Fast flares in very-high energies are usually associated with HBL sources (Aharonian et al., 2007; Albert et al., 2007f), FSRQs (Aleksić et al., 2011a; H. E. S. S. Collaboration et al., 2021), or radio galaxies (Aharonian et al., 2006d; Aleksić et al., 2014). On the other hand, BL Lac is the only observed LBL/IBL object with intraday variability ranging in sub-hours, even minutes scale. This poses a challenge to standard models of blazar variability.

5.2.2   MAGIC analysis of the 2019/2020 observations

Significance of the signals and TS map

The BL Lac was observed in flaring state in May 02, 2019, and the observations performed under ToO request by both MAGIC telescopes, were triggered by the HE γ-ray high state measured by *Fermi*-LAT. The MAGIC observations cover a period of data-taking from May 03 to May 07 when the flux of the source was found to be below the MAGIC sensitivity. The observations have been carried out during *dark-time* under good atmospheric conditions and in *stereoscopic mode*, for an overall observational time of 5.08 h and the zenith angles ranging from $43°$ to $53°$. The analysis has been performed with MARS v2.19.15 starting from *Superstar*[5] data and with standard image cleaning and cut in atmospheric transparency, as measured with LIDAR (when available) was set at $T_{9\ km} = 0.85$. The sample of MC simulated events used for training and testing (see section 4.3.1.1) is the version relative to period ST 03.11 RING-WOBBLE in the zenith angle range $5° \div 62°$. The image cleaning cuts used are the OSA standard cleaning, $\mathrm{Lvl}_1 - \mathrm{Lvl}_2(6.0 - 3.5)$. The BL Lac has been detected to a significance level of $20.61\,\sigma$, with a total of $N_{\mathrm{ON}} = 1741$, $N_{\mathrm{OFF}} = 937.3 \pm 17.7$, and excess $N_{\mathrm{ex}} = 803.7 \pm 49.3$ in LE. In table 5.1 the significance value for each night of observations are displayed[6].

---

[5]*SuperStar* is an executable in MARS that merge two Star files with individual-image parameters, from MAGIC-1 and MAGIC-2, to a Stereo-Parameter file. It performs the stereoscopic reconstruction of the shower parameters (direction, ground impact, altitude, etc) and can also reconstruct the energy from lookup tables (see section 4.3.1.1.

[6]Wiki page link.

TABLE 5.1: BL Lac flare May 2019 - Significance of the signal.

Date	MJD	obs_time (h)	σ LE	σ FR	σ HE
May 03	58606	0.76	6.22	0.84	–
May 04	58607	0.98	13.34	5.06	1.22
May 05	58608	1.21	20.60	11.46	5.22
May 06	58609	0.98	3.21	2.55	0.36
May 07	58610	1.16	3.43	0.82	1.22

In fig. 5.2 the squared angular distance (θ^2) distribution between the reconstructed event direction and the nominal source position in the camera and the normalized off-events θ distribution represented by the gray histogram are displayed. The vertical dashed line defines the signal region below which the detection significance is computed.

On July 2019, BL Lac was found again in flaring state, and ToO observations were collected in the period July 22-27. Since the MC period is the same of May 2019, the overall setup for the analysis is not changed. The total data-taking time was 3.29 h, with a significance level of 3.9 σ, a total of $N_{\text{ON}} = 785$, $N_{\text{OFF}} = 664.0 \pm 14.9$, and excess $N_{\text{ex}} = 121.0 \pm 31.7$ in LE.

On the end of 2019, the source was in high state yet, and ToO observations were collected in the period December 2019, 12-January 2020, 3÷5-17-18. For this part of the analysis have been used the MC period ST03.12 in the zenith angle range $5° \div 62°$, and the same image cleaning cuts for the observations performed during dark-time conditions. The measurements in the nights of January 2020, 03-04-05 were collected under moderate and bright moon (NSB: $3 \div 5$), and in this case the analysis started from *Calibrated* data[7], and the used parameters were Lvl_1-Lvl_2 ($8.0 - 5.0$), noise level added in the MC and off-data (Mean-RMS:$3.5 - 1.4$), and DC level listed in table 4.1. The BL Lac was found to a significance level of 1.9 σ, with a total of $N_{\text{ON}} = 477$, $N_{\text{OFF}} = 431.7 \pm 12.0$, and excess $N_{\text{ex}} = 45.3 \pm 24.9$ in LE.

In table 5.2s the significance values for the observations in the period May, July and December 2019, and January 2020 are tabulated[8].

In fig. 5.3 and fig. 5.4 the squared angular distance (θ^2) distribution between the reconstructed event direction, the source position in the camera and the normalized off-events are displayed.

---

[7]*Calibrated* data are raw data in which the Hillas parametrization have not been still applied.
[8]Wiki page link.
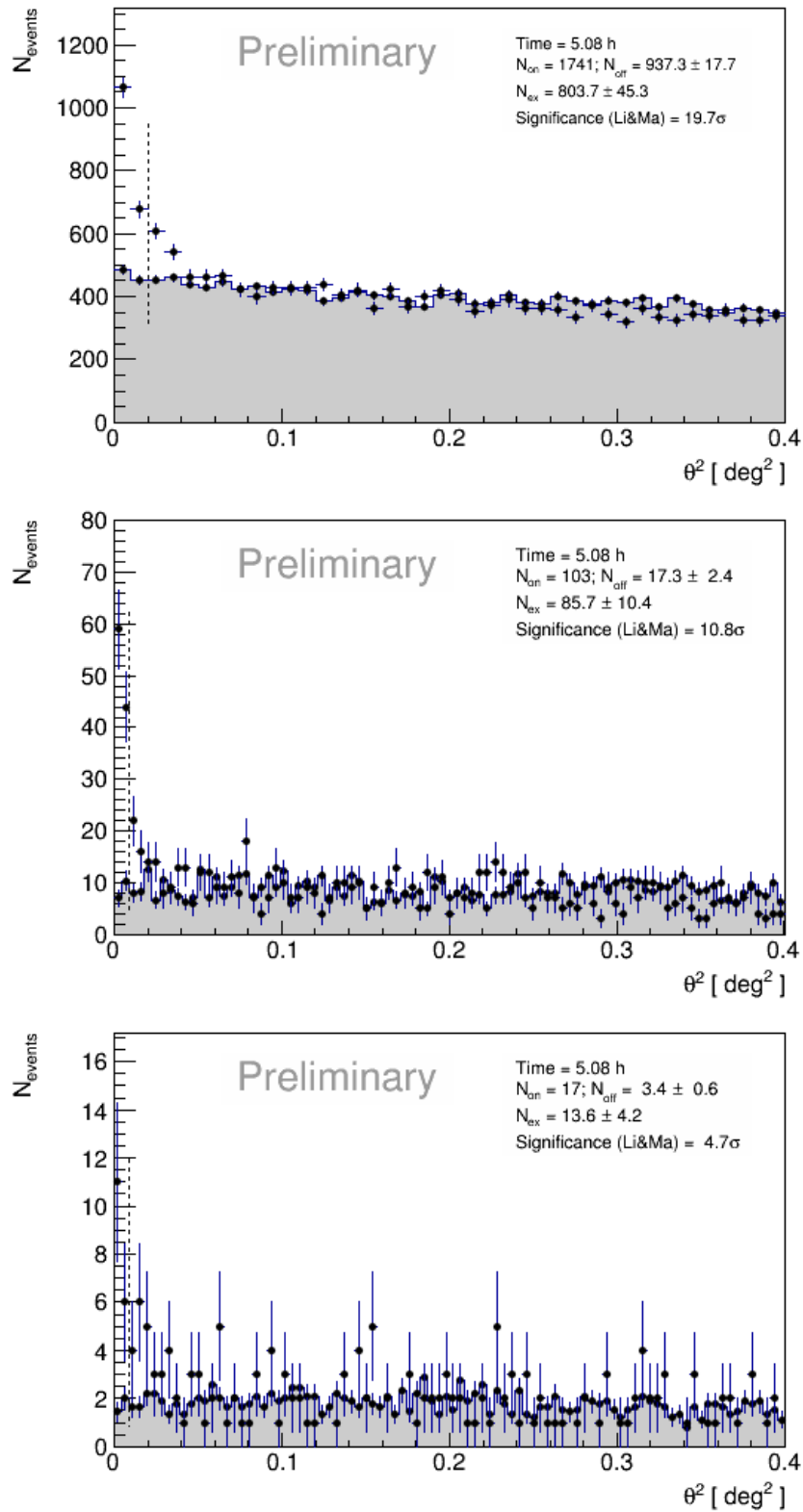
FIGURE 5.2: θ^2 distribution relative to the entire period May 2019, as output of ODIE tool (section 4.3.1.1). *From top to bottom:* LE, FR and HE analysis.
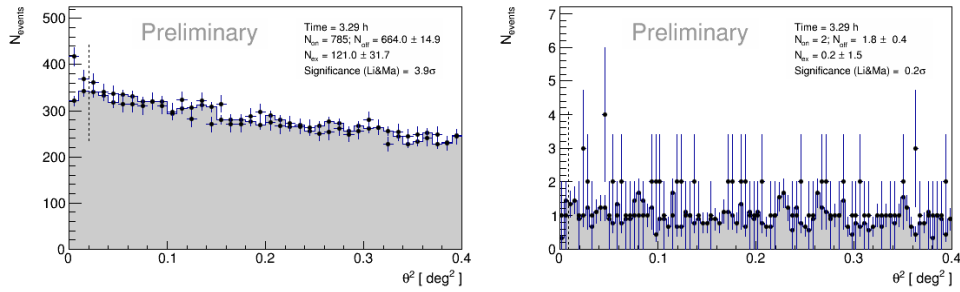
FIGURE 5.3: θ^2 distribution relative to the entire period July 2019, as output of ODIE tool. *On the left*: LE analysis. *On the right*: HE analysis.
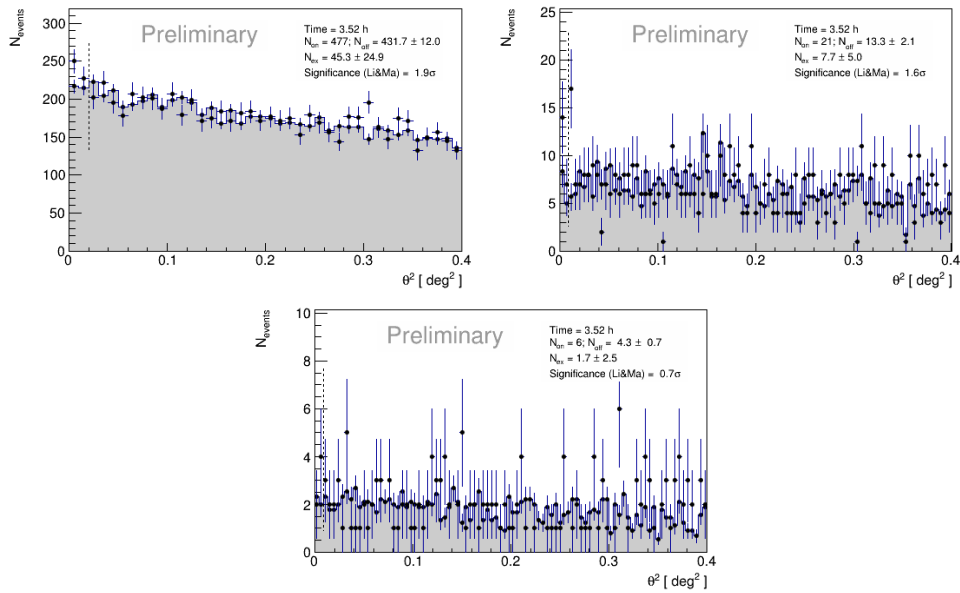
FIGURE 5.4: θ^2 distribution relative to the entire period December 12, 2019, January 03-05 (moon nights) and January 17-18, as output of ODIE tool. *On the top left & right*: LE and FR analysis. *On the bottom*: HE analysis.

TABLE 5.2: BL Lac flare May, July and December 2019, January 2020 -
Significance of the signal.

Date	MJD	obs_time (h)	σ LE	σ FR	σ HE
May 03-07	$58606 - 58610$	5.08	19.7	10.8	4.7
July 22-27	$58685 - 58691$	3.29	3.9	–	0.2
Dec 2019/Jan 2020	$58837/58850 - 58852$ $58864 - 58865$	3.52	1.9	1.6	0.6

LE is the acronym for Low Energy analysis and it consists of $\sim 1.2\%$ sensitivity of Crab nebula. Regarding the Full Range (FR) and High Energy (HE) the values of sensitivity are 0.7% and $\sim 1\%$ of Crab nebula respectively. All the cuts have been optimized on Crab nebula data collected in the same period of BL Lac observations and under same conditions for both MC periods. table 5.3. In fig. 5.5 the Crab sanity check for both MC periods are displayed.

TABLE 5.3: Optimized cuts on Crab nebula. The PSF is characterized by a single parameter *psf40* define as the sigma of the 2D-gaussian ($\sim 40\%$ containment radius).

Cuts	LE	FR	HE
Odie.signalCutPSF40	0.02	0.009	0.0087
Odie.psf40	0.083	0.060	0.049
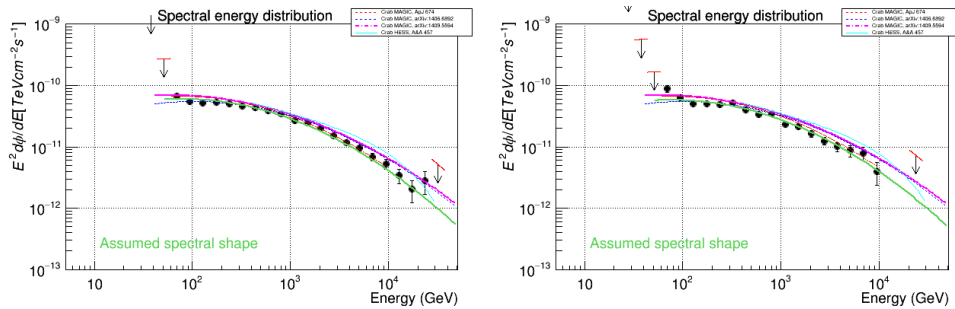
FIGURE 5.5: Crab sanity check performed with cuts listed in table 5.3 relative to MC period ST.0311 (*on the left*) and ST.0312 (*on the right*), as output of FLUTE tool (section 4.3.1.1).

The TS maps – representing the significance of the signals – of BL Lac during its flaring state in May 2019 are displayed in fig. 5.6.
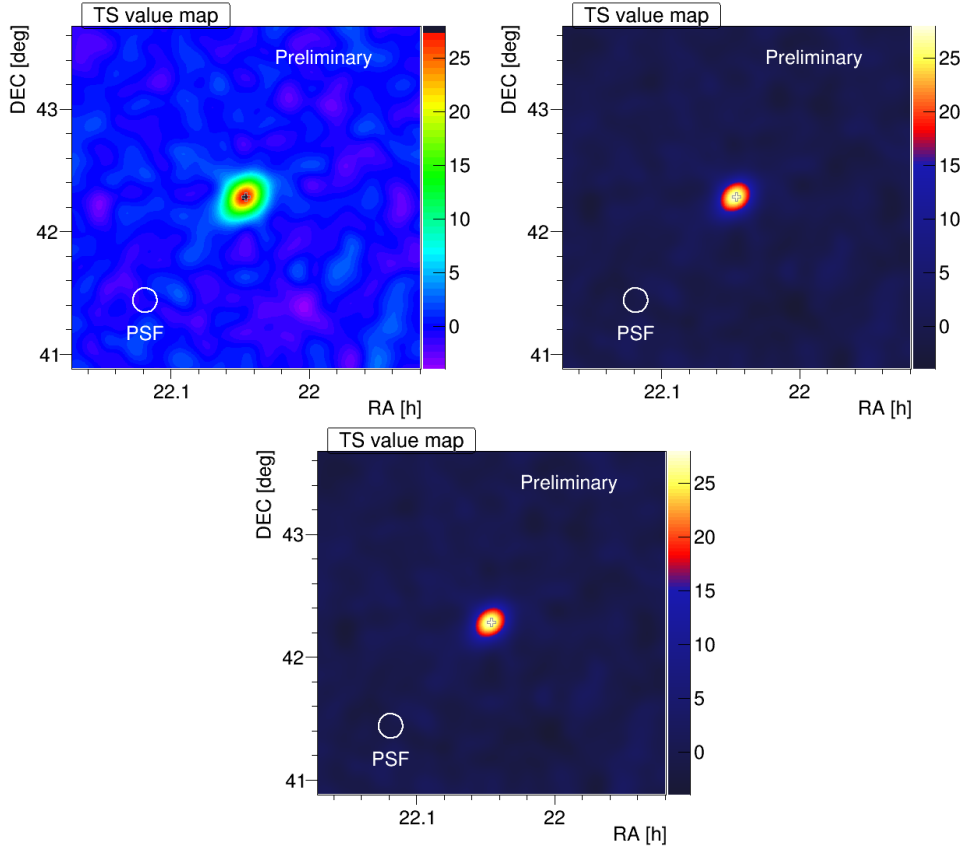
FIGURE 5.6: The TS map of BL Lac flare May 2019, as output of CAS-PAR tool (section 4.3.1.1). *On the top left & right*: LE and FR analysis, *On the bottom*: HE analysis.

SED and Light Curve

The BL Lac SED (fig. 5.7) has been computed, with *FOLD* tool, in 7 energy bins from 79.6 GeV to 50.2 TeV and fitted with a power-law (PL) function $[\text{TeV}^{-1} \text{ cm}^{-2} \text{ s}^{-1}]$

$$\frac{dN}{dE} = 1.43 \times 10^{-10} \pm 8.07 \times 10^{-12} \cdot \left(\frac{E}{300 \text{ GeV}}\right)^{-2.82 \pm 0.09} \tag{5.2}$$

with a $\chi^2/\text{d.o.f.} = 8.42/5$.

The night-wise light curve (LC) above 200 GeV of May 2019 flaring state is displayed in fig. 5.8, and the stacked LC of the three periods considered in this work is shown in fig. 5.9.
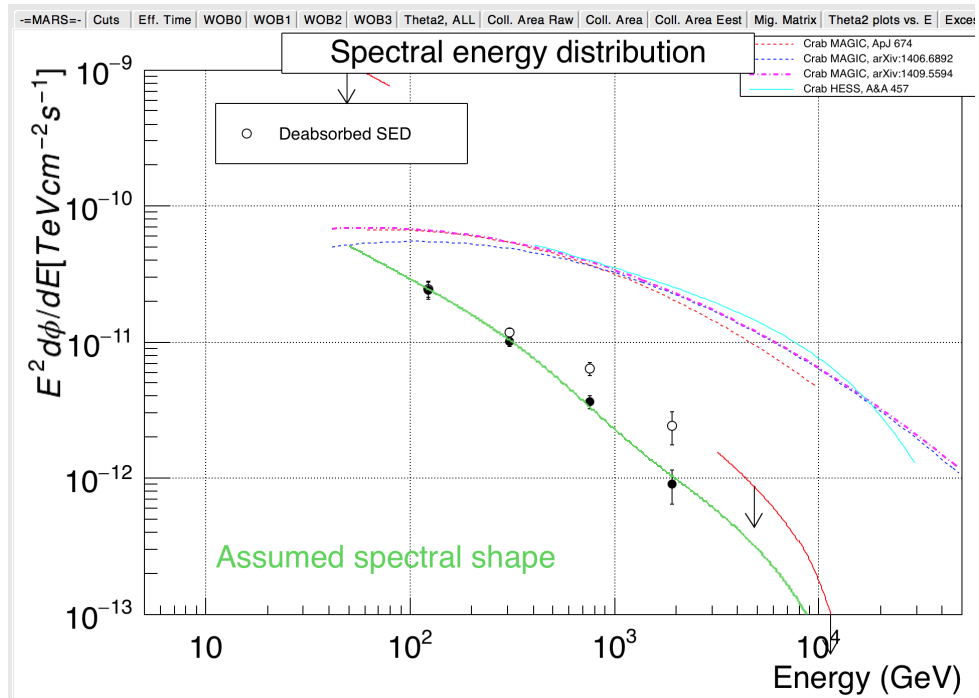
FIGURE 5.7: BL Lac Spectral Energy Distribution relative to the entire period May 2019, fitted with a power-law function. The absorbed spectrum, computed with EBL absorption Domínguez et al., 2011, is also shown.
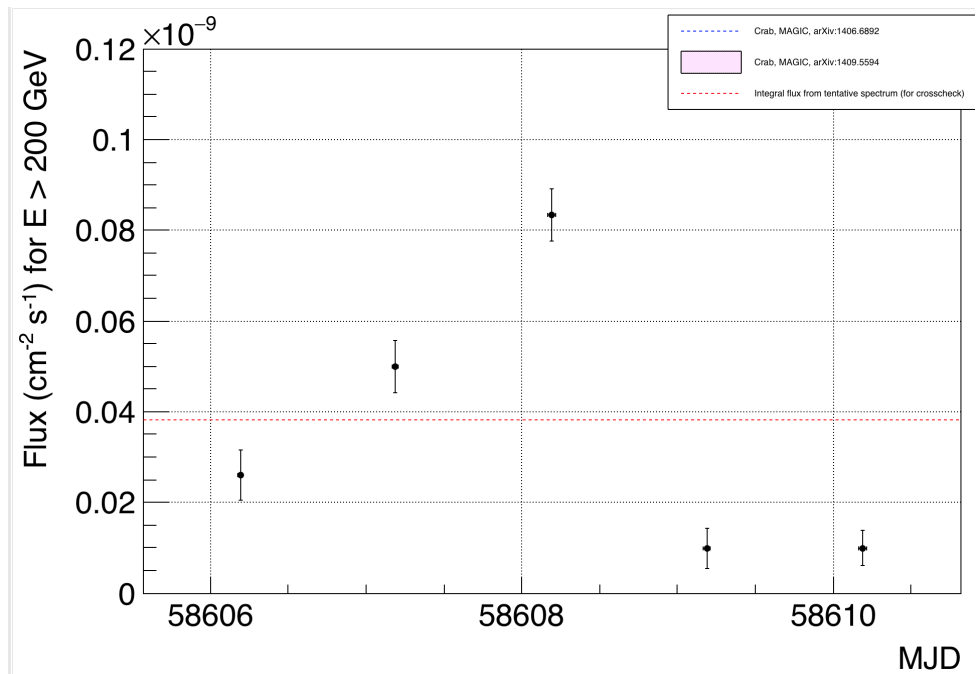
FIGURE 5.8: BL Lac light curve above 200 GeV relative to the entire period May 2019.
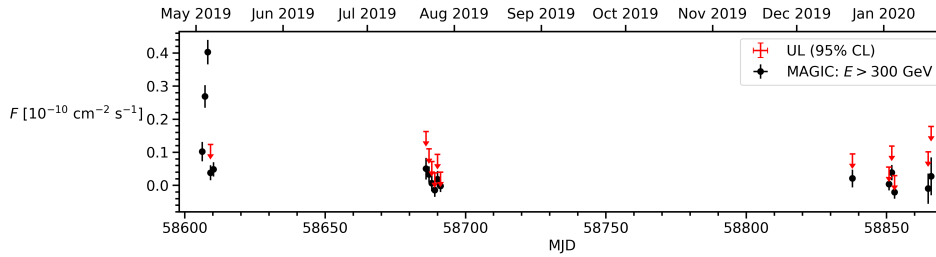
FIGURE 5.9: BL Lac stacked light curve above 300 GeV.

5.2.3 *Fermi*-LAT analysis

In coincidence with MAGIC observations, *Fermi*-LAT analysis with FERMIPY V0.17.3 of BL Lac source listed in the 4FGL catalog (4FGL J2202.7+4216; Abdollahi et al., 2020a) have been performed also. The analysis have been done in a RoI width of $10°$, binsize= $0.1°$, in CEL coordinates, 8 energy bin in range 100 MeV ÷ 500 GeV. The quality cuts in zenith angle has been applied ($z_{max} = 90$, DATA_QUAL>0 && LAT_CONFIG==1 && ABS(ROCK_ANGLE)<5), the used event class is 128 relative to point source analysis, and event type 3 relative to FRONT+BACK (section 1.1) data analyzed with the IRF P8R3_SOURCE_V2[9], and PASS8 data. In the analysis were used the provided by *Fermi* collaboration isotropic (ISO_P8R3_SOURCE_V2_v1) and galactic diffuse (GLL_IEM_V07) models[10].

Regarding the likelihood analysis, a region of $15°$ around the source has been considered, and the prefactor and index parameters of sources within $3°$ from the BL Lac location have been set as free, as well as for those sources with TS > 10, while for those with TS < 5 the parameters have been fixed. For computing the SED a PL models has been assumed in order to overlap the MAGIC observations. In the 4FGL the BL Lac is parameterized with a *lognormal distribution* (LP), but in the periods under investigation the spectrum is equally fitted by a simple PL[11] (see table 5.4), as resulting by the *curvature test*[12].

$$\text{TS}_{\text{curvature}} = -2\ln\frac{L_{\text{LP}}}{L_{\text{PL}}} \tag{5.3}$$

where L_{LP} and L_{PL} represent the likelihood values for both LP and PL fitting models.

The BL Lac SED has been then fitted with a power-law (PL) function $[\text{MeV}^{-1}\,\text{cm}^{-2}\,\text{s}^{-1}]$ as in eq. (5.2)

$$\frac{dN}{dE} = N_0 \cdot \left(\frac{E}{1\,\text{GeV}}\right)^{\gamma} \tag{5.4}$$

In table 5.5 the parameter values as results of the likelihood analysis are tabulated.

---

[9]*Fermi*-LAT performance.
[10]*Fermi*-LAT background model.
[11]The TS$_{\text{curvature}} \sim 9 < 25$, and 25 is the reference level to prefer LP to PL, in this case.
[12]Curvature test webpage.

TABLE 5.4: Curvature Test parameters.

Period	logLikelihood PL	logLikelihood LP	$TS_{curvature}$	TS
May 2019	-5853.122	-5848.537	9.170	890.371
July 2019	-12398.527	-12394.748	7.557	51.580

TABLE 5.5: BL Lac SED parameters. The unit of N_0 is $[\text{MeV}^{-1} \text{ cm}^{-2} \text{ s}^{-1}]$.

Period	N_0	γ
May 2019	$1.39 \times 10^{-13} \pm 9.65 \times 10^{-15}$	$1.82 \pm 4.80 \times 10^{-02}$
July 2019	$2.96 \times 10^{-13} \pm 1.58 \times 10^{-14}$	$1.92 \pm 3.68 \times 10^{-02}$

In fig. 5.10 and fig. 5.11 the counts map, the spectrum and the residual are displayed, relative to the BL Lac analysis of flare May 2019 and July 2019 respectively.
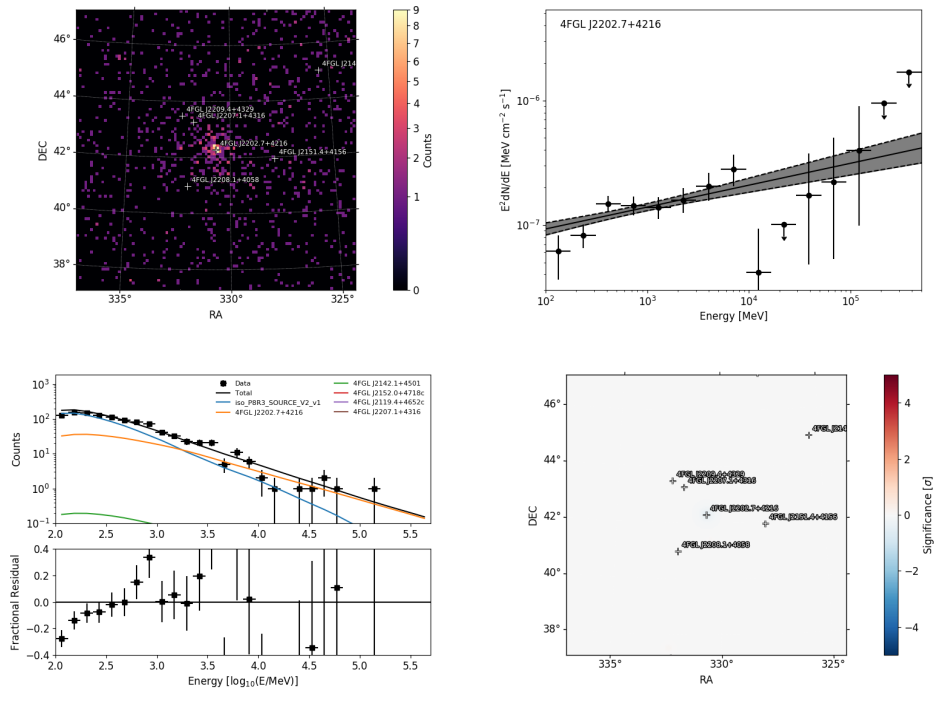
FIGURE 5.10: *Fermi*-LAT analysis of BL Lac during its flaring state in May 2019. *On the top left & right*: counts map and SED fitted with PL parameters listed in table 5.5. *On the bottom left & right*: counts spectrum with residuals and residuals map.
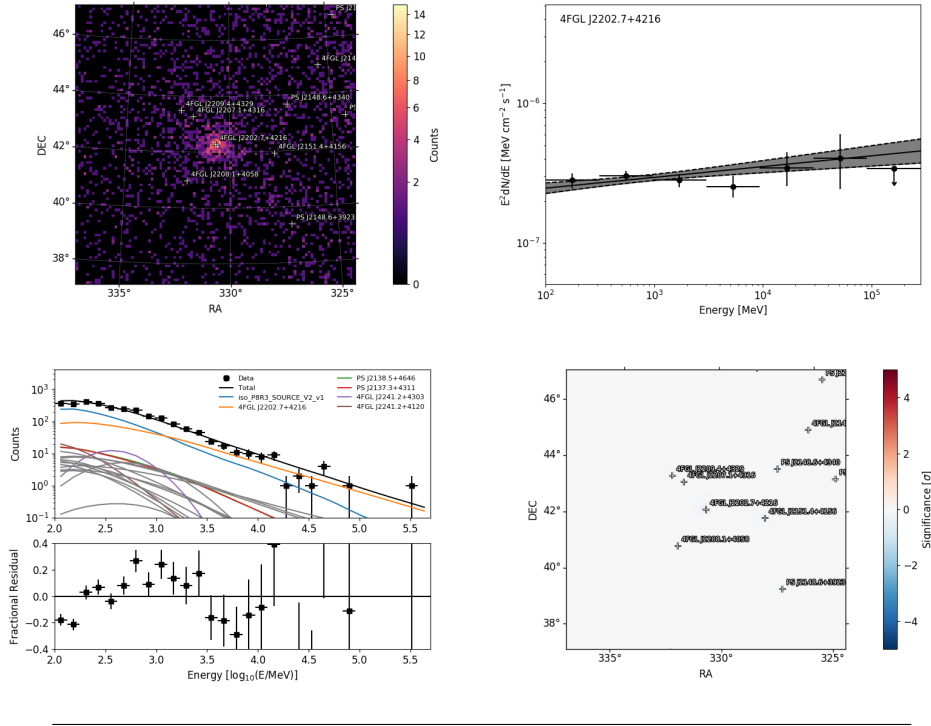
FIGURE 5.11: *Fermi*-LAT analysis of BL Lac during its flaring state in July 2019. *On the top left & right*: counts map and SED fitted with LP parameters listed in table 5.5. *On the bottom left & right*: counts spectrum with residuals and residuals map.

In the period December 2019-January 2020, in coincidence with MAGIC observations, the *Fermi*-LAT analysis of BL Lac has been performed with the same setup illustrated above, but in this case the curvature test has underlined that the preferred fit function by the likelihood analysis is a *LogParabola* (LP) function.

TABLE 5.6: Curvature Test parameters.

Period	logLikelihood PL	logLikelihood LP	$TS_{curvature}$	TS
Dec2019-Jan20	-26014.102	-25959.831	108.543	45.847

The BL Lac SED has been then fitted with a LP function $[\mathrm{MeV^{-1}\ cm^{-2}\ s^{-1}}]$ as in eq. (5.2)

$$\frac{dN}{dE} = N_0 \cdot \left(\frac{E}{E_b}\right)^{-\left(\alpha + \beta \log\left(\frac{E}{E_b}\right)\right)} \tag{5.5}$$

In table 5.7 the parameter values as a results of the likelihood analysis are shown.

In fig. 5.12 the counts map, the spectrum and the residual relative to the BL Lac analysis in the period December 2019-January 2020 are displayed.

TABLE 5.7: BL Lac SED parameters. The unit of N_0 is $[\mathrm{MeV}^{-1}\ \mathrm{cm}^{-2}\ \mathrm{s}^{-1}]$.

Period	N_0	E_b (MeV)	α	β
Dec19-Jan20	$1.93 \times 10^{-12} \pm 2.30 \times 10^{-13}$	7.48×10^{02}	$1.97 \pm 4.28 \times 10^{-02}$	$1.95 \pm 1.78 \times 10^{-02}$
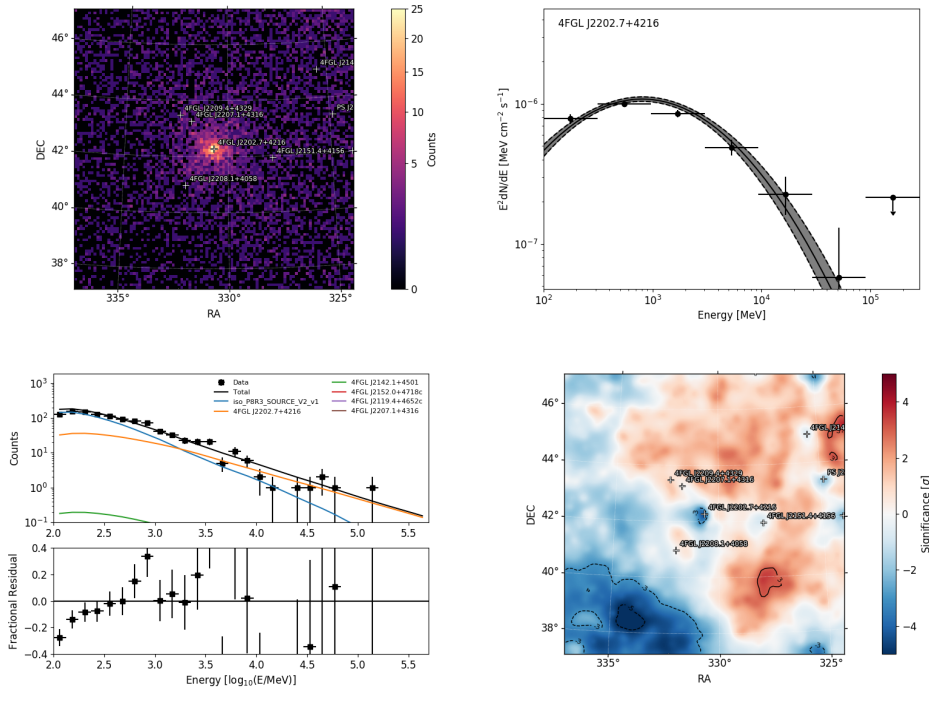
FIGURE 5.12: *Fermi*-Lat analysis of BL Lac during its flaring state in the period December 2019-January 2020. *On the top left & right*: counts map and SED fitted with PL parameters listed in table 5.7. *On the bottom left & right*: counts spectrum with residuals and residuals map.

5.2.4 Multi-wavelength light curves

In order to study the flaring behaviour of BL Lac during its high states in the three periods described in section 5.2.2, several LCs have been computed with 6 h and 12 h and 1 day time binning (fig. 5.13, fig. 5.14, fig. 5.15 and fig. 5.16).

A MWL observing campaign was active during the BL Lac flare of May 2019 (fig. 5.17). In addition to *Fermi*-LAT and MAGIC measurements, the available data are from

- the *Swift*-XRT instrument, covers the X-ray energy range $0.2 \div 10$ keV

- the optical observations of KVA and University of Siena Observatory in *R*-band

- the IRAM millimeter data

- the radio data from OVRO and Metsähovi Radio Observatory (37 GHz)[13].
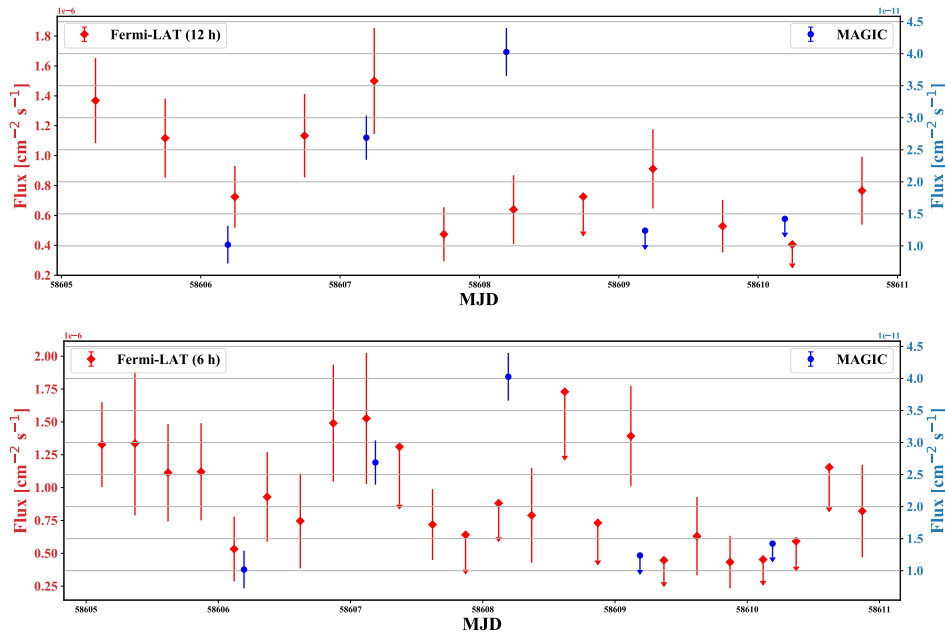
FIGURE 5.13: Comparison of *Fermi*-LAT and MAGIC LCs of BL Lac during its flaring state on May 2019. *On the top*: the *Fermi*-LAT LC is computed with time binning of 12 h spaced to be almost in coincidence with MAGIC observations. The data-taking is the day-range May 02-08, 2019. *On the bottom*: the *Fermi*-LAT LC is binned in time binning of 6 h.
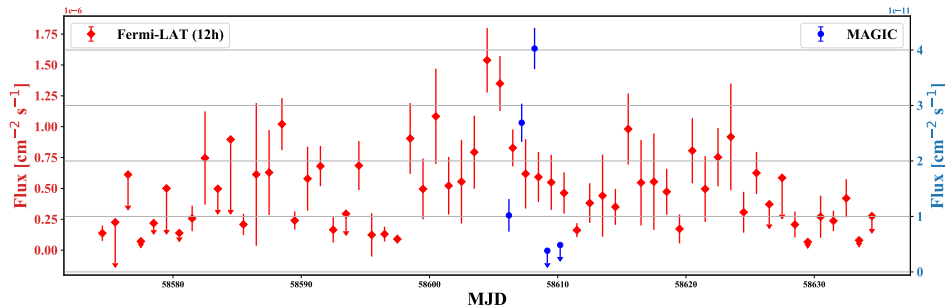
FIGURE 5.14: Comparison of *Fermi*-LAT and MAGC LC of BL Lac during its flaring state on May 2019. The *Fermi*-LAT LC is computed with time binning of 12 h in the period April 01 - May 31, 2019.

---

[13]Metsähovi BL Lacs project webpage.
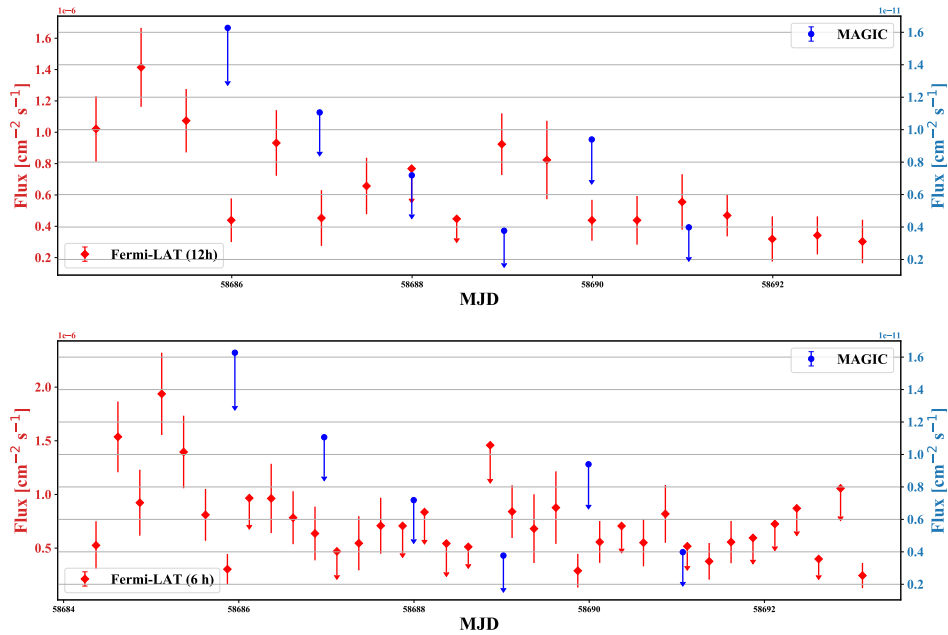
FIGURE 5.15: Comparison of *Fermi*-LAT and MAGC LC of BL Lac during its high state on July 2019. The data-taking is the day-range July 20-28, 2019.*On the top*: the *Fermi*-LAT LC is computed with time binning of 12 h, spaced to be almost in coincidence with MAGIC observations. *On the bottom*: the *Fermi*-LAT LC is binned in time binning of 6 h.
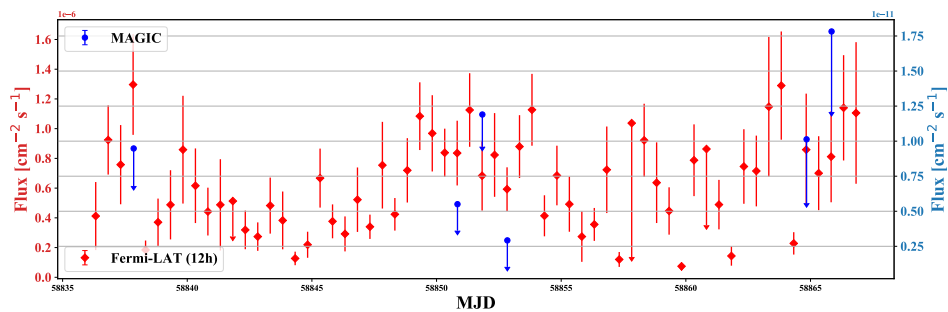
FIGURE 5.16: Comparison of *Fermi*-LAT and MAGC LC of BL Lac during its high state in the period December 2020-January 2019. The data-taking is the day-range December 19, 2019 - January 18, 2020. The *Fermi*-LAT LC is computed with time binning of 12 h spaced to be in almost in coincidence with MAGIC observations.
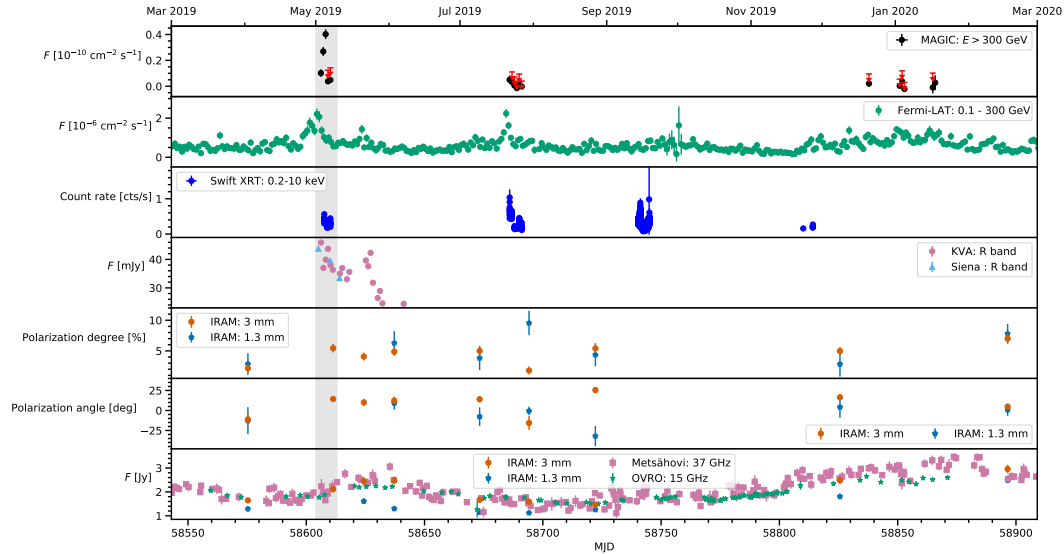
FIGURE 5.17: Comparison of multi-wavelength light curves obtained with different telescopes ranging from radio to HE and VHE γ rays. *Credit: MAGIC Collaboration in prep (corresponding authors: Sofia Ventura and Daniel Morcuende).*

5.2.5 Discussion

The BL Lac is known to be a very highly variable source in the entire electromagnetic spectrum. The source have shown also several fast flaring states in VHE γ rays observed by MAGIC and VERITAS telescopes (see discussion in section 5.2.1). A definitive explanation on the nature and origin site responsible for these fast flares is still debated and MWL observing campaigns are crucial for answering open-questions.

On May 2019, the BL Lac has been found in high state by *Fermi*-LAT monitoring of the sky, and VHE γ-ray observations have been triggered for the MAGIC telescopes. The overall sensitivity has been $\sim 20\,\sigma$ in the whole data-taking period, May 03$\div$07, 2019. The LC relative to this period displays an interesting *rising* and *decay* pattern (fig. 5.18), which is fitted with a double-exponential function starting from

$$F(t) = F_0 \cdot e^{-\frac{t-t_{\text{peak}}}{\tau}} \tag{5.6}$$

where $F_0 = (6.0 \pm 2.8) \times 10^{-11}\,\text{cm}^{-2}\text{s}^{-1}$, $\tau_{\text{peak}} = 5860.8 \pm 0.2\,\text{MJD}$, and τ gives values of rise and decay time scales of $1.0 \pm 0.7\,\text{day}$ and $0.5 \pm 0.2\,\text{day}$ respectively (fig. 5.18).

Other episodes of fast flares similar to the previous one have been detected by VERITAS in 2011, they are characterized by a decay time of 13 ± 4 min (Arlen et al., 2013), and in 2016, a slow rise of $\tau \sim 140 \pm 25$ min followed by a more rapid decay of $\tau \sim 36 \pm 8$ min (Abeysekara et al., 2018a) have been observed. A fast flare has been
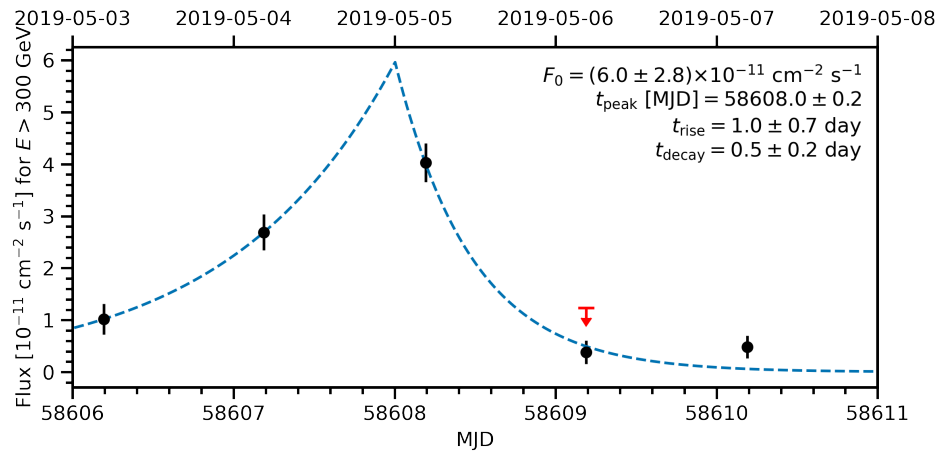
FIGURE 5.18: BL Lac flare May 2019. The observed LC has been fitted with a double exponential function to estimate the rising time and the decay time. *Credit: MAGIC Collaboration in prep (corresponding authors: Sofia Ventura and Daniel Morcuende).*

also detected by the MAGIC telescopes on June 2015, characterized by a variability timescale of $\tau = 26 \pm 8$ min (MAGIC Collaboration et al., 2019),. The flare of May 2019, instead, is characterized by a *rise* and *decay* time slightly longer with respect those observed by VERITAS and MAGIC, and that suggests to investigate novel scenarios in which the site responsible for the particle acceleration is farther from the central BH. Indeed radio observations performed by Metsähovi Radio Observatory have shown a very little activity at 37 GHz in coincidence with the VHE γ-ray flare. Moreover, the HE high states seem to happen slightly before the VHE flares, as displayed in fig. 5.13, fig. 5.14, fig. 5.15 and fig. 5.16; this feature is in common with the previous fast flare of BL Lac detected by MAGIC in 2015. The VHE state of May 2019 has been accompanied by variability in the optical band, while in X-ray range has been less prominent, as displayed in fig. 5.17.

During the flaring state in May 2019, both the HE and VHE spectra are fitted by a simple power-law function, as shown in eq. (5.2) and table 5.5. In particular, the *Fermi*-LAT SED displays a rising trend of the function, while the MAGIC SED a decreasing one. At some energy in between the two SEDs seems to be located the position of the second peak due to IC-scattering, as explained by SSC model (fig. 5.7, fig. 5.10 top right, and table 5.4). On the other hand, the *Fermi*-LAT SED relative to the period December 2019-January 2020 is fitted by a logparabola function, as resulting by the *curvature test* (table 5.6 and fig. 5.12 top right). In this case, the curvature of the spectrum shows that the position of the IC-peak is located in the energy range explored by *Fermi*-LAT, and then below the sensitivity of the MAGIC telescopes. Indeed the VHE observations set upper limits on the flux estimations since the significance of the detection of the source is less than 5σ in the VHE band. As reported in MAGIC Collaboration et al., 2019, during the fast flare the SED was fitted by LP

(eq. (5.1)) showing that the IC-peak is located in the energy range compatible with the IACTs' sensitivity. As a speculation, the evolution of the SED in the HE regime has to be considered as the precursor of high states at higher energies that could lead to the detection of the BL Lac by IACTs (above $5\,\sigma$ in less than $1\,h$, see table 5.1). The BL Lac is classified with a LP spectrum in the 4FGL *Fermi*-LAT catalog in agreement with its long term spectral behavior which is dominated by low states that are not detectable by IACTs since the VHE are reached by the tail of the second hump in the SSC scenario. If the spectral shape of the source changes during its higher states, passing from LP to PL, that could represent a good indication of flaring states detectable even at very-high energies. As a probe of this hypothesis, the evidence that the high state in HE is slightly before that one in VHE should be tested (fig. 5.17). However, in the case of BL Lac, the VHE observations are always triggered by the HE high state, usually in the *Fermi*-LAT regime, and this evidence could lead to observational bias and caveats. Moreover, the changing of the BL Lac spectral model in the *Fermi*-LAT regime may be evidence of the *shifting* of the second peak in the SED of the source leading to the *transition* from LBL/IBL to HBL behavior during *flaring* states.

The intra-night variability of BL Lac during May 2019 flare has still to be studied in view of the MAGIC collaboration paper in preparation, together with correlation studies and searches of lags in the LCs (section 3.2.1.2). This point represents a future development of the work already done, together with the modeling of the broadband emission. Several models have to be tested, like those already used in MAGIC Collaboration et al., 2019, assuming *two-zone* SSC (jet-in-jet interaction), *one-zone* of emission interacting with external photon field, and star/cloud-jet interaction (Perucho, Bosch-Ramon, and Barkov, 2017; see also discussion in section 5.2.1). As said earlier, all the previous scenarios are not able to properly reproduce the MWL observations and overcome the observational bias. A promising model is represented by relativistic magnetic reconnection which can convert magnetic energy into particle acceleration (Jormanainen et al., 2022).

5.3 1RXS J081201.8+023735 Detection & EHBL Catalog

Several questions are still open about the mechanisms powering blazar jets and the cosmological origin of Our Universe. In this context, the study of the extreme nature of blazars, and the extension of the known-source population are crucial, since nowadays only a few number of hard-TeV blazars have been detected. One of the goal of the MAGIC Collaboration is performing multi-year observing campaigns of promising EHBL candidates on the basis of their spectral properties in the radio, X-rays and HE γ rays as well as the redshift. A first EHBL catalog of 10 sources has been published by the collaboration (Acciari et al., 2020) with the observations

collected between 2010 and 2017, corresponding to a total of 262 h of observations
(fig. 5.19).

Source	Epochs	Detection significance $[\sigma]$	E_{thr} [TeV]	Flux $[10^{-12}\ \mathrm{cm}^{-2}\ \mathrm{s}^{-1}]$	$\Gamma_{VHE,intr}$
TXS 0210+515	2015, 2016, 2017	5.9	0.2	1.6 ± 0.5	1.6 ± 0.3
TXS 0637-128	2017	1.7	0.3	< 8.9	–
BZB J0809+3455	2015	0.4	0.15	< 3.7	–
RBS 0723	2013, 2014	5.4	0.2	2.6 ± 0.5	2.7 ± 1.2
1ES 0927+500	2012, 2013	1.2	0.15	< 5.1	–
RBS 0921	2016	-0.4	0.15	< 8.6	–
1ES 1426+428	2010	2.1	0.2	< 9.3	–
	2012	6.0	0.2	6.1 ± 1.1	1.8 ± 0.5
	2013	1.8	0.2	< 5.1	–
1ES 2037+521	2016	7.5	0.3	1.8 ± 0.4	2.0 ± 0.5
RGB J2042+244	2015	3.7	0.2	1.9 ± 0.5	1.7 ± 0.6
RGB J2313+147	2015	-0.9	0.2	< 1.5	–
1ES 0229+200	2013-2017	9.0	0.2	2.1 ± 0.3	1.8 ± 0.1

FIGURE 5.19: The sources listed in the first EHBL catalog of the
MAGIC collaboration. *Credit: Tab.1 in Acciari et al., 2020; Arbet-Engels
et al., 2022.*

Prior to the MAGIC observing campaign only 1ES 1426+428 was a known VHE
emitter, and among the sources listed in the catalog, the archetypal hard-TeV EHBL
1ES 0229+200 is used as reference source. The intrinsic spectral index[14] of EHBLs
is usually harder ($\Gamma_{\mathrm{VHE,intr}} \leq 2$) than that of other blazar classes leading to to high-
energy SED component peaking around TeV energies, lying in the VHE range cov-
ered by IACTs. In the catalog the hardest source is TXS 0210+515 with $\Gamma_{\mathrm{VHE,intr}} \leq=$
1.2 ± 0.3, while the softer one is RBS 0723 ($\Gamma_{\mathrm{VHE,intr}} \leq= 2.8 \pm 0.3$). On the other
hand, the synchrotron peak is expected to lye in the X-ray regime. In this sense the
MAGIC observations werecomplemented by a simultaneous X-ray coverage pro-
vided by Swift-XRT, on-board the Neil Gehrels Swift Observatory ($0.3 \div 10$ keV),
and Nuclear Spectroscopic Telescope Array (NuSTAR) (when available; $3 \div 79$ keV).
In the energy range $0.3 \div 10$ keV the observed spectra are fitted with a simple PL
function with hard spectral index $\Gamma \leq 2$, indicating the synchrotron peak frequency
is around 1 keV, and for those source, like RGB J2313+147, with softer spectral index
the synchrotron peak is located below 1 keV. In this case, during the observations the
soften sources do not behave as an extreme blazar, and a clear *harder-when-brighter*
behaviour is identified for each source of the catalog (section 3.2.1.1). This feature
is quite common in BL Lac objects (Pian et al., 1998; Krawczynski et al., 2004; Ac-
ciari et al., 2021). On summer 2016, the MAGIC observations of 1ES 2344+514 were
shown the temporarily EHBL behaviour of the source, characterized by a power-law
spectrum with a hard index of $\Gamma = 1.93 \pm 0.06$, associated with a synchrotron peak

---

[14]The intrinsic spectrum is obtained correcting the effect of the EBL absorption using model tem-
plates, as Franceschini, Rodighiero, and Vaccari, 2008.

frequency above 1 keV. During low-state, the synchrotron peak is instead about an order of magnitude lower (MAGIC Collaboration Acciari et al., 2020; Arbet-Engels et al., 2022).

Another very important aspect of the MWL observing campaign is the study related with the *leptonic* or *hadronic* interpretation of the MWL SED. The common used, by the MAGIC collaboration, leptonic scenarios are the *single-zone* SSC (Asano et al., 2014), and the *spine-layer* model (Ghisellini, Tavecchio, and Chiaberge, 2005; Tavecchio and Ghisellini, 2008). In the first approach, the emitting zone is a conical jet structure filled by ultra-relativistic electrons moving downstream and accelerated by turbulence effects, while in the second one the emission is associated with shocks occurring in a stratified electron plasma jet with the central part (*spine*) moving faster than the surrounding layer. As discussed in sections 2.2 and 3.2.1, the emission is boosted leading to enhanced IC-scattering responsible for the VHE γ-ray emission (Tavecchio and Ghisellini, 2016). On the other hand, regarding the hadronic approach, the adopted model is a *lepto-hadronic* scenario in which the first SED component at lower frequencies is due to the synchrotron emission of electrons, while the second hump is the result of the proton-synchrotron radiation (Cerruti et al., 2015).

In the context of leptonic models, the spine-layer is preferred because is able to overcame the low magnetization and equipartition issue associated with single-zone SSC model. Indeed the latter requires a very low magnetization of the emitting region, and the observed electron energy density U_e is several order of magnitude above the magnetic field energy density U_B. The ratio U_B/U_e is an indication of the equipartition of the system that should be ~ 1, while in the case of single-zone SSC model is ~ 10. On the other hand, even in the case of proton-synchrotron mechanism, the required MF is much larger in order to compensate the lower efficiency of the proton-synchrotron mechanism, and U_B highly dominates over U_e, and the system is still out of equipartition. Moreover this scenario is able to provide estimations on the neutrino flux, as product of the $p\gamma$-interaction in the jet, but for the tested sources, listed in the catalog, its value is low and remains below the sensitivity of current neutrino telescopes (for more details see Acciari et al., 2020 and section 2.3 and fig. 5.20).

1RXS J081201.8+023735 represents one of the new detected sources detected by the MAGIC telescopes at VHE, and the results of the analysis described in section 5.3.1 were presented in two main conferences (Ventura et al., 2021; Arbet-Engels et al., 2022).

5.3.1 About the source

The BL Lac object 1RXS J081201.8+023735 (also know as RX J0812.0+0237 or RGB J0812+026; R.A. $8^h 12^m 1.860^s$, Dec. $2°37'33.10''$) is located at a redshift of $z = 0.1721 \pm 0.0002$ (Becerra González et al., 2021), and is classified as an extreme blazar (EHBL;
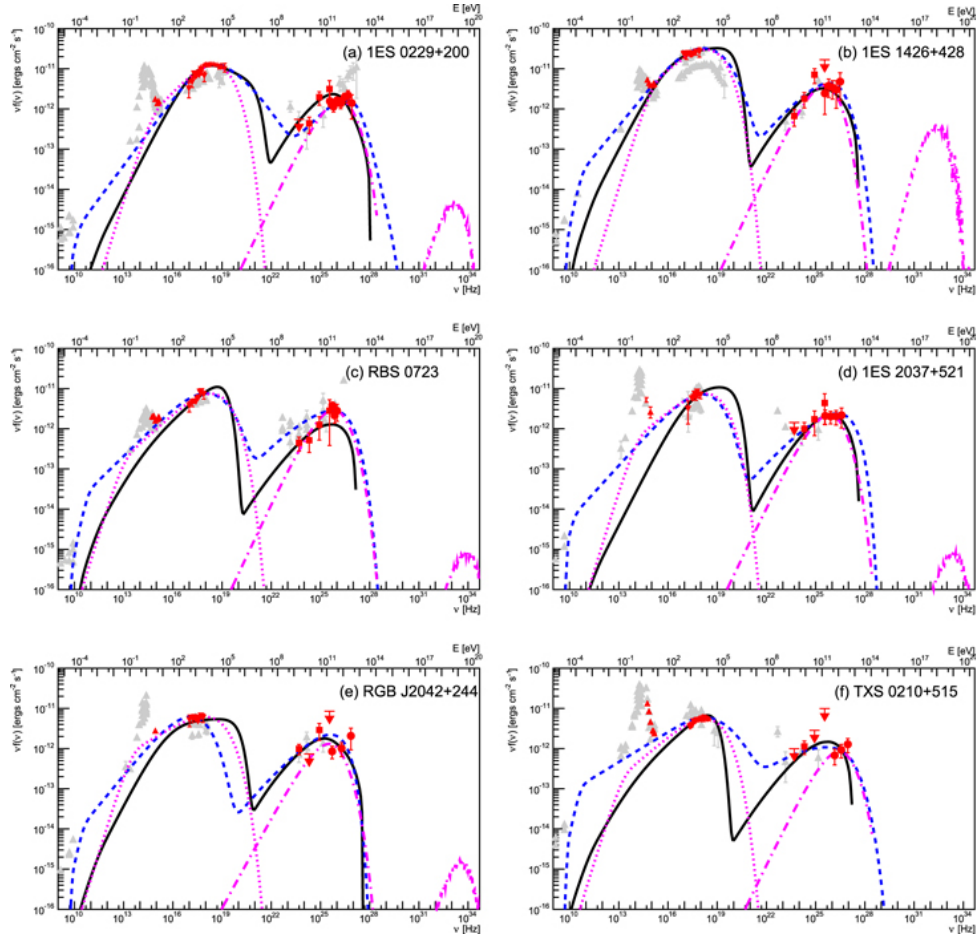
FIGURE 5.20: Examples of broadband SED. The blue dashed line is the result of the conical jet SSC model (Asano et al., 2014). The black continuous line represents the outcome of the spine–layer model (Ghisellini, Tavecchio, and Chiaberge, 2005). The dashed-dotted magenta line is the outcome of the proton-synchrotron model (Cerruti et al., 2015). The third bump in the proton synchrotron model is the expected neutrino flux. *Credit: fig.3 in Acciari et al., 2020.*

see section 3.2.1 and fig. 3.6). Its optical spectrum is dominated by the host galaxy, as typically occurs in extreme blazars, and through the study of few optical features is possible to establish the redshift of the source. The information on the redshift is crucial to determine the EBL absorption suffered by the γ-ray spectrum, especially in the VHE regime (section 3.2.3). Optical studies can also provide informations on the nature and characteristics of the possible BLR, fundamental in modeling the MWL SED. Indeed the latter indicates that the MWL SED of the source indicates the presence of the host galaxy and the synchrotron peak is shifted to higher frequencies in comparison with less energetic blazars (Biteau et al., 2020), such as the prototype BL Lac, and the overall flux properties in radio, X-ray and HE (MeV $\div$ GeV) bands are compatible with those of 1ES 0229+200, the archetypal EHBL (Tavecchio et al., 2009). The EHBL behavior of 1RXS J081201.8+023735 is also supported by archival measurement from ROSAT at 1 keV (Voges et al., 1999), and the source is listed in

4FGL *Fermi*-LAT catalog (Abdollahi et al., 2020a), and was classified like VHE candidate in the 2WHSP catalog (2WHSP J081201.7+023732; Chang et al., 2017. 1RXS J081201.8+023735 was detected for the first time at VHE by the MAGIC telescopes in the period 2019/2020 (Ventura et al., 2021; Arbet-Engels et al., 2022, and see section 5.3.2).

5.3.2 MAGIC analysis

Significance of the signal

The MAGIC observations cover a period of data-taking from January 02 to April 12, 2019, and between December 27, 2019, and February 21, 2020, corresponding to observing cycle XIV and XV. The observations were carried out under the acceptance of the observing proposal submitted to the collaboration in order to "hunt" new EHBL candidates and extend their population even at VHE. The observations were carried out under *dark-time* and good-quality atmospheric conditions and *stereoscopic mode*, for a total observing time of 48.74 h, and at zenith angle range $45° < z < 50°$. The analysis has been performed starting from *Superstar* data with MARS v2.19.15 with standard image cleaning, transmission parameter 0.85 (when available), and the MC data sample, used for training and testing (see section 4.3.1.1) are the version relative to period ST 03.11 RINGWOBBLE and ST 03.12 RINGWOBBLE in the zenith angle range $5° ÷ 62°$. The image cleaning cuts used are the OSA standard cleaning, $\text{Lvl}_1 - \text{Lvl}_2$ (6.0 − 3.5). The 1RXS J081201.8+023735 has been found to a significance level of $5.21\,\sigma$, with a total of $N_{\text{ON}} = 13460$, $N_{\text{OFF}} = 12772.3 \pm 65.2$, and excess $N_{\text{ex}} = 687.7 \pm 133.1$ in LE. In table 5.8 the significance value of the observing periods[15] are tabulated.

TABLE 5.8: 1RXS J081201.8+023735 observing cycle XIV/XVI - Significance of the signal.

Date	MJD	obs_time (h)	σ LE	σ FR
Cycle XIV	$58485 - 58485$	36.91	3.16	2.46
Cycle XV	$58844 - 58900$	11.83	5.29	3.48
Cycle XIV-XV	$--$	48.74	5.21	3.87

In fig. 5.21 the squared angular distance (θ^2) distribution between the reconstructed event direction and the nominal source position in the camera, and the normalized off-events θ distribution represented by the gray histogram are

---

[15]Wiki page link.

displayed. The vertical dashed line defines the signal region below which the detection significance is computed.
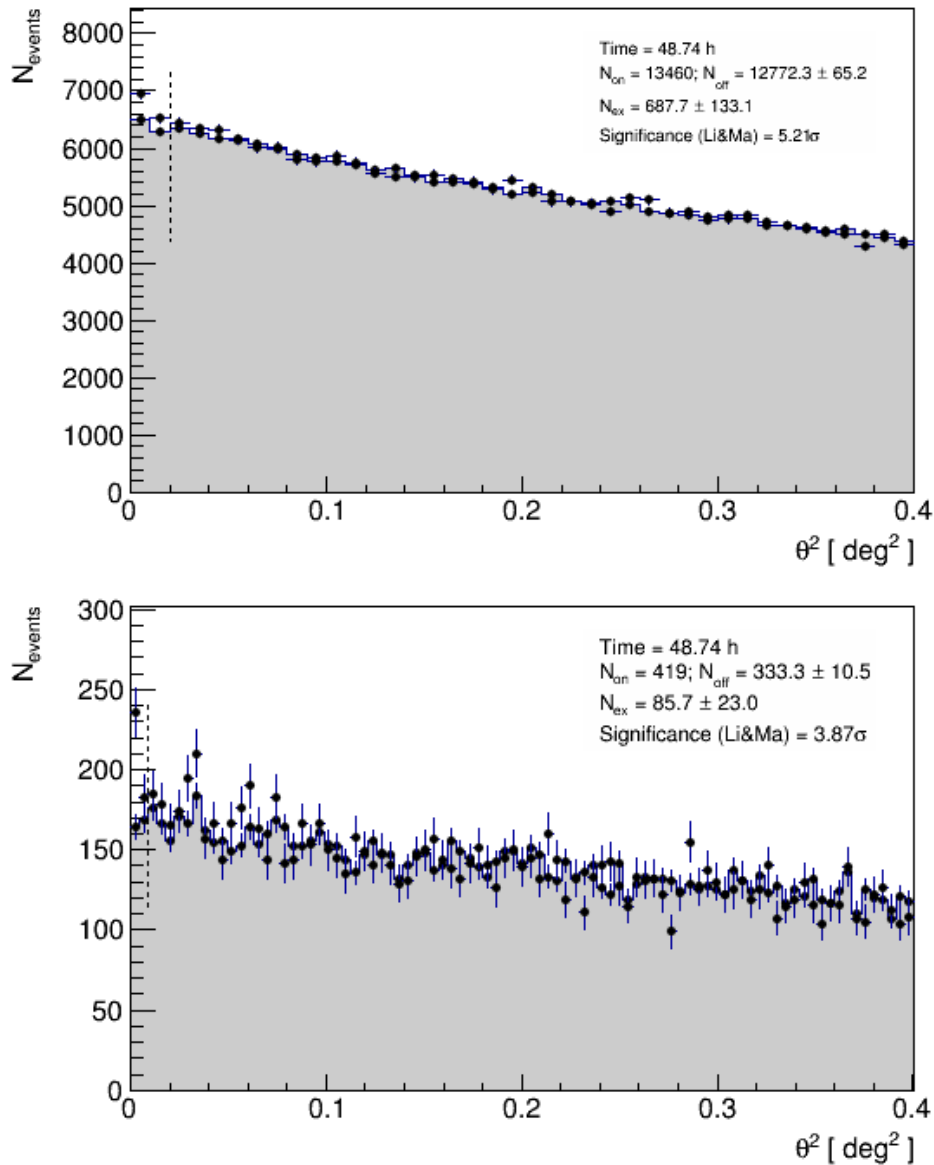
FIGURE 5.21: θ^2 distribution relative to the observing period cycle XIV-XV, as output of ODIE tool. *From the top to the bottom*: LE and FR analysis.

LE is the acronym for Low Energy analysis and consist of $\sim 1.2\%$ sensitivity of Crab nebula. Regarding the Full Range (FR) respectively. All the cuts are optimized on Crab nebula data collected in the same period of 1RXS J081201.8+023735 observations and under same conditions for both MC period. table 5.9. In fig. 5.22 the Crab sanity check for the stacked MC period is displayed.

TABLE 5.9: Optimized cuts on Crab nebula.

Cuts	LE	FR	HE
Odie.signalCutPSF40	0.083	0.060	0.052
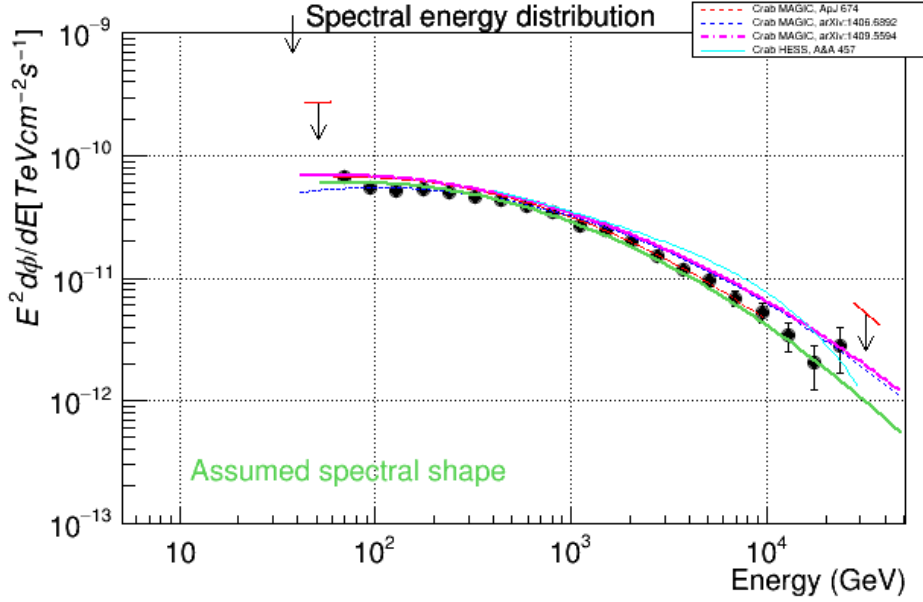
FIGURE 5.22: Crab sanity check performed with cuts listed in table 5.9 relative to stacked MC period ST.031 and ST.0312.

Spectral Energy Distribution

The 1RXS J081201.8+023735 SED (fig. 5.23) has been computed, stacking the observations of the two different MC periods with FOAM, and then with *FOLD* tools, in 3 energy bins in the range $99.0 \div 470.5$ GeV and fitted with a power-law (PL) function [TeV^{-1} cm^{-2} s^{-1}]

$$\frac{dN}{dE} = (1.63 \pm 0.35) \cdot 10^{-11} \cdot \left(\frac{E}{249.53 \text{ GeV}} \right)^{-2.58 \pm 0.33} \tag{5.7}$$

with a $\chi^2/\text{d.o.f.} = 10.471/5$.
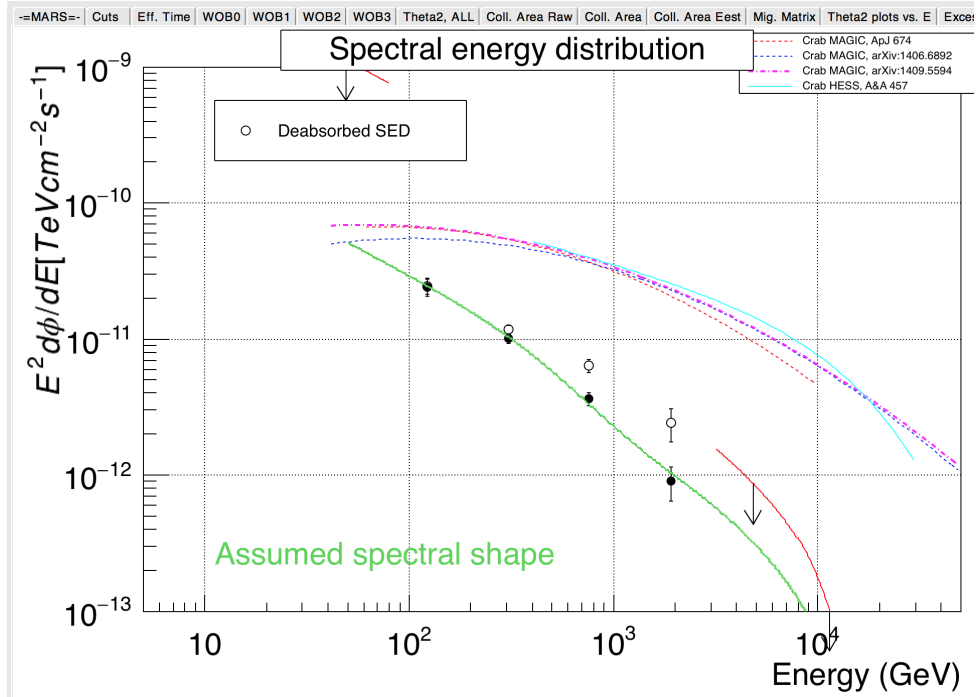
FIGURE 5.23: 1RXS J081201.8+023735 Spectral Energy Distribution relative to the MAGIC observing campaign cycle XIV-XV, fitted with power-law function. The intrinsic spectrum, computed with EBL absorption Domínguez et al., 2011, is also shown.

5.3.3 *Fermi*-LAT analysis

The *Fermi*-LAT analysis of 1RXS J081201.8+023735, listed in the 4FGL catalog (4FGL J0812.0+0237; Abdollahi et al., 2020a) has been performed with FERMIPY v0.17.3 using 12 years of data ($247017601 \div 625708805$ MET). The analysis has been computed in a RoI width of $10°$, binsize= $0.1°$, in CEL coordinates, 8 energy bins in range 300 MeV $\div$ 500 GeV. The quality cuts in zenith angle has been applied ($z_{max} = 90$, DATA_QUAL>0 && LAT_CONFIG==1 && ABS(ROCK_ANGLE)<5), the used event class is 128 relative to point source analysis, and event type 3 relative to FRONT+BACK data (section 1.1) analyzed with the IRF P8R3_SOURCE_V2, and PASS8 data. In the analysis have been used the isotropic (ISO_P8R3_SOURCE_V2_V1) and galactic diffuse (GLL_IEM_V07) models provided by the *Fermi* collaboration.

Regarding the likelihood analysis, a region of $15°$ around the source has been considered, and the prefactor and index parameters of sources within $3°$ from the BL Lac location have been set as free, as well as for those sources with TS > 10, while for those with TS < 5 the parameters have been fixed. For computing the SED a PL spectral models has been assumed, as parameterized in the 4FGL catalog. As a result, the logLikelihood is -77354.676, the total TS is ~ 320, and the 1RXS J081201.8+023735 SED is fitted with a power-law (PL) function [$\text{MeV}^{-1}\,\text{cm}^{-2}\,\text{s}^{-1}$] as
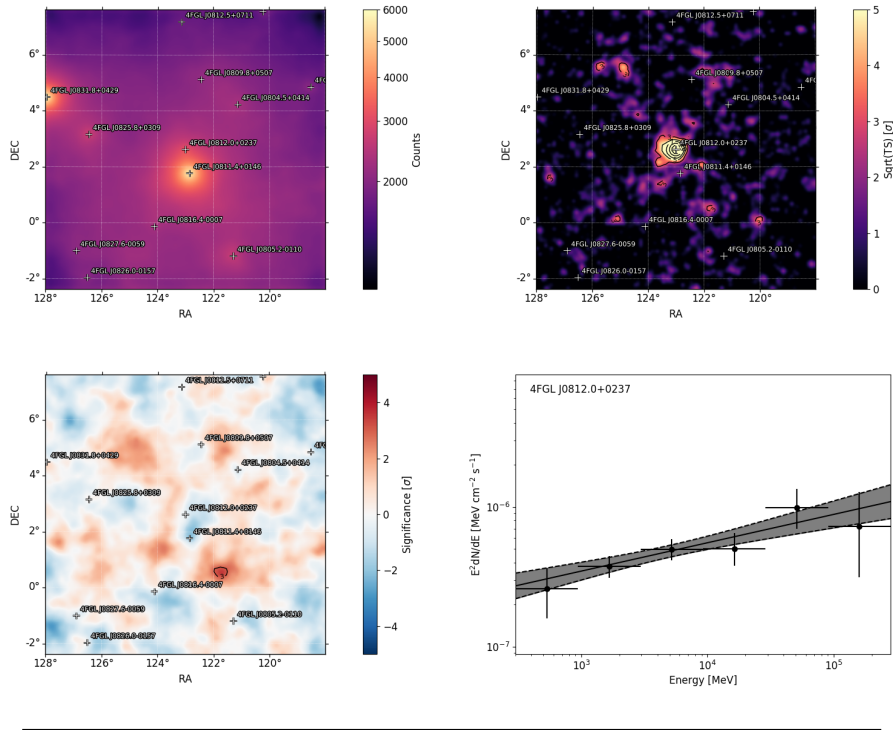
FIGURE 5.24: *Fermi*-LAT analysis of 1RXS J081201.8+023735 in a time
range or 12 years. *On the top left & right*: counts map and TS map. *On
the bottom left & right*: SED fitted with eq. (5.8) and residuals map.

in eq. (5.8)

$$\frac{dN}{dE} = (2.63 \pm 0.44) \cdot 10^{-14} \cdot \left(\frac{E}{4.18 \text{ GeV}}\right)^{-1.80 \pm 0.12} \tag{5.8}$$

In fig. 5.24 the counts map, the spectrum and the residual relative to the 1RXS
J081201.8+023735 analysis of 12 years of data-taking are displayed.

5.3.4 Multi-wavelength analysis

As already mentioned, in order to obtain a broadband view of the source under in-
vestigation, the MWL coverage is crucial to build the overall SED. The MAGIC ob-
servations were complemented by simultaneous data in the optical/UV and X-rays
performed by the Swift satellite monitoring. The X-ray spectral analysis confirms
the EHBL nature of the source, making it an ideal target to test particle accelera-
tion models in blazar jets. In fig. 5.25 the MWL SED of 1RXS J081201.8+023735 is
displayed.
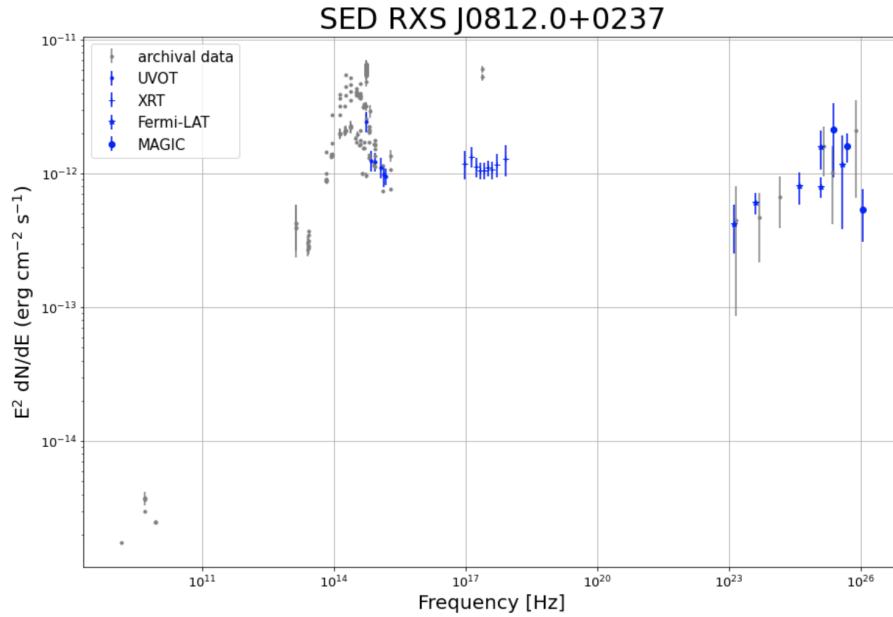
FIGURE 5.25: MWL SED of 1RXS J081201.8+023735 built with archival data, UVOT and XRT data by Swift satellite, *Fermi*-LAT and MAGIC data. *Credit: Ventura et al., 2021.*

5.3.5 Discussion

As said earlier, the EHBLs represent ideal laboratories for testing physical theories and they are used as cosmological probe. From the observing point of view they present some spectral differences, and depending on the *hardness* of the VHE γ-ray spectrum (Γ_γ) two main different class can be studied (Biteau et al., 2020)

I **Extreme-Synchrotron sources**:in this first class are included those sources displaying softer index of the intrinsic VHE γ-ray spectrum ($\Gamma_\gamma > 2$); these sources are ideal tool to study particle acceleration within the jet, and emission mechanisms

II **Extreme-TeV sources** (hard-TeV blazars):in the second class are listed the *hardest* objects displaying the spectral index $\Gamma_\gamma < 2$; in this case propagation effects in the Universe to constrain the intensity of the EBL (section 3.2.3), the strength of the IGMF (section 3.3), fundamental and MM physics (section 2.3) can be studied. These sources are supposed to be the acceleration site of UHE CRs, and then responsible for the neutrino emission.

As discussed in section 5.3 three models have been used by the MAGIC collaboration to interpret the broadband SED of the sources listed in first EHBL catalog

1. a time-dependent modeling of the observed emission due to leptons relativistically moving in an expanding conical jet. The low and high SED components arising from the same region, *one-zone* model (Asano et al., 2014)

2. the so-called spine-layer model characterized by two emission regions within the jet, *two-zone* model (Ghisellini, Tavecchio, and Chiaberge, 2005)

3. an hybrid scenario in which the low SED component is due to synchrotron emission of leptons, while the highest one to proton-synchrotron radiation responsible for the VHE γ-ray emission (Cerruti et al., 2015). This scenario is the link with the neutrino and multi-messenger astronomy.

In fig. 5.20 the broadband SEDs of the sources listed in the first EHBL catalog with the relative fitting model as results of the three scenarios listed above are displayed.

In this framework, the *hunting* of new EHBL candidates represents one of the effort made by the MAGIC collaboration in order to amply the number of sources in view of the second EHBL catalog. For proposing the observation of EHBL candidates, such as 1RXS J081201.8+023735, the standard procedure is the submission of observing proposals that will be accepted or rejected by an internal panel of the collaboration (TaC). If the proposal will be accepted the requested observing time will be allocated by the TaC. Multi-wavelength observing campaign and monitoring are crucial in order to select, among the many known blazars, the EBHL candidates. Four main criteria are used

1. **X-ray band** observations characterized by

   - the first SED peak with $\nu > 10^{17}$ Hz (1 keV)

   - hard spectrum in soft X-ray ($\Gamma_{\text{X-ray}} < 2$), measurements performed by Swift-XRT

   - the synchrotron tail lies in hard X-ray, energy range covered by Swift-BAT and NuSTAR satellites

2. **MeV-GeV (HE) band**: the sources listed in 3FHL (Ajello et al., 2017) and 4FGL catalogs (Abdollahi et al., 2020b), built with measurements performed by *Fermi*-LAT instrument

3. the ratio between the X-ray flux and radio flux $\frac{\text{Flux}_{\text{X-ray}}}{\text{Flux}_{\text{Radio}}} \gg 1$, and the sources listed in Bonnoli et al., 2015

4. **Redshift** that should be $z \leq 0.2$.

As an example, the archetypal EHBL source is the 1ES 0229+200 (fig. 5.20 a) that displays the synchrotron peak at $\nu > 10^{17}$ Hz, the IC-peak at ~ 10 TeV, and its redshift is $z \sim 0.14$.

The EBHL candidate 1RXS J081201.8+023735, which were proposed to the collaboration, and measured during observing cycle XIV-XV, satisfies all the previous points

- its radio, X-ray, and HE γ-ray fluxes are comparable with those of 1ES 0229+200

- the location of the MWL SED synchrotron peak is around $4\,\text{keV}$ ($\nu \sim 10^{17.5}\,\text{Hz}$; fig. 5.23)

- the source is listed among the *Fermi*-LAT objects (section 5.3.3)

- the estimated redshift from optical spectroscopy measurements is $z = 0.1721 \pm 0.0002$ (Becerra González et al., 2021)

Since the spectral index is soft ($\Gamma = 2.58 \pm 0.33$; eq. (5.7)), 1RXS J081201.8+023735 can be classified as **Extreme-Synchrotron source** (class I), and, for that reason, represent a promising source to study the particle acceleration processes within the jet and the emission mechanism. Moreover, several theoretical scenarios can be tested, such as hybrid-scenarios (Cerruti et al., 2015), and models in which turbulence driven electron acceleration within the jet (single-zone model, Asano et al., 2014). 1RXS J081201.8+023735 will be listed in the second EHBL catalog and it is a new source in the TeV-sky listed in the reference catalog of VHE γ-ray astronomy, the TeVCat, named as TeV J0812+026[16] (fig. 5.26), published in date 2021-01-24, and presented at 43$^{\text{rd}}$ COSPAR conference in the same year (Ventura et al., 2021).

Source Name:	1RXS J081201.8+023735
Source Type:	XGal | Blzr | BLLac | HBL
Distance:	z=0.1721
GLON:	219.9907
GLAT:	19.0945
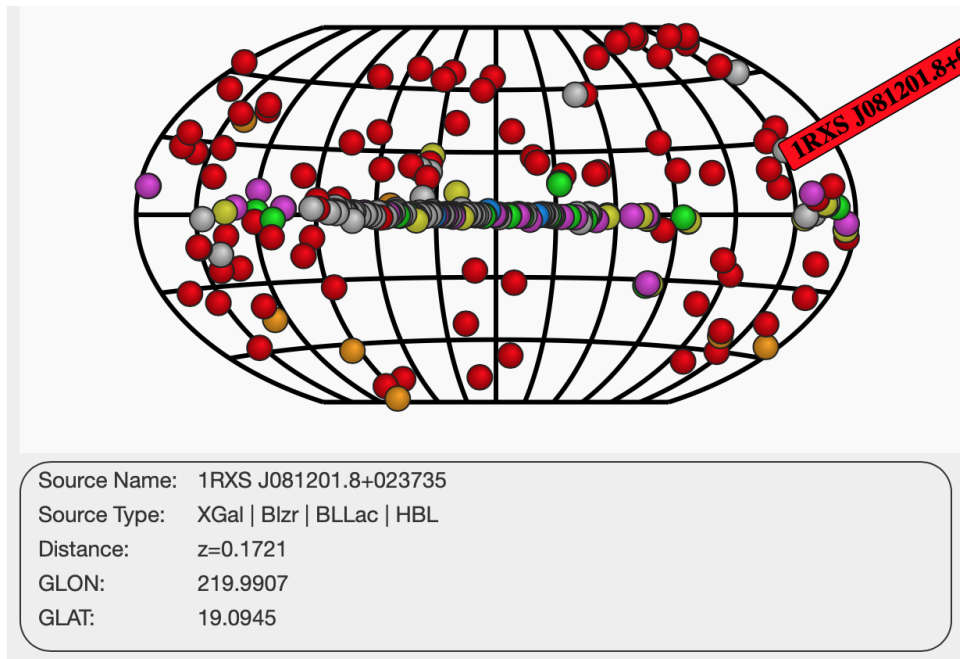
FIGURE 5.26: The 1RXS J081201.8+023735 location in the TeV sky. *Credit: 1RXS J081201.8+023735 on TeVCat.*

---

[16] 1RXS J081201.8+023735 on TeVCat.

6 Chasing the *PeVatron* in the Galactic Center with CTA

THE chapter is devoted to the description of the complex scenario represented by the Galactic Center (GC) region, and its violent and extreme behaviour observable at the highest energies. In particular, a detailed treatment of the diffuse γ-ray emission is illustrated, and its impact on the present date interpretations of the observations, and the crucial role plays in the definition of the *background* model used in the analysis chain of γ-ray detectors' data. Several simulations have also been performed in view of the CTA era in order to understand if the several suggested scenarios, as explanations of the observed *excess*, will be disentangled, and if a synthetic population of unresolved sources is worth including in the CTA data challenge II (DC II).

6.1 Context

Our Galaxy is pervaded by diffuse gaseous matter in the form of ionized, atomic and molecular phases, detectable at several wavelengths, from radio to InfraRed (IR), UV band and even in γ rays. The CRs accelerated within the Milky Way by several astrophysical sources (sections 2.1 and 3.1) interact with the diffuse gaseous component (sections 3.1.3 and 3.1.4) and produce γ rays mainly via π^0 decay, producing a large scale γ-ray component clearly observable in the whole Galactic Plane (GP; fig. 3.5), firstly detected by EGRET onboard of CGRO satellite (Hunter et al., 1997) and then detected by the next generation *Fermi*-LAT (section 1.1) with increased statistics and sensitivity (Ackermann et al., 2012a). The role of several astrophysical sources are also supposed to be part of the observed γ-ray diffuse emission. Single sources, like supernova remnants (SNRs, section 3.1.1), pulsar wind nebulae (PWNe, section 3.1.2) and young stellar clusters (YSCs) are supposed to be the site in which high energetic CRs are accelerated, and through the interaction of the latter with a gaseous cloud in the vicinity of the sources produce a *local* γ-ray enhancement, usually positionally in coincidence with the cloud itself (section 3.1.3).

As said in section 2.1.3, the galactic CRs, accelerated by astrophysical sources, are deflected and confined by the galactic magnetic field (MF), for that reason a non-negligible component of the measured diffuse emission is due to CR diffusion throughout the Galaxy, which returns the large-scale component of the γ-ray flux. The dominant component of this flux is associated with the hadronic CRs interacting with the interstellar medium (ISM) gaseous matter , and producing γ rays via π^0 decay (Stecker, 1970; Dermer, 1986), promoting γ rays as tracers of gaseous dense clouds. On the other hand, the leptonic CR component contributes to the γ-ray emission via Inverse Compton (IC) scattering and bremsstrahlung with different spectral shape and spatial distribution, allowing to disentangle its effect to the measured flux.

While the role of the diffuse γ-ray component is crucial at high energies and widely accepted by the astroparticle community, its "presence" even at very high energy is still strongly debated. Recent observations of Tibet As-γ (Amenomori et al., 2021a) and LHAASO (Cao et al., 2023a) have shown the evidence that the diffuse CR component is present also at the highest energies, and confirmed by HAWC observations of the GP too (Abeysekara et al., 2021). As said in chapters 3 and 4, the field of view (FoV) of IACTs is restricted to portion of sky observable at the geographic location of the instruments. In particular, the GP is better explorable from the southern hemisphere, where currently are located the 5 H.E.S.S. telescopes (section 1.1). In the next years, several Small Sized Telescopes (SSTs) and Medium Sized Telescopes (MSTs) will be built by the CTA consortium (section 4.3.2) in order to properly investigate the complex region of the Milky Way Galactic Plane (section 4.3.2; Acharyya et al., 2021).

The impact of the diffuse γ-ray component is evident when the analysis of γ-ray data is carried out. In this framework, the efforts of the theoretical astroparticle community to provide increasingly realistic models able to reproduce the observed emission, represent an intriguing "playground" in which phenomenological templates featured by different set of parameters are used in the analysis chain of data. These models are often the outcomes of numerical codes – DRAGON (Evoli et al., 2017a; Evoli et al., 2008) has been used in this work – that propagate the CRs within the Galaxy resolving the transport equation (sections 2.1.2 and 2.1.5; Berezinskii et al., 1990). The results are tuned on present date measurements of satellite instruments, such as PAMELA (Adriani et al., 2011), AMS-02 (Aguilar et al., 2015) and CREAM (Ahn et al., 2010), and the outcomes become the inputs of numerical codes that convolve and integrate along the line-of-sight the CR density profiles with the gaseous matter, enclosed in the Milky Way, in form of high resolution HEALPIX (Górski et al., 2005) projection maps accounting the diffuse γ-ray emission (for major details see chapter 4 in Ventura, 2018). In this work has been used GAMMASKY (Di Bernardo et al., 2013; Evoli et al., 2012), while an open source version is now available, the HERMES code Dundovic et al., 2021.

For understanding and modelling the γ-ray diffuse emission, especially at higher energies, it is crucial the capability to describe and reproduce the CR transport within the Milky Way, and through the interactions with the interstellar gas – locked in complex structures – it is possible to estimate the expected emission in each part of the Galaxy. The reproducibility of the large-scale CR-*sea* is an important aspect in the current, and especially, next generation telescopes since it has a key role in the definition of the *background* model, a crucial ingredient in the analysis chain of γ-ray data.
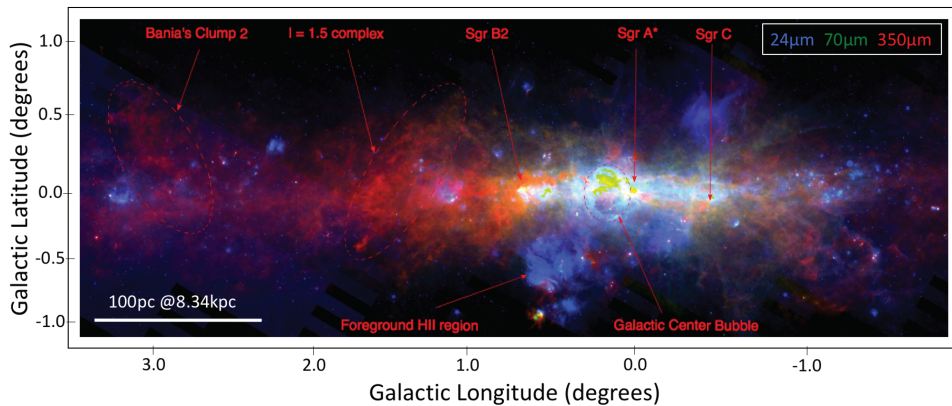
FIGURE 6.1: Image of the inner few degrees of the Milky Way around the Galactic Centre at sub-mm to mid-IR wavelengths. *Credit: fig.1 in Longmore and Kruijssen, 2018*.

In this work, a phenomenological model featured by *inhomogeneous diffusion* has been extensively used to analyze HE and VHE real and simulated data (section 6.1.1) in the peculiar Galactic Center (GC) . This region is the perfect laboratory to study phenomena and physical processes that may be occurring in many other galactic nuclei. The current observations show the evidence for a central massive black hole – the compact radio source Sgr A* with a mass of $\sim 4.4 \cdot 10^6 M_\odot$ – and a dense and luminous star cluster – in which early-type stars have been forming in the vicinity of the black hole recently – as well as several components of neutral, ionized, and extremely hot gas (fig. 6.1), representing a presently not fully understood *paradox of youth* (Genzel, Eisenhauer, and Gillessen, 2010). Several astrophysical observations show that the GC seems to have significant star formation and a large rate of supernova explosions compared to the average value in the Galaxy. The star formation rate (SFR) in the inner few degrees away from the GC is of order 1% of the SFR in the Galaxy, with a factor of 250 higher than the mean rate in the Milky Way (Figer et al., 2004). This should be the consequence of the presence of a large amount of molecular gas filling the inner part of the Galactic bulge (section 6.1.2).

6.1.1 Modelling the gamma-ray Diffuse Emission

The requirement to analyze γ-ray data has prompted the theroretical astroparticle community to provide increasingly realistic models for the diffuse emission able to compute and reproduce the observations. The large-scale *background*, detected by EGRET and *Fermi*-LAT at high energies, is explained in terms of galactic CR population (CR-*sea*) diffusing within the Galaxy.

For building a realistic phenomenological model to reproduce the observations, the starting point is a physical model for the CR density distribution in the Galaxy. In this work the DRAGON numerical code has been used to solve the transport equation. The code is designed to simulate all processes related to galactic CR transport, such as diffusion, re-acceleration, convection, energy-losses and spallation, for all CR species, from heavy nuclei to protons, antiprotons, and leptons. DRAGON works in both 2D and 3D mode, and in both cases it is possible to implement *anisotropic* diffusion (see below). The code further includes the nuclear cross section database, interstellar radiation field model, and gas distribution map of the Milky Way, as adopted in the public version of GALPROP[1] (Vladimirov et al., 2011; for major details see Evoli et al., 2017b). In DRAGON the inclusion of detailed distribution of the major galactic accelerators, as SNRs, to modelling the source term of the diffusion equation is fundamental (see section 2.1.4 and eq. (2.10)). In this work the Case and Bhattacharya, 1998, distribution has been adopted, where – for deriving the *surface brightness-to-diameter* relation from the galactic rotational curve – have been used radio and X-ray observations[2], leading to the SNR radial distribution (fig. 6.2)

$$f(r) = A \sin\left(\frac{\pi r}{r_0} + \theta_0\right)^{-\beta r} \tag{6.1}$$

where $A = 1.96 \pm 1.38 \text{ kpc}^{-2}$, $r_0 = 17.2 \pm 1.9 \text{ kpc}$, $\theta_0 = 0.08 \pm 0.33$ and $\beta = 0.13 \pm 0.08$ kpc^{-1}.

As mentioned above, different propagation setups can be used in the code, in this framework two major *types* have been considered

A **homogeneous** and isotropic, the standard conventional diffusion in the quasilinear theory (section 2.1.5) in which the diffusion coefficient (eq. (2.13)) is $\delta = 0.5$ – compatible with a Kraichnan spectrum of the ISM turbulence (Gaggero et al., 2014) – and it is assumed uniform in the whole Galaxy, predicting a uniform spectral index for primary CRs, $E^\Gamma \to \Gamma \sim 2.7 \div 2.8$, as observed at the Earth position (eq. (2.2); Workman et al., 2022). In this work it is named *base model*

---

[1] GALPROP webpage.

[2] $R_\odot = 8.5$ kpc is the Sun galactocentric distance and $V_\odot = 220$ km/s is its velocity respect to Galactic Centre.
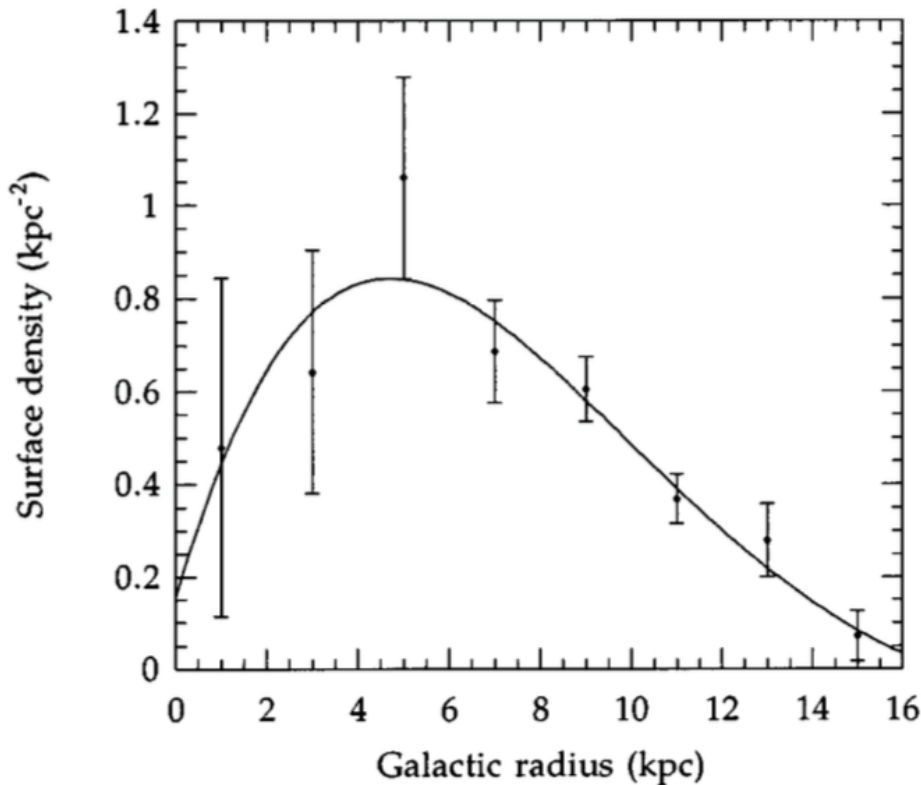
FIGURE 6.2: Supernova Remnants Radial Distribution and *best*-fit described by eq. (6.1). The scaled total number of shell SNRs in region of interest is $(56 \pm 4)/f_z$, where the error on the number of SNRs represents the uncertainty in the radio brightness-to-diameter (Σ-D) relation and f_z represents the incompleteness due to the lack of selection effects. *Credit: Fig.7 in Case and Bhattacharya, 1998.*

B **inhomogeneous** and anisotropic, in this case the diffusion coefficient (eq. (6.2)) has a linear dependence with galactocentric distance, rigidity and advection velocities, increasing approaching the GC (Gaggero et al., 2015b). An additional hardening is present at ~ 250 GeV/n (Gaggero et al., 2015b). In this work it is called *gamma model*.

The first case, type A, is implemented also in GALPROP (Vladimirov et al., 2011) code, used, for instance, by the *Fermi*-LAT collaboration. In the last case, type B, the diffusion coefficient is parametrized as

$$D \propto \left(\frac{E}{E_0} \right)^{\delta(r)} \tag{6.2}$$

where $\delta(r) = ar + b$ for $r < 11$ kpc, in which $a = 0.035$ kpc and $b = 0.21$ leading to $\delta_{r_\odot} = 0.5$. All the parameters have been tuned to consistently reproduce observed CR spectra at the Earth position, and *Fermi*-LAT γ-ray data on the whole sky. The physical interpretation of this choice lies in the assumption of a smooth transition

between a dominant parallel escape along the poloidal component[3] of the regular galactic MF, and a perpendicular escape associated with the regular field lying in the plane (Cerri et al., 2017). In this interpretation, in the inner Galaxy δ is lower, while in the outer Galaxy, the scaling is steeper. Moreover, an advective wind for $r < 6.5$ kpc increases as the perpendicular distance from the galactic plane (GP) increases, as observed in X-ray by ROSAT (Snowden et al., 1997). The diffusion coefficient in eq. (2.13) is also set up with an exponential dependence with the vertical distance (z) from the GP. Assuming then a uniform CR source spectral index across the whole Galaxy, the CR spectral index is dependent to the galactocentric distance, and leads to a longitude-dependent (r) γ-ray spectrum along the GP. This parametrization is in good agreement with the results shown in fig. 6.3 of γ-ray analysis of *Fermi*-LAT data[4].
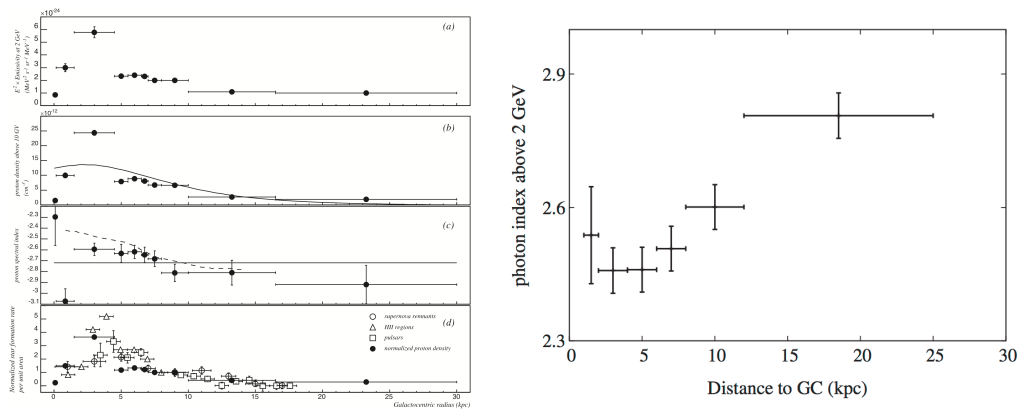
FIGURE 6.3: *On the left*: the radial distributions across the Galaxy of (a) the γ-ray emissivity per H atom measured at 2 GeV; (b) the proton flux integrated above 10 GV, with the prediction from the GALPROP (solid curve); (c) the proton spectral index, with statistical error bars and the prediction for proton rigidities above 1 TV from the same GALPROP (solid line) and from Gaggero et al., 2015a (dashed line). *Credit: fig. 8 in Acero et al., 2016. On the right*: the distribution of the photon index of the galactic diffuse γ-ray emission associated with the gas distribution in different rings. *Credit: fig. 6 in Yang, Aharonian, and Evoli, 2016.*

Finally, a spectral hardening has been introduced in the proton and helium source spectra at 250 GeV/n, in order to reproduce the local propagated spectra measured by PAMELA (Adriani et al., 2011), AMS-02 (Aguilar et al., 2015) and CREAM (Ahn et al., 2010) (see fig. 6.4). This feature has assumed to be present in the whole Galaxy, as may be expected if it is produced by propagation effects. Furthermore, in

---

[3]In presence of the poloidal MF component the parallel and perpendicular components of diffusion coefficient (eqs. (2.11) and (2.13)) have a different rigidity dependence getting stronger at low galactocentric radii.

[4]However, in Yang, Aharonian, and Evoli, 2016, the CR spectrum at the GC is slightly softer than that found by the *Fermi*-LAT collaboration.

order to match KASCADE-Grande results (Apel et al., 2013), a cutoff at $5\,\mathrm{PeV/n}$ has been introduced in the CR source spectra.
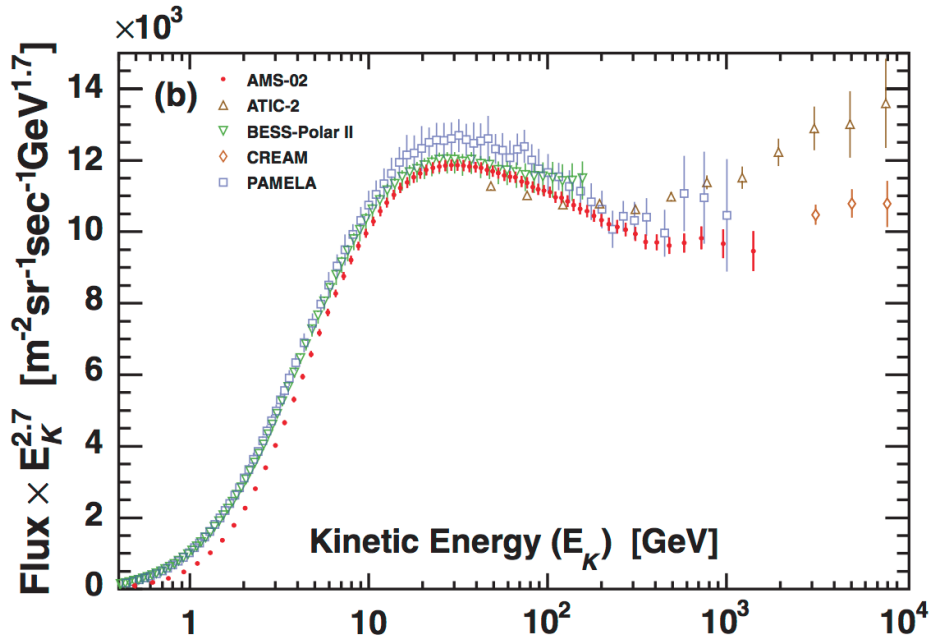
FIGURE 6.4: The flux as a function of kinetic energy E_k multiplied by $E_K^{2.7}$ compared with recent measurements by ATIC, BESS, PAMELA and CREAM. For the AMS results $E_K = \sqrt{R^2 + M_p^2} - M_p$ where M_p is the proton mass, and R is the rigidity. The figure shows the hardening above $\sim 250\,\mathrm{GeV/nucleon}$. *Credit: fig. 3.b in Aguilar et al., 2015.*

All the ingredients allow *gamma model* to predict the hardening of CR propagated spectrum and γ-ray emissivity as observed in the inner Galaxy, providing a viable solution to the long-standing MILAGRO anomaly[5]. Indeed, standard conventional model (here *base model*) are not able to properly fit the γ-ray observations (Ackermann et al., 2012a), which are instead reproduced by the *gamma model* (Gaggero et al., 2015a; Gaggero et al., 2015b; Acero et al., 2016; Yang, Aharonian, and Evoli, 2016; Grasso et al., 2017; Ventura, 2018).

Once the setup is formed, the numerical code computes the CR spatial distribution in the whole Galaxy, and the outcomes are included as input in the second code GAMMASKY that returns the π^0, IC and bremsstrahlung components of the γ-ray diffuse emission integrating the convolution of the spatially-dependent CR spectrum, gas/radiation density distributions and proper nuclear cross-sections along the line-of-sight. The GAMMASKY outcomes are *all*-sky maps organized in high resolution

---

[5]In particular, an excess of the diffuse emission in the inner GP at 15 TeV with respect to the predictions of conventional models (Abdo et al., 2008) was observed.

HEALPIX projection maps, where each pixel has the same surface value in sr accounting the intensity of the γ-ray diffuse emission from the correspondent region of the sky, and all the map is stored in a single array containing all the pixels.

The π^0 component is dominant in the GC region, because of the incremented number of targets consisting in the dense gaseous clouds filling the inner Galaxy. Assuming a reasonable choice of interstellar radiation field (ISRF) template, the γ-ray opacity in the CMZ is considered negligible, but above several TeVs the impact of γ γ-absorption is increasingly important and cannot be excluded. In the updated version of DRAGON2[6], this radiative effect is included together with updated cross-section values allowing to propagate multi-PeV CRs and then achieving multi-TeV γ-ray maps (Evoli et al., 2018; De La Torre Luque et al., 2021). The evolution of the internal code version GAMMASKY, is now publicly available under the name of HERMES, in which several updates improve the capability of the code thanks to the inclusion of updated nuclear cross-sections, ISRF models, a variety of multi-messenger and multi-wavelength radiative processes, spanning from the radio domain up to high-energy gamma rays and neutrino production[7] (Dundovic et al., 2021).

6.1.2   Modelling the Galactic Center Interstellar Environment

The Galactic Center (GC) of the Milky Way is the perfect laboratory for studying phenomena and physical processes that may be occurring in many other galactic nuclei. The observations show the evidence for a central massive black hole – the compact radio source Sgr A* – and a dense and luminous star cluster, as well as several components of neutral, ionized, and hot gas (Genzel, Eisenhauer, and Gillessen, 2010). The inner part of the GC is represented by the so-called *Central Molecular Zone* (CMZ) which represents one of the densest environment of the Galaxy.

As said earlier, once the CR profile distribution has been computed with DRAGON, the γ-ray emission has to be computed considering the distribution of targets for CR interactions within the Galaxy. The targets are included in 2D maps with informations on the column density of the interstellar gas locked in the Milky Way, and observed at different wavelengths. Indeed, the space between the stars of Our Own Galaxy is not empty, but rich interstellar environment populated by extremely rarefied ordinary matter (the interstellar medium, ISM), relativistic particles (CRs) and electromagnetic fields. New stars form out of the reservoir of matter given by the ISM, in its densest and coldest regions. During their life stars emit electromagnetic radiation in the interstellar space and enrich the matter locked in their interior in heavy elements. Part of this matter eventually returns to the ISM via powerful stellar winds or violent supernova explosions. The latter process is thought to power as

---

[6]DRAGON2 webpage.
[7]HERMES webpage.

well the injection of CRs in the interstellar space. One of the most interesting aspects is the interplay between the interstellar environment and stars.

The ISM accounts for $10\% \div 15\%$ of the visible mass of the Galaxy and it has a highly inhomogeneous in distribution. Roughly half of the ISM mass is located in clouds occupying only a small fraction of the galactic volume, containing very cold ($T = 10 \div 20$ K) molecular gas and cold ($T = 30 \div 100$ K) atomic gas. The rest of the interstellar matter constitute the *intra*-cloud medium in form of warm atomic gas, warm ionized gas and hot ionized gas. The chemical composition of the ISM is similar to that of the solar system (Asplund, Grevesse, and Jacques Sauval, 2006): $\sim 74\%$ of hydrogen, $\sim 25\%$ of helium and $\sim 1.2\%$ of heavier elements, the so-called *metals*. More than 50% of the metals are locked in solid dust grains responsible for the obscuration and reddening of starlight, and represent an important component in many non-thermal processes.

Our Galaxy is divided in a thin and a thick disk, an inner bulge, and a spherical halo (Robin et al., 2003). The Milky Way extends over more than 60 kpc from its center (Kalberla and Dedes, 2008). The solar system resides in the disk at a radius of approximately $R_{\odot} = 8.5$ kpc (Kerr and Lynden-Bell, 1986), and the stars of the disk rotate around the GC in nearly circular orbits. The neutral hydrogen line indicates the presence of a spiral structure, similar to that seen in other external galaxies.

Neutral atomic hydrogen (HI) can be *counted* through the observations of the 21-cm line, and the measured quantities are the intensity of the line (*brightness temperature*) and the Doppler shift, which is related to the velocity with respect to the local standard of rest (LSR) frame. Instead the hydrogen molecular component (H$_2$) is not directly observable, and then it is traced by other ISM molecular transitions, such as those associated with ^{12}CO ($J = 1 \rightarrow 0$) – which is observed at wavelength of 2.6mm, CS – HCN, and more. The molecular gas is contained in clouds forming giant complexes (size of a few tens of pc and mass up to 10^6 $M_{\odot}$) down to small cores (size of a few pc and mass up to 10^3 $M_{\odot}$). For deriving the H$_2$ column densities is used the conversion factor (Lebrun et al., 1983)

$$X_{\text{CO}} = \frac{N(\text{H}_2)}{W_{\text{CO}}} \tag{6.3}$$

where W_{CO} represent the mass of the molecular cloud. Several methods, involving different tracers including γ rays, are used to estimate the X_{CO} conversion factor, but none of them – because of the optically thick line of ^{12}CO – is a good mass tracer (Dickman, 1975; Lebrun et al., 1983; Dame, Hartmann, and Thaddeus, 2001). In any case, all these methods converge to a common value of order of magnitude around $X_{\text{CO}} \sim 2 \times 10^{20}$ cm^{-2}K^{-1}km^{-1}s. The molecular gas is of particular interest in CR studies since represent the major target of CR interactions leading to secondary γ-ray via π^0 decay (for a more complete description of the galactic ISM see chapter 3 of Ventura, 2018).

In this work to compute the γ-ray model for the background emission have been used the gas distribution map of GALPROP, and a detailed analytical and dynamical description of the gas distribution in the inner Galaxy (Ferrière, Gillard, and Jean, 2007). Moreover, another analytical representation of the CMZ has been used to perform simulations in view of the Cherenkov Telescopes Array (CTA) era (section 6.3). In this case, the γ-ray emission from the CMZ has been computed *illuminating* the gas distribution – obtained through CS molecular lines emission – with the $1/r$ *PeVatron* profile observed by H.E.S.S. in the GC (HESS Collaboration et al., 2016).

The inner region of the Milky Way is known as Galactic bulge (GB) and corresponds to the central ~ 3 kpc, subdivided in the outer molecular ring ($r > 1.5$ kpc) largely devoid of interstellar gas, and in the *nuclear* bulge (inner 300 pc) The molecular gas (H_2) is concentrated in the central molecular zone (CMZ), an asymmetric layer extending in projection out to $r \sim 200$ pc[8] (Burton and Liszt, 1978; Liszt and Burton, 1980). The CMZ itself contains a ring-like feature with mean radius ~ 180 pc, the so-called 180-pc molecular ring, and, inside that, a thin sheet populated by dense molecular clouds, known as the GC disk population or the GC molecular disk (Bally et al., 1987; Bally et al., 1988). Due to the important interstellar extinction along the line-of-sight and the complex motion of gas structures, a certain description of the GC gas distribution is still not available. The internal disk has a torus structure with a thickness ~ 45 pc and a total hydrogen mass $\sim 2.0 \times 10^7 M_\odot$, with $\sim 4 \times 10^6 M_\odot$ in the inner disk and $\sim 1.6 \times 10^7 M_\odot$ in the outer torus. The vertical hydrogen mass distribution is asymmetric: at higher latitudes ($0.5° < l < 4°$) corresponds to $\sim 2.9 \times 10^7 M_\odot$, while at negative latitudes ($-4° < l < -2°$) it is $\sim 1.1 \times 10^7 M_\odot$. The total hydrogen mass in the CMZ is $\sim 6 \times 10^7 M_\odot$, and the interstellar matter in the central region is extremely clumpy and trapped in small, compact molecular clouds, which an average hydrogen density of $\sim 10^3$ cm^{-3}. The remaining 10% of the interstellar matter forms a diffuse, homogeneously distributed *intra*-cloud medium, with an average hydrogen density ~ 10 cm^{-3}. Furthermore the strong UV radiation field due to the numerous high-mass stars embedded in the GB cause the thin *intra*-cloud medium to be both warm and ionized.

For estimating the H_2 column density (n_{H_2}), through measurements of line tracers, it is widely used the X_{CO}-factor, assumed to be an outward radial gradient in order to reproduce the γ-ray observations performed by EGRET, dropping from $\sim 1.5 \times 10^{20}$ cm^{2}K^{-1}km^{-1}s at $r = r_\odot$ to $\sim 4 \times 10^{19}$ cm^{-2}K^{-1}km^{-1}s at $r = 2$ kpc, and extrapolating its value for $r = 0$ to be $\sim (2 \div 4) \times 10^{19}$ cm^{-2}K^{-1}km^{-1}s. (fig. 6.5; Strong et al., 2004). The value of X_{CO} near the GC remains fairly uncertain and the notion that N_{H_2} is proportional to $W_{^{12}CO}$ may be questionable Huettemeister et al., 1998. Once the value of X_{CO} is known, the H_2 spatial distribution can be inferred from CO line emission measurements.

---

[8]More precisely, $r \sim 250$ pc at positive longitudes and $r \sim 150$ pc at negative longitudes.
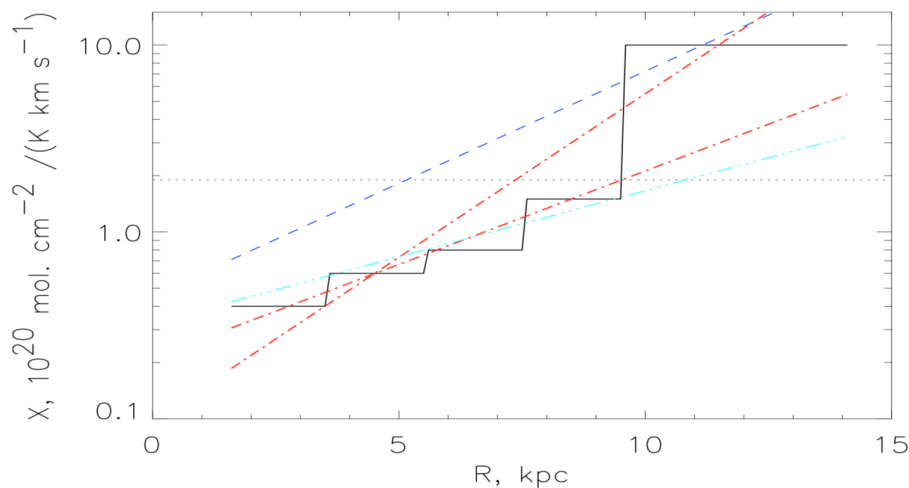
FIGURE 6.5: X_{CO} as function of r. Solid black line represents γ-ray data. Dash-dot red line represents data using metallicity gradient. *Credit:* fig. 2 in Strong et al., 2004

The presence of a galactic *spike* could be responsible for the observed asymmetric distribution and non-circular motions of the interstellar gas close to the GC since the clouds move in the gravitational potential of a barred galaxy (Binney and Merrifield, 1998; Sormani et al., 2018). Although the numerous gaps and uncertainties in observing data, a theoretical gas distribution model can be builded starting from the sky maps of molecular line emissions and transforming the measured line-of-sight velocity into line-of-sight distance, even if the poor knowledge of the true gas kinematics close to the GC makes this kind of method unreliable (Ferrière, Gillard, and Jean, 2007). The CMZ projected onto the Galactic plane has the shape of a 500 pc $\times$ 200 pc ellipse tilted at 70° to the line-of-sight toward positive longitudes (Sawada et al., 2004). The GC molecular disk appears planar and closely aligned with the Galactic plane and the thickness of the disk is approximated to 30 pc. The H_2 density can be inferred from the local H_2 mass of the CMZ and the value of X_{CO} factor, estimating a total mass in the CMZ of $\sim 1.9 \times 10^7 M_\odot$. In fig. 6.6 the projected molecular gas content in the CMZ is shown.

In the model the GB disk is an elliptical disk with semi-major axis 1.6 kpc, and an hole of size 800 pc $\times$ 258 pc in the middle, just large enough to enclose the CMZ. The GB disk is further tilted at $\alpha = 13.5°$ out of the Galactic plane. The total H_2 and HI[9] masses in the GB region are $\sim 5.3 \times 10^7 M_\odot$ (Sanders, Solomon, and Scoville, 1984) and $\sim 5.2 \times 10^6 M\odot$ of HI respectively (Liszt and Burton, 1980). Moreover, the H_2 and HI mass content of the GB hole is $\sim 3.4 \times 10^7 M_\odot$ and $3.5 \times 10^6 M_\odot$ respectively. The GB disk extends out to $r_\perp = 1.14$ kpc[10] on each side of the GC (fig. 6.8).

---

[9]The HI mass is supposed to be distributed as H_2 mass with a total mass of 8.8% of the H_2 mass, and a thickness of 90 pc (fig. 6.7).

[10] That is the radius at half-maximum density.
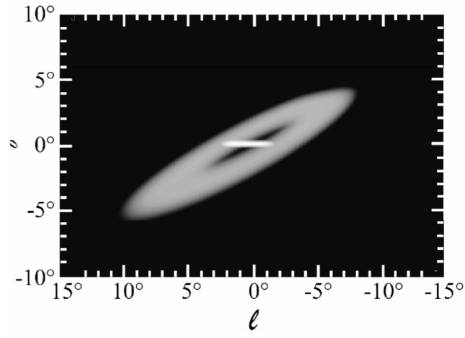
FIGURE 6.6: Projection of the CMZ – molecular gas – (bright area) and the holed GB disk (fainter area) onto the plane of the sky. *Credit: fig. 4 in Ferrière, Gillard, and Jean, 2007.*
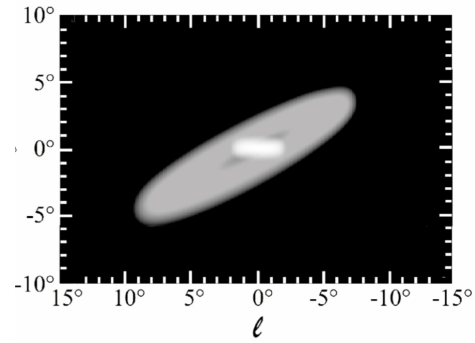
FIGURE 6.7: Projection of the CMZ – atomic gas – (bright area) and the holed GB disk (fainter area) onto the plane of the sky. *Credit: fig. 4 in Ferrière, Gillard, and Jean, 2007.*

The total space-averaged mass density of interstellar gas in the GB is related to the hydrogen space-averaged density through

$$\langle \rho \rangle = 1.453 \cdot m_{\mathrm{p}} \langle n_{\mathrm{H}} \rangle \tag{6.4}$$

where m_{p} is the proton mass (fig. 6.9; for major detail about the 3D analytical model see Ferrière, Gillard, and Jean, 2007).
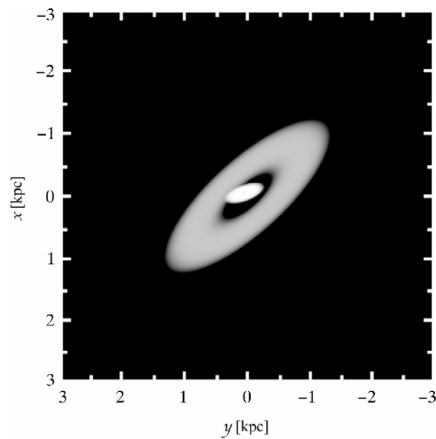
FIGURE 6.8: Projection of the CMZ (bright area) and the holed GB disk (fainter area) onto the Galactic plane. Displayed here is the H_2 map. The Hi map looks identical, except for this hardly noticeable difference that the GB-disk-to-CMZ luminosity ratio is slightly greater. *Credit: fig. 5 in Ferrière, Gillard, and Jean, 2007.*
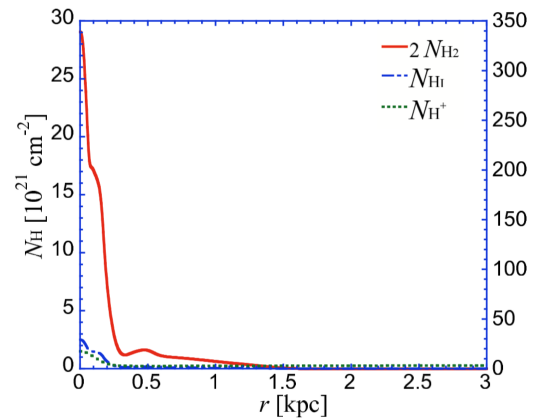
FIGURE 6.9: Azimuthally-averaged column densities through the Galactic disk of interstellar hydrogen nuclei in molecular form (solid line), atomic form (dot-dashed line) and ionized form (dotted line) and associated surface densities of total interstellar matter, as functions of Galactic radius. *Credit: fig. 6 in Ferrière, Gillard, and Jean, 2007.*

For having a reliable description of the central region is desirable to estimate the *filling* factor – the ratio between the space-averaged density and the true density – of the different gas phases, but it is hard to obtain and only some upper-limits are given (Rodríguez-Fernández et al., 2001).

In summary, the main components in the GC are molecular (H_2) and atomic (HI) hydrogen. HI, which is inferred from 21-cm lines, is less than 10% of the total mass. While, H_2 is not observed directly, and – except for the densest clumps where for instace CS of HCN lines emission are used – the column density can be inferred from several tracers, most commonly from the ^{12}CO lines emission and the X_{CO} factor. This requires a conversion factor which has been estimated to be $X_{CO}(r \sim 0) \sim 0.5 \times 10^{20}$ cm^{-2} K^{-1} km^{-1} s with a factor 2 uncertainty (Ferrière, Gillard, and Jean, 2007). In this work has been adopted $X_{CO}(r \sim 0) = 0.65 \times 10^{20}$ cm^{-2} K^{-1} km^{-1} s because this value returns the best agreement with the integrated mass distribution, based on the CS emission map reported in HESS Collaboration et al., 2016. **The quoted uncertainty on this parameter directly applies to the diffuse γ-ray emission normalization. This effect, however, is degenerate with that of varying the CR (poorly known) source density at the GC** (see section 6.5).

6.1.3 Gamma-ray observation of the Galactic Centre region

This section reports the recent observations performed by currently operating IACTs towards the GC position. A detailed description of the complex scenario surrounding the interpretation of the observed VHE γ-ray emission has been presented in section 3.1.3.1.

In 2006, the H.E.S.S. collaboration reported for the first time the detection of diffuse γ-ray emission from the inner Galaxy (Aharonian et al., 2006b). The VHE emission was found to approximately trace the column density of the ISM traced by CO and CS molecular lines emission, and it extends over about 2 degrees in galactic longitude along the Galactic Plane (GP) corresponding to the dubbed central *Galactic Ridge* region.

Above TeV energies the CR leptonic component is believed to be negligible because of the energy losses afflicting synchrotron and Inverse Compton mechanisms, caused by strong MFs – as strong as $\sim 100\,\mu$G (Crocker et al., 2010) – and dense IR radiation field in the inner Galaxy respectively. The emission observed by H.E.S.S. was then interpreted as primarily originated by the interactions of high and very-high energy CR hadrons (mostly protons) with the dense gaseous mater enclosed in the molecular clouds filling the GC region. As shown in sections 2.2 and 2.2, the pp interaction produces pions, and the neutral pion rapidly decay in γ rays. The spectral index of the observed γ-ray emission $\Gamma = -2.29 \pm 0.07_{\text{stat}} \pm 0.20_{\text{sys}}$ was significantly

harder considering that measured at the Earth position due to CR propagation and diffusion within the Galaxy (sections 2.1 and 3.1.4 and eq. (2.2)).

Recently, the H.E.S.S. collaboration released the new measurements, obtained with ~ 250 h of data-taking and increased statistics, that allowed to extend the explored energy range and to perform a better study of the morphology of the emission (HESS Collaboration et al., 2016; H. E. S. S. Collaboration et al., 2018a). Here the energy spectrum of the diffuse γ-ray emission from an annulus (of radius $\sim 0.45°$; *pacman* region) centered on the HESS J1745-290 point source was measured in the range $0.2 \div 45$ TeV (fig. 3.4). The spectrum was found to follow a power-law (PL) with index $\Gamma_{\text{HESS16}} = -2.32 \pm 0.05_{\text{stat}} \pm 0.11_{\text{sys}}$ extending up to the maximal measured energy with no statistically significant evidence of a cutoff (see fig. 6.10).
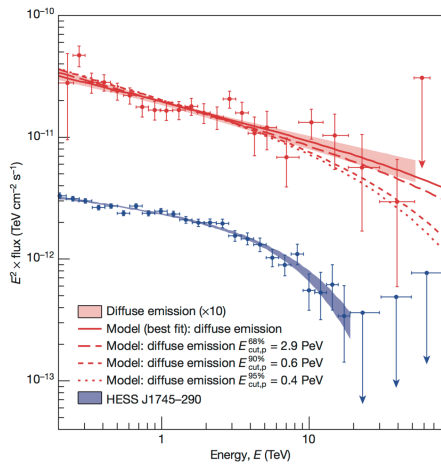
FIGURE 6.10: H.E.S.S. data of the GC region. The blue and red bands are the best fit of the source, while the red line is the expected emission from π^0 decay. *Credit: fig.3 in HESS Collaboration et al., 2016.*
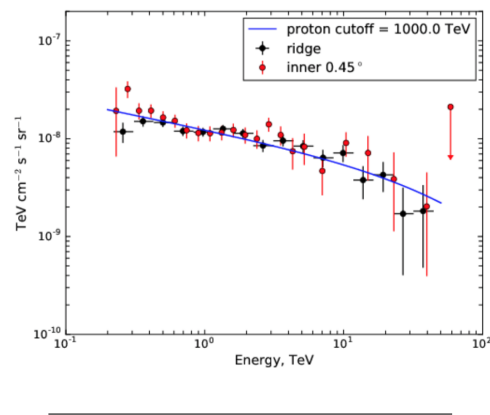
FIGURE 6.11: H.E.S.S. data of the GC ridge region, $|l| < 1°, |b| < 0.3°$ (black points). The *pacman* region are the red data from the previous work (HESS Collaboration et al., 2016). The blue line is the γ-ray spectrum resulting from a power-law proton spectrum with a cutoff at 1 PeV and a spectral index of ~ 2.4. *Credit: fig. 5 in H. E. S. S. Collaboration et al., 2018a.*

Assuming that the emission is originated by proton-proton scattering, that implies the presence of a population of primary protons in the region extending up to energies close to ~ 1 PeV with a power-law (PL) spectrum with index close to ~ 2.4 due to the slowly increasing behaviour of the pp scattering cross section with energy (Patrignani et al., 2016).

The emission extends throughout the whole molecular gas complex in the GC region the *Central Molecular Zone* (fig. 3.4) which roughly extends along a disk of about 250 pc radius from the GC. More precisely, in the Galactic Ridge, defined by $|l| < 1°$, $|b| < 0.3°$ included in the CMZ [11] , the H.E.S.S. collaboration (H. E. S. S. Collaboration et al., 2018a) measured a uniform spectral index $\Gamma_{\text{HESS18}} = -2.28 \pm 0.03_{\text{stat}} \pm 0.2_{\text{syst}}$ up to 45 TeV which is compatible with that measured in the inner

---

[11] $1°$ corresponds to ~ 150 pc at the GC distance (~ 8.5 kpc).

pacman region (see fig. 6.11) suggesting that a single population of particles fills the entire CMZ. The leptonic origin of the emission is disfavoured unless the primary electrons are continuously re-accelerated throughout the whole CMZ.

Since the angular profile of the emission – peaked on HESS J1745-290 – and the steepness of the photon indexes, the H.E.S.S. collaboration proposed the central source as the possible origin of the CR population in the CMZ region. This source is positionally compatible with Sgr A* supermassive black hole. However, as suggested by the H.E.S.S. collaboration, the current data cannot provide definitive answers about the nature of this source because the point-like source HESS J1745-290 itself remains unidentified. Several plausible candidates were suggested by the H.E.S.S. collaboration to be the potential counterparts of the observed γ-ray emission. Among them there are Sgr A* (Aharonian and Neronov, 2005), pulsar wind nebula (PWN) G359.95-0.04 (Wang, Lu, and Gotthelf, 2006; Hinton and Aharonian, 2007) and annihilation of dark matter (Belikov, Zaharijas, and Silk, 2012; Acharyya et al., 2021; Abe et al., 2023).

Although the observed spectrum of HESS J1745-290 is suppressed above $\sim 10\,\mathrm{TeV}$, this might be explained by the attenuation due to $\gamma\gamma$ scattering absorption in the presence of a dense radiation field surrounding the source ((Celli, Palladino, and Vissani, 2017). The H.E.S.S. Collaboration claimed a $1/r$ radial profile of the primary CR density up to $200\,\mathrm{pc}$ as expected for a quasi-continuous injection of protons into the CMZ from a centrally located accelerator on a timescale t exceeding the characteristic time of diffusive escape of particles from the region (see Aharonian, 2004 and fig. 6.12). This interpretation promote the center of the Milky Was as the astrophysical site in which a *PeVatron* may exist, and CRs are accelerated in the vicinity of a SMBH, and continuously injected in the sorrowing environment (section 3.1.3.1 and eqs. (3.1) and (6.5)). This interpretation is also motivated noting that the knee of the CR spectrum – at $\sim 3\,\mathrm{PeV/n}$ – is thought to mark the maximal rigidity reachable by Galactic accelerators.

In fig. 6.13 the compared spectrum with H.E.S.S., MAGIC and VERITAS observations is displayed. In particular in MAGIC Collaboration et al., 2020b, the diffuse γ-ray spectrum in a region of $\sim 150\,\mathrm{pc}$ in width, favors on a $\sim 2\sigma$ level a cutoff in the γ-ray spectrum over a simple power law. The 1σ confidence level for the cutoff energy ranging from $10\,\mathrm{TeV}$ to $80\,\mathrm{TeV}$, corresponding to primary CR proton energies of $\sim 0.1 \div 1\,\mathrm{PeV}$. This finding means that the data are still marginally compatible with the *PeVatron* scenario, even if the measured spectral index, $\Gamma \sim 2$, is harder than that measured by H.E.S.S.. Moreover the deduced CR density profile is still compatible with the $1/r$ profile obtained by H.E.S.S.. On the other hand, in Adams et al., 2021, the diffuse γ-ray emission observed by VERITAS has no evidence of a cutoff, and is compatible with a pure power law with index $\Gamma = 2.19 \pm 0.20$, favoring the *PeVatron* scenario.
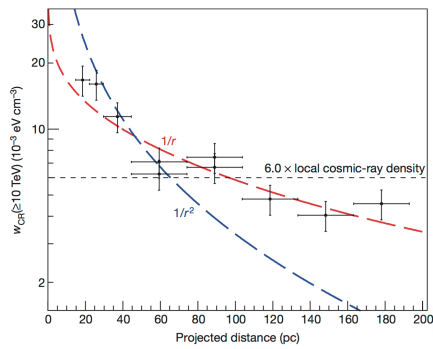
FIGURE 6.12: The best fit of a $1/r^\alpha$ profile to the data is found for $\alpha = 1.10 \pm 0.12$ (1σ). The $1/r$ radial profile is adopted by the H.E.S.S. Collaboration. *Credit: fig. 2 in HESS Collaboration et al., 2016.*
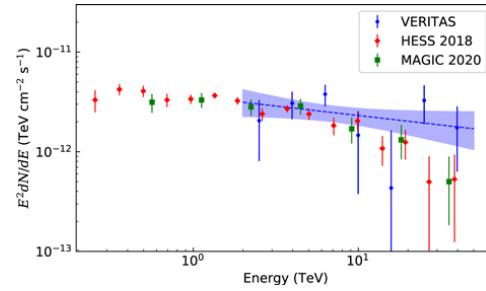
FIGURE 6.13: Differential energy spectrum from the Galactic Ridge ($|l| < 1°, |b| < 0.3°$) emission measured by VERITAS (blue; Adams et al., 2021), H.E.S.S. (red; H. E. S. S. Collaboration et al., 2018a), and MAGIC (green; MAGIC Collaboration et al., 2020b). *Credit: fig.5 in Adams et al., 2021.*

Several theoretical models try to explain how astrophysical sources may accelerate particle up to PeV energies (Berezinskii et al., 1990; Malkov and Drury, 2001). Current IACTs have not detected any *PeVatrons* because of their limited sensitivity above a few tens of TeV. Recently, LHAASO collaboration (Cao et al., 2021) has reported the detection of γ rays above 100 TeV from 12 galactic sources, including Crab nebula (Lhaaso Collaboration et al., 2021) with an event at 1.12 PeV establishing Crab as a possible *PeVatron* (fig. 3.3). In this framework, Sgr A* represents a viable *PeVatron* candidate, since the spectrum of the observed emission has no evidence of a cutoff till ~ 50 TeV. Nowadays, Sgr A* has experiencing its quiet phase, and it is unable to provide the required acceleration power to continuously accelerate CRs, but during the last $10^6 \div 0^7$ years it could have been in active phase associated with its accretion onto the SMBH may have powered strong relativistic jets able to accelerate particles up to the PeV. Recent X-ray observations suggest the violent past of Sgr A*, as evidence of the observed X-ray outbursts (Clavel et al., 2013) and an outflow from the GC (Su, Slatyer, and Finkbeiner, 2010).

The *PeVatron* interpretation results, however, strongly relies on the poorly known gas distribution in the GC region. As said earlier, the molecular gas distribution is inferred from the radio lines emission of tracers (*i.e.* CO, CS, HCN, NH$_3$) integrated along the line-of-sight. The distance is derived on the basis of the Doppler shift of the emission lines, and on a dynamical model of the gas motion (rotation curves), giving rise to strong systematics and uncertainties on the 3D position of clouds. Moreover the CMZ is filled by dense molecular clouds that may partially absorb the lines emission, and then underestimate the proper gas density. As a consequence, it is difficult to firmly establish if the peaked γ-ray emission observed by H.E.S.S., MAGIC and VERITAS from the GC is due to a gas distribution more peaked than expected or to a CR distribution increasing towards the GC. The further estimated $1/r$ profile is itself strongly dependent on the poorly known 3D distribution of molecular clouds, and

then on their real distance from the center.

An alternative explanation of the H.E.S.S. observations was proposed in Gaggero et al., 2017a; Ventura, 2018, in which the bulk of the Galactic Ridge emission could be originated by the diffuse steady-state Galactic CR-*sea*[12], which is able to naturally reproduce the γ-ray diffuse emission spectrum in the Galactic Ridge. Under this assumption the required spectral index of the diffuse γ-ray emission has to be significantly harder than the local one. The *gamma model* (section 6.1.1) satisfies the requirement of the spectral index hardening approaching the GC, and its parameterization is justified by recent results of the *Fermi* collaboration (fig. 6.3). Indeed, the measured γ-ray diffuse emission in the range $0.1 \div 100$ GeV is not properly reproduced by conventional model, as *base model* or the GALPROP outcome, stressing the presence of an *excess* at higher energies (Ackermann et al., 2012a; Acero et al., 2016). On the other hand, the scenario proposed with *gamma model* (Gaggero et al., 2015a; Gaggero et al., 2015b; Gaggero et al., 2017a; Ventura, 2018) predicts a CR proton spectral index $\Gamma_{CR}(r \sim 0) = \Gamma_{CR}(r_\odot) - a r_\odot$. As a consequence, since $\Gamma_{CR}(r_\odot) \sim 2.7$ above ~ 300 GeV, this implies $\Gamma_{CR}(r \sim 0) \sim 2.4$, independently on the (poorly known) value of δ measured at the Earth position. Moreover, independent analysis of *Fermi*-LAT data performed in Gaggero et al., 2017a; Ventura, 2018, have shown the agreement with the H.E.S.S. observation and *Fermi*-LAT data at lower energies, the energies where *gamma model* is validated against *Fermi*-LAT data on larger galactic scales.

Discovering the nature of *PeVatrons* in our Galaxy is thus of particular interest because it is linked with the understanding the origins of galactic CRs. In this framework the detected spectra and morphologies of the astrophysical sources, and their variability could constrains models of VHE γ-ray emission. Indeed, correlated variability in different wave bands would suggest a common origin of the emissions, while variability timescales could constrain the nature of the acceleration mechanism (Ballantyne, Schumann, and Ford, 2011) or the size of the emission region. Nowadays no variability has been detected in the TeV emission from the direction of Sgr A* (Aharonian et al., 2009; Ahnen et al., 2017b; Adams et al., 2021), suggesting a differing origin of the VHE γ-ray emission with respect to the variable IR and X-ray observed emission (Wang, Lu, and Gotthelf, 2006). As said earlier, *Fermi*-LAT detected a 3 GeV *excess* from the GC (Ackermann et al., 2017), and among the proposed explanations there are an unresolved point source population (Macias et al., 2018; Buschmann et al., 2020) , annihilation of dark matter particles (Leane and Slatyer, 2019) , or it is associated with the large scale CR component.

---

[12]The CR-*sea* is defined as the large scale CR population due to the bulk of CR accelerators present in the whole Galaxy after diffusing in the turbulent galactic magnetic field (sections 2.1 and 3.1.4).

Several attempts try to explain the observed *excess* **at HE and VHE γ rays with a local component, while in this work the observed emission could be naturally explained in terms of the large scale background (CR-*sea*) emission which gets harder approaching the GC.** Even if this interpretations relies on several uncertainties, mainly related with the poorly known gas distribution in the inner Galaxy, the evidence of a radial dependence of the diffusion coefficient is becoming widely accepted by the astroparticle community. The requirement of a realistic description of the γ-ray background model, especially at GeV and TeV energies is crucial, because above its permeating flux astrophysical sources could be detected and analyzed. The complexity of the analysis of galactic sources in current γ-ray detectors' analysis chain, requires the use of a background model supported by catalogs of known sources in order to perform a likelihood 3D analysis returning the spectral (and eventual morphological) parameters of the source under investigation. In this context, it is crucial to adopt proper background models which cannot over/under estimate the contribution of the observed γ-ray emission, by H.E.S.S. (HESS Collaboration et al., 2016; H. E. S. S. Collaboration et al., 2018a), by MAGIC (MAGIC Collaboration et al., 2020b), by VERITAS (Adams et al., 2021), and recently also at higher energies by HAWC (Abeysekara et al., 2021), by Tibet AS-γ (Amenomori et al., 2021a) and by LHAASO (Cao et al., 2021).

6.2   Untangling the complexity in the Galactic Center region

This section is devoted to the description of the impact of background models in the analysis of γ-ray data. Two main region of the inner Galaxy are considered, HESS J1741-302 and the Central Molecular Zone. The HE γ-ray data have been estimated with an *ad-hoc* analysis of *Fermi*-LAT observations, while the VHE data come from the major currently operating IACTs, H.E.S.S., MAGIC and VERITAS.

Four models reproducing the γ-ray diffuse emission have been scrutinized against γ-ray observations in the CMZ. The models accounts for the same parameterization of nuclear cross-section, ISRF and gas distribution map (section 6.1.1). On the other hand, the parametrization differs in the choice of the radial dependence of the diffusion coefficient, and the inclusion of the *hardening* at 250 GeV/n, as measured by PAMELA (Adriani et al., 2011), AMS-02 (Aguilar et al., 2015) and CREAM (Ahn et al., 2010). The first is *gamma model*, which is widely described in section 6.1.1 (type B). In the second, the background model is set without the additional hardening at 250 GeV/n, and it is called *gamma model without hardening*. The third model is *base model*, described in section 6.1.1 (type A). While the last representation is the *conventional* description of the CR diffusion, without the additional hardening at 250 GeV/n.

The inner ring of the Galaxy, is modelled with the analytical description reported in section 6.1.2, while the remain rings are considered the same used in GALPROP. Since the observations of the inner ring of our Galaxy are affected by large uncertainties and systematics, the present parametrization represents an extension at the GC position of the trend tuned on local data, and an extrapolation at higher energies.

In fig. 6.14 are displayed four views of the expected emission from the CMZ at 10 GeV, coincident with the Galactic Ridge fig. 3.4. Starting from the top left, *Gamma Model*, *Gamma Model without hardening*, *Base Model*, and *Conventional* diffusion.
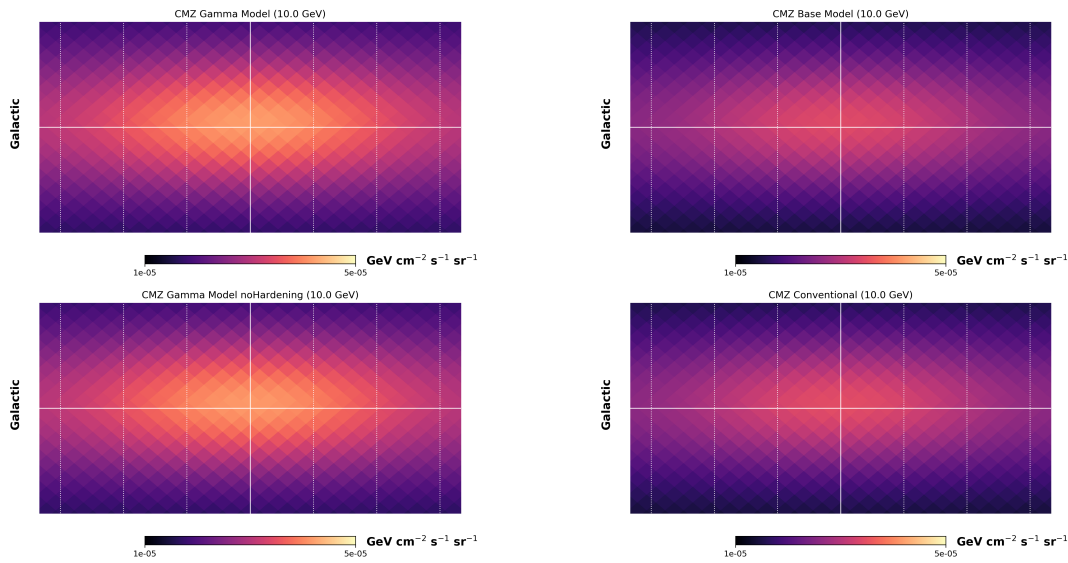
FIGURE 6.14: View of the γ-ray expected emission as outcome of *Gamma Model*, *Gamma Model without hardening*, *Base Model* and *Conventional* diffusion. The representations are obtained at 10 GeV, and in a region corresponding to the Galactic Ridge ($|l| < 1°$, $|b| < 0.3°$; fig. 3.4). *Credit: fig.1 in Ventura, 2022*.

The four models have been compared with the observed data by currently operating gamma-ray observatories. In particular, a detailed analysis of $\sim$ 10 years of PASS8 (Bruel et al., 2018) *Fermi*-LAT data extracted with FERMI SCIENCE TOOLS v11R5P3[13], and performed with the last version of IRFs (P8R3_CLEAN_V2), recommended quality cuts (DATA_QUAL==1) && (LAT_CONFIG==1) event class 256 for extended sources analysis, isotropic background (iso_P8R3_CLEAN_V2), and 4FGL catalog (Abdollahi et al., 2020a). The *Fermi*-LAT analysis has been performed with codes developed on purpose for this work by the author. The codes compute *all*-sky maps in HEALPIX projection method (Górski et al., 2005) of the complete dataset returning a counts-map, the exposure map, and the source map (accounting of all source models listed in the 4FGL caatalog). A detailed description of the procedure is reported in Ventura, 2018, chapter 4.

---

[13]FermiTool.

In fig. 6.15 *top* is displayed the energy spectrum from 1 GeV to more than 50 TeV of the γ-ray emission observed in the inner part of the CMZ, the *Galactic Ridge*, as defined in H. E. S. S. Collaboration et al., 2018a, and corresponding to $|l| < 1°$, $|b| < 0.3°$ in extension. The *Fermi*-LAT data has been compared with H.E.S.S. (H. E. S. S. Collaboration et al., 2018a), MAGIC (MAGIC Collaboration et al., 2020b) and VERITAS (Adams et al., 2021) measurements. The expected diffuse γ-ray emission of the four phenomenological models described above is also displayed. It is useful to note that at the *Fermi*-LAT energies all the models can reproduce the observed *excess* in the Galactic Ridge, while at higher energies – essentially at that energies reachable by IACTs – the four energy spectra reproduce a different behaviour of the modelled γ-ray diffuse emission. In particular the measured emission is reproduced by the *Gamma Model*, but not properly by the other three models.

In fig. 6.15 *bottom*, the measured *Fermi*-LAT and H.E.S.S. data are compared with the expected γ-ray emission computed with *Gamma Model*. The blue band represents the uncertainty in the normalization of the spectrum of the diffuse emission. Indeed in Ferrière, Gillard, and Jean, 2007, for estimating the gas mass of the inner ring of Our Galaxy, has been considered the so-called X_{CO} factor (Dickman, 1975) equals to $\sim (2 \div 4) \times 10^{19}$ cm^{-2}K^{-1}km^{-1}s with an uncertainty of order 2. This causes a corresponding uncertainty in the prediction of the model used to compute the expected γ-ray emission from the region, stressing the diffuse model dependence on the poorly known gas distribution in the GC region.

For performing the *Fermi*-LAT analysis two HEALPIX maps with flux informations have been subtracted: the first is the total counts map with all type of events, and the second is the source maps with predicted counts computed with spectral and morphological parameters listed in the catalog and obtained with the diffuse model used by the collaboration (`gll_iem_v06`). Several point-like sources are present in the region that have to be subtracted from the total emission (counts map) of the region under investigation, in this case the inner CMZ. In the work presented in Ventura, Grasso, and Marinelli, 2019, has been used the *Fermi*-LAT 8 Years (FL8Y) list of sources[14] which contains 8 sources in the region under investigation. The catalog was built assuming the same diffuse model of 4FGL– that is the performed version of FL8Y – `gll_iem_v06` described in Acero et al., 2016. The FL8Y source list is based on the first 8 years of science data of *Fermi*-LAT reconstructed with the PASS8 algorithm.

On the top of fig. 6.16 the H.E.S.S. and *Fermi*-LAT data points are in good agreement between the two datasets which overlap at few hundred GeV and can actually be fitted with a single power law with index $\Gamma_{GR} = -2.36 \pm 0.03$. In the same plot is displayed the predictions of the *gamma model* with and without (dashed line) the contribution of the CMZ (inner ring) in order to obtain the *foreground* emission. In this

---

[14]FL8Y catalog.
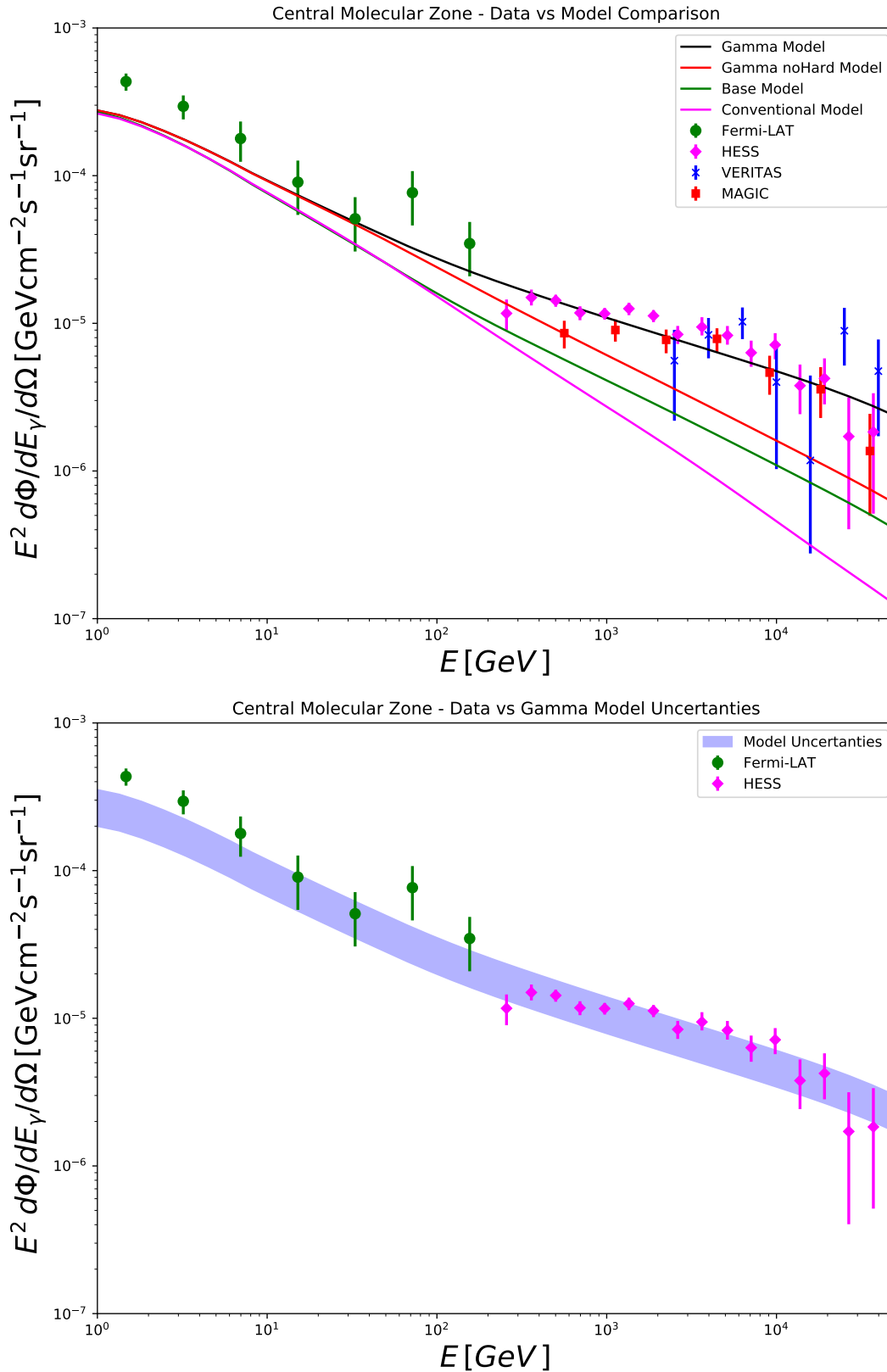
FIGURE 6.15: *Top*: Compared energy spectra of γ-ray diffuse emission from the Galactic Ridge with *Fermi*-LAT, H.E.S.S. (H. E. S. S. Collaboration et al., 2018a), MAGIC (MAGIC Collaboration et al., 2020b) and VERITAS (Adams et al., 2021) data. *Bottom*: *Gamma Model* energy spectrum compared with *Fermi*-LAT and H.E.S.S. data in the Galactic Ridge region. The blue band represents the systematic error due to the uncertainty in the estimation of the $X_{\rm CO}$ factor at the GC position. *Credit: fig. 2 in Ventura, 2022.*
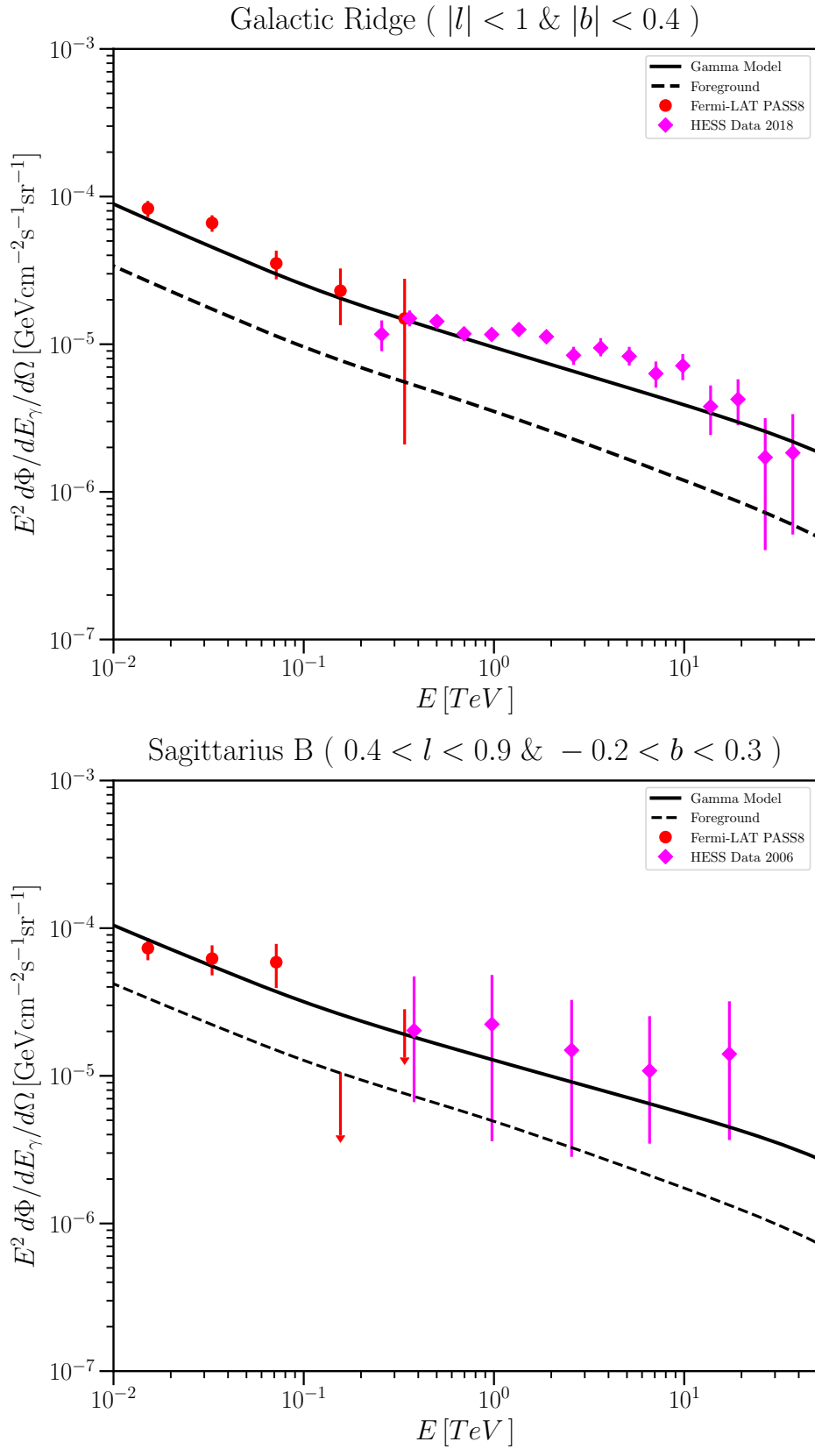
FIGURE 6.16: *Top:* the diffuse emission spectrum of the Galactic ridge region with H.E.S.S. data (H. E. S. S. Collaboration et al., 2018a). *Bottom:* the dissuse spectrum is computed for Sgr B region (Yang, Jones, and Aharonian, 2015). *Fermi*-LAT spectral points represent the *excess* counts derived in that analysis using 10 years of PASS8 data and subtracting the expected counts of point-like sources in the FL8Y source list. The solid lines represent the total diffuse emission spectrum computed with the *gamma model* accounting for the contribution of the diffuse background computed on the basis of the same model (dashed line). *Credit: fig.2 in Ventura, Grasso, and Marinelli, 2019.*

case, the *foreground* emission underestimates the combined *Fermi*-LAT and H.E.S.S. data, which are on the contrary better reproduced by the combined effect of the *foreground* emission in addition to the expected flux computed only in the inner ring, corresponding to the CMZ. In the same region of interest, other diffuse backgrounds, such as isotropic extragalactic emission and *Fermi* bubble have been considered subdominant. Moreover, it has been checked that the *gamma model* background is basically coincident with the high-energy extrapolation of the `gll_iem_v06` diffuse model used to compute the point and extended sources' models listed in FL8Y, used to build the HEALPIX source map.

A sub-region at the rim of the CMZ, approximatively centered on the Sgr B complex has also been observed by the H.E.S.S. telescopes Yang, Jones, and Aharonian, 2015, and *on the bottom* of fig. 6.16 is displayed the H.E.S.S. and *Fermi*-LAT data comparison, and the *gamma model* outcome for Sgr B. Even in this case *gamma model* provides a good description of the data.

The relevance to compare HE *Fermi*-LAT data with VHE data is to stress that even at higher energies the contribution of the CR-*sea* is crucial. Indeed, at few GeVs the *gamma model* predicts the same emission of conventional diffusion, which assumes a uniform CR spectrum in the whole Galaxy, and it provides a safe evidence that at those energies the emission is dominated by the CR-*sea*. Therefore, the absence of a pronounced feature at higher energies is a further evidence against the presence of a new component in the CR population in that region.

6.3 An *hidden* accelerator in the GC region? HESS J1741-302

The intriguing scenario represented by the γ-ray *excess* in the Galactic Center region has motivated several theoretical efforts, invoking a broad variety of physical processes, to explain the observed emission. In this context, the search of regions farther from the inner CMZ showing hard spectral index close to ~ 2.4 assumes a key role. Indeed, as long as inner regions are used to test both the *PeVatron* and diffuse scenarios, a definitive explanation could be not achieved. Due to the largest uncertainties on the gas density distribution in the central Galaxy both the *PeVatron* and *gamma diffuse* scenarios can reproduce the observed data (figs. 6.12, 6.15 and 6.16). As shown in Ventura, 2018, the luminosity profile associated with the Galactic Ridge region, is peaked in the central region corresponding to the so-called *pacman* region (fig. 3.4 top; HESS Collaboration et al., 2016). This luminosity profile is not properly reproduced by the *gamma model* itself, that on the contrary provides a flat profile in the *pacman* region. This finding seems to support the evidence that in the vicinity of Sgr A* the contribution of a local source is required to explain the VHE γ-ray observations. On the other hand, moving away from the center and approaching the edge of the CMZ, the contribution of the *large-scale background* emission featured by

the *hardening* (section 6.1.1) could properly reproduce the data, and at some extent, becomes dominant (fig. 6.17).
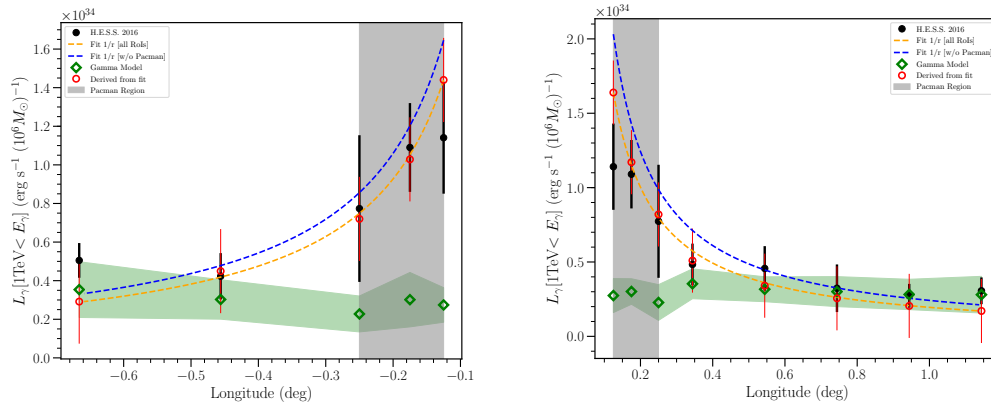
FIGURE 6.17: Luminosity profile computed considering the 8 regions at positive longitudes from GC *on the right*, while in *on the left* is shown the luminosity profile for 5 RoIs at negative longitudes. Two *fits* are reported as follow: the yellow-dashed line is obtained considering all the RoIs, while the blue-dashed line considering only the five circular region (excluding the first 3 points of *pacman on the right*). *On the left* is reported the same approach. A representation of the RoIs is shown in fig. 3.4. The red dots represent the luminosities derived from the fits parameters. The green shaded area represents the 1σ errors. *Credit: fig. 5.7 in Ventura, 2018*.

One of the farther region from Sgr A* considered in this work is HESS J1741-302 discovered by the H.E.S.S. telescopes (H. E. S. S. Collaboration et al., 2018c) during its galactic plane survey (fig. 3.2; H. E. S. S. Collaboration et al., 2018d), and laying on the GP at an angular distance $l = -1.7°$ from the GC (R.A. $17^h41^m15.4^s$, Dec. $-30°22'37.4''$). The observed spectrum extends from 0.1 to 10 TeV following a single-power law with index $\Gamma_{J1741\text{-}302} = -2.3 \pm 0.2_{stat} \pm 0.2_{sys}$ with no evidence of a cutoff (fig. 6.18).

No clear astrophysical counterparts have been identified for that source. Among several plausible origins of its emission, the H.E.S.S. collaboration proposed a massive molecular cloud (cloud 8), at a distance of 260 ± 40 pc from the GC, as one of the most plausible counterpart. The mass of that cloud – derived from the CO line emission – was estimated to be 6.8×10^4 $M_\odot$. Two main scenarios have been suggested by the H.E.S.S. collaboration to explain the observed emission in which the parental particle population, responsible for such emission, extends up to tens of TeVs in a *leptonic* scenario, or hundreds of TeVs in an *hadronic* interpretation. In the first scenario the emission is explained by the interaction of accelerated electrons coming from a nowadays unresolved source, with energies of hundreds of TeV, undergoing IC scattering off CMB or ambient radiation fields. This field could be associated with a relic PWN, the source PSR B1737-30, or binary scenario associated with the
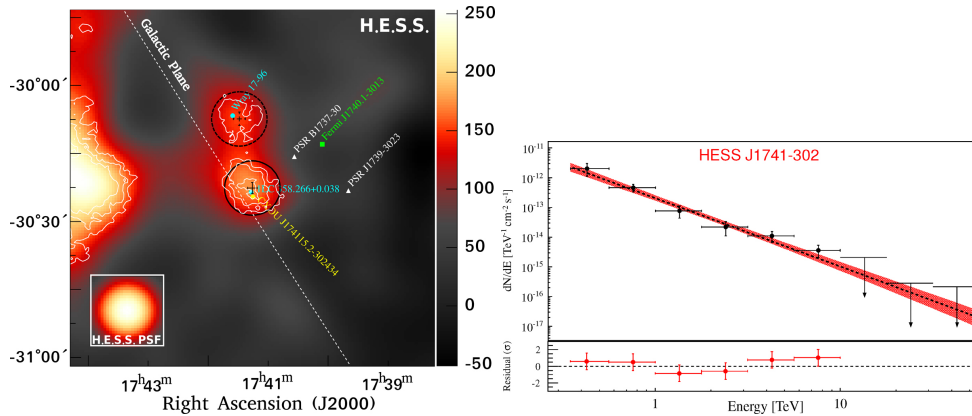
FIGURE 6.18: *On the left*: γ-ray excess map of the region around HESS J1741-302. The black circle shows the source region used for extracting the spectrum, while the black cross indicates the value and 1σ error interval of the best fit position of the source. The white dashed line indicates the orientation of the Galactic plane. *On the right*: VHE γ-ray spectrum of HESS J1741-302. The black dots show the flux points, while the red shaded region represents the 68% confidence interval for the fitted spectral model. The dashed black line shows the best fit power-law function. *Credit: fig.1 and fig.2 in H. E. S. S. Collaboration et al., 2018c.*

compact radio source 1LC 358.266+00.038. However, the absence of a detected HE γ-ray counterpart, X-ray emission from PWN and variability, combined with the point-like nature of the source[15] disfavor the leptonic scenario. On the other hand in the hadronic scenario, the observed emission arises from the interactions of CRs with the dense molecular cloud filling the region. This represents the most plausible astrophysical source associated with HESS J1741-302.

At the present observation state, HESS J1741-302 could be an *active* or *passive* astrophysical source. In the first case, at that position of the sky an *hidden* accelerator is covert, which locally accelerates particles interacting with the cloud responsible for the VHE emission. On the other hand, in the *passive* case, the massive cloud is lightened by the *large-scale background* component represented by the CR-*sea*, in which the whole galactic CR population confined within the Galaxy is responsible for the observed flux. The last interpretation is considerable under the assumption of *harder* diffusion approaching the GC. Indeed, the presence of such cloud is of crucial interest since represents a natural target to probe *how* and *if* the galactic CR population properties change with the galoctocentric distance R.

As previously done for the Galactic Ridge and Sgr B analysis (figs. 6.15 and 6.16) H.E.S.S. and *Fermi*-LAT data have been compared in order to extend the measured emission spectrum to lower energies. A circular region of radius 0.1° centered on the source position has been considered to estimate the *Fermi*-LAT γ-ray emission and

---

[15]The size of the source is 0.1° that is compatible with H.E.S.S. PSF.

the outcome of *gamma model*. Even in this case, the *Fermi*-LAT analysis has been computed with the same approach described above, and considering the sources listed in the FL8Y catalog. As displayed in fig. 6.19, the measured spectrum by H.E.S.S. extends steadily down to few GeVs bridging with *Fermi*-LAT data. The spectral index resulting from the *best-fit* of *Fermi*-LAT and H.E.S.S. data is $\Gamma_{J1741\text{-}302} = -2.24 \pm 0.08$ which is in agreement with the *gamma model* prediction in the inner galaxy (fig. 6.3). The data have also been compared with the predicted emission from both *PeVatron* and *gamma model*. Even in this case, the *gamma model* prediction matches the observed spectrum remarkably well. On the other hand, the predicted flux under the *PeVatron* hypothesis under-estimate the observed flux and it is compatible with the expected *foreground* as output of *gamma model* (fig. 6.19 *dashed blue line*).
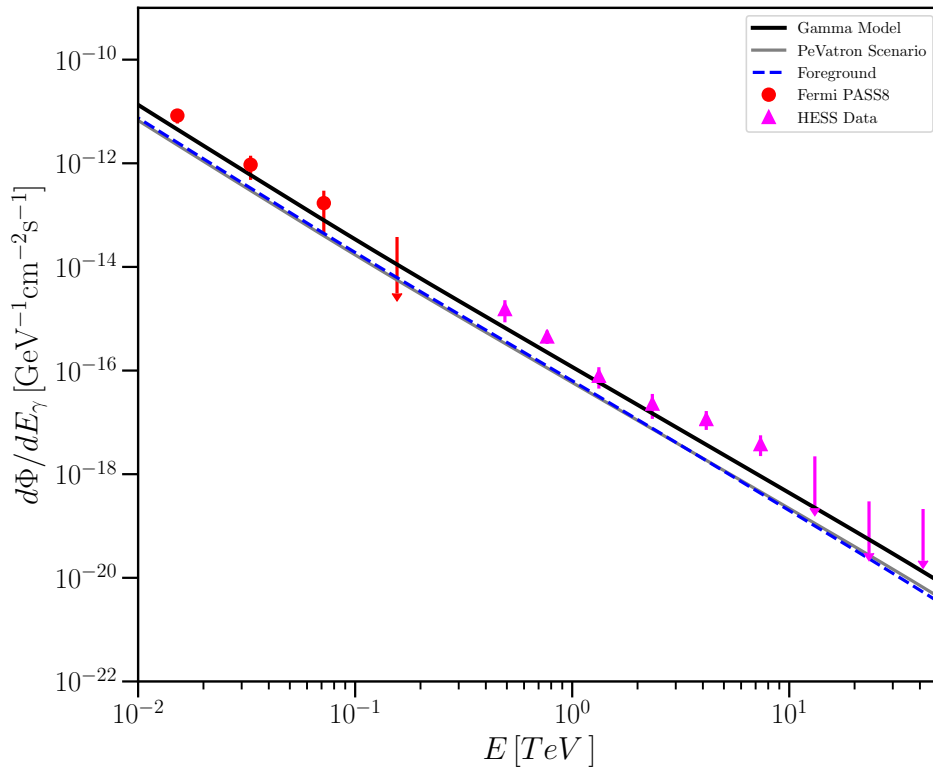
FIGURE 6.19: Comparison of H.E.S.S. data (H. E. S. S. Collaboration et al., 2018c) and *Fermi*-LAT *excess counts* from a circular region of angular radius $0.1°$ centered on the position of HESS J1741-302. The solid line is the prediction of the *gamma model* under the hypothesis of CR *large-scale background* interactions with the cloud 8 (at $R = 260 \, \text{pc}$), identified in H. E. S. S. Collaboration et al., 2018c. The grey line represents the prediction of CR interactions in the *PeVatron model* derived extrapolating the CR density profile reported in HESS Collaboration et al., 2016 to the position of cloud 8. The dashed blue line epresents the expected emission from the foreground emission as predicted by *gamma modelCredit: fig.2 in Ventura, Grasso, and Marinelli, 2019*.

For computing the γ-ray flux associated with the CR density at the HESS J1741-302 position, it has been used the eq. 1 in HESS Collaboration et al., 2016

$$F_\gamma(\geq E_\gamma) \approx 4.6 \times 10^{-10} \left(\frac{M_5}{d_{\mathrm{kpc}}^2} \right) w_{\mathrm{CR}}(\geq 10 E_\gamma) \ \mathrm{erg} \ [\mathrm{cm}^{-2} \ \mathrm{s}^{-1}] \qquad (6.5)$$

where M_5 is the cloud mass in units of $10^5 \ M_\odot$, d_{kpc} the distance in unit of kpc. Applying eq. (6.5) to cloud 8, where $M_5/d_{\mathrm{kpc}}^2 = 0.0094$, and the CR density from *gamma model* $w_{\mathrm{CR}}(\geq 4 \ TeV) \simeq 0.1$ eV/cm^{-3}, as the result $F_\gamma(\geq 0.4 \ TeV) \simeq 5 \times 10^{-13}$ erg cm^{-2}s^{-1}. This finding is very close to the measured flux by the H.E.S.S. collaboration (1.2×10^{-12} erg cm^{-2} s^{-1}), and accounting for a comparable background contribution (fig. 6.19) Moreover, for comparing the *gamma model* predictions with the *PeVatron* outcome, it has been used the CR profile in fig. 6.12 (HESS Collaboration et al., 2016) obtaining a w_{CR} value less than half the value predicted by the *gamma model* at the position of cloud 8 implying an emission significantly lower than the observed one.

The obtained results seem to support the *passive* scenario, in which the cloud is not illuminated by a *PeVatron* at the GC position, 200 pc far away from cloud 8, but rather by the galactic CR population featured by *hard inhomogeneous* diffusion.

6.3.1 Simulation Template and Analysis

As said earlier, the currently available informations on HESS J1741-302 are inadequate for converging to a definitive explanation. At some extent, under the *hadronic* interpretation of the observed emission, both the local source and the galactic CR-*sea* could reproduce the observations. In order to converge for a definitive classification of HESS J1741-302, some simulation in view of the next generation Cherenkov Telescope Array (CTA; section 4.3.2) have been implemented. This section is devoted to explain the simulation template used to compute the energy spectrum associated with HESS J1741-302.

The high-level analysis of CTA is performed similarly to that adopted by the *Fermi*-LAT collaboration, and relies on 3D likelihood analysis, in which fundamental ingredients are the *diffuse background model* and the spectral and morphological parameterization of the sources listed in the catalog. In this work two main background model have been used

  a the first is *gamma model* described in section 6.1.1 (type B)

  b the second is a combination of *gamma model*, for the predicted emission from ring 2 (1.5 kpc) to the last one (ring 9), and the *PeVatron* template in the ring 0 associated with the CMZ. This template has been analytically computed convolving the $1/r$ profile in fig. 6.12 with the CTA IRF and the gas distribution map derived by CS molecular line emission, as used in HESS Collaboration

et al., 2016. The ring 1 has not been considered since HESS J1741-302 is located within the region accounted in the ring.

The aim of this approach is to perform the 3D analysis of HESS J1741-302 applying two different background model in order to understand if there are differences in the simulated energy spectra, and if CTA will be capable to detect the source and disentangle among different scenarios.

A box of $15° \times 6°$, centered on HESS J1741-302 position, has been simulated for a total exposure time of 10 h, in the energy range $0.03 \div 100$ TeV, with CTOOLS, and for comparison with GAMMAPY v.1.0(section 4.3.2), using the CTA IRFs `Prod3bv2` [16] , in the case of CTOOLS, and `Prod5 v0.1` [17], in the case of GAMMAPY, relative to the CTA Observatory South (50 h). All the sources listed in the DC I[18] and positionally included in the box are considered, excluding the dark matter candidate and the low latitude *FermiBubble*. The source under investigation, HESS J1741-302, has been modelled as an extend source with a radial gaussian profile, and a simple power-law spectral model, with the parameters listed in H. E. S. S. Collaboration et al., 2018c. In table 6.1 are tabulated the major parameters of the simulation template.

TABLE 6.1: Morphological and spectral parameters used for modelling HESS J1741-302.

RA (°)	DEC (°)	σ (°)	N_0 (TeV^{-1} cm^{-2} s^{-1})	E_0 (TeV)	Γ
265.310	-30.377	0.068	2.1×10^{-13}	1	-2.3

With CTOOLS to simulate the events the class to use is `ctobssim`, and `ctselect` for selecting the events in the desired energy range. `ctskymap` to compute the skymap, and `ctlike` to perform the likelihood analysis. For computing the residual map is used `ctremap`, and for obtaining the spectrum `ctbutterfly`.

On the other hand, with GAMMAPY the classes to use are `MapDatasetEventSampler` to simulate the events or `Dataset.fake()`. `Map.from_geom`, `fill_events` and `sum_over_axes` for creating the skymap.

`Fit(optimize_opts={"print_level": 1})` to perform the likelihood analysis, and `plot_residuals_spatial` to display the residuals map. `FluxProfileEstimator` to compute the flux profile, and `FluxPointsEstimator` to obtain the flux points and then the spectrum. It is also possible to perform the source detection and the significance map with the class `TSMapEstimator`, and the method

`find_peaks(maps["sqrt_ts"], threshold=5, min_distance="0.25 deg")`.

---

[16] Prod3bv2 webpage.
[17] Prod5 v0.1 webpage.
[18] First Data Challenge webpage.
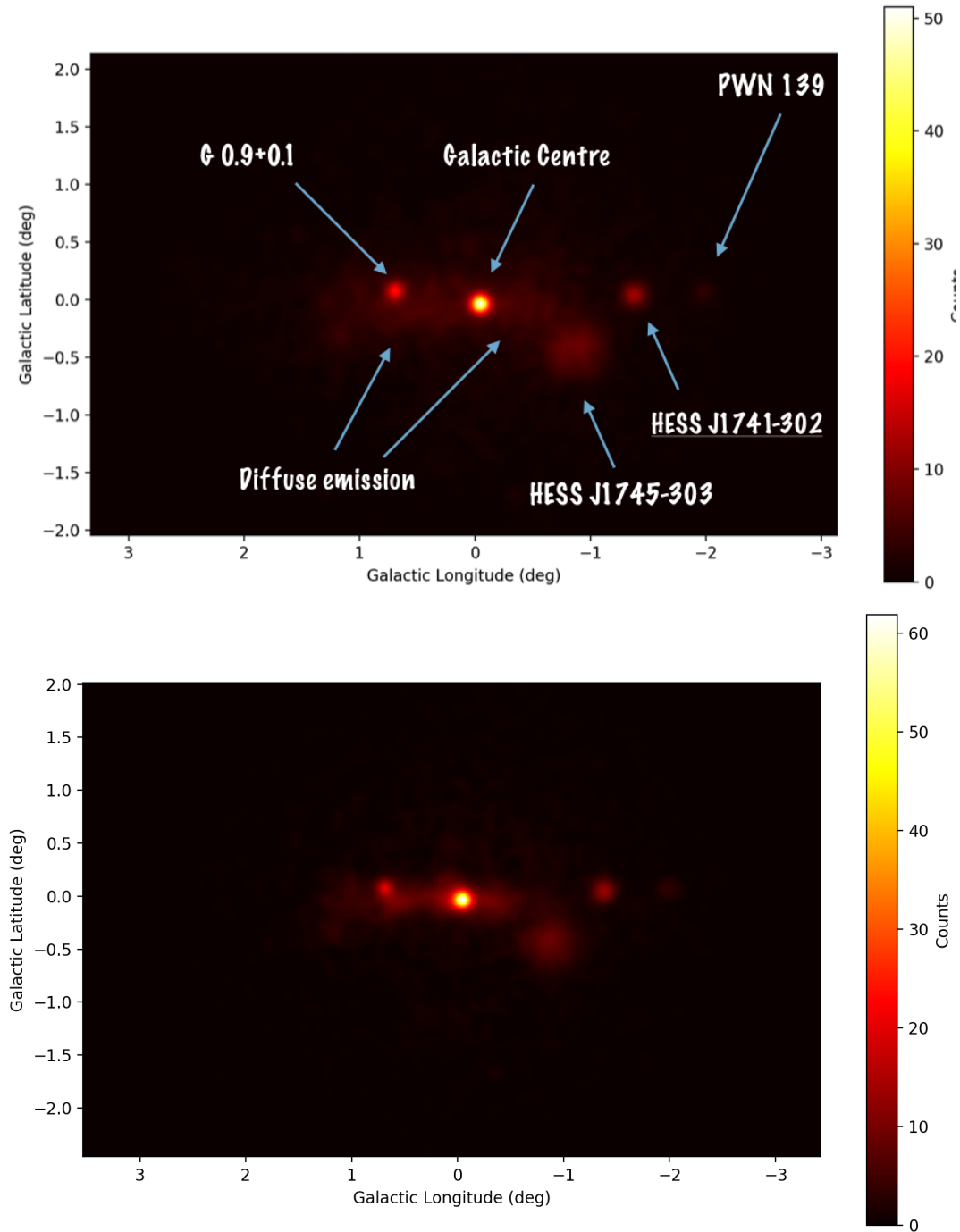
FIGURE 6.20: Skymap of the setup a (*top*) and of the setup b (*bottom*).

Two different setups have been used for simulating the γ-ray emission from the selected box, one for each background model defined above (a, b)

1. in the first setup has been considered HESS J1741-302 and all the sources listed in the DC I within the simulated box area. Dark matter candidates a *FermiBubble* have not been included. For accounting the background model has been used the (a) definition, *gamma model*

2. the second setup shares with the first all the conditions, except for the background model, that is le (b) definition, *gamma model* as foreground + *PeVatron* in the CMZ.

Once the event maps (fig. 6.20) are computed the 3D likelihood analysis can be performed. The first setup has been divided in 10 energy bins in the range $0.03 \div 100$ TeV into a FoV of $10°$ ($1 \, \mathrm{bin} = 0.02° \times 0.02°$), while the second setup has been binned in 30 equally spaced energy bins. The fit procedure has been performed iteratively, starting from the 3 brighter sources HESS J1741-302, GC and G0.9+0.1, till the last iteration including 8 sources, when the residuals have been considered acceptable (fig. 6.21). At each step, the spatial and spectral residuals have been checked, and in case the residuals were no flat, one other source component was added. In the fitting procedure the spatial coordinates of the sources, excluded HESS J1741-302, have been fixed, as well as the spectral normalization.
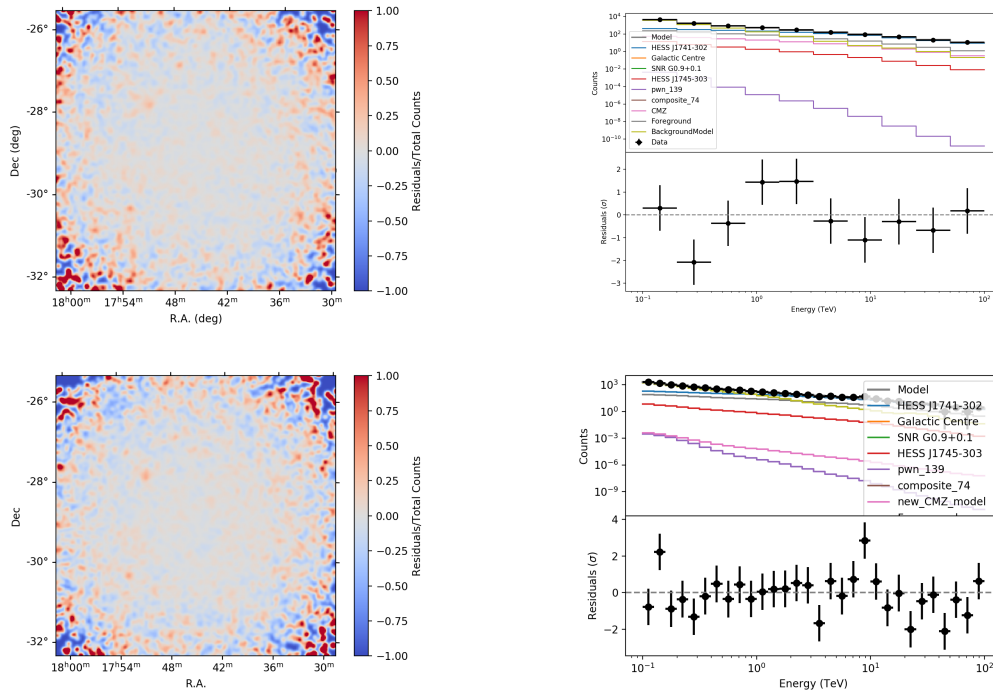
FIGURE 6.21: *On the top left & right*: spatial and spectral residuals of the setup a. *On the bottom left & right*: spatial and spectral residuals of the setup b. In both cases, the fitting procedure ended after 5 iteration and a total of 8 sources and 22 parameters fitted.

The results of the likelihood analysis are tabulated in tables 6.2 and 6.3.

TABLE 6.2: Likelihood analysis of HESS J1741-302, spatial parameters.

	TS	RA (°)	DEC (°)	σ (°)
First setup	2606.81	265.3111 ± 0.0034	-30.3785 ± 0.0030	0.0686 ± 0.0021
Second setup	3140.84	65.305 ± 0.003	-30.374 ± 0.003	0.0686 ± 0.0021

TABLE 6.3: Likelihood analysis of HESS J1741-302, spectral parameters.

	N_0 (TeV^{-1} cm^{-2} s^{-1})	Γ
First setup	$(1.930 \pm 0.066) \times 10^{-13}$	-2.252 ± 0.023
Second setup	$(2.136 \pm 0.067) \times 10^{-13}$	-2.345 ± 0.021
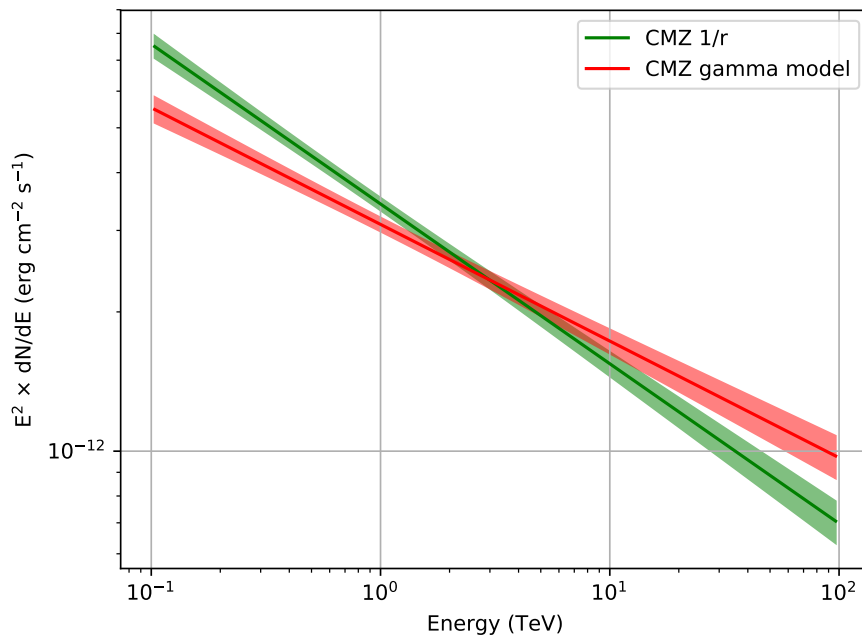
FIGURE 6.22: The red spectrum is computed considering the CMZ ring as "illuminated" by the inhomogeneous CR-*sea*. The green spectrum is obtained considering the central ring as "illuminated" by the central *PeVatron* described in HESS Collaboration et al., 2016.

In fig. 6.22 the *butterfly* plot with the HESS J1741-302 spectra computed with the two setups is displayed. In green is represented the HESS J1741-302 spectrum as the result of the simulation obtained considering the CMZ illuminated by the central

PeVatron, as supported in HESS Collaboration et al., 2016. While the red spectrum is obtained considering the CMZ illuminated by the galactic CR population (the CR-*sea*) as predicted by *gamma model*.

As suggested by the same figure, the difference between the two spectra in both normalization and spectral index, are evident and separated over the instrumental precision, making of CTA a plausible *PeVatron* discriminator.

6.4   An *hidden* population in the GC region?

As said earlier, nowadays a definitive explanation on the nature of diffuse γ-ray emission observed in the GC region by H.E.S.S., MAGIC and VERITAS, has not been achieved yet. Several sources of uncertainties surrounding the tested approaches developed to explain the observations. At the first place the difficulty to properly estimate the gas density in the inner Galaxy, and its dynamical distribution in compact and dense clumps. That because the GC is a complex region to study at each wavelength since it is obscured along the line-of-site from the foreground emission. Another crucial difficulty is the detection of sources, especially CR accelerators that are enveloped in the region. As already mentioned, the source model adopted in this work to compute the CR spatial profile (fig. 6.2), provides an extrapolation at the GC position of the SNR profile observed in the outer Galaxy, and vanishes at the GC position. However, an exceptional supernova rate is expected to fill the inner Galaxy, and then improve the number of potential CR accelerators.

The central SMBH Sgr A* is extremely inactive at present date, and the GC region is often compared with the one of starbust galaxies, in which massive star formation occurs, many SNRs are visible in radio and X-ray (Ponti et al., 2015), and PWNe are also numerous in the complex GC region (Muno et al., 2008; Johnson, Dong, and Wang, 2009). An exceptional SN rate is then expected featuring the inner Galaxy, and in Jouvin, Lemière, and Terrier, 2017, the central 300 pc have been modelled assuming three different and realistic 3D spatial distributions. The first region is assumed as a uniform cylinder region centred at the Sgr A* position(with an estimated $SN_{rate} = 6.4 \cdot 10^{-4}$ yr^{-1}. The second one is associated with the *central disc*, corresponding to the accretion disk around Sgr A*, and modelled with a spherical shape with the center at the Sgr A* position. The estimated rate is $SN_{rate} = 4 \cdot 10^{-5}$ yr^{-1}. The last region is compatible with the *Quintuplet cluster*, and it is shaped as a uniform sphere centered at R.A. $17^h46^m13.9^s$, $Dec-28°49'48''$ with an associated rate of $SN_{rate} = 4 \cdot 10^{-5}$ yr^{-1}. Finally, at ~ 30 pc from Sgr A* is located the *Arches cluster*, with a mass of $\sim 10^4$ M$_\odot$, ~ 2.5 Myr, in which young massive stars live and fill the region with their strong winds able to accelerate CRs even at higher energies. This region is although too young to experience SN explosions, leading to model the region with a radial disk spatial shape with radius $r = 0.13°$, and the spectral

model derived by the *stellar wind bubble model* of Morlino et al., 2021, parametrized as a power-law with exponetial cutoff.

The 3D spatial distribution described above has been used by Jouvin, Lemière, and Terrier, 2017, to compute the γ-ray emission due to CRs accelerated by SNRs residing in inner parsecs of the Galaxy, associated with a starburst effect, and interacting with the dense molecular clouds in the region (Macias and Gordon, 2014). All the SNRs have been considered as core collapse since around $2/3$ of the massive stars detected in the inner Galaxy are located inside of these three massive starburst clusters suggesting the existence of isolated high-mass star formation (Mauerhan et al., 2010); thus no type Ia SNs are considered (for major details on the SN classification see section 3.1.1), also know as *paradox of youth* (Genzel, Eisenhauer, and Gillessen, 2010). Even if the real SN spatial distribution is unclear, it is observed to be non-uniform and concentrated in the inner 30 pc of the Milky Way. This high SN concentration could be responsible for the higher detected CR density peaking towards the GC. In Jouvin, Lemière, and Terrier, 2017, the deduced γ-ray emission (fig. 6.23) is compatible with the H.E.S.S. observations in the inner 200 pc (HESS Collaboration et al., 2016).
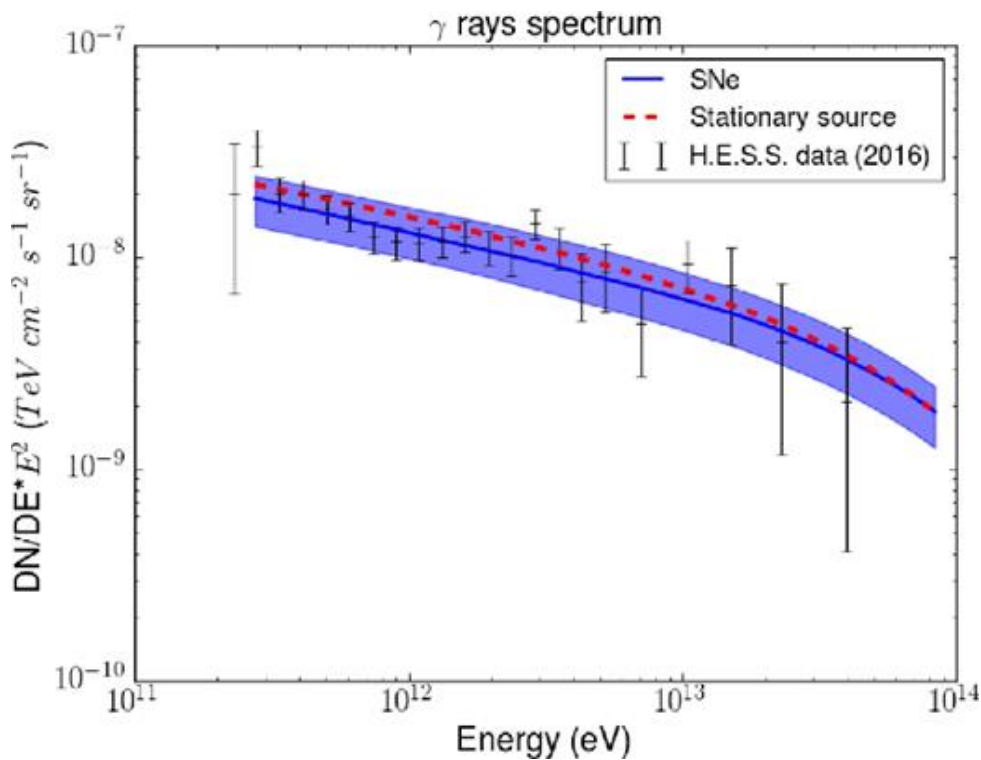
FIGURE 6.23: In blue the spectrum generated from 100 SN temporal and spatial distributions, and in red the spectrum from a stationary source at the GC. Both are extracted from an annulus centred at Sgr A* with inner and outer radii of $0.15°$ and $0.45°$. The black points are the H.E.S.S. data (HESS Collaboration et al., 2016). *Credit: fig.3 in Jouvin, Lemière, and Terrier, 2017.*

In particular, the estimated CR density profile is peaked toward the Quintuplet cluster and central disc, and at higher longitudes the CR density is compatible with that observed by H.E.S.S.. However, in the central $30\,\mathrm{pc}$ the SNR contribution alone are not able to overlap the observations implying the contribution of a central stationary-state source to explain the measurements.

The 3D model, of steady CR injection by a nowadays unresolved population of SNRs and PWNe, described above is able to reproduced the measured VHE γ-ray *excess* under both the assumption of isotropic and anisotropic CR diffusion. In the first scenario, the diffusion coefficient is considered equal to that observed locally ($\sim 2.7 \div 2.8$, eq. (2.2)), while in the second it is harder approaching the GC, since in this region the observed MF structure is poloidal and the perpendicular CR escape is of advective origin rather than diffusive.

6.4.1 Simulation Template and Analysis

As discussed above, it is reductive thinking that in the CMZ the only source capable to accelerate CRs is Sgr A*. From the observational point of view many candidate CR accelerators filling the region, like SNRs, PWNe, and young stellar cluster (YSCs). In this framework and following the work of Jouvin, Lemière, and Terrier, 2017, a set of simulations in view of the CTA era have been computed. In this sense, a synthetic population template accounting of currently undetected SNRs, PWNe and YSC has been used . The SNR template accounts of ~ 70 objects resulting from SNe explosion in $100\,\mathrm{kyr}$ of integration time (the same time range used to build the upcoming GPS), and it has been supplied by Pierre Cristofari. The obtained SNRs have been evolved with a code supplied by Michele Fiori to get the PWNe template (fig. 6.24). The spectral and morphological template of Arches cluster (YSC) has been provided by Giovanni Morlino.

The sources in the SNRs, PWN and YSC templates have been simulated through multiple events simulation with GAMMAPY for a total of $10\,\mathrm{h}$ and $50\,\mathrm{h}$ exposure time, in the energy range $0.1 \div 100\,\mathrm{TeV}$, with the IRF PROD5 relative to the observation site CTA South $50\,\mathrm{h}$, in a box of $5° \times 2°$ centered on $(l, b) = (0°, 0°)$. Together with the sources listed in the three templates, in the simulation has been considered the background model provided by the CTA consortium, the same used for building the upcoming Galactic Plane Survey (GPS). This *background model* is the updated version of *gamma model* described in section 6.1.1. The updated *gamma model* assumes the same non-uniform CR transport scenario of *gamma model*, but it is computed with the updated DRAGON2 and HERMES codes, In the first code have been updated the nuclear cross-sections that allow to simulate even PeVCRs, and the ISRF map with the more recent results. Regarding the second, HERMES represents the evolution of GAMMASKY in which are included additional high-energy radiative processes, and a new version of the gas distribution map, the same used to build the *gll_iem_v06*,
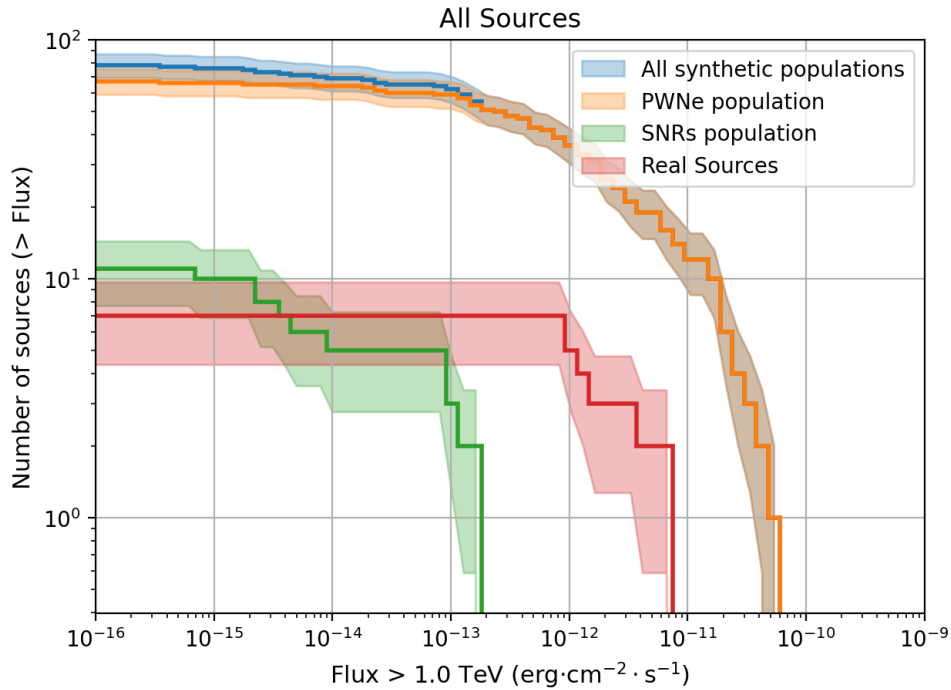
FIGURE 6.24: Above TeV energies the major contribution is due to the PWN population. *Credit: Michele Fiori.*

has been used to compute HEALPIX maps of the diffuse γ-ray emission (De La Torre Luque et al., 2023).

The aim of this simulation is to provide the spectrum of a region compatible with the Galactic Ridge ($|l| < 1°, |b| < 0.3°$), and to compare the result with the currently available observations by H.E.S.S., MAGIC, and VERITAS from the same region (fig. 6.13). If the simulated spectrum is at least compatible with the observations, it is worth including this synthetic population among the list of sources in the updated DC II, which will contain a list of known and unknown sources and candidates that are considered to be detectable by CTA. Indeed, at present date, in the GC region are listed only two sources, evidence extremely unlikely.

In fig. 6.25 the simulation outcomes are displayed, in particular the skymap (50 h) and the flux profile. The 3D analysis it is ongoing since some caveats have been arise from the first analysis presented at the Spring CTAO Collaboration Meeting 2023 in Granada (Spain). The certain inconsistency of the 3D analysis is not shown in this work and represent an extension of the project for the future.
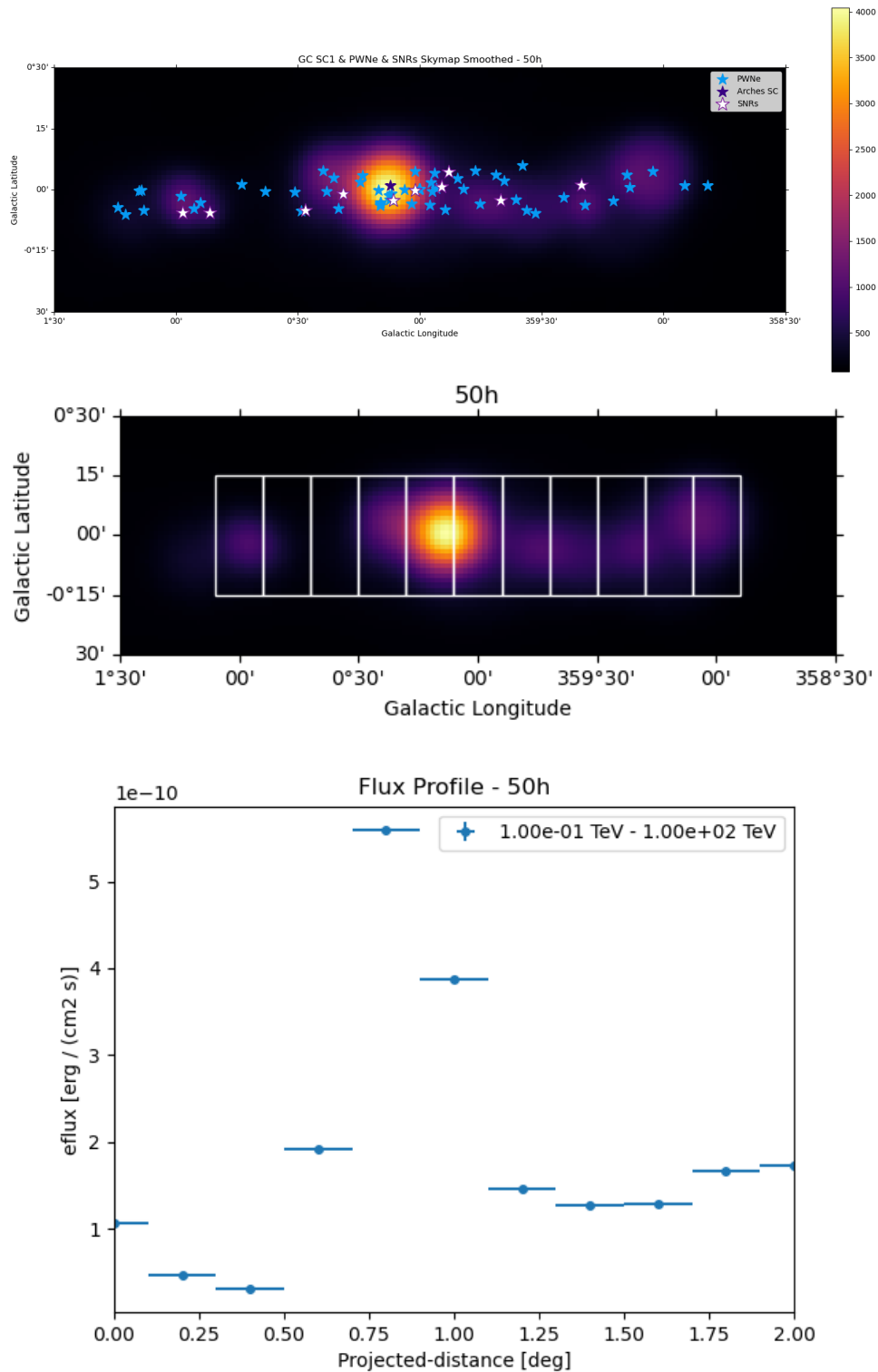
FIGURE 6.25: *On the top*: the simulated skymap. The positions of the sources listed in the synthetic template are also displayed. *In the middle*: the regions in which the flux profile (*on the bottom*) has been computed.

6.5 Discussion

The nature of the VHE γ-ray emission observed in the GC region is still unknown and debated. The H.E.S.S. collaboration (HESS Collaboration et al., 2016; H. E. S. S. Collaboration et al., 2018a) interprets the observed γ-ray *excess* in terms of the *PeVatron* scenario, in which the inferred CR density is compatible with CR escaping from a *stationary* source that continuously injects CRs in the region. The *PeVatron* is associated with the SMBH Sgr A* at the center of the Milky Way, or with a hidden accelerator located in its vicinity, for instance associated with a compact *Stellar Wind Cluster* Aharonian, Yang, and de Oña Wilhelmi, 2019; Morlino et al., 2021.

The *PeVatron* interpretation relies on very poor informations on the molecular gas distribution featuring the complex GC region. Indeed, it is known to be one of the densest environment of the Milky Way, in which the gaseous matter is clumpy and its dynamical behaviour is not properly understood (section 6.1.2). The dense molecular clouds represent the ideal target for the CR interactions producing γ rays mainly via π^0 decay. The X_{CO} conversion factor is used for obtaining useful informations on the mass content of the clouds, but its direct measurements at the GC position vanishes, and only extrapolations of local observations can be used (see fig. 6.5 and Ferrière, Gillard, and Jean, 2007). As a consequence the X_{CO} value in the inner Galaxy has an uncertainties of a factor of 2.

As discussed in section 6.1.1, several observational evidences (Acero et al., 2016; Yang, Aharonian, and Evoli, 2016) show that the HE γ-ray *excess* could be naturally explained accounting of inhomogeneous CR transport model, in which the anisotropic propagation is due to the linear dependence of the diffusion coefficient with galactocentric distance, rigidity and advection velocities, and the predicted flux increases approaching the GC (Gaggero et al., 2015b). The outcome of this model provides an *hardening* of the spectral index of the diffuse γ-ray emission in the inner Galaxy at higher energies, while in the MeV $\div$ GeV regime it is in agreement with the prediction of uniform (*conventional*) diffusion accounting of local measurements. In this framework, the observed γ-ray emission from the Galactic Ridge ($|l| < 1°$, $|b| < 0.3°$) has been explained in terms of the galactic CRs' contribution, CR-*sea*, which are accelerated by all the galactic sources[19] and confined within the Galaxy by the galactic MF.

In fig. 6.14 the outcomes of four phenomenological models of the diffuse emission computed with a different set of parameters are displayed. In particular, as displayed in fig. 6.15 (*top*), the expected flux of each model is in agreement with HE *Fermi*-LAT data, while at higher energies, those reached by IACTs, only the parameterization featuring *gamma model* could naturally explain the observations. Moreover, the inclusion of the *hardening* at 250 GeV/n, as observed by PAMELA (Adriani

---

[19]In the model the *source term* accounting of a analytical profile extrapolated at the GC position, and computed starting from radio observation of known SNRs in the galactic plane (section 6.1.1).

et al., 2011), AMS-02 (Aguilar et al., 2015) and CREAM (Ahn et al., 2010), is crucial in reproducing the data (fig. 6.15, *top*, black line), while the *conventional* diffusion scenario mismatches the data. It is useful to note that, for the analysis chain that performs likelihood 3D fit using a *conventional background model* it is natural to expect an *excess* (especially at higher energies) mainly because a *conventional* approach to some extent underestimate the real contribution of the diffuse emission, especially in the GC region.

As said earlier, these phenomenological models suffer of the poor understanding on the complex and clumpy gas distribution in the inner Galaxy, and the effective mass of the gaseous matter in the region (fig. 6.15 *bottom*). Moreover, *gamma model* represents an extension at the GC position of the behaviour observed between $8 \, \mathrm{kpc}$ and $3 \, \mathrm{kpc}$, and tuned on local data. Finally, at the highest energies the predicted flux by the models is strongly dependent by the parameterization choice (fig. 6.15 *top*).

At present observation-state, both *PeVatron* and *inhomogeneous diffusion* scenario may naturally explain the observed spectra in the innermost part of Our Own Galaxy (fig. 6.16). The opportunity to clarify the intricate panorama in the GC region may be given by the observation of regions farther from Sgr A*, especially at VHE γ rays. Indeed, as displayed in fig. 6.17, the expectations of *gamma model* in the inner parsecs underestimate the observed luminosities by H.E.S.S. (HESS Collaboration et al., 2016), while at farther radii the diffuse component seems to better reproduce the observations. It is useful to note that the region close to Sgr A* is characterized by $\gamma\gamma$-absorption due to the strong radiation field. Under this hypothesis, moving away from the Galactic Ridge at the edge of the CMZ, the search of promising candidates assumes a key role. In particular, the dense and compact molecular clouds could represent ideal laboratories to test and study several phenomenological models and scenarios.

In this context, the recently discovered HESS J1741-302 (H. E. S. S. Collaboration et al., 2018c) may represent an ideal target for testing the impact of several suggested scenarios (Ventura, Grasso, and Marinelli, 2019). As displayed in fig. 6.19, the discrimination between *inhomogeneous* diffusion (*gamma model*) and *PeVatron* scenario cannot be achieved with currently available data. All the expectations hinge on the next generation Cherenkov Telescope Array (Gueta, 2022) with its improved angular resolution and sensitivity, and in view of CTA era the HESS J1741-302 has been simulated for a total exposure time of $10 \, \mathrm{h}$. In order to reach useful physical informations, and the possibility to untangling among scenarios, two main setups have been implemented. In both setups the *foreground* model is represented by *gamma model*, while the *background* model, in the first setup the CMZ is illuminated by *gamma model*, and in the second by the central *PeVatron*. As clearly displayed in fig. 6.22 the improved performance of CTA may be able to disentangle between *PeVatron* and *inhomogeneous diffusion* scenarios, and "put an end" on the long-standing theoretical discussion on the origin of the GC *excess*. Moreover the detection of a

cutoff in the measured spectra will give the definitive interpretation on the nature and origin of the emission independently by models (Celli, Aharonian, and Gabici, 2020) and it will promote CTA as a plausible *PeVatron* discriminator.

As said in section 6.4, the SN rate in the GC region is extremely high, and the star formation rate (SFR) is comparable to that of starbust galaxies. Many massive stars have been detected in this complex region, and since the end of the life of massive star is represented by core collapse SNe and consequently SNRs, an exceptional CR density is expected filling the region. In radio and X-ray wavebands several particle accelerator candidates have been detected, and starting from the available observations it is possible to estimate a realistic nowadays unresolved population of particle accelerators, namely SNRs, PWNe and YSCs. Starting from the work of Jouvin, Lemière, and Terrier, 2017, a set of simulations have been implemented in order to understand if the computed spectrum from a region compatible with the Galactic Ridge is comparable with the currently available data, and to include the synthetic population as part of the DC II. As clearly displayed in fig. 6.25 the morphological extension of the emission is extraordinary in coincidence with that currently observed and displayed in fig. 6.15. Moreover, the flux profile is peaked towards the center, as obtained by the observations. The inclusion of this synthetic population in the list of sources of DC II is strongly recommended.

7 Summary and Conclusions

I N the last two decades a novel face of Our Universe has been unveiled through the observations performed with "gamma eyes" in the most energetic part of the electromagnetic spectrum. The interplay of HE and VHE γ-ray measurements has allowed to check and define the extreme flavour of the galactic and extra-galactic sky, in which powerful sources accelerate particles at the highest energies. The accelerated particles then interact with the environment in which they travel before reaching the Earth, where they are directly and indirectly detected. The nature of such interactions can be either leptonic or hadronic in origin, and many theoretical efforts are performed in order to understand and to describe the physical mechanisms driving the secondary production of γ rays.

This work is focused on the HE and VHE γ-ray observations from both the inner parsecs of Our Galaxy, in its quiescent phase, and the core of external galaxies, which are going through their active phase, known as active galactic nuclei (AGNs).

In chapter 5 the VHE γ-ray emission from two blazars has been analyzed by means of MAGIC observations, complemented with HE γ-ray data from the *Fermi*-LAT satellite.

In this framework, the blazar **BL Lacertae**, the prototype of BL Lac objects, represents an ideal laboratory for the study of variability pattern thanks to the long-term multi-wavelength coverage. In this context, VHE γ-ray observations are crucial to study the source evolution during its *flaring* state, when the flux of BL Lac exceeds of several order of magnitude its value during the quiescent phases, too faint to be observed by ground-based telescopes of the present generation. The BL Lac was found in *flaring* state in May 2019 in several ranges of the electromagnetic spectrum, spanning from optical to VHE γ-ray. The detection of high state in the HE regime with *Fermi*-LAT triggered MAGIC observations, and the source was found at $\sim 20\,\sigma$ significance level. The *flaring* pattern of this event is characterized by a *rise* time and a *decay* time longer in comparison with the previous flares observed by both VERITAS and MAGIC telescopes. For those events, the short time-scale has been interpreted as due to a small knot interacting within the jet or in a region out of the jet itself. However, a definitive explanation has not been reached, since all tested

scenarios share several caveats. In this intricate panorama, dense multi-wavelength observing campaigns are crucial, together with further measurements in the VHE γ-ray domain. The longer time of rise-and-decay featuring the BL Lac flare of May 2019 could be due to an interaction occurring farther away from the inner jet region, such as a star/cloud-jet interaction or due to reconnection mechanisms in turbulent plasma. Considering the BL Lac behaviour during the *flaring* state even at lower γ-ray energies, the *Fermi*-LAT light curves show that in this regime the peak of the flare occurs slightly before the one in the VHE γ rays. However, in the case of BL Lac, the VHE observations are always triggered by the HE high state, usually in the *Fermi*-LAT regime, evidence could lead to observational bias and caveats. Moreover, the source is cataloged with HE γ-ray logParabola spectral shape in the 4FGL *Fermi*-LAT catalog, and, indeed, that is the best-fit of its emitted flux during the quiescent phase. In the presence of a fast flare, instead, the HE γ-ray spectral behaviour of the source is well described with a simple power-law profile. In the period December 2019-January 2020, BL Lac was found again in high state, but not high enough to detect the source also at VHE γ rays with MAGIC. In this case, the spectral behaviour in the *Fermi*-LAT regime was reproduced by a logParabola, confirming that the Inverse Compton (IC) peak in the Synchrotron Self Compton (SSC) scenario lies in the HE γ rays, and only the vanishing tail of the emission reaches the highest energies leading to a non-detection of the source in the energy range covered by MAGIC. Thanks to this study it is possible to infer that the spectral trend of BL Lac in the $\mathrm{MeV} \div \mathrm{GeV}$ regime could be related with the detectability of the source even at very high energies, and at some extent could disentangle among the several suggested scenarios explaining the physics of its emission.Moreover, the changing of the BL Lac spectral model in the *Fermi*-LAT regime may be evidence of the *shifting* of the second peak in the SED of the source leading to the *transition* from LBL/IBL to HBL behavior during *flaring* states.

Blazars represents also powerful probes in cosmology and for studying the processes occurring at the higher energies featuring the IC-peak in the SSC scenario, in the fundamental and multi-messenger (MM) physics. In this context, Extreme High-frequency peaked BL Lac (EHBL) objects assume a key role. They are powerful laboratories for the study of leptonic, hadronic or mixed scenarios. Moreover, EHBLs are believed to be among the places in which high energy neutrinos could be produced by UHE CRs, and also responsible for the processes occurring through the interaction of high energy photons with the Inter Galactic Magnetic Field (IGMF), and Extragalactic Background Light (EBL).

Nowadays only a few EHBLs have been detected at VHE γ rays, and extending their known population represents one of the efforts pursued by the MAGIC collaboration. Multi-wavelength observing campaigns are also crucial for *hunting* promising candidates, and model their emission at very high energies. In chapter 5 has been presented the first-time detection at VHE of **1RXS J081201.8+023735** at VHE

performed during the cycles XIV and XV of the MAGIC observing campaign, and it was found at $5.21\,\sigma$ significance level. This source is of particular interest since its spectral index in the VHE domain is soft allowing to test several leptonic scenarios. Moreover, the source was listed in the reference catalog of TeV sources, TeVCat, in January 2021 due to the discovery of gamma-ray emission obtained with this study, and the work was presented at 43$^{\mathrm{rd}}$ COSPAR conference in Ventura et al., 2021.

The extragalactic sky is not the only venue in which the most energetic and powerful phenomena occur. Even Our Galaxy represents an intriguing environment in which many astrophysical sources are responsible for the extreme and non-thermal behaviour of the Milky Way. In this framework, the study of the **diffuse γ-ray emission** represent a fundamental topic in the astroparticle and high-energy astrophysics community. Since particles are accelerated by galactic sources, escape from their origin sites and diffuse throughout the Galaxy, interact with the interstellar medium (ISM), and produce γ rays, which permeate the whole galactic plane (GP). The diffuse γ-ray emission is evident at the energies covered by *Fermi*-LAT, but it is still disputed to exist at the highest energies as well, even if very recent measurements show the presence of diffuse emission above 100 TeV resulting from primary particles with energies above 1 PeV.

The modelling of the diffuse γ-ray emission is a challenge in the theoretical astroparticle physics, since this emission assumes a key role in the context of HE and VHE measurements, representing the only robust method providing the *background* model to implement in the analysis chain of observational data.

The conventional approach to the CR propagation provides the uniform diffusion featured by a constant diffusion coefficient in the whole Galaxy. On the other hand, in this work has been considered a novel approach to the standard propagation, described in chapter 6, in which the diffusion coefficient is featured by a linear dependence with galactocentric distance, rigidity and advective velocities. Under these assumptions the diffusion is not isotropic, and the spectrum gets harder approaching the inner Galaxy, where the observed VHE γ-ray emission puzzles the astroparticle community. Indeed, a VHE γ-ray *excess* has been found to trace the gaseous dense matter filling the Galactic Center (GC) region. The nature of such emission is still debated and several scenarios have been suggested to explain the observations. In this work two of them have been considered: the *PeVatron* and the *inhomogeneous* diffusion scenarios (*gamma model*), which have been tested and scrutinized against *Fermi*-LAT, H.E.S.S., MAGIC and VERITAS data. Two main regions of the inner part of the central molecular zone (CMZ) have been studied, the Galactic Ridge and Sgr B. In these regions both the approaches may reproduce the data, in particular regarding the diffusion scenario several ingredients are crucial, namely the radial dependence of the diffusion coefficient and the observed *hardening* at 250 GeV/n. Under these assumptions the *inhomogeneous* diffusion scenario

may naturally explain the data, whereas the conventional approach fails. This work was presented in several conferences: 37$^{\text{th}}$ ICRC (Ventura, 2022), TAUP 2023 and TeVPA 2023.

In order to achieve a definitive explanation to the phenomenon, the study of farther regions from the central SMBH Sgr A* could represent a viable solution to the problem. Indeed, moving away at the edge of the CMZ, the impact of the central *PeVatron* is reduced since its profile decays as $1/r$. On the other hand, the *inhomogeneous* diffusion scenario assumes an increasing effect, and this suggests the feasibility of such a test for the diffusion model.

In chapter 6 has been also considered the recently detected source **HESS J1741-302**, and the comparison of H.E.S.S. measurements and *Fermi*-LAT data analyzed by the author has allowed to test both the scenarios. In this case the *inhomogeneous* diffusion approach properly reproduces the observations, while the *PeVatron* scenario underestimates the emission. HESS J1741-302 is considered of particular interest since at that position a dense molecular cloud – the ideal target for CRs interaction – is present, and what has to be understood is the nature of the source "illuminating" the cloud: if the CRs are accelerated by the central *PeVatron* or by the galactic CR population undergoing harder diffusion. This work was presented at 36$^{\text{th}}$ ICRC conference in Ventura, Grasso, and Marinelli, 2019.

Nowadays a definitive explanation cannot be achieved, but the next generation IACT, the Cherenkov Telescope Array (CTA), with its improved performances, could provide the useful data to have the definitive explanation. In this framework, in chapter 6 have been described a set of simulations performed in view of the CTA era, in which HESS J1741-302 has been simulated under two main setups. In the first the CMZ has been illuminated by the galactic CRs undergoing *inhomogeneous* diffusion, while in the second the central *PeVatron* illuminates the region. From the comparison of the two simulated spectra, it is possible to disentangle between the two scenarios, that are well resolved with the expected precision in CTA observations.

In the future the CTA observations will be able to provide a definitive explanation to the long-standing discussion on the origin of the GC *excess*, especially if a *cutoff* will be detected and they could promote CTA as a *PeVatron* discriminator. The importance to model the diffuse emission in an increasingly realistic way resides on the evidence that the phenomenological models are used in the analysis chain of data as the *background model* above which the detection of a source is possible. In this sense, the requirement neither to underestimate nor to overestimate the predicted γ-ray diffuse emission is crucial. Moreover, the choice of a model rather than another implies a different level of the predicted background emission leading to different parametrization of the source under investigation. In particular, as displayed in fig. 6.22, the normalization and the spectral index in the spectral model of the source changes when using different background models.

In view of the CTA era, the CTAO consortium has provided the astroparticle community of a Data Challenge (DC) accounting of simulated flux from a list of nowadays known and unknown sources. In the CMZ only two objects are listed, and this representation seems unlikely since in the inner Galaxy the supernova rate is extraordinary high implying the presence of several particle accelerators, like SNRs, PWNe and young stellar clusters. All these sources confined in the central parsecs could provide a viable solution to the GC *excess* since the expected flux from this nowadays **unresolved population** of particle accelerators is compatible with the H.E.S.S. observations. The synthetic population is then simulated in order to obtain the spectrum of the whole region filled by the population, and to compare it with the currently available data. In this framework the aim of the simulation is to understand if the synthetic population is worth including in the new version of the Data Challenge (DC II). The morphology of the simulated population is compatible with that observed at VHE γ rays, as well as the flux profile. Considering the findings in this work it is strongly recommended to include the synthetic population in the DC II of CTA.

The extreme flavour of the Universe is accessible with ground-based telescopes, which have provided to the astroparticle and high energy astrophysics community many observations of both the galactic and extragalactic sky giving the opportunity to study the powerful, violent and non-thermal phenomena occurring in the Cosmos. With present date instruments a lot of new physics can be done, but many expectations hinge on the upcoming Cherenkov Telescope Array.

7.1 Future Steps . . .

The further developments of this work are many, and a list of future steps follows.

- A paper on the BL Lac flaring state in 2019-2020 is in preparation, and at least three major models have to be tested on the MWL SED of the source. Moreover, the intra-night variability study has to be performed together with correlation studies in search of relative lags between bands in the MWL light curves.

- 1RXS J081201.8+023735 will be included in the second EHBL catalog of the MAGIC collaboration, and in this context the MWL SED has to be modelled.

- The simulations of HESS J1741-302 have to be updated and extended with more exposure time, since in the GC key science project the total time budget reserved for this kind of observations is $500\,\mathrm{h}$. Moreover the setups have to be changed including the new version of *gamma model*, the same used for the upcoming Galactic Plane Survey (GPS), and the conventional propagation scenario in order to have at least three plausible scenarios to compare.

- The caveats found in the synthetic population of SNRs, PWNe and YSC have to be properly addressed in order to perform the 3D likelihood analysis.

- The search of *PeVatrons* in the Galaxy is of fundamental relevance, and in this perspective the *hunting* of promising candidate is crucial. Here, the observation of HESS J1848-018 has been proposed to the MAGIC collaboration in the Observing Cycle XV, but due to the COVID-19 shutdown the measurements have not been performed. This source represents an interesting target for testing several scenarios, in particular the stellar wind bubbles as CRs factories. The combination with contemporary LST-1 observations would also be extremely beneficial.

- In order to disentangle between *PeVatron* and *inhomogeneous* diffusion, the identification of regions farther away from Sgr A*, at the rim of the CMZ, is crucial. An interesting region is represented by the *Bania Clump*, a complex, dense and giant molecular cloud located at $\sim 500 \div 800$ pc away from the GC (fig. 7.1). In this case, a detailed 3D gas distribution template is crucial.
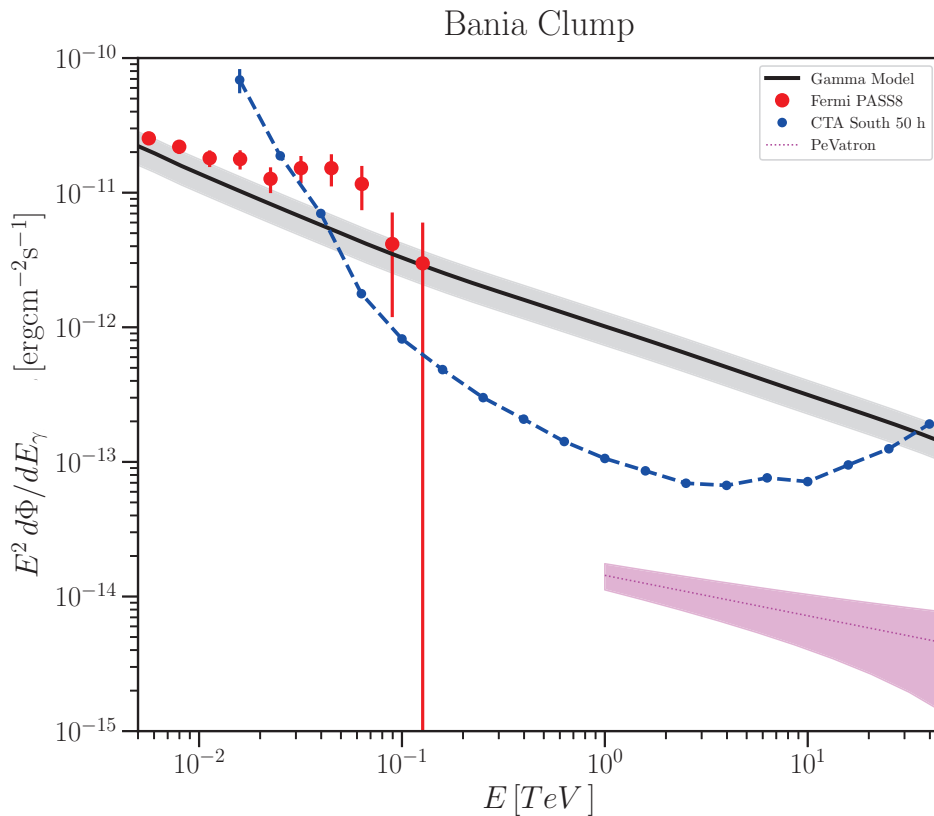
FIGURE 7.1: The *Fermi*-LAT data are compared with the expected emission of *gamma model*, and the CTA sensitivity curve. Note that the source seems to be detectable by CTA. *Credit: fig. 5.11 in Ventura, 2018*.

Bibliography

Aab, A. et al. (2014). "Depth of maximum of air-shower profiles at the Pierre Auger Observatory. I. Measurements at energies above $10^{17.8}$ eV". In: *PhRvD* 90.12, 122005, p. 122005. DOI: `10.1103/PhysRevD.90.122005`. arXiv: `1409.4809 [astro-ph.HE]`.

Aartsen, M. G. et al. (2016). "Observation and Characterization of a Cosmic Muon Neutrino Flux from the Northern Hemisphere Using Six Years of IceCube Data". In: *ApJ* 833.1, 3, p. 3. DOI: `10.3847/0004-637X/833/1/3`. arXiv: `1607.08006 [astro-ph.HE]`.

Abbasi, R. U. et al. (2005). "A Study of the Composition of Ultra-High-Energy Cosmic Rays Using the High-Resolution Fly's Eye". In: *ApJ* 622, pp. 910–926. DOI: `10.1086/427931`. eprint: `astro-ph/0407622`.

Abbott, B. P. et al. (2017). "Multi-messenger Observations of a Binary Neutron Star Merger". In: *ApJL* 848.2, L12, p. L12. DOI: `10.3847/2041-8213/aa91c9`. arXiv: `1710.05833 [astro-ph.HE]`.

Abdalla, H. et al. (2019). "A very-high-energy component deep in the γ-ray burst afterglow". In: *Nature* 575.7783, pp. 464–467. DOI: `10.1038/s41586-019-1743-9`. arXiv: `1911.08961 [astro-ph.HE]`.

Abdo, A. A. et al. (2007). "Discovery of TeV Gamma-Ray Emission from the Cygnus Region of the Galaxy". In: *ApJL* 658.1, pp. L33–L36. DOI: `10.1086/513696`. arXiv: `astro-ph/0611691 [astro-ph]`.

Abdo, A. A. et al. (2008). "A Measurement of the Spatial Distribution of Diffuse TeV Gamma-Ray Emission from the Galactic Plane with Milagro". In: *ApJ* 688, 1078-1083, pp. 1078–1083. DOI: `10.1086/592213`. arXiv: `0805.0417`.

Abdo, A. A. et al. (2009). "The Large-Scale Cosmic-Ray Anisotropy as Observed with Milagro". In: *ApJ* 698.2, pp. 2121–2130. DOI: `10.1088/0004-637X/698/2/2121`. arXiv: `0806.2293 [astro-ph]`.

Abdo, A. A. et al. (2010a). "Fermi-Lat Discovery of GeV Gamma-Ray Emission from the Young Supernova Remnant Cassiopeia A". In: *ApJL* 710, pp. L92–L97. DOI: `10.1088/2041-8205/710/1/L92`. arXiv: `1001.1419 [astro-ph.HE]`.

Abdo, A. A. et al. (2010b). "Observation of Supernova Remnant IC 443 with the Fermi Large Area Telescope". In: *ApJ* 712.1, pp. 459–468. DOI: `10.1088/0004-637X/712/1/459`. arXiv: `1002.2198 [astro-ph.HE]`.

Abdo, A. A. et al. (2011a). "Fermi Large Area Telescope Observations of Markarian 421: The Missing Piece of its Spectral Energy Distribution". In: *ApJ* 736.2,

131, p. 131. DOI: 10.1088/0004−637X/736/2/131. arXiv: 1106.1348 [astro-ph.HE].

Abdo, A. A. et al. (2011b). "The First Fermi Multifrequency Campaign on BL Lacertae: Characterizing the Low-activity State of the Eponymous Blazar". In: *ApJ* 730.2, 101, p. 101. DOI: 10.1088/0004−637X/730/2/101. arXiv: 1101.5905 [astro-ph.HE].

Abdollahi, S. et al. (2020a). "Fermi Large Area Telescope Fourth Source Catalog". In: *ApJS* 247.1, 33, p. 33. DOI: 10.3847/1538−4365/ab6bcb. arXiv: 1902.10045 [astro-ph.HE].

Abdollahi, S. et al. (2020b). "VizieR Online Data Catalog: The Fermi LAT fourth source catalog (4FGL) (Abdollahi+, 2020)". In: *VizieR Online Data Catalog*, J/ApJS/247/33, J/ApJS/247/33.

Abe, H. et al. (2023). "Search for Gamma-Ray Spectral Lines from Dark Matter Annihilation up to 100 TeV toward the Galactic Center with MAGIC". In: *PhRvL* 130.6, 061002, p. 061002. DOI: 10.1103/PhysRevLett.130.061002. arXiv: 2212.10527 [astro-ph.HE].

Abe, K. et al. (2012). "Search for Antihelium with the BESS-Polar Spectrometer". In: *PhRvL* 108.13, 131301, p. 131301. DOI: 10.1103/PhysRevLett.108.131301. arXiv: 1201.2967 [astro-ph.CO].

Abeysekara, A. and VERITAS Collaboration (2017). "VERITAS Long Term Monitoring of Gamma-Ray Emission from the BL Lacertae Object". In: *35th International Cosmic Ray Conference (ICRC2017)*. Vol. 301. International Cosmic Ray Conference, p. 610. DOI: 10.22323/1.301.0610.

Abeysekara, A. U. et al. (2017). "Observation of the Crab Nebula with the HAWC Gamma-Ray Observatory". In: *ApJ* 843.1, 39, p. 39. DOI: 10.3847/1538−4357/aa7555. arXiv: 1701.01778 [astro-ph.HE].

Abeysekara, A. U. et al. (2018a). "Multiwavelength Observations of the Blazar BL Lacertae: A New Fast TeV Gamma-Ray Flare". In: *ApJ* 856.2, 95, p. 95. DOI: 10.3847/1538−4357/aab35c. arXiv: 1802.10113 [astro-ph.HE].

Abeysekara, A. U. et al. (2018b). "Very-high-energy particle acceleration powered by the jets of the microquasar SS 433". In: *Nature* 562.7725, pp. 82–85. DOI: 10.1038/s41586−018−0565−5.

Abeysekara, A. U. et al. (2019a). "All-sky Measurement of the Anisotropy of Cosmic Rays at 10 TeV and Mapping of the Local Interstellar Magnetic Field". In: *ApJ* 871.1, 96, p. 96. DOI: 10.3847/1538−4357/aaf5cc. arXiv: 1812.05682 [astro-ph.HE].

Abeysekara, A. U. et al. (2019b). "Measurement of the Crab Nebula Spectrum Past 100 TeV with HAWC". In: *ApJ* 881.2, 134, p. 134. DOI: 10.3847/1538−4357/ab2f7d. arXiv: 1905.12518 [astro-ph.HE].

Abeysekara, A. U. et al. (2020). "The Great Markarian 421 Flare of 2010 February: Multiwavelength Variability and Correlation Studies". In: *ApJ* 890.2, 97, p. 97. DOI: 10.3847/1538−4357/ab6612. arXiv: 2002.03567 [astro-ph.HE].

Abeysekara, A. U. et al. (2021). "HAWC observations of the acceleration of very-high-energy cosmic rays in the Cygnus Cocoon". In: *Nature Astronomy* 5, pp. 465–471. DOI: 10.1038/s41550-021-01318-y. arXiv: 2103.06820 [astro-ph.HE].

Abeysekara, Anushka Udara et al. (2021). "Galactic Gamma-Ray Diffuse Emission at TeV energies with HAWC Data". In: *PoS* ICRC2021, p. 835. DOI: 10.22323/1.395.0835.

Abraham, J. et al. (2010). "The fluorescence detector of the Pierre Auger Observatory". In: *Nuclear Instruments and Methods in Physics Research A* 620.2-3, pp. 227–251. DOI: 10.1016/j.nima.2010.04.023.

Abramowski, A. et al. (2012). "The 2010 Very High Energy γ-Ray Flare and 10 Years of Multi-wavelength Observations of M 87". In: *ApJ* 746.2, 151, p. 151. DOI: 10.1088/0004-637X/746/2/151. arXiv: 1111.5341 [astro-ph.CO].

Abramowski, A. et al. (2015). "The 2012 Flare of PG 1553+113 Seen with H.E.S.S. and Fermi-LAT". In: *ApJ* 802.1, 65, p. 65. DOI: 10.1088/0004-637X/802/1/65. arXiv: 1501.05087 [astro-ph.HE].

Accardo, L. et al. (2014). "High Statistics Measurement of the Positron Fraction in Primary Cosmic Rays of 0.5-500 GeV with the Alpha Magnetic Spectrometer on the International Space Station". In: *PhRvL* 113.12, 121101, p. 121101. DOI: 10.1103/PhysRevLett.113.121101.

Acciari, V. A. et al. (2009a). "Observation of Extended Very High Energy Emission from the Supernova Remnant IC 443 with VERITAS". In: *ApJL* 698.2, pp. L133–L137. DOI: 10.1088/0004-637X/698/2/L133. arXiv: 0905.3291 [astro-ph.HE].

Acciari, V. A. et al. (2009b). "Veritas Observations of a Very High Energy γ-Ray Flare From the Blazar 3C 66A". In: *ApJL* 693.2, pp. L104–L108. DOI: 10.1088/0004-637X/693/2/L104. arXiv: 0901.4527 [astro-ph.HE].

Acciari, V. A. et al. (2010). "Observations of the Shell-type Supernova Remnant Cassiopeia A at TeV Energies with VERITAS". In: *ApJ* 714.1, pp. 163–169. DOI: 10.1088/0004-637X/714/1/163. arXiv: 1002.2974 [astro-ph.HE].

Acciari, V. A. et al. (2011). "Spectral Energy Distribution of Markarian 501: Quiescent State Versus Extreme Outburst". In: *ApJ* 729.1, 2, p. 2. DOI: 10.1088/0004-637X/729/1/2. arXiv: 1012.2200 [astro-ph.HE].

Acciari, V. A. et al. (2020). "New Hard-TeV Extreme Blazars Detected with the MAGIC Telescopes". In: *ApJS* 247.1, 16, p. 16. DOI: 10.3847/1538-4365/ab5b98. arXiv: 1911.06680 [astro-ph.HE].

Acciari, V. A. et al. (2021). "Multiwavelength variability and correlation studies of Mrk 421 during historically low X-ray and γ-ray activity in 2015-2016". In: *MNRAS* 504.1, pp. 1427–1451. DOI: 10.1093/mnras/staa3727. arXiv: 2012.01348 [astro-ph.HE].

Acero, F. et al. (2010). "Localizing the VHE γ-ray source at the Galactic Centre". In: *MNRAS* 402, pp. 1877–1882. DOI: 10.1111/j.1365-2966.2009.16014.x. arXiv: 0911.1912.

Acero, F. et al. (2016). "Development of the Model of Galactic Interstellar Emission for Standard Point-source Analysis of Fermi Large Area Telescope Data". In: *ApJS* 223, 26, p. 26. DOI: 10.3847/0067-0049/223/2/26. arXiv: 1602.07246 [astro-ph.HE].

Acharyya, A. et al. (2019). "Monte Carlo studies for the optimisation of the Cherenkov Telescope Array layout". In: *Astroparticle Physics* 111, pp. 35–53. DOI: 10.1016/j.astropartphys.2019.04.001. arXiv: 1904.01426 [astro-ph.IM].

Acharyya, A. et al. (2021). "Sensitivity of the Cherenkov Telescope Array to a dark matter signal from the Galactic centre". In: *JCAP* 2021.1, 057, p. 057. DOI: 10.1088/1475-7516/2021/01/057. arXiv: 2007.16129 [astro-ph.HE].

Ackermann, M. et al. (2011a). "A Cocoon of Freshly Accelerated Cosmic Rays Detected by Fermi in the Cygnus Superbubble". In: *Science* 334.6059, p. 1103. DOI: 10.1126/science.1210311.

Ackermann, M. et al. (2011b). "The Second Catalog of Active Galactic Nuclei Detected by the Fermi Large Area Telescope". In: *ApJ* 743.2, 171, p. 171. DOI: 10.1088/0004-637X/743/2/171. arXiv: 1108.1420 [astro-ph.HE].

Ackermann, M. et al. (2012a). "Fermi-LAT Observations of the Diffuse γ-Ray Emission: Implications for Cosmic Rays and the Interstellar Medium". In: *ApJ* 750, 3, p. 3. DOI: 10.1088/0004-637X/750/1/3. arXiv: 1202.4039 [astro-ph.HE].

Ackermann, M. et al. (2012b). "The Fermi Large Area Telescope on Orbit: Event Classification, Instrument Response Functions, and Calibration". In: *ApJS* 203, 4, p. 4. DOI: 10.1088/0067-0049/203/1/4. arXiv: 1206.1896 [astro-ph.IM].

Ackermann, M. et al. (2013). "Detection of the Characteristic Pion-Decay Signature in Supernova Remnants". In: *Science* 339.6121, pp. 807–811. DOI: 10.1126/science.1231160. arXiv: 1302.3307 [astro-ph.HE].

Ackermann, M. et al. (2015). "Multiwavelength Evidence for Quasi-periodic Modulation in the Gamma-Ray Blazar PG 1553+113". In: *ApJL* 813.2, L41, p. L41. DOI: 10.1088/2041-8205/813/2/L41. arXiv: 1509.02063 [astro-ph.HE].

Ackermann, M. et al. (2017). "The Fermi Galactic Center GeV Excess and Implications for Dark Matter". In: *ApJ* 840, 43, p. 43. DOI: 10.3847/1538-4357/aa6cab. arXiv: 1704.03910 [astro-ph.HE].

Adams, C. B. et al. (2021). "VERITAS Observations of the Galactic Center Region at Multi-TeV Gamma-Ray Energies". In: *ApJ* 913.2, 115, p. 115. DOI: 10.3847/1538-4357/abf926. arXiv: 2104.12735 [astro-ph.HE].

Adriani, O. et al. (2009a). "An anomalous positron abundance in cosmic rays with energies 1.5-100GeV". In: *Nature* 458.7238, pp. 607–609. DOI: 10.1038/nature07942. arXiv: 0810.4995 [astro-ph].

Adriani, O. et al. (2009b). "New Measurement of the Antiproton-to-Proton Flux Ratio up to 100 GeV in the Cosmic Radiation". In: *PhRvL* 102.5, 051101, p. 051101. DOI: 10.1103/PhysRevLett.102.051101. arXiv: 0810.4994 [astro-ph].

Adriani, O. et al. (2010). "PAMELA Results on the Cosmic-Ray Antiproton Flux from 60 MeV to 180 GeV in Kinetic Energy". In: *Physical Review Letters* 105.12, 121101,

p. 121101. DOI: `10.1103/PhysRevLett.105.121101`. arXiv: `1007.0821 [astro-ph.HE]`.

Adriani, O. et al. (2011). "PAMELA Measurements of Cosmic-Ray Proton and Helium Spectra". In: *Science* 332, p. 69. DOI: `10.1126/science.1199172`. arXiv: `1103.4055 [astro-ph.HE]`.

Aguilar, M. et al. (2013). "First Result from the Alpha Magnetic Spectrometer on the International Space Station: Precision Measurement of the Positron Fraction in Primary Cosmic Rays of 0.5-350 GeV". In: *PhRvL* 110.14, 141102, p. 141102. DOI: `10.1103/PhysRevLett.110.141102`.

Aguilar, M. et al. (2015). "Precision Measurement of the Proton Flux in Primary Cosmic Rays from Rigidity 1 GV to 1.8 TV with the Alpha Magnetic Spectrometer on the International Space Station". In: *Physical Review Letters* 114.17, 171103, p. 171103. DOI: `10.1103/PhysRevLett.114.171103`.

Aharonian, F. and A. Neronov (2005). "High-Energy Gamma Rays from the Massive Black Hole in the Galactic Center". In: *ApJ* 619, pp. 306–313. DOI: `10.1086/426426`. eprint: `astro-ph/0408303`.

Aharonian, F. et al. (2005a). "Detection of TeV γ-ray emission from the shell-type supernova remnant RX J0852.0-4622 with HESS". In: *A&A* 437.1, pp. L7–L10. DOI: `10.1051/0004-6361:200500130`. arXiv: `astro-ph/0505380 [astro-ph]`.

Aharonian, F. et al. (2005b). "Discovery of Very High Energy Gamma Rays Associated with an X-ray Binary". In: *Science* 309.5735, pp. 746–749. DOI: `10.1126/science.1113764`. arXiv: `astro-ph/0508298 [astro-ph]`.

Aharonian, F. et al. (2005c). "Very high energy gamma rays from the composite SNR G 0.9+0.1". In: *A&A* 432.2, pp. L25–L29. DOI: `10.1051/0004-6361:200500022`. arXiv: `astro-ph/0501265 [astro-ph]`.

Aharonian, F. et al. (2006a). "A low level of extragalactic background light as revealed by γ-rays from blazars". In: *Nature* 440.7087, pp. 1018–1021. DOI: `10.1038/nature04680`. arXiv: `astro-ph/0508073 [astro-ph]`.

Aharonian, F. et al. (2006b). "Discovery of very-high-energy γ-rays from the Galactic Centre ridge". In: *Nature* 439, pp. 695–698. DOI: `10.1038/nature04467`. eprint: `astro-ph/0603021`.

Aharonian, F. et al. (2006c). "Energy dependent γ-ray morphology in the pulsar wind nebula HESS J1825-137". In: *A&A* 460.2, pp. 365–374. DOI: `10.1051/0004-6361:20065546`. arXiv: `astro-ph/0607548 [astro-ph]`.

Aharonian, F. et al. (2006d). "Fast Variability of Tera-Electron Volt γ Rays from the Radio Galaxy M87". In: *Science* 314.5804, pp. 1424–1427. DOI: `10.1126/science.1134408`. arXiv: `astro-ph/0612016 [astro-ph]`.

Aharonian, F. et al. (2007). "An Exceptional Very High Energy Gamma-Ray Flare of PKS 2155-304". In: *ApJL* 664.2, pp. L71–L74. DOI: `10.1086/520635`. arXiv: `0706.0797 [astro-ph]`.

Aharonian, F. et al. (2008). "Energy Spectrum of Cosmic-Ray Electrons at TeV Energies". In: *PhRvL* 101.26, 261104, p. 261104. DOI: `10.1103/PhysRevLett.101.261104`. arXiv: `0811.3894 [astro-ph]`.

Aharonian, F. et al. (2009). "Spectrum and variability of the Galactic center VHE γ-ray source HESS J1745-290". In: *A&A* 503, pp. 817–825. DOI: `10.1051/0004-6361/200811569`. arXiv: `0906.1247 [astro-ph.GA]`.

Aharonian, F. et al. (2021). "Performance test of the electromagnetic particle detectors for the LHAASO experiment". In: *Nuclear Instruments and Methods in Physics Research A* 1001, 165193, p. 165193. DOI: `10.1016/j.nima.2021.165193`.

Aharonian, F. A. (2000). "TeV gamma rays from BL Lac objects due to synchrotron radiation of extremely high energy protons". In: *NewA* 5.7, pp. 377–395. DOI: `10.1016/S1384-1076(00)00039-7`. arXiv: `astro-ph/0003159 [astro-ph]`.

– (2004). *Very high energy cosmic gamma radiation : a crucial window on the extreme Universe*. World Scientific Publishing Co. DOI: `10.1142/4657`.

Aharonian, F. A. et al. (1997a). "The potential of ground based arrays of imaging atmospheric Cherenkov telescopes. I. Determination of shower parameters". In: *Astroparticle Physics* 6, pp. 343–368. DOI: `10.1016/S0927-6505(96)00069-2`.

– (1997b). "The potential of the ground based arrays of imaging atmospheric Cherenkov telescopes. II. Gamma ray flux sensitivities". In: *Astroparticle Physics* 6, pp. 369–377. DOI: `10.1016/S0927-6505(96)00070-9`.

Aharonian, F. A. et al. (2001). "A search for gamma-ray emission from the Galactic plane in the longitude range between 37° and 43°". In: *A&A* 375, pp. 1008–1017. DOI: `10.1051/0004-6361:20010898`.

Aharonian, F. A. et al. (2002). "A search for TeV gamma-ray emission from SNRs, pulsars and unidentified GeV sources in the Galactic plane in the longitude range between -2 deg and 85 deg." In: *A&A* 395, pp. 803–811. DOI: `10.1051/0004-6361:20021347`. arXiv: `astro-ph/0209360 [astro-ph]`.

Aharonian, F. A. et al. (2004). "High-energy particle acceleration in the shell of a supernova remnant". In: *Nature* 432.7013, pp. 75–77. DOI: `10.1038/nature02960`. arXiv: `astro-ph/0411533 [astro-ph]`.

Aharonian, Felix, Ruizhi Yang, and Emma de Oña Wilhelmi (2019). "Massive stars as major factories of Galactic cosmic rays". In: *Nature Astronomy* 3, pp. 561–567. DOI: `10.1038/s41550-019-0724-0`. arXiv: `1804.02331 [astro-ph.HE]`.

Ahn, H. S. et al. (2010). "Discrepant Hardening Observed in Cosmic-ray Elemental Spectra". In: *ApJL* 714, pp. L89–L93. DOI: `10.1088/2041-8205/714/1/L89`. arXiv: `1004.1123 [astro-ph.HE]`.

Ahnen, M. L. et al. (2017a). "A cut-off in the TeV gamma-ray spectrum of the SNR Cassiopeia A". In: *MNRAS* 472.3, pp. 2956–2962. DOI: `10.1093/mnras/stx2079`. arXiv: `1707.01583 [astro-ph.HE]`.

Ahnen, M. L. et al. (2017b). "Observations of Sagittarius A* during the pericenter passage of the G2 object with MAGIC". In: *A&A* 601, A33, A33. DOI: `10.1051/0004-6361/201629355`. arXiv: `1611.07095 [astro-ph.HE]`.

Ahnen, M. L. et al. (2017c). "Performance of the MAGIC telescopes under moonlight". In: *Astroparticle Physics* 94, pp. 29–41. DOI: 10.1016/j.astropartphys.2017.08.001. arXiv: 1704.00906 [astro-ph.IM].

Ajello, M. et al. (2017). "VizieR Online Data Catalog: The third Fermi-LAT >10GeV catalog (3FHL) (Ajello+, 2017)". In: *VizieR Online Data Catalog*, J/ApJS/232/18, J/ApJS/232/18.

Ajello, M. et al. (2021). "Fermi Large Area Telescope Performance after 10 Years of Operation". In: *ApJS* 256.1, 12, p. 12. DOI: 10.3847/1538-4365/ac0ceb. arXiv: 2106.12203 [astro-ph.IM].

Albert, A. et al. (2020a). "3HWC: The Third HAWC Catalog of Very-high-energy Gamma-Ray Sources". In: *ApJ* 905.1, 76, p. 76. DOI: 10.3847/1538-4357/abc2d8. arXiv: 2007.08582 [astro-ph.HE].

Albert, A. et al. (2020b). "HAWC J2227+610 and Its Association with G106.3+2.7, a New Potential Galactic PeVatron". In: *ApJL* 896.2, L29, p. L29. DOI: 10.3847/2041-8213/ab96cc. arXiv: 2005.13699 [astro-ph.HE].

Albert, J. et al. (2006). "Observation of Gamma Rays from the Galactic Center with the MAGIC Telescope". In: *ApJL* 638, pp. L101–L104. DOI: 10.1086/501164. eprint: astro-ph/0512469.

Albert, J. et al. (2007a). "Discovery of Very High Energy γ-Ray Emission from the Low-Frequency-peaked BL Lacertae Object BL Lacertae". In: *ApJL* 666.1, pp. L17–L20. DOI: 10.1086/521550. arXiv: astro-ph/0703084 [astro-ph].

Albert, J. et al. (2007b). "Discovery of Very High Energy Gamma Radiation from IC 443 with the MAGIC Telescope". In: *ApJL* 664.2, pp. L87–L90. DOI: 10.1086/520957. arXiv: 0705.3119 [astro-ph].

Albert, J. et al. (2007c). "Observation of VHE γ-rays from Cassiopeia A with the MAGIC telescope". In: *A&A* 474.3, pp. 937–940. DOI: 10.1051/0004-6361:20078168. arXiv: 0706.4065 [astro-ph].

Albert, J. et al. (2007d). "Observations of Markarian 421 with the MAGIC Telescope". In: *ApJ* 663.1, pp. 125–138. DOI: 10.1086/518221. arXiv: astro-ph/0603478 [astro-ph].

Albert, J. et al. (2007e). "Unfolding of differential energy spectra in the MAGIC experiment". In: *Nuclear Instruments and Methods in Physics Research A* 583.2-3, pp. 494–506. DOI: 10.1016/j.nima.2007.09.048. arXiv: 0707.2453 [astro-ph].

Albert, J. et al. (2007f). "Variable Very High Energy γ-Ray Emission from Markarian 501". In: *ApJ* 669.2, pp. 862–883. DOI: 10.1086/521382. arXiv: astro-ph/0702008 [astro-ph].

Albert, J. et al. (2008). "Implementation of the Random Forest method for the Imaging Atmospheric Cherenkov Telescope MAGIC". In: *Nuclear Instruments and Methods in Physics Research A* 588.3, pp. 424–432. DOI: 10.1016/j.nima.2007.11.068. arXiv: 0709.3719 [astro-ph].

Aleksić, J. et al. (2011a). "MAGIC Discovery of Very High Energy Emission from the FSRQ PKS 1222+21". In: *ApJL* 730.1, L8, p. L8. DOI: 10.1088/2041-8205/730/1/L8. arXiv: 1101.4645 [astro-ph.HE].

Aleksić, J. et al. (2011b). "Observations of the Crab Pulsar between 25 and 100 GeV with the MAGIC I Telescope". In: *ApJ* 742.1, 43, p. 43. DOI: 10.1088/0004-637X/742/1/43. arXiv: 1108.5391 [astro-ph.HE].

Aleksić, J. et al. (2012). "Phase-resolved energy spectra of the Crab pulsar in the range of 50-400 GeV measured with the MAGIC telescopes". In: *A&A* 540, A69, A69. DOI: 10.1051/0004-6361/201118166. arXiv: 1109.6124 [astro-ph.HE].

Aleksić, J. et al. (2014). "Black hole lightning due to particle acceleration at sub-horizon scales". In: *Science* 346.6213, pp. 1080–1084. DOI: 10.1126/science.1256183. arXiv: 1412.4936 [astro-ph.HE].

Aleksić, J. et al. (2016a). "The major upgrade of the MAGIC telescopes, Part I: The hardware improvements and the commissioning of the system". In: *Astroparticle Physics* 72, pp. 61–75. DOI: 10.1016/j.astropartphys.2015.04.004. arXiv: 1409.6073 [astro-ph.IM].

– (2016b). "The major upgrade of the MAGIC telescopes, Part II: A performance study using observations of the Crab Nebula". In: *Astroparticle Physics* 72, pp. 76–94. DOI: 10.1016/j.astropartphys.2015.02.005. arXiv: 1409.5594 [astro-ph.IM].

Aleksić, J. et al. (2010). "Search for an extended VHE emission from Mrk 421 and Mrk 501 with the MAGIC Telescope". In: *A&A* 524, A77. DOI: 10.1051/0004-6361/201014747. URL: https://doi.org/10.1051/0004-6361/201014747.

Aleksić, J. et al. (2012). "High zenith angle observations of PKS5-304 with the MAGIC-I telescope". In: *A&A* 544, A75. DOI: 10.1051/0004-6361/201218796. URL: https://doi.org/10.1051/0004-6361/201218796.

Aliu, E. et al. (2008). "Observation of Pulsed γ-Rays Above 25 GeV from the Crab Pulsar with MAGIC". In: *Science* 322.5905, p. 1221. DOI: 10.1126/science.1164718. arXiv: 0809.2998 [astro-ph].

Aliu, E. et al. (2013). "Discovery of TeV Gamma-Ray Emission toward Supernova Remnant SNR G78.2+2.1". In: *ApJ* 770.2, 93, p. 93. DOI: 10.1088/0004-637X/770/2/93. arXiv: 1305.6508 [astro-ph.HE].

Aloisio, Roberto, Eugenio Coccia, and Francesco Vissani (2018). *Multiple Messengers and Challenges in Astroparticle Physics*. DOI: 10.1007/978-3-319-65425-6.

Alves Batista, Rafael and Andrey Saveliev (2021). "The Gamma-Ray Window to Intergalactic Magnetism". In: *Universe* 7.7, p. 223. DOI: 10.3390/universe7070223. arXiv: 2105.12020 [astro-ph.HE].

Ambrosio, M. et al. (2003). "Search for cosmic ray sources using muons detected by the MACRO experiment". In: *Astroparticle Physics* 18, pp. 615–627. DOI: 10.1016/S0927-6505(02)00164-0. eprint: hep-ph/0204188.

Ambrosone, Antonio et al. (2022). "Observable signatures of cosmic rays transport in Starburst Galaxies on gamma-ray and neutrino observations". In: *MNRAS* 515.4, pp. 5389–5399. DOI: 10.1093/mnras/stac2133. arXiv: 2203.03642 [astro-ph.HE].

Amenomori, M. et al. (2005). "Large-Scale Sidereal Anisotropy of Galactic Cosmic-Ray Intensity Observed by the Tibet Air Shower Array". In: *ApJL* 626, pp. L29–L32. DOI: 10.1086/431582. eprint: astro-ph/0505114.

Amenomori, M. et al. (2010). "On Temporal Variations of the Multi-TeV Cosmic Ray Anisotropy Using the Tibet III Air Shower Array". In: *ApJ* 711.1, pp. 119–124. DOI: 10.1088/0004-637X/711/1/119. arXiv: 1001.2646 [astro-ph.HE].

Amenomori, M. et al. (2017). "Northern Sky Galactic Cosmic Ray Anisotropy between 10 and 1000 TeV with the Tibet Air Shower Array". In: *ApJ* 836.2, 153, p. 153. DOI: 10.3847/1538-4357/836/2/153. arXiv: 1701.07144 [astro-ph.HE].

Amenomori, M. et al. (2019). "First Detection of Photons with Energy beyond 100 TeV from an Astrophysical Source". In: *PhRvL* 123.5, 051101, p. 051101. DOI: 10.1103/PhysRevLett.123.051101. arXiv: 1906.05521 [astro-ph.HE].

Amenomori, M. et al. (2021a). "First Detection of sub-PeV Diffuse Gamma Rays from the Galactic Disk: Evidence for Ubiquitous Galactic Cosmic Rays beyond PeV Energies". In: *PhRvL* 126.14, 141101, p. 141101. DOI: 10.1103/PhysRevLett.126.141101. arXiv: 2104.05181 [astro-ph.HE].

Amenomori, M. et al. (2021b). "Gamma-Ray Observation of the Cygnus Region in the 100-TeV Energy Region". In: *PhRvL* 127.3, 031102, p. 031102. DOI: 10.1103/PhysRevLett.127.031102. arXiv: 2107.01064 [astro-ph.HE].

Anderhub, H. et al. (2013). "Design and operation of FACT - the first G-APD Cherenkov telescope". In: *Journal of Instrumentation* 8.6, P06008, P06008. DOI: 10.1088/1748-0221/8/06/P06008. arXiv: 1304.1710 [astro-ph.IM].

Ando, Shin'ichiro and John F. Beacom (2005). "Revealing the Supernova Gamma-Ray Burst Connection with TeV Neutrinos". In: *PhRvL* 95.6, 061103, p. 061103. DOI: 10.1103/PhysRevLett.95.061103. arXiv: astro-ph/0502521 [astro-ph].

Ansoldi, S. et al. (2018). "The Blazar TXS 0506+056 Associated with a High-energy Neutrino: Insights into Extragalactic Jets and Cosmic-Ray Acceleration". In: *ApJL* 863.1, L10, p. L10. DOI: 10.3847/2041-8213/aad083. arXiv: 1807.04300 [astro-ph.HE].

Antonucci, Robert (1993). "Unified models for active galactic nuclei and quasars." In: *ARA&A* 31, pp. 473–521. DOI: 10.1146/annurev.aa.31.090193.002353.

Apel, W. D. et al. (2011). "Kneelike Structure in the Spectrum of the Heavy Component of Cosmic Rays Observed with KASCADE-Grande". In: *Physical Review Letters* 107.17, 171104, p. 171104. DOI: 10.1103/PhysRevLett.107.171104. arXiv: 1107.5885 [astro-ph.HE].

Apel, W. D. et al. (2013). "KASCADE-Grande measurements of energy spectra for elemental groups of cosmic rays". In: *Astroparticle Physics* 47, pp. 54–66. DOI: 10.1016/j.astropartphys.2013.06.004.

Araudo, A. T., V. Bosch-Ramon, and G. E. Romero (2013). "Gamma-ray emission from massive stars interacting with active galactic nuclei jets". In: *MNRAS* 436.4, pp. 3626–3639. DOI: 10.1093/mnras/stt1840. arXiv: 1309.7114 [astro-ph.HE].

Arbet-Engels, A. et al. (2022). "Extreme blazars under the eyes of MAGIC". In: *37th International Cosmic Ray Conference*, p. 865. DOI: 10.22323/1.395.0865.

Arcadi, Giorgio et al. (2018). "The waning of the WIMP? A review of models, searches, and constraints". In: *European Physical Journal C* 78.3, 203, p. 203. DOI: 10.1140/epjc/s10052-018-5662-y. arXiv: 1703.07364 [hep-ph].

Archambault, S. et al. (2016). "Discovery of very high energy gamma rays from 1ES 1440+122". In: *MNRAS* 461.1, pp. 202–208. DOI: 10.1093/mnras/stw1319. arXiv: 1608.02769 [astro-ph.HE].

Archambault, S. et al. (2017). "Search for Magnetically Broadened Cascade Emission from Blazars with VERITAS". In: *ApJ* 835.2, 288, p. 288. DOI: 10.3847/1538-4357/835/2/288. arXiv: 1701.00372 [astro-ph.HE].

Archer, A. et al. (2014). "Very-high Energy Observations of the Galactic Center Region by VERITAS in 2010-2012". In: *ApJ* 790, 149, p. 149. DOI: 10.1088/0004-637X/790/2/149. arXiv: 1406.6383 [astro-ph.HE].

Archer, A. et al. (2016). "TeV Gamma-Ray Observations of the Galactic Center Ridge by VERITAS". In: *ApJ* 821, 129, p. 129. DOI: 10.3847/0004-637X/821/2/129. arXiv: 1602.08522 [astro-ph.HE].

Archer, A. et al. (2018). "Measurement of cosmic-ray electrons at TeV energies by VERITAS". In: *Phys. Rev. D* 98 (6), p. 062004. DOI: 10.1103/PhysRevD.98.062004. URL: https://link.aps.org/doi/10.1103/PhysRevD.98.062004.

Arlen, T. et al. (2013). "Rapid TeV Gamma-Ray Flaring of BL Lacertae". In: *ApJ* 762.2, 92, p. 92. DOI: 10.1088/0004-637X/762/2/92. arXiv: 1211.3073 [astro-ph.HE].

Armstrong, J. W., B. J. Rickett, and S. R. Spangler (1995). "Electron density power spectrum in the local interstellar medium". In: *ApJ* 443, pp. 209–221. DOI: 10.1086/175515.

Asano, Katsuaki et al. (2014). "Time-dependent Models for Blazar Emission with the Second-order Fermi Acceleration". In: *ApJ* 780.1, 64, p. 64. DOI: 10.1088/0004-637X/780/1/64. arXiv: 1311.0936 [astro-ph.HE].

Asaoka, Y. et al. (2002). "Measurements of Cosmic-Ray Low-Energy Antiproton and Proton Spectra in a Transient Period of Solar Field Reversal". In: *PhRvL* 88.5, 051101, p. 051101. DOI: 10.1103/PhysRevLett.88.051101. arXiv: astro-ph/0109007 [astro-ph].

Asplund, M., N. Grevesse, and A. Jacques Sauval (2006). "The solar chemical composition". In: *Nuclear Physics A* 777, pp. 1–4. DOI: 10.1016/j.nuclphysa.2005.06.010. eprint: astro-ph/0410214.

Atoyan, A. and C. D. Dermer (2004). "TeV Emission from the Galactic Center Black Hole Plerion". In: *ApJL* 617, pp. L123–L126. DOI: 10.1086/427390. eprint: astro-ph/0410243.

Atwood, W. B. et al. (2009). "The Large Area Telescope on the Fermi Gamma-Ray Space Telescope Mission". In: *ApJ* 697, pp. 1071–1102. DOI: 10.1088/0004-637X/697/2/1071. arXiv: 0902.1089 [astro-ph.IM].

Axford, W. I., E. Leer, and G. Skadron (1977). "The acceleration of cosmic rays by shock waves". In: *International Cosmic Ray Conference* 11, pp. 132–137.

Bahcall, John N., Chris Flynn, and Andrew Gould (1992). "Local Dark Matter from a Carefully Selected Sample". In: *ApJ* 389, p. 234. DOI: 10.1086/171201.

Ballantyne, D. R., M. Schumann, and B. Ford (2011). "Modelling the time-dependence of the TeV γ-ray source at the Galactic Centre". In: *MNRAS* 410.3, pp. 1521–1526. DOI: 10.1111/j.1365-2966.2010.17533.x. arXiv: 1008.2661 [astro-ph.HE].

Bally, J. et al. (1987). "Galactic center molecular clouds. I - Spatial and spatial-velocity maps". In: *ApJS* 65, pp. 13–82. DOI: 10.1086/191217.

– (1988). "Galactic center molecular clouds. II - Distribution and kinematics". In: *ApJ* 324, pp. 223–247. DOI: 10.1086/165891.

Banasiński, P., W. Bednarek, and J. Sitarek (2016). "Orphan γ-ray flares from relativistic blobs encountering luminous stars". In: *MNRAS* 463.1, pp. L26–L30. DOI: 10.1093/mnrasl/slw149. arXiv: 1607.07725 [astro-ph.HE].

Barbato, F. C. T. et al. (2016). "The VSiPMT project". In: *Nuovo Cimento C Geophysics Space Physics C* 39.1, 253, p. 253. DOI: 10.1393/ncc/i2016-16253-6.

Barkov, Maxim V., Felix A. Aharonian, and Valentí Bosch-Ramon (2010). "Gamma-ray Flares from Red Giant/Jet Interactions in Active Galactic Nuclei". In: *ApJ* 724.2, pp. 1517–1523. DOI: 10.1088/0004-637X/724/2/1517. arXiv: 1005.5252 [astro-ph.HE].

Barres de Almeida, Ulisses (2022). "Status of R&D for the Southern Wide-Field Gamma-ray Observatory (SWGO)". In: *44th COSPAR Scientific Assembly. Held 16-24 July*. Vol. 44, p. 2400.

Bartels, R., S. Krishnamurthy, and C. Weniger (2016). "Strong Support for the Millisecond Pulsar Origin of the Galactic Center GeV Excess". In: *Physical Review Letters* 116.5, 051102, p. 051102. DOI: 10.1103/PhysRevLett.116.051102. arXiv: 1506.05104 [astro-ph.HE].

Bartoli, B. et al. (2015). "Study of the Diffuse Gamma-Ray Emission from the Galactic Plane with ARGO-YBJ". In: *ApJ* 806.1, 20, p. 20. DOI: 10.1088/0004-637X/806/1/20. arXiv: 1507.06758 [astro-ph.IM].

Beach, A. S. et al. (2001). "Measurement of the Cosmic-Ray Antiproton-to-Proton Abundance Ratio between 4 and 50 GeV". In: *PhRvL* 87.27, 271101, p. 271101. DOI: 10.1103/PhysRevLett.87.271101. arXiv: astro-ph/0111094 [astro-ph].

Becerra González, J. et al. (2021). "Optical spectral characterization of the gamma-ray blazars S4 0954+65, TXS 1515-273, and RX J0812.0+0237". In: *MNRAS* 504.4, pp. 5258–5269. DOI: 10.1093/mnras/stab1274. arXiv: 2010.14532 [astro-ph.HE].

Bednarek, W. (1993). "On the Gamma-Ray Emission from 3C 279". In: *ApJL* 402, p. L29. DOI: 10.1086/186692.

Bednarek, W. and R. J. Protheroe (1997). "Gamma-rays from interactions of stars with active galactic nucleus jets". In: *MNRAS* 287.3, pp. L9–L13. DOI: 10.1093/mnras/287.3.L9. arXiv: astro-ph/9612073 [astro-ph].

Bednarek, W. and J. Sitarek (2021). "Absorption effects in the blazar's γ-ray spectra due to luminous stars crossing the jet". In: *MNRAS* 503.2, pp. 2423–2431. DOI: 10.1093/mnras/stab554. arXiv: 2102.11589 [astro-ph.HE].

Bednarek, W. and T. Sobczak (2013). "Gamma-rays from millisecond pulsar population within the central stellar cluster in the galactic centre." In: *MNRAS* 435, pp. L14–L18. DOI: 10.1093/mnrasl/slt084. arXiv: 1306.4760 [astro-ph.HE].

Begelman, Mitchell C., Andrew C. Fabian, and Martin J. Rees (2008). "Implications of very rapid TeV variability in blazars". In: *MNRAS* 384.1, pp. L19–L23. DOI: 10.1111/j.1745-3933.2007.00413.x. arXiv: 0709.0540 [astro-ph].

Belikov, A. V., G. Zaharijas, and J. Silk (2012). "Study of the gamma-ray spectrum from the Galactic Center in view of multi-TeV dark matter candidates". In: *PhRvD* 86.8, 083516, p. 083516. DOI: 10.1103/PhysRevD.86.083516. arXiv: 1207.2412 [astro-ph.HE].

Bell, A. R. (1978a). "The acceleration of cosmic rays in shock fronts. I". In: *MNRAS* 182, pp. 147–156. DOI: 10.1093/mnras/182.2.147.

– (1978b). "The acceleration of cosmic rays in shock fronts. II". In: *MNRAS* 182, pp. 443–455. DOI: 10.1093/mnras/182.3.443.

Bell, A. R. et al. (2013). "Cosmic-ray acceleration and escape from supernova remnants". In: *MNRAS* 431, pp. 415–429. DOI: 10.1093/mnras/stt179. arXiv: 1301.7264 [astro-ph.HE].

Berezinskii, V. S. and S. I. Grigor'eva (1988). "A bump in the ultra-high energy cosmic ray spectrum". In: *A&A* 199, pp. 1–12.

Berezinskii, V. S. et al. (1990). *Astrophysics of cosmic rays*.

Berezinsky, V., A. Gazizov, and S. Grigorieva (2006). "On astrophysical solution to ultrahigh energy cosmic rays". In: *PhRvD* 74.4, 043005, p. 043005. DOI: 10.1103/PhysRevD.74.043005. eprint: hep-ph/0204357.

Bernlöhr, K. et al. (2003). "The optical system of the H.E.S.S. imaging atmospheric Cherenkov telescopes. Part I: layout and components of the system". In: *Astroparticle Physics* 20, pp. 111–128. DOI: 10.1016/S0927-6505(03)00171-3. eprint: astro-ph/0308246.

Bernlöhr, K. et al. (2013). "Monte Carlo design studies for the Cherenkov Telescope Array". In: *Astroparticle Physics* 43, pp. 171–188. DOI: 10.1016/j.astropartphys.2012.10.002. arXiv: 1210.3503 [astro-ph.IM].

Bernlöhr, Konrad (2008). "Simulation of imaging atmospheric Cherenkov telescopes with CORSIKA and sim_ telarray". In: *Astroparticle Physics* 30.3, pp. 149–158. DOI: 10.1016/j.astropartphys.2008.07.009. arXiv: 0808.2253 [astro-ph].

Bertone, Gianfranco and Dan Hooper (2018). "History of dark matter". In: *Reviews of Modern Physics* 90.4, 045002, p. 045002. DOI: `10.1103/RevModPhys.90.045002`. arXiv: `1605.04909 [astro-ph.CO]`.

Bignami, G. F., P. A. Caraveo, and R. C. Lamb (1983). "An identification for "GEMINGA" (2CG 195+04) 1E 0630+178 : a unique object in the error box of the high-energy gamma-ray source." In: *ApJL* 272, pp. L9–L13. DOI: `10.1086/184107`.

Biland, A. et al. (2008). "The Active Mirror Control of the MAGIC Telescopes". In: *International Cosmic Ray Conference*. Vol. 3. International Cosmic Ray Conference, pp. 1353–1356. DOI: `10.48550/arXiv.0709.1574`. arXiv: `0709.1574 [astro-ph]`.

Binney, J. and M. Merrifield (1998). *Galactic Astronomy*.

Binns, W. R. et al. (2007). "OB Associations, Wolf Rayet Stars, and the Origin of Galactic Cosmic Rays". In: *SSRv* 130, pp. 439–449. DOI: `10.1007/s11214-007-9195-1`. arXiv: `0707.4645`.

Bird, D. J. et al. (1994). "The cosmic-ray energy spectrum observed by the Fly's Eye". In: *ApJ* 424, pp. 491–502. DOI: `10.1086/173906`.

Biteau, J. et al. (2020). "Progress in unveiling extreme particle acceleration in persistent astrophysical jets". In: *Nature Astronomy* 4, pp. 124–131. DOI: `10.1038/s41550-019-0988-4`. arXiv: `2001.09222 [astro-ph.HE]`.

Blanch, Oscar (2020a). "Detection of a bright very-high-energy gamma-ray flare from BL Lac with the MAGIC telescopes". In: *The Astronomer's Telegram* 14032, p. 1.

– (2020b). "GRB 201216C: MAGIC detection in very high energy gamma rays". In: *The Astronomer's Telegram* 14275, p. 1.

– (2020c). "MAGIC detection of very-high-energy gamma-ray flaring activity from BL Lacertae during the current historical optical and high-energy gamma-ray flare". In: *The Astronomer's Telegram* 13963, p. 1.

Blandford, R. D. and J. P. Ostriker (1978). "Particle acceleration by astrophysical shocks". In: *ApJL* 221, pp. L29–L32. DOI: `10.1086/182658`.

Blandford, R. D. and D. G. Payne (1982). "Hydromagnetic flows from accretion disks and the production of radio jets." In: *MNRAS* 199, pp. 883–903. DOI: `10.1093/mnras/199.4.883`.

Blandford, R. D. and R. L. Znajek (1977). "Electromagnetic extraction of energy from Kerr black holes." In: *MNRAS* 179, pp. 433–456. DOI: `10.1093/mnras/179.3.433`.

Blasi, P., E. Amato, and D. Caprioli (2007). "The maximum momentum of particles accelerated at cosmic ray modified shocks". In: *MNRAS* 375, pp. 1471–1478. DOI: `10.1111/j.1365-2966.2006.11412.x`. eprint: `astro-ph/0612424`.

Blasi, Pasquale and Giovanni Morlino (2023). "High energy cosmic rays and gamma rays from star clusters: the case of Cygnus OB2". In: *MNRAS*. DOI: `10.1093/mnras/stad1662`. arXiv: `2306.03762 [astro-ph.HE]`.

Błażejowski, M. et al. (2000). "Comptonization of Infrared Radiation from Hot Dust by Relativistic Jets in Quasars". In: *ApJ* 545.1, pp. 107–116. DOI: `10.1086/317791`. arXiv: `astro-ph/0008154 [astro-ph]`.

Blumenthal, George R. and Robert J. Gould (1970). "Bremsstrahlung, Synchrotron Radiation, and Compton Scattering of High-Energy Electrons Traversing Dilute Gases". In: *Reviews of Modern Physics* 42.2, pp. 237–271. DOI: 10.1103/RevModPhys.42.237.

Bolmont, J. et al. (2014). "The camera of the fifth H.E.S.S. telescope. Part I: System description". In: *Nuclear Instruments and Methods in Physics Research A* 761, pp. 46–57. DOI: 10.1016/j.nima.2014.05.093. arXiv: 1310.5877 [astro-ph.IM].

Bonnoli, G. et al. (2015). "An emerging population of BL Lacs with extreme properties: towards a class of EBL and cosmic magnetic field probes?" In: *MNRAS* 451.1, pp. 611–621. DOI: 10.1093/mnras/stv953. arXiv: 1501.01974 [astro-ph.HE].

Bosch-Ramon, V. (2015). "Non-thermal emission from standing relativistic shocks: an application to red giant winds interacting with AGN jets". In: *A&A* 575, A109, A109. DOI: 10.1051/0004-6361/201425208. arXiv: 1501.03118 [astro-ph.HE].

Bosch-Ramon, V., M. Perucho, and M. V. Barkov (2012). "Clouds and red giants interacting with the base of AGN jets." In: *A&A* 539, A69, A69. DOI: 10.1051/0004-6361/201118622. arXiv: 1201.5279 [astro-ph.HE].

Bose, D. et al. (2022). "Galactic and extragalactic sources of very high energy gamma rays". In: *European Physical Journal Special Topics* 231.1, pp. 27–66. DOI: 10.1140/epjs/s11734-022-00434-8. arXiv: 2201.06789 [astro-ph.HE].

Bottaro, Salvatore et al. (2022). "Closing the window on WIMP Dark Matter". In: *European Physical Journal C* 82.1, 31, p. 31. DOI: 10.1140/epjc/s10052-021-09917-9. arXiv: 2107.09688 [hep-ph].

Böttcher, M. and S. D. Bloom (2000). "Analyzing the Multiwavelength Spectrum of BL Lacertae during the 1997 July Outburst". In: *AJ* 119.2, pp. 469–477. DOI: 10.1086/301201. arXiv: astro-ph/9806249 [astro-ph].

Böttcher, M. et al. (2013). "Leptonic and Hadronic Modeling of Fermi-detected Blazars". In: *ApJ* 768.1, 54, p. 54. DOI: 10.1088/0004-637X/768/1/54. arXiv: 1304.0605 [astro-ph.HE].

Böttcher, Markus (2007). "Modeling the emission processes in blazars". In: *Ap&SS* 309.1-4, pp. 95–104. DOI: 10.1007/s10509-007-9404-0. arXiv: astro-ph/0608713 [astro-ph].

Bradač, Maruša et al. (2008). "Revealing the Properties of Dark Matter in the Merging Cluster MACS J0025.4-1222". In: *ApJ* 687.2, pp. 959–967. DOI: 10.1086/591246. arXiv: 0806.2320 [astro-ph].

Bruel, P. et al. (2018). "Fermi-LAT improved Pass~8 event selection". In: *arXiv e-prints*, arXiv:1810.11394, arXiv:1810.11394. DOI: 10.48550/arXiv.1810.11394. arXiv: 1810.11394 [astro-ph.IM].

Brun, Rene and Fons Rademakers (1997). "ROOT — An object oriented data analysis framework". In: *Nuclear Instruments and Methods in Physics Research A* 389.1, pp. 81–86. DOI: 10.1016/S0168-9002(97)00048-X.

Burton, W. B. and H. S. Liszt (1978). "The gas distribution in the central region of the Galaxy. I - Atomic hydrogen". In: *ApJ* 225, pp. 815–842. DOI: 10.1086/156547.

Buschmann, Malte et al. (2020). "Foreground mismodeling and the point source explanation of the Fermi Galactic Center excess". In: *PhRvD* 102.2, 023023, p. 023023. DOI: 10.1103/PhysRevD.102.023023. arXiv: 2002.12373 [astro-ph.HE].

Bykov, A. M. (2014). "Nonthermal particles and photons in starburst regions and superbubbles". In: *A&A Rv* 22, 77, p. 77. DOI: 10.1007/s00159-014-0077-8. arXiv: 1511.04608 [astro-ph.HE].

Calderone, G. et al. (2013). "Black hole mass estimate for a sample of radio-loud narrow-line Seyfert 1 galaxies". In: *MNRAS* 431.1, pp. 210–239. DOI: 10.1093/mnras/stt157. arXiv: 1212.1181 [astro-ph.CO].

Cao, Zhen et al. (2021). "Ultrahigh-energy photons up to 1.4 petaelectronvolts from 12 γ-ray Galactic sources". In: *Nature* 594.7861, pp. 33–36. DOI: 10.1038/s41586-021-03498-z.

Cao, Zhen et al. (2023a). "Measurement of ultra-high-energy diffuse gamma-ray emission of the Galactic plane from 10 TeV to 1 PeV with LHAASO-KM2A". In: *arXiv e-prints*, arXiv:2305.05372, arXiv:2305.05372. DOI: 10.48550/arXiv.2305.05372. arXiv: 2305.05372 [astro-ph.HE].

– (2023b). "The First LHAASO Catalog of Gamma-Ray Sources". In: *arXiv e-prints*, arXiv:2305.17030, arXiv:2305.17030. DOI: 10.48550/arXiv.2305.17030. arXiv: 2305.17030 [astro-ph.HE].

Caprioli, Damiano (2015). ""Espresso" Acceleration of Ultra-high-energy Cosmic Rays". In: *ApJL* 811.2, L38, p. L38. DOI: 10.1088/2041-8205/811/2/L38. arXiv: 1505.06739 [astro-ph.HE].

Carr, T. D., M. D. Desch, and J. K. Alexander (1983). "Physics of the Jovian magnetosphere. 7. Phenomenology of magnetospheric radio emissions." In: *Physics of the Jovian Magnetosphere*, pp. 226–284.

Case, G. L. and D. Bhattacharya (1998). "A New Σ-D Relation and Its Application to the Galactic Supernova Remnant Distribution". In: *ApJ* 504, pp. 761–772. DOI: 10.1086/306089. eprint: astro-ph/9807162.

Cavasinni, V., D. Grasso, and L. Maccione (2006). "TeV neutrinos from supernova remnants embedded in giant molecular clouds". In: *Astroparticle Physics* 26, pp. 41–49. DOI: 10.1016/j.astropartphys.2006.04.009. eprint: astro-ph/0604004.

Celli, S., A. Palladino, and F. Vissani (2017). "Neutrinos and γ-rays from the Galactic Center Region after H.E.S.S. multi-TeV measurements". In: *European Physical Journal C* 77, 66, p. 66. DOI: 10.1140/epjc/s10052-017-4635-x. arXiv: 1604.08791 [astro-ph.HE].

Celli, Silvia, Felix Aharonian, and Stefano Gabici (2020). "Spectral Signatures of Pevatrons". In: *ApJ* 903.1, 61, p. 61. DOI: 10.3847/1538-4357/abb805. arXiv: 2009.05999 [astro-ph.HE].

Cerri, S. S. et al. (2017). "A signature of anisotropic cosmic-ray transport in the gamma-ray sky". In: *JCAP* 10, 019, p. 019. DOI: 10.1088/1475-7516/2017/10/019. arXiv: 1707.07694 [astro-ph.HE].

Cerruti, M. et al. (2015). "A hadronic origin for ultra-high-frequency-peaked BL Lac objects". In: *MNRAS* 448.1, pp. 910–927. DOI: 10.1093/mnras/stu2691. arXiv: 1411.5968 [astro-ph.HE].

Chang, Y. L. et al. (2017). "2WHSP: A multi-frequency selected catalogue of high energy and very high energy γ-ray blazars and blazar candidates". In: *A&A* 598, A17, A17. DOI: 10.1051/0004-6361/201629487. arXiv: 1609.05808 [astro-ph.HE].

Chernyakova, M. et al. (2011). "The High-energy, Arcminute-scale Galactic Center Gamma-ray Source". In: *ApJ* 726.2, 60, p. 60. DOI: 10.1088/0004-637X/726/2/60. arXiv: 1009.2630 [astro-ph.HE].

Chiaberge, M., A. Capetti, and A. Celotti (1999). "The HST view of FR I radio galaxies: evidence for non-thermal nuclear sources". In: *A&A* 349, pp. 77–87. DOI: 10.48550/arXiv.astro-ph/9907064. arXiv: astro-ph/9907064 [astro-ph].

Clark, G. W., G. P. Garmire, and W. L. Kraushaar (1968). "Observation of High-Energy Cosmic Gamma Rays". In: *ApJL* 153, p. L203. DOI: 10.1086/180252.

Clavel, M. et al. (2013). "Echoes of multiple outbursts of Sagittarius A$^?$ revealed by Chandra". In: *A&A* 558, A32, A32. DOI: 10.1051/0004-6361/201321667. arXiv: 1307.3954 [astro-ph.HE].

Clowe, Douglas, Anthony Gonzalez, and Maxim Markevitch (2004). "Weak-Lensing Mass Reconstruction of the Interacting Cluster 1E 0657-558: Direct Evidence for the Existence of Dark Matter". In: *ApJ* 604.2, pp. 596–603. DOI: 10.1086/381970. arXiv: astro-ph/0312273 [astro-ph].

Clowe, Douglas et al. (2006). "A Direct Empirical Proof of the Existence of Dark Matter". In: *ApJL* 648.2, pp. L109–L113. DOI: 10.1086/508162. arXiv: astro-ph/0608407 [astro-ph].

Commichau, Sebastian Caspar (2007). "Observation of very high energy gamma-rays from the Galactic Center with the MAGIC telescope, considering geomagnetic field effects on the imaging technique". PhD thesis. Eidgenossische Technische Hochschule, Zurich, Switzerland.

Compton, A. H. (1933). "A Geographic Study of Cosmic Rays". In: *Physical Review* 43, pp. 387–403. DOI: 10.1103/PhysRev.43.387.

Connaughton, V. et al. (2016). "Fermi GBM Observations of LIGO Gravitational-wave Event GW150914". In: *ApJL* 826.1, L6, p. L6. DOI: 10.3847/2041-8205/826/1/L6. arXiv: 1602.03920 [astro-ph.HE].

Cordes, J. M. and T. J. W. Lazio (2002). "NE2001.I. A New Model for the Galactic Distribution of Free Electrons and its Fluctuations". In: *ArXiv Astrophysics e-prints*. eprint: astro-ph/0207156.

Costamante, L. (2017). "Blazars in the FERMI Era - A Review". In: *XII Multifrequency Behaviour of High Energy Cosmic Sources Workshop (MULTIF2017)*, p. 61.

Costamante, L. et al. (2001). "Extreme synchrotron BL Lac objects. Stretching the blazar sequence". In: *A&A* 371, pp. 512–526. DOI: 10.1051/0004-6361:20010412. arXiv: astro-ph/0103343 [astro-ph].

Crocker, R. M. et al. (2010). "A lower limit of 50 microgauss for the magnetic field near the Galactic Centre". In: *Nature* 463, pp. 65–67. DOI: `10.1038/nature08635`. arXiv: `1001.1275 [astro-ph.GA]`.

Crocker, R. M. et al. (2011). "γ-rays and the far-infrared-radio continuum correlation reveal a powerful Galactic Centre wind". In: *MNRAS* 411, pp. L11–L15. DOI: `10.1111/j.1745-3933.2010.00983.x`. arXiv: `1009.4340`.

Cummings, A. C. et al. (2016). "Galactic Cosmic Rays in the Local Interstellar Medium: Voyager 1 Observations and Model Results". In: *ApJ* 831.1, 18, p. 18. DOI: `10.3847/0004-637X/831/1/18`.

Dame, T. M., D. Hartmann, and P. Thaddeus (2001). "The Milky Way in Molecular Clouds: A New Complete CO Survey". In: *ApJ* 547, pp. 792–813. DOI: `10.1086/318388`. eprint: `astro-ph/0009217`.

DAMPE Collaboration et al. (2017). "Direct detection of a break in the teraelectron-volt cosmic-ray spectrum of electrons and positrons". In: *Nature* 552.7683, pp. 63–66. DOI: `10.1038/nature24475`. arXiv: `1711.10981 [astro-ph.HE]`.

Dar, Arnon and Ari Laor (1997). "Hadronic Production of TeV Gamma-Ray Flares from Blazars". In: *ApJL* 478.1, pp. L5–L8. DOI: `10.1086/310544`. arXiv: `astro-ph/9610252 [astro-ph]`.

De La Torre Luque, P. et al. (2021). "Implications of current nuclear cross sections on secondary cosmic rays with the upcoming DRAGON2 code". In: *JCAP* 2021.3, 099, p. 099. DOI: `10.1088/1475-7516/2021/03/099`. arXiv: `2101.01547 [astro-ph.HE]`.

De La Torre Luque, P. et al. (2023). "Galactic diffuse gamma rays meet the PeV frontier". In: *A&A* 672, A58, A58. DOI: `10.1051/0004-6361/202243714`. arXiv: `2203.15759 [astro-ph.HE]`.

Dermer, C. D. (1986). "Secondary production of neutral pi-mesons and the diffuse galactic gamma radiation". In: *A&A* 157, pp. 223–229.

Di Bernardo, G. et al. (2013). "Cosmic ray electrons, positrons and the synchrotron emission of the Galaxy: consistent analysis and implications". In: *JCAP* 3, 036, p. 036. DOI: `10.1088/1475-7516/2013/03/036`. arXiv: `1210.4546 [astro-ph.HE]`.

Dickman, R. L. (1975). "A survey of carbon monoxide emission in dark clouds". In: *ApJ* 202, pp. 50–57. DOI: `10.1086/153951`.

Domínguez, A. et al. (2011). "Extragalactic background light inferred from AEGIS galaxy-SED-type fractions". In: *MNRAS* 410.4, pp. 2556–2578. DOI: `10.1111/j.1365-2966.2010.17631.x`. arXiv: `1007.1459 [astro-ph.CO]`.

Donato, F., D. Maurin, and R. Taillet (2002). "beta -radioactive cosmic rays in a diffusion model: Test for a local bubble?" In: *A&A* 381, pp. 539–559. DOI: `10.1051/0004-6361:20011447`. eprint: `astro-ph/0108079`.

Drury, L. O. et al. (2001). "Test of galactic cosmic-ray source models - Working Group Report". In: *SSRv* 99, pp. 329–352.

Dundovic, A. et al. (2021). "Simulating the Galactic multi-messenger emissions with HERMES". In: *A&A* 653, A18, A18. DOI: 10.1051/0004-6361/202140801. arXiv: 2105.13165 [astro-ph.HE].

Einstein, Albert (1916). "Näherungsweise Integration der Feldgleichungen der Gravitation". In: *Sitzungsberichte der Königlich Preussischen Akademie der Wissenschaften*, pp. 688–696.

Ellis, John et al. (1984). "Supersymmetric relics from the big bang". In: *Nuclear Physics B* 238.2, pp. 453–476. DOI: 10.1016/0550-3213(84)90461-9.

Elmegreen, B. G. and J. Scalo (2004). "Interstellar Turbulence I: Observations and Processes". In: *ARA&A* 42, pp. 211–273. DOI: 10.1146/annurev.astro.41.011802.094859. eprint: astro-ph/0404451.

Evoli, C. et al. (2008). "Cosmic ray nuclei, antiprotons and gamma rays in the galaxy: a new diffusion model". In: *JCAP* 10, 018, p. 018. DOI: 10.1088/1475-7516/2008/10/018. arXiv: 0807.4730.

– (2012). "Common Solution to the Cosmic Ray Anisotropy and Gradient Problems". In: *Physical Review Letters* 108.21, 211102, p. 211102. DOI: 10.1103/PhysRevLett.108.211102. arXiv: 1203.0570 [astro-ph.HE].

Evoli, C. et al. (2017a). "Cosmic-ray propagation with DRAGON2: I. numerical solver and astrophysical ingredients". In: *JCAP* 2, 015, p. 015. DOI: 10.1088/1475-7516/2017/02/015. arXiv: 1607.07886 [astro-ph.HE].

Evoli, C. et al. (2017b). "Cosmic-ray propagation with DRAGON2: II. Nuclear interactions with the interstellar gas". In: *ArXiv e-prints*. arXiv: 1711.09616 [astro-ph.HE].

Evoli, Carmelo et al. (2018). "Cosmic-ray propagation with DRAGON2: II. Nuclear interactions with the interstellar gas". In: *JCAP* 2018.7, 006, p. 006. DOI: 10.1088/1475-7516/2018/07/006. arXiv: 1711.09616 [astro-ph.HE].

Fan, Yi-Zhong and Tsvi Piran (2008). "High-energy γ-ray emission from gamma-ray bursts — before GLAST". In: *Frontiers of Physics in China* 3.3, pp. 306–330. DOI: 10.1007/s11467-008-0033-z. arXiv: 0805.2221 [astro-ph].

Fatuzzo, M. and F. Melia (2012). "Diffusive Cosmic-Ray Acceleration in Sagittarius A*". In: *ApJL* 757.1, L16, p. L16. DOI: 10.1088/2041-8205/757/1/L16. arXiv: 1208.4658 [astro-ph.GA].

Feng, Jonathan L. (2010). "Dark Matter Candidates from Particle Physics and Methods of Detection". In: *ARA&A* 48, pp. 495–545. DOI: 10.1146/annurev-astro-082708-101659. arXiv: 1003.0904 [astro-ph.CO].

Feng, Jonathan L. and Jason Kumar (2008). "Dark-Matter Particles without Weak-Scale Masses or Weak Interactions". In: *PhRvL* 101.23, 231301, p. 231301. DOI: 10.1103/PhysRevLett.101.231301. arXiv: 0803.4196 [hep-ph].

Fermi, E. (1949). "On the Origin of the Cosmic Radiation". In: *Physical Review* 75, pp. 1169–1174. DOI: 10.1103/PhysRev.75.1169.

Ferrière, K., W. Gillard, and P. Jean (2007). "Spatial distribution of interstellar gas in the innermost 3 kpc of our galaxy". In: *A&A* 467, pp. 611–627. DOI: 10.1051/0004-6361:20066992. eprint: astro-ph/0702532.

Fichtel, C. E. et al. (1975). "High-energy gamma-ray results from the second small astronomy satellite". In: *ApJ* 198, pp. 163–182. DOI: 10.1086/153590.

Figer, D. F. et al. (2004). "An Extended Star Formation History for the Galactic Center from Hubble Space Telescope NICMOS Observations". In: *ApJ* 601, pp. 319–339. DOI: 10.1086/380392. eprint: astro-ph/0309757.

Finke, Justin D., Soebur Razzaque, and Charles D. Dermer (2010). "Modeling the Extragalactic Background Light from Stars and Dust". In: *ApJ* 712.1, pp. 238–249. DOI: 10.1088/0004-637X/712/1/238. arXiv: 0905.1115 [astro-ph.HE].

Fomin, V. P. et al. (1994). "New methods of atmospheric Cherenkov imaging for gamma-ray astronomy. I. The false source method". In: *Astroparticle Physics* 2.2, pp. 137–150. DOI: 10.1016/0927-6505(94)90036-1.

Forbush, S. E. (1954). "World-Wide Cosmic-Ray Variations, 1937-1952". In: *J. Geophys. Res.* 59, pp. 525–542. DOI: 10.1029/JZ059i004p00525.

Fossati, G. et al. (1998). "A unifying view of the spectral energy distributions of blazars". In: *MNRAS* 299.2, pp. 433–448. DOI: 10.1046/j.1365-8711.1998.01828.x. arXiv: astro-ph/9804103 [astro-ph].

Fraija, N. and M. Araya (2016). "The Gigaelectronvolt Counterpart of VER J2019+407 in the Northern Shell of the Supernova Remnant G78.2+2.1 (γ Cygni)". In: *ApJ* 826.1, 31, p. 31. DOI: 10.3847/0004-637X/826/1/31. arXiv: 1605.00571 [astro-ph.HE].

Franceschini, A., G. Rodighiero, and M. Vaccari (2008). "Extragalactic optical-infrared background radiation, its time evolution and the cosmic photon-photon opacity". In: *A&A* 487.3, pp. 837–852. DOI: 10.1051/0004-6361:200809691. arXiv: 0805.1841 [astro-ph].

Frank, I. M. and I. E. Tamm (1937). "Coherent visible radiation of fast electrons passing through matter". In: *Compt. Rend. Acad. Sci. URSS* 14.3, pp. 109–114. DOI: 10.3367/UFNr.0093.196710o.0388.

Fruck, C. et al. (2011). "Atmospheric Evaluation with LIDAR for Magic". In: *Cosmic Rays for Particle and Astroparticle Physics*. Ed. by S. Giani, C. Leroy, and P. G. Rancoita, pp. 167–172. DOI: 10.1142/9789814329033_0022.

Fruck, Christian (2015). "The galactic center resolved with MAGIC and a new technique for atmospheric calibration". PhD thesis. Munich University of Technology, Germany.

Fruck, Christian et al. (2014). "A novel LIDAR-based Atmospheric Calibration Method for Improving the Data Analysis of MAGIC". In: *arXiv e-prints*, arXiv:1403.3591, arXiv:1403.3591. DOI: 10.48550/arXiv.1403.3591. arXiv: 1403.3591 [astro-ph.IM].

Fryer, Chris et al. (2019). "Core-Collapse Supernovae and Multi-Messenger Astronomy". In: *BAAS* 51.3, 122, p. 122.

Fujita, Yutaka, Kohta Murase, and Shigeo S. Kimura (2017). "Sagittarius A* as an origin of the Galactic PeV cosmic rays?" In: *JCAP* 2017.4, 037, p. 037. DOI: 10.1088/1475-7516/2017/04/037. arXiv: 1604.00003 [astro-ph.HE].

Fukami, S. et al. (2022). "Very-high-energy gamma-ray emission from GRB 201216C detected by MAGIC". In: *37th International Cosmic Ray Conference*, p. 788. DOI: 10.22323/1.395.0788.

Fuke, H. et al. (2005). "Search for Cosmic-Ray Antideuterons". In: *PhRvL* 95.8, 081101, p. 081101. DOI: 10.1103/PhysRevLett.95.081101. arXiv: astro-ph/0504361 [astro-ph].

Fukugita, M., C. J. Hogan, and P. J. E. Peebles (1998). "The Cosmic Baryon Budget". In: *ApJ* 503.2, pp. 518–530. DOI: 10.1086/306025. arXiv: astro-ph/9712020 [astro-ph].

Funk, S. (2008). "VHE Gamma-ray supernova remnants". In: *Advances in Space Research* 41, pp. 464–472. DOI: 10.1016/j.asr.2007.04.076. eprint: astro-ph/0701471.

Funk, Stefan (2015a). "Ground- and Space-Based Gamma-Ray Astronomy". In: *Annual Review of Nuclear and Particle Science* 65, pp. 245–277. DOI: 10.1146/annurev-nucl-102014-022036. arXiv: 1508.05190 [astro-ph.HE].

– (2015b). "Indirect detection of dark matter with γ rays". In: *Proceedings of the National Academy of Science* 112.40, pp. 12264–12271. DOI: 10.1073/pnas.1308728111. arXiv: 1310.2695 [astro-ph.HE].

Gaensler, Bryan M. and Patrick O. Slane (2006). "The Evolution and Structure of Pulsar Wind Nebulae". In: *ARA&A* 44.1, pp. 17–47. DOI: 10.1146/annurev.astro.44.051905.092528. arXiv: astro-ph/0601081 [astro-ph].

Gaggero, D. et al. (2013). "Three-Dimensional Model of Cosmic-Ray Lepton Propagation Reproduces Data from the Alpha Magnetic Spectrometer on the International Space Station". In: *Physical Review Letters* 111.2, 021102, p. 021102. DOI: 10.1103/PhysRevLett.111.021102. arXiv: 1304.6718 [astro-ph.HE].

Gaggero, D. et al. (2015a). "Gamma-ray sky points to radial gradients in cosmic-ray transport". In: *PhRvD* 91.8, 083012, p. 083012. DOI: 10.1103/PhysRevD.91.083012. arXiv: 1411.7623 [astro-ph.HE].

Gaggero, D. et al. (2015b). "The Gamma-Ray and Neutrino Sky: A Consistent Picture of Fermi-LAT, Milagro, and IceCube Results". In: *ApJL* 815, L25, p. L25. DOI: 10.1088/2041-8205/815/2/L25. arXiv: 1504.00227 [astro-ph.HE].

Gaggero, D. et al. (2015c). "Towards a realistic astrophysical interpretation of the gamma-ray Galactic center excess". In: *JCAP* 12, 056, p. 056. DOI: 10.1088/1475-7516/2015/12/056. arXiv: 1507.06129 [astro-ph.HE].

Gaggero, D. et al. (2017a). "Diffuse Cosmic Rays Shining in the Galactic Center: A Novel Interpretation of H.E.S.S. and Fermi-LAT γ -Ray Data". In: *Physical Review Letters* 119.3, 031101, p. 031101. DOI: 10.1103/PhysRevLett.119.031101. arXiv: 1702.01124 [astro-ph.HE].

Gaggero, D. et al. (2017b). "Hard Cosmic Ray Sea in the Galactic Center: a consistent interpretation of H.E.S.S. and *Fermi*-LAT γ-ray data". In: *ArXiv e-prints*. arXiv: 1707.08473 [astro-ph.HE].

– (2017c). "The very high energy gamma-ray (and neutrino) Galactic Center diffuse emission". In: *Proceedings of the European Physical Society Conference on High Energy Physics. 5-12 July*, p. 14. DOI: 10.22323/1.314.0014.

Gaggero, Daniele et al. (2014). "PAMELA and AMS-02 e$^+$ and e$^-$ spectra are reproduced by three-dimensional cosmic-ray modeling". In: *PhRvD* 89.8, 083007, p. 083007. DOI: 10.1103/PhysRevD.89.083007. arXiv: 1311.5575 [astro-ph.HE].

Gammaldi, V. et al. (2016). "Analysis of the very inner Milky Way dark matter distribution and gamma-ray signals". In: *PhRvD* 94.12, 121301, p. 121301. DOI: 10.1103/PhysRevD.94.121301. arXiv: 1607.02012 [astro-ph.HE].

Garrappa, S. and S. Buson (2019). "Fermi-LAT detection of increasing gamma-ray activity of the blazar BL Lacertae". In: *The Astronomer's Telegram* 12718, p. 1.

Gaug, Markus (2006). "Calibration of the MAGIC telescope and observation of gamma ray bursts". PhD thesis. Autonomous University of Barcelona, Spain.

Gehrels, Neil and Péter Mészáros (2012). "Gamma-Ray Bursts". In: *Science* 337.6097, p. 932. DOI: 10.1126/science.1216793. arXiv: 1208.6522 [astro-ph.HE].

Genzel, R., F. Eisenhauer, and S. Gillessen (2010). "The Galactic Center massive black hole and nuclear star cluster". In: *Reviews of Modern Physics* 82, pp. 3121–3195. DOI: 10.1103/RevModPhys.82.3121. arXiv: 1006.0064.

Ghisellini, G., F. Haardt, and R. Svensson (1998). "Thermalization by synchrotron absorption in compact sources: electron and photon distributions". In: *MNRAS* 297.2, pp. 348–354. DOI: 10.1046/j.1365-8711.1998.01442.x. arXiv: astro-ph/9712166 [astro-ph].

Ghisellini, G. and L. Maraschi (1996). "High energy variability and blazar emission models." In: *Blazar Continuum Variability*. Ed. by H. Richard Miller, James R. Webb, and John C. Noble. Vol. 110. Astronomical Society of the Pacific Conference Series, pp. 436–449.

Ghisellini, G., F. Tavecchio, and M. Chiaberge (2005). "Structured jets in TeV BL Lac objects and radiogalaxies. Implications for the observed properties". In: *A&A* 432.2, pp. 401–410. DOI: 10.1051/0004-6361:20041404. arXiv: astro-ph/0406093 [astro-ph].

Ghisellini, G. et al. (1998). "A theoretical unifying scheme for gamma-ray bright blazars". In: *MNRAS* 301.2, pp. 451–468. DOI: 10.1046/j.1365-8711.1998.02032.x. arXiv: astro-ph/9807317 [astro-ph].

Ghisellini, G. et al. (2011). "The transition between BL Lac objects and flat spectrum radio quasars". In: *MNRAS* 414.3, pp. 2674–2689. DOI: 10.1111/j.1365-2966.2011.18578.x. arXiv: 1012.0308 [astro-ph.CO].

Ghisellini, G. et al. (2017). "The Fermi blazar sequence". In: *MNRAS* 469.1, pp. 255–266. DOI: 10.1093/mnras/stx806. arXiv: 1702.02571 [astro-ph.HE].

Giannios, Dimitrios, Dmitri A. Uzdensky, and Mitchell C. Begelman (2009). "Fast TeV variability in blazars: jets in a jet". In: *MNRAS* 395.1, pp. L29–L33. DOI: 10.1111/j.1745-3933.2009.00635.x. arXiv: 0901.1877 [astro-ph.HE].

Gilmore, Rudy C. et al. (2012). "Semi-analytic modelling of the extragalactic background light and consequences for extragalactic gamma-ray spectra". In: *MNRAS* 422.4, pp. 3189–3207. DOI: 10.1111/j.1365-2966.2012.20841.x. arXiv: 1104.0671 [astro-ph.CO].

Gini, Corrado (1921). "Measurement of Inequality of Incomes". In: *The Economic Journal* 31.121, pp. 124–125. ISSN: 0013-0133. DOI: 10.2307/2223319. eprint: https://academic.oup.com/ej/article-pdf/31/121/124/27606330/ej0124.pdf. URL: https://doi.org/10.2307/2223319.

Ginzburg, V. L. and S. I. Syrovatskii (1964). *The Origin of Cosmic Rays*.

Giommi, P., P. Padovani, and E. Perlman (2000). "Detection of exceptional X-ray spectral variability in the TeV BL Lac 1ES 2344+514". In: *MNRAS* 317.4, pp. 743–749. DOI: 10.1046/j.1365-8711.2000.03353.x. arXiv: astro-ph/9907377 [astro-ph].

Glampedakis, Kostas and Leonardo Gualtieri (2018). "Gravitational Waves from Single Neutron Stars: An Advanced Detector Era Survey". In: *Astrophysics and Space Science Library*. Ed. by Luciano Rezzolla et al. Vol. 457. Astrophysics and Space Science Library, p. 673. DOI: 10.1007/978-3-319-97616-7_12. arXiv: 1709.07049 [astro-ph.HE].

Górski, K. M. et al. (2005). "HEALPix: A Framework for High-Resolution Discretization and Fast Analysis of Data Distributed on the Sphere". In: *ApJ* 622, pp. 759–771. DOI: 10.1086/427976. eprint: astro-ph/0409513.

Grasso, D. and L. Maccione (2005). "Sgr A East as a possible high energy neutron factory in the Galactic Centre". In: *Astroparticle Physics* 24, pp. 273–288. DOI: 10.1016/j.astropartphys.2005.07.005. eprint: astro-ph/0504323.

Grasso, D. et al. (2009). "On possible interpretations of the high energy electron-positron spectrum measured by the Fermi Large Area Telescope". In: *Astroparticle Physics* 32, pp. 140–151. DOI: 10.1016/j.astropartphys.2009.07.003. arXiv: 0905.0636 [astro-ph.HE].

Grasso, D. et al. (2017). "Hard Cosmic Ray Sea in the Galactic Center: a consistent interpretation of H.E.S.S. and Fermi-LAT γ -ray data". In: *35th International Cosmic Ray Conference (ICRC2017)*. Vol. 301. International Cosmic Ray Conference, p. 739. DOI: 10.22323/1.301.0739.

Greisen, K. (1966). "End to the Cosmic-Ray Spectrum?" In: *Physical Review Letters* 16, pp. 748–750. DOI: 10.1103/PhysRevLett.16.748.

Guépin, Claire et al. (2018). "Pevatron at the Galactic Center: multi-wavelength signatures from millisecond pulsars". In: *JCAP* 2018.7, 042, p. 042. DOI: 10.1088/1475-7516/2018/07/042. arXiv: 1806.03307 [astro-ph.HE].

Gueta, O. (2022). "The Cherenkov Telescope Array: layout, design and performance". In: *37th International Cosmic Ray Conference*, p. 885. DOI: 10.22323/1.395.0885. arXiv: 2108.04512 [astro-ph.IM].

Guo, Yi-Qing et al. (2013). "A hybrid model of GeV-TeV gamma ray emission from the Galactic center". In: *Journal of Physics G Nuclear Physics* 40.6, 065201, p. 065201. DOI: 10.1088/0954-3899/40/6/065201. arXiv: 1303.6394 [astro-ph.HE].

H. E. S. S. Collaboration et al. (2014). "Search for extended γ-ray emission around AGN with H.E.S.S. and Fermi-LAT". In: *A&A* 562, A145, A145. DOI: 10.1051/0004-6361/201322510. arXiv: 1401.2915 [astro-ph.HE].

H. E. S. S. Collaboration et al. (2017). "Characterizing the γ-ray long-term variability of PKS 2155-304 with H.E.S.S. and Fermi-LAT". In: *A&A* 598, A39, A39. DOI: 10.1051/0004-6361/201629419. arXiv: 1610.03311 [astro-ph.HE].

H. E. S. S. Collaboration et al. (2018a). "Characterising the VHE diffuse emission in the central 200 parsecs of our Galaxy with H.E.S.S." In: *A&A* 612, A9, A9. DOI: 10.1051/0004-6361/201730824. arXiv: 1706.04535 [astro-ph.HE].

H. E. S. S. Collaboration et al. (2018b). "Detection of variable VHE γ-ray emission from the extra-galactic γ-ray binary LMC P3". In: *A&A* 610, L17, p. L17. DOI: 10.1051/0004-6361/201732426. arXiv: 1801.06322 [astro-ph.HE].

H. E. S. S. Collaboration et al. (2018c). "HESS J1741-302: a hidden accelerator in the Galactic plane". In: *A&A* 612, A13, A13. DOI: 10.1051/0004-6361/201730581. arXiv: 1711.01350 [astro-ph.HE].

H. E. S. S. Collaboration et al. (2018d). "The H.E.S.S. Galactic plane survey". In: *A&A* 612, A1, A1. DOI: 10.1051/0004-6361/201732098. arXiv: 1804.02432 [astro-ph.HE].

H. E. S. S. Collaboration et al. (2018e). "The population of TeV pulsar wind nebulae in the H.E.S.S. Galactic Plane Survey". In: *A&A* 612, A2, A2. DOI: 10.1051/0004-6361/201629377. arXiv: 1702.08280 [astro-ph.HE].

H. E. S. S. Collaboration et al. (2020a). "Detection of very-high-energy γ-ray emission from the colliding wind binary η Car with H.E.S.S." In: *A&A* 635, A167, A167. DOI: 10.1051/0004-6361/201936761. arXiv: 2002.02336 [astro-ph.HE].

H. E. S. S. Collaboration et al. (2020b). "Resolving acceleration to very high energies along the jet of Centaurus A". In: *Nature* 582.7812, pp. 356–359. DOI: 10.1038/s41586-020-2354-1. arXiv: 2007.04823 [astro-ph.HE].

H. E. S. S. Collaboration et al. (2021). "H.E.S.S. and MAGIC observations of a sudden cessation of a very-high-energy γ-ray flare in PKS 1510−089 in May 2016". In: *A&A* 648, A23, A23. DOI: 10.1051/0004-6361/202038949. arXiv: 2012.10254 [astro-ph.HE].

Hagen-Thorn, V. A. et al. (2002). "Analysis of the long-term polarization behaviour of BL Lac". In: *A&A* 385, pp. 55–61. DOI: 10.1051/0004-6361:20020145.

Halpern, J. P. and S. S. Holt (1992). "Discovery of soft X-ray pulsations from the γ-ray source Geminga". In: *Nature* 357.6375, pp. 222–224. DOI: 10.1038/357222a0.

Hartman, R. C. et al. (1999). "The Third EGRET Catalog of High-Energy Gamma-Ray Sources". In: *ApJS* 123.1, pp. 79–202. DOI: 10.1086/313231.

Haungs, Andreas, Heinigerd Rebel, and Markus Roth (2003). "Energy spectrum and mass composition of high-energy cosmic rays". In: *Reports on Progress in Physics* 66.7, pp. 1145–1206. DOI: `10.1088/0034-4885/66/7/202`.

Hauser, Michael G. and Eli Dwek (2001). "The Cosmic Infrared Background: Measurements and Implications". In: *ARA&A* 39, pp. 249–307. DOI: `10.1146/annurev.astro.39.1.249`. arXiv: `astro-ph/0105539 [astro-ph]`.

Heck, D. et al. (1998). *CORSIKA: a Monte Carlo code to simulate extensive air showers.*

Helder, E. A. et al. (2009). "Measuring the Cosmic-Ray Acceleration Efficiency of a Supernova Remnant". In: *Science* 325, p. 719. DOI: `10.1126/science.1173383`. arXiv: `0906.4553 [astro-ph.GA]`.

Hervet, O., C. Boisson, and H. Sol (2016). "An innovative blazar classification based on radio jet kinematics". In: *A&A* 592, A22, A22. DOI: `10.1051/0004-6361/201628117`. arXiv: `1605.02272 [astro-ph.HE]`.

Hess, F. V. (1912). "Ü ber Beobachtungen der durchdringenden Strahlung bei sieben Freiballonfahrt." In: *Physikalische Zeitschrif* 13, 1084.

HESS Collaboration et al. (2016). "Acceleration of petaelectronvolt protons in the Galactic Centre". In: *Nature* 531, pp. 476–479. DOI: `10.1038/nature17147`. arXiv: `1603.07730 [astro-ph.HE]`.

Hillas, A. M. (1984). "The Origin of Ultra-High-Energy Cosmic Rays". In: *ARA&A* 22, pp. 425–444. DOI: `10.1146/annurev.aa.22.090184.002233`.

– (1985). "Cerenkov Light Images of EAS Produced by Primary Gamma Rays and by Nuclei". In: *19th International Cosmic Ray Conference (ICRC19), Volume 3*. Vol. 3. International Cosmic Ray Conference, p. 445.

Hinshaw, G. et al. (2013). "Nine-year Wilkinson Microwave Anisotropy Probe (WMAP) Observations: Cosmological Parameter Results". In: *ApJS* 208.2, 19, p. 19. DOI: `10.1088/0067-0049/208/2/19`. arXiv: `1212.5226 [astro-ph.CO]`.

Hinton, J. A. and F. A. Aharonian (2007). "Inverse Compton Scenarios for the TeV Gamma-Ray Emission of the Galactic Center". In: *ApJ* 657, pp. 302–307. DOI: `10.1086/510283`. eprint: `astro-ph/0607557`.

Hinton, J. A. and W. Hofmann (2009). "Teraelectronvolt Astronomy". In: *ARA&A* 47.1, pp. 523–565. DOI: `10.1146/annurev-astro-082708-101816`. arXiv: `1006.5210 [astro-ph.HE]`.

Hirotani, Kouichi and Hung-Yi Pu (2016). "Energetic Gamma Radiation from Rapidly Rotating Black Holes". In: *ApJ* 818.1, 50, p. 50. DOI: `10.3847/0004-637X/818/1/50`. arXiv: `1512.05026 [astro-ph.HE]`.

Horns, D. (2005). "TeV γ-radiation from Dark Matter annihilation in the Galactic center". In: *Physics Letters B* 607.3-4, pp. 225–232. DOI: `10.1016/j.physletb.2004.12.057`. arXiv: `astro-ph/0408192 [astro-ph]`.

Hovatta, T. et al. (2009). "Doppler factors, Lorentz factors and viewing angles for quasars, BL Lacertae objects and radio galaxies". In: *A&A* 494.2, pp. 527–537. DOI: `10.1051/0004-6361:200811150`. arXiv: `0811.4278 [astro-ph]`.

Huettemeister, S. et al. (1998). "Molecular gas in the Galactic center region. III. Probing shocks in molecular cores". In: *A&A* 334, pp. 646–658. eprint: `astro-ph/9803054`.

Hunter, S. D. et al. (1997). "EGRET Observations of the Diffuse Gamma-Ray Emission from the Galactic Plane". In: *ApJ* 481, pp. 205–240. DOI: `10.1086/304012`.

Ibarra, Alejandro, David Tran, and Christoph Weniger (2013). "Indirect Searches for Decaying Dark Matter". In: *International Journal of Modern Physics A* 28.27, 1330040, p. 1330040. DOI: `10.1142/S0217751X13300408`. arXiv: `1307.6434 [hep-ph]`.

IceCube Collaboration (2013). "Evidence for High-Energy Extraterrestrial Neutrinos at the IceCube Detector". In: *Science* 342.6161, 1242856, p. 1242856. DOI: `10.1126/science.1242856`. arXiv: `1311.5238 [astro-ph.HE]`.

IceCube Collaboration et al. (2018a). "Multimessenger observations of a flaring blazar coincident with high-energy neutrino IceCube-170922A". In: *Science* 361.6398, eaat1378, eaat1378. DOI: `10.1126/science.aat1378`. arXiv: `1807.08816 [astro-ph.HE]`.

IceCube Collaboration et al. (2018b). "Neutrino emission from the direction of the blazar TXS 0506+056 prior to the IceCube-170922A alert". In: *Science* 361.6398, pp. 147–151. DOI: `10.1126/science.aat2890`. arXiv: `1807.08794 [astro-ph.HE]`.

Icecube Collaboration et al. (2023). "Observation of high-energy neutrinos from the Galactic plane". In: *Science* 380.6652, pp. 1338–1343. DOI: `10.1126/science.adc9818`. arXiv: `2307.04427 [astro-ph.HE]`.

Inoue, Susumu et al. (2013). "Gamma-ray burst science in the era of the Cherenkov Telescope Array". In: *Astroparticle Physics* 43, pp. 252–275. DOI: `10.1016/j.astropartphys.2013.01.004`. arXiv: `1301.3014 [astro-ph.HE]`.

Johnson, S. P., H. Dong, and Q. D. Wang (2009). "A large-scale survey of X-ray filaments in the Galactic Centre". In: *MNRAS* 399.3, pp. 1429–1440. DOI: `10.1111/j.1365-2966.2009.15362.x`. arXiv: `0910.4944 [astro-ph.HE]`.

Jormanainen, J. et al. (2022). "Confronting observations of VHE gamma-ray blazar flares with reconnection models". In: *37th International Cosmic Ray Conference*, p. 867. DOI: `10.22323/1.395.0867`. arXiv: `2109.08529 [astro-ph.HE]`.

Jorstad, Svetlana G. et al. (2005). "Polarimetric Observations of 15 Active Galactic Nuclei at High Frequencies: Jet Kinematics from Bimonthly Monitoring with the Very Long Baseline Array". In: *AJ* 130.4, pp. 1418–1465. DOI: `10.1086/444593`. arXiv: `astro-ph/0502501 [astro-ph]`.

Jouvin, L., A. Lemière, and R. Terrier (2017). "Does the SN rate explain the very high energy cosmic rays in the central 200 pc of our Galaxy?" In: *MNRAS* 467, pp. 4622–4630. DOI: `10.1093/mnras/stx361`. arXiv: `1703.10398 [astro-ph.HE]`.

Kalberla, P. M. W. and L. Dedes (2008). "Global properties of the H I distribution in the outer Milky Way. Planar and extra-planar gas". In: *A&A* 487, pp. 951–963. DOI: `10.1051/0004-6361:20079240`. arXiv: `0804.4831`.

Katz, U. F. (2020). "Cherenkov light imaging in astroparticle physics". In: *Nuclear Instruments and Methods in Physics Research A* 952, 161654, p. 161654. DOI: `10.1016/j.nima.2018.11.113`. arXiv: `1901.00146 [astro-ph.IM]`.

Kaufmann, S. et al. (2011). "1ES 0229+200: an extreme blazar with a very high minimum Lorentz factor". In: *A&A* 534, A130, A130. DOI: `10.1051/0004-6361/201117215`. arXiv: `1109.3628 [astro-ph.HE]`.

Kellermann, H. et al. (2012). "Absolute Measurement of the Reflectivity and the Point Spread Function of the MAGIC Telescopes". In: *Astroparticle*, pp. 77–81. DOI: `10.1142/9789814405072_0014`.

Kellermann, K. I. et al. (1989). "VLA Observations of Objects in the Palomar Bright Quasar Survey". In: *AJ* 98, p. 1195. DOI: `10.1086/115207`.

Kellermann, K. I. et al. (2003). "Superluminal Motion and Relativistic Beaming in Blazar Jets". In: *High Energy Blazar Astronomy*. Ed. by Leo O. Takalo and Esko Valtaoja. Vol. 299. Astronomical Society of the Pacific Conference Series, p. 117. DOI: `10.48550/arXiv.astro-ph/0211398`. arXiv: `astro-ph/0211398 [astro-ph]`.

Kerr, F. J. and D. Lynden-Bell (1986). "Review of galactic constants". In: *MNRAS* 221, pp. 1023–1038. DOI: `10.1093/mnras/221.4.1023`.

Kerr, M. (2019). "Fermi LAT Detection of the Recent Glitch in the Vela Pulsar (PSR J0835-4510)". In: *The Astronomer's Telegram* 12481, p. 1.

Kobayashi, Shiho and Peter Mészáros (2003). "Gravitational Radiation from Gamma-Ray Burst Progenitors". In: *ApJ* 589.2, pp. 861–870. DOI: `10.1086/374733`. arXiv: `astro-ph/0210211 [astro-ph]`.

Kohnle, A. et al. (1996). "Stereoscopic imaging of air showers with the first two HEGRA Cherenkov telescopes". In: *Astroparticle Physics* 5.2, pp. 119–131. DOI: `10.1016/0927-6505(96)00011-4`.

Kolmogorov, A. N. (1991). "The local structure of turbulence in incompressible viscous fluid for very large Reynolds numbers". In: *Proceedings of the Royal Society of London Series A* 434, pp. 9–13. DOI: `10.1098/rspa.1991.0075`.

Kopper, C. and IceCube Collaboration (2017). "Observation of Astrophysical Neutrinos in Six Years of IceCube Data". In: *35th International Cosmic Ray Conference (ICRC2017)*. Vol. 301. International Cosmic Ray Conference, p. 981. DOI: `10.22323/1.301.0981`.

Kosack, K. et al. (2004). "TeV Gamma-Ray Observations of the Galactic Center". In: *ApJL* 608, pp. L97–L100. DOI: `10.1086/422469`. eprint: `astro-ph/0403422`.

Kraichnan, R. H. (1965). "Inertial-Range Spectrum of Hydromagnetic Turbulence". In: *Physics of Fluids* 8, pp. 1385–1387. DOI: `10.1063/1.1761412`.

Kranich, D. (2003). "TeV Observations of BL Lac Objects (Invited Talk)". In: *High Energy Blazar Astronomy*. Ed. by Leo O. Takalo and Esko Valtaoja. Vol. 299. Astronomical Society of the Pacific Conference Series, p. 3.

Krawczynski, H. et al. (2004). "Multiwavelength Observations of Strong Flares from the TeV Blazar 1ES 1959+650". In: *ApJ* 601.1, pp. 151–164. DOI: 10.1086/380393. arXiv: astro-ph/0310158 [astro-ph].

Krymskii, G. F. (1977). "A regular mechanism for the acceleration of charged particles on the front of a shock wave". In: *Akademiia Nauk SSSR Doklady* 234, pp. 1306–1308.

Kumar, Pawan and Bing Zhang (2015). "The physics of gamma-ray bursts & relativistic jets". In: *PhR* 561, pp. 1–109. DOI: 10.1016/j.physrep.2014.09.008. arXiv: 1410.0679 [astro-ph.HE].

Kusunose, Masaaki and Fumio Takahara (2012). "A Leptonic Model of Steady High-energy Gamma-Ray Emission from Sgr A*". In: *ApJ* 748.1, 34, p. 34. DOI: 10.1088/0004-637X/748/1/34. arXiv: 1201.5438 [astro-ph.HE].

Lacroix, Thomas et al. (2016). "Connecting the new H.E.S.S. diffuse emission at the Galactic Center with the Fermi GeV excess: A combination of millisecond pulsars and heavy dark matter?" In: *PhRvD* 94.12, 123008, p. 123008. DOI: 10.1103/PhysRevD.94.123008. arXiv: 1603.05977 [astro-ph.HE].

Lähteenmäki, A. and E. Valtaoja (1999). "Total Flux Density Variations in Extragalactic Radio Sources. III. Doppler Boosting Factors, Lorentz Factors, and Viewing Angles for Active Galactic Nuclei". In: *ApJ* 521.2, pp. 493–501. DOI: 10.1086/307587.

Leane, Rebecca K. and Tracy R. Slatyer (2019). "Revival of the Dark Matter Hypothesis for the Galactic Center Gamma-Ray Excess". In: *PhRvL* 123.24, 241101, p. 241101. DOI: 10.1103/PhysRevLett.123.241101.

Leane, Rebecca K. et al. (2018). "GeV-scale thermal WIMPs: Not even slightly ruled out". In: *PhRvD* 98.2, 023016, p. 023016. DOI: 10.1103/PhysRevD.98.023016. arXiv: 1805.10305 [hep-ph].

Lebrun, F. et al. (1983). "Gamma-rays from atomic and molecular gas in the first galactic quadrant". In: *ApJ* 274, pp. 231–236. DOI: 10.1086/161440.

Lefa, E., F. A. Aharonian, and F. M. Rieger (2011). ""Leading Blob" Model in a Stochastic Acceleration Scenario: The Case of the 2009 Flare of Mkn 501". In: *ApJL* 743.1, L19, p. L19. DOI: 10.1088/2041-8205/743/1/L19. arXiv: 1108.4568 [astro-ph.HE].

Lhaaso Collaboration et al. (2021). "Peta-electron volt gamma-ray emission from the Crab Nebula". In: *Science* 373, pp. 425–430. DOI: 10.1126/science.abg5137. arXiv: 2111.06545 [astro-ph.HE].

Li, T. P. and Y. Q. Ma (1983). "Analysis methods for results in gamma-ray astronomy." In: *ApJ* 272, pp. 317–324. DOI: 10.1086/161295.

LIGO Scientific Collaboration, B. P. Abbott, et al. (2017). "Gravitational Waves and Gamma-Rays from a Binary Neutron Star Merger: GW170817 and GRB 170817A". In: *ApJL* 848.2, L13, p. L13. DOI: 10.3847/2041-8213/aa920c. arXiv: 1710.05834 [astro-ph.HE].

LIGO Scientific Collaboration and Virgo Collaboration, B. P. Abbott, et al. (2016). "Observation of Gravitational Waves from a Binary Black Hole Merger". In: *PhRvL* 116.6, 061102, p. 061102. DOI: `10.1103/PhysRevLett.116.061102`. arXiv: `1602.03837 [gr-qc]`.

Linden, Tim, Elizabeth Lovegrove, and Stefano Profumo (2012). "The Morphology of Hadronic Emission Models for the Gamma-Ray Source at the Galactic Center". In: *ApJ* 753.1, 41, p. 41. DOI: `10.1088/0004-637X/753/1/41`. arXiv: `1203.3539 [astro-ph.HE]`.

Liszt, H. S. and W. B. Burton (1980). "The gas distribution in the central region of the Galaxy. III - A barlike model of the inner-Galaxy gas based on improved H I data". In: *ApJ* 236, pp. 779–797. DOI: `10.1086/157803`.

Liu, H. T. and J. M. Bai (2006). "Absorption of 10-200 GeV Gamma Rays by Radiation from Broad-Line Regions in Blazars". In: *ApJ* 653.2, pp. 1089–1097. DOI: `10.1086/509097`. arXiv: `0807.3135 [astro-ph]`.

Liu, Tong, Wei-Min Gu, and Bing Zhang (2017). "Neutrino-dominated accretion flows as the central engine of gamma-ray bursts". In: *NewAR* 79, pp. 1–25. DOI: `10.1016/j.newar.2017.07.001`. arXiv: `1705.05516 [astro-ph.HE]`.

Lodders, K., H. Palme, and H. P. Gail (2009). "Abundances of the Elements in the Solar System". In: *Landolt Börnstein* 4B, p. 712. DOI: `10.1007/978-3-540-88055-4_34`. arXiv: `0901.1149 [astro-ph.EP]`.

Longair, Malcolm S. (2011). *High Energy Astrophysics*.

Longmore, Steven and J. M. Diederik Kruijssen (2018). "Constraints on the Distribution of Gas and Young Stars in the Galactic Centre in the Context of Interpreting Gamma Ray Emission Features". In: *Galaxies* 6.2, p. 55. DOI: `10.3390/galaxies6020055`. arXiv: `1805.06287 [astro-ph.GA]`.

Lorenz, E. and MAGIC Telescope Design Group (1997). "The design of a 17 m ⌀ air Cerenkov telescope for VHE gamma ray astronomy above 20 GeV". In: *Proceedings of the Fourth Compton Symposium*. Ed. by Charles D. Dermer, Mark S. Strickman, and James D. Kurfess. Vol. 410. American Institute of Physics Conference Series, pp. 1611–1615. DOI: `10.1063/1.54042`.

Lorenz, Eckart and Robert Wagner (2012). "Very-High Energy Gamma-Ray Astronomy: A 23-Year Success Story in Astroparticle Physics". In: *From Ultra Rays to Astroparticles*. Ed. by Brigitte Falkenburg and Wolfgang Rhode, p. 143. DOI: `10.1007/978-94-007-5422-5_6`.

Lucarelli, F. et al. (2008). "The central pixel of the MAGIC telescope for optical observations". In: *Nuclear Instruments and Methods in Physics Research A* 589.3, pp. 415–424. DOI: `10.1016/j.nima.2008.03.007`.

Lunardini, Cecilia and Soebur Razzaque (2012). "High Energy Neutrinos from the Fermi Bubbles". In: *PhRvL* 108.22, 221102, p. 221102. DOI: `10.1103/PhysRevLett.108.221102`. arXiv: `1112.4799 [astro-ph.HE]`.

Mac Low, M.-M. and R. McCray (1988). "Superbubbles in disk galaxies". In: *ApJ* 324, pp. 776–785. DOI: `10.1086/165936`.

Macias, Oscar and Chris Gordon (2014). "Contribution of cosmic rays interacting with molecular clouds to the Galactic Center gamma-ray excess". In: *PhRvD* 89.6, 063515, p. 063515. DOI: 10.1103/PhysRevD.89.063515. arXiv: 1312.6671 [astro-ph.HE].

Macias, Oscar et al. (2018). "Galactic bulge preferred over dark matter for the Galactic centre gamma-ray excess". In: *Nature Astronomy* 2, pp. 387–392. DOI: 10.1038/s41550-018-0414-3. arXiv: 1611.06644 [astro-ph.HE].

Madau, Piero and Lucia Pozzetti (2000). "Deep galaxy counts, extragalactic background light and the stellar baryon budget". In: *MNRAS* 312.2, pp. L9–L15. DOI: 10.1046/j.1365-8711.2000.03268.x. arXiv: astro-ph/9907315 [astro-ph].

Madejski, Greg M. et al. (1999). "X-Ray Observations of BL Lacertae during the 1997 Outburst and Association with Quasar-like Characteristics". In: *ApJ* 521.1, pp. 145–154. DOI: 10.1086/307524. arXiv: astro-ph/9902167 [astro-ph].

MAGIC Collaboration et al. (2008). "Very-High-Energy gamma rays from a Distant Quasar: How Transparent Is the Universe?" In: *Science* 320.5884, p. 1752. DOI: 10.1126/science.1157087. arXiv: 0807.2822 [astro-ph].

MAGIC Collaboration et al. (2019). "A fast, very-high-energy γ-ray flare from BL Lacertae during a period of multi-wavelength activity in June 2015". In: *A&A* 623, A175, A175. DOI: 10.1051/0004-6361/201834010. arXiv: 1901.01733 [astro-ph.HE].

MAGIC Collaboration et al. (2020a). "Broadband characterisation of the very intense TeV flares of the blazar 1ES 1959+650 in 2016". In: *A&A* 638, A14, A14. DOI: 10.1051/0004-6361/201935450. arXiv: 2002.00129 [astro-ph.HE].

MAGIC Collaboration et al. (2020b). "MAGIC observations of the diffuse γ-ray emission in the vicinity of the Galactic center". In: *A&A* 642, A190, A190. DOI: 10.1051/0004-6361/201936896. arXiv: 2006.00623 [astro-ph.HE].

MAGIC Collaboration et al. (2023). "Study of the GeV to TeV morphology of the γ Cygni SNR (G 78.2+2.1) with MAGIC and Fermi-LAT. Evidence for cosmic ray escape". In: *A&A* 670, A8, A8. DOI: 10.1051/0004-6361/202038748. arXiv: 2010.15854 [astro-ph.HE].

MAGIC Collaboration Acciari, V. A. et al. (2020). "An intermittent extreme BL Lac: MWL study of 1ES 2344+514 in an enhanced state". In: *MNRAS* 496.3, pp. 3912–3928. DOI: 10.1093/mnras/staa1702. arXiv: 2006.06796 [astro-ph.HE].

Maier, G. (2019). "Performance of the Cherenkov Telescope Array". In: *36th International Cosmic Ray Conference (ICRC2019)*. Vol. 36. International Cosmic Ray Conference, p. 733. DOI: 10.22323/1.358.0733. arXiv: 1907.08171 [astro-ph.IM].

Maier, G. and J. Holder (2017). "Eventdisplay: An Analysis and Reconstruction Package for Ground-based Gamma-ray Astronomy". In: *35th International Cosmic Ray Conference (ICRC2017)*. Vol. 301. International Cosmic Ray Conference, p. 747. DOI: 10.22323/1.301.0747. arXiv: 1708.04048 [astro-ph.IM].

Majumdar, P. et al. (2005). "Monte Carlo simulation for the MAGIC telescope". In: *29th International Cosmic Ray Conference (ICRC29), Volume 5.* Vol. 5. International Cosmic Ray Conference, p. 203.

Malkov, M. A. and L. O. Drury (2001). "Nonlinear theory of diffusive acceleration of particles by shock waves". In: *Reports on Progress in Physics* 64, pp. 429–481. DOI: 10.1088/0034-4885/64/4/201.

Mannheim, K. (1993). "The proton blazar." In: *A&A* 269, pp. 67–76. DOI: 10.48550/arXiv.astro-ph/9302006. arXiv: astro-ph/9302006 [astro-ph].

– (1998). "Possible Production of High-Energy Gamma Rays from Proton Acceleration in the Extragalactic Radio Source Markarian 501". In: *Science* 279, p. 684. DOI: 10.1126/science.279.5351.684. arXiv: astro-ph/9803241 [astro-ph].

Mannheim, K. and P. L. Biermann (1989). "Photomeson production in active galactic nuclei." In: *A&A* 221, pp. 211–220.

– (1992). "Gamma-ray flaring of 3C 279 : a proton-initiated cascade in the jet ?" In: *A&A* 253, pp. L21–L24.

Marchini, Alessandro et al. (2019). "Enhancement of optical flux from the active blazar BL Lacertae". In: *The Astronomer's Telegram* 12722, p. 1.

Marinelli, A. et al. (2017). "High Energy Neutrino expectations from the Central Molecular Zone". In: *35th International Cosmic Ray Conference (ICRC2017).* Vol. 301. International Cosmic Ray Conference, p. 939. DOI: 10.22323/1.301.0939.

Marscher, Alan P. (2014). "Turbulent, Extreme Multi-zone Model for Simulating Flux and Polarization Variability in Blazars". In: *ApJ* 780.1, 87, p. 87. DOI: 10.1088/0004-637X/780/1/87. arXiv: 1311.7665 [astro-ph.HE].

Marscher, Alan P. et al. (2008). "The inner jet of an active galactic nucleus as revealed by a radio-to-γ-ray outburst". In: *Nature* 452.7190, pp. 966–969. DOI: 10.1038/nature06895.

Massey, Richard, Thomas Kitching, and Johan Richard (2010). "The dark matter of gravitational lensing". In: *Reports on Progress in Physics* 73.8, 086901, p. 086901. DOI: 10.1088/0034-4885/73/8/086901. arXiv: 1001.1739 [astro-ph.CO].

Mastichiadis, A. and J. G. Kirk (1997). "Variability in the synchrotron self-Compton model of blazar emission." In: *A&A* 320, pp. 19–25. DOI: 10.48550/arXiv.astro-ph/9610058. arXiv: astro-ph/9610058 [astro-ph].

Mauerhan, J. C. et al. (2010). "Isolated Wolf-Rayet Stars and O Supergiants in the Galactic Center Region Identified Via Paschen-α Excess". In: *ApJ* 725, 188-199, pp. 188–199. DOI: 10.1088/0004-637X/725/1/188. arXiv: 1009.2769 [astro-ph.SR].

Mayer-Hasselwander, H. A. et al. (1982). "Large-scale distribution of galactic gamma radiation observed by COS-B". In: *A&A* 105.1, pp. 164–175.

Mészáros, P., S. Razzaque, and B. Zhang (2004). "GeV-TeV emission from γ-ray bursts". In: *NewAR* 48.5-6, pp. 445–451. DOI: 10.1016/j.newar.2003.12.022.

Meszaros, P., M. J. Rees, and H. Papathanassiou (1994). "Spectral Properties of Blast-Wave Models of Gamma-Ray Burst Sources". In: *ApJ* 432, p. 181. DOI: `10.1086/174559`. arXiv: `astro-ph/9311071 [astro-ph]`.

Miller, J. S., H. B. French, and S. A. Hawley (1978). "The spectrum and magnitude of the galaxy associated with BL Lacertae." In: *ApJL* 219, pp. L85–L87. DOI: `10.1086/182612`.

Mirabel, I. F. (2012). "Gamma-Ray Binaries Revealed". In: *Science* 335.6065, p. 175. DOI: `10.1126/science.1215895`. arXiv: `1201.3317 [astro-ph.HE]`.

Mirzoyan, R. (1997). "On the Calibration Accuracy of Light Sensors in Atmospheric Cherenkov Fluorescence and Neutrino Experiments". In: *International Cosmic Ray Conference*. Vol. 7. International Cosmic Ray Conference, p. 265.

Mirzoyan, Razmik (2014). "Discovery of Very High Energy Gamma-Ray Emission From Gravitationally Lensed Blazar S3 0218+357 With the MAGIC Telescopes". In: *The Astronomer's Telegram* 6349, p. 1.

– (2019). "MAGIC detection of an increased activity from BL Lacertae at very-high-energy gamma rays". In: *The Astronomer's Telegram* 12724, p. 1.

Mitchell, J. W. et al. (1996). "Measurement of 0.25-3.2 GeV Antiprotons in the Cosmic Radiation". In: *Physical Review Letters* 76, pp. 3057–3060. DOI: `10.1103/PhysRevLett.76.3057`.

Moralejo, A. et al. (2009). "MARS, the MAGIC Analysis and Reconstruction Software". In: *arXiv e-prints*, arXiv:0907.0943, arXiv:0907.0943. DOI: `10.48550/arXiv.0907.0943`. arXiv: `0907.0943 [astro-ph.IM]`.

Morlino, G. et al. (2010). "Spatial structure of X-ray filaments in SN 1006". In: *MNRAS* 405, pp. L21–L25. DOI: `10.1111/j.1745-3933.2010.00851.x`. arXiv: `0912.2972 [astro-ph.HE]`.

Morlino, G. et al. (2021). "Particle acceleration in winds of star clusters". In: *MNRAS* 504.4, pp. 6096–6105. DOI: `10.1093/mnras/stab690`. arXiv: `2102.09217 [astro-ph.HE]`.

Morlino, Giovanni (2021). "Particle acceleration at the termination shock of stellar clusters' wind". In: *arXiv e-prints*, arXiv:2108.01870, arXiv:2108.01870. DOI: `10.48550/arXiv.2108.01870`. arXiv: `2108.01870 [astro-ph.HE]`.

Morris, M. and E. Serabyn (1996). "The Galactic Center Environment". In: *ARA&A* 34, pp. 645–702. DOI: `10.1146/annurev.astro.34.1.645`.

Morris, Paul J., William J. Potter, and Garret Cotter (2019). "The feasibility of magnetic reconnection powered blazar flares from synchrotron self-Compton emission". In: *MNRAS* 486.2, pp. 1548–1562. DOI: `10.1093/mnras/stz920`. arXiv: `1810.04139 [astro-ph.HE]`.

Moskalenko, I. V. and A. W. Strong (1998). "Production and Propagation of Cosmic-Ray Positrons and Electrons". In: *ApJ* 493, pp. 694–707. DOI: `10.1086/305152`. eprint: `astro-ph/9710124`.

Mücke, A. and R. J. Protheroe (2001). "A proton synchrotron blazar model for flaring in Markarian 501". In: *Astroparticle Physics* 15.1, pp. 121–136. DOI: 10.1016/S0927-6505(00)00141-9. arXiv: astro-ph/0004052 [astro-ph].

Mücke, A. et al. (2003). "BL Lac objects in the synchrotron proton blazar model". In: *Astroparticle Physics* 18.6, pp. 593–613. DOI: 10.1016/S0927-6505(02)00185-8. arXiv: astro-ph/0206164 [astro-ph].

Muno, M. P. et al. (2008). "A Catalog of Diffuse X-Ray-emitting Features within 20 pc of Sagittarius A*: Twenty Pulsar Wind Nebulae?" In: *ApJ* 673.1, pp. 251–263. DOI: 10.1086/521641. arXiv: 0707.1907 [astro-ph].

Neronov, Andrii, Dmitri V. Semikoz, and Ksenia Ptitsyna (2017). "Strong constraints on hadronic models of blazar activity from Fermi and IceCube stacking analysis". In: *A&A* 603, A135, A135. DOI: 10.1051/0004-6361/201630098. arXiv: 1611.06338 [astro-ph.HE].

Neshpor, Yu. I. et al. (2001). "BL Lac: A New Ultrahigh-Energy Gamma-Ray Source". In: *Astronomy Reports* 45.4, pp. 249–254. DOI: 10.1134/1.1361316. arXiv: astro-ph/0111448 [astro-ph].

Nilsson, K. et al. (2018). "Long-term optical monitoring of TeV emitting blazars. I. Data analysis". In: *A&A* 620, A185, A185. DOI: 10.1051/0004-6361/201833621. arXiv: 1810.01751 [astro-ph.HE].

Nishimura, J et al. (1997). "Observations of high energy primary electrons and their astrophysical significance". In: *Advances in Space Research* 19.5. Cosmic radiation: Spectra and Composition, pp. 767–770. ISSN: 0273-1177. DOI: https://doi.org/10.1016/S0273-1177(96)00144-5. URL: https://www.sciencedirect.com/science/article/pii/S0273117796001445.

Oort, J. H. (1932). "The force exerted by the stellar system in the direction perpendicular to the galactic plane and some related problems". In: *BAN* 6, p. 249.

Ostankov, A. et al. (2000). "A study of the new hemispherical 6-dynodes PMT from electron tubes". In: *Nuclear Instruments and Methods in Physics Research A* 442.1-3, pp. 117–123. DOI: 10.1016/S0168-9002(99)01208-5.

Otte, Adam Nepomuk (2007). "Observation of VHE γ-rays from the vicinity of magnetized neutron stars and development of new photon-detectors for future ground based γ-ray detectors". PhD thesis. Munich University of Technology, Germany.

Paglione, Timothy A. D. et al. (1996). "Diffuse Gamma-Ray Emission from the Starburst Galaxy NGC 253". In: *ApJ* 460, p. 295. DOI: 10.1086/176969.

Paoletti, R. et al. (2008). "The global trigger system of the magic telescope array". In: *2008 IEEE Nuclear Science Symposium Conference Record*, pp. 2781–2783. DOI: 10.1109/NSSMIC.2008.4774948.

Park, N. and VERITAS Collaboration (2015). "Performance of the VERITAS experiment". In: *34th International Cosmic Ray Conference (ICRC2015)*. Vol. 34. International Cosmic Ray Conference, p. 771. arXiv: 1508.07070 [astro-ph.IM].

Parker, E. N. (1965). "The passage of energetic charged particles through interplanetary space". In: *Planet. Space Sci.* 13, pp. 9–49. DOI: 10.1016/0032-0633(65)90131-5.

Patel, S. et al. (2022). "VTSCat: The VERITAS Catalog of Gamma-Ray Observations". In: *37th International Cosmic Ray Conference*, p. 812. DOI: 10.22323/1.395.0812. arXiv: 2108.06424 [astro-ph.HE].

Patrignani, C. et al. (2016). "Review of Particle Physics". In: *Chin. Phys.* C40.10, p. 100001. DOI: 10.1088/1674-1137/40/10/100001.

Pecimotika, M. et al. (2022). "Performance of the Cherenkov Telescope Array in the presence of clouds". In: *37th International Cosmic Ray Conference*, p. 773. DOI: 10.22323/1.395.0773. arXiv: 2107.14544 [astro-ph.IM].

Perucho, M., V. Bosch-Ramon, and M. V. Barkov (2017). "Impact of red giant/AGB winds on active galactic nucleus jet propagation". In: *A&A* 606, A40, A40. DOI: 10.1051/0004-6361/201630117. arXiv: 1706.06301 [astro-ph.HE].

Pian, Elena et al. (1998). "BeppoSAX Observations of Unprecedented Synchrotron Activity in the BL Lacertae Object Markarian 501". In: *ApJL* 492.1, pp. L17–L20. DOI: 10.1086/311083. arXiv: astro-ph/9710331 [astro-ph].

Pierre Auger Collaboration et al. (2007). "Correlation of the Highest-Energy Cosmic Rays with Nearby Extragalactic Objects". In: *Science* 318, p. 938. DOI: 10.1126/science.1151124. arXiv: 0711.2256.

Pisanti, Ofelia (2019). "Astrophysical neutrinos: theory". In: *Journal of Physics Conference Series*. Vol. 1263. Journal of Physics Conference Series, p. 012004. DOI: 10.1088/1742-6596/1263/1/012004. arXiv: 1906.12258 [astro-ph.CO].

Planck Collaboration et al. (2016). "Planck 2015 results. X. Diffuse component separation: Foreground maps". In: *A&A* 594, A10, A10. DOI: 10.1051/0004-6361/201525967. arXiv: 1502.01588 [astro-ph.CO].

Planck Collaboration et al. (2020). "Planck 2018 results. VI. Cosmological parameters". In: *A&A* 641, A6, A6. DOI: 10.1051/0004-6361/201833910. arXiv: 1807.06209 [astro-ph.CO].

Poincaré, M. (1905). "Sur la dynamique de l'électron". In: *Comptes rendus de l'Académie des Sciences* 140.1507.

Ponti, G. et al. (2015). "The XMM-Newton view of the central degrees of the Milky Way". In: *MNRAS* 453.1, pp. 172–213. DOI: 10.1093/mnras/stv1331. arXiv: 1508.04445 [astro-ph.HE].

Prince, Raj (2021). "Broad-band study of BL Lac during flare of 2020: spectral evolution and emergence of HBL component". In: *MNRAS* 507.4, pp. 5602–5612. DOI: 10.1093/mnras/stab2486. arXiv: 2105.00221 [astro-ph.HE].

Protheroe, R. J. and P. L. Biermann (1997). "Photon-photon absorption above a molecular cloud torus in blazars". In: *Astroparticle Physics* 6.3-4, pp. 293–300. DOI: 10.1016/S0927-6505(96)00063-1. arXiv: astro-ph/9608052 [astro-ph].

Punch, M. et al. (1992). "Detection of TeV photons from the active galaxy Markarian 421". In: *Nature* 358.6386, pp. 477–478. DOI: 10.1038/358477a0.

Pushkin, Kirill and Marcel Villani (2021). *Shielding Materials for Low Radioactive Background Projects*. DOI: 10.13140/RG.2.2.14097.76642.

Qin, Longhua et al. (2023). "Constraints on extragalactic background light using TeV observations of BL Lacertae objects". In: *MNRAS* 521.4, pp. 6219–6227. DOI: 10.1093/mnras/stad531. arXiv: 2302.08032 [astro-ph.HE].

Quinn, J. et al. (1996). "Detection of Gamma Rays with E > 300 GeV from Markarian 501". In: *ApJL* 456, p. L83. DOI: 10.1086/309878.

Raiteri, C. M. et al. (2009). "WEBT multiwavelength monitoring and XMM-Newton observations of <ASTROBJ>BL Lacertae</ASTROBJ> in 2007-2008. Unveiling different emission components". In: *A&A* 507.2, pp. 769–779. DOI: 10.1051/0004-6361/200912953. arXiv: 0909.1701 [astro-ph.HE].

Raiteri, C. M. et al. (2013). "The awakening of BL Lacertae: observations by Fermi, Swift and the GASP-WEBT". In: *MNRAS* 436.2, pp. 1530–1545. DOI: 10.1093/mnras/stt1672. arXiv: 1309.1282 [astro-ph.HE].

Ravasio, M. et al. (2002). "BL Lacertae: Complex spectral variability and rapid synchrotron flare detected with BeppoSAX". In: *A&A* 383, pp. 763–772. DOI: 10.1051/0004-6361:20011828. arXiv: astro-ph/0201307 [astro-ph].

Reeves, Hubert et al. (1973). "On the Origin of Light Elements". In: *ApJ* 179, pp. 909–930. DOI: 10.1086/151928.

Reimer, Anita, Markus Böttcher, and Sara Buson (2019). "Cascading Constraints from Neutrino-emitting Blazars: The Case of TXS 0506+056". In: *ApJ* 881.1, 46, p. 46. DOI: 10.3847/1538-4357/ab2bff. arXiv: 1812.05654 [astro-ph.HE].

Ritt, Stefan (2008). "Design and performance of the 6 GHz waveform digitizing chip DRS4". In: *2008 IEEE Nuclear Science Symposium Conference Record*, pp. 1512–1515. DOI: 10.1109/NSSMIC.2008.4774700.

Roberts, Morton S. (1966). "A High-Resolution 21-CM Hydrogen-Line Survey of the Andromeda Nebula". In: *ApJ* 144, p. 639. DOI: 10.1086/148645.

Robin, A. C. et al. (2003). "A synthetic view on structure and evolution of the Milky Way". In: *A&A* 409, pp. 523–540. DOI: 10.1051/0004-6361:20031117.

Rodríguez-Fernández, N. J. et al. (2001). "Warm H_2 in the Galactic center region". In: *A&A* 365, pp. 174–185. DOI: 10.1051/0004-6361:20000020. eprint: astro-ph/0010182.

Rodríguez-Ramírez, Juan Carlos, Elisabete M. de Gouveia Dal Pino, and Rafael Alves Batista (2019). "Very-high-energy Emission from Magnetic Reconnection in the Radiative-inefficient Accretion Flow of SgrA*". In: *ApJ* 879.1, 6, p. 6. DOI: 10.3847/1538-4357/ab212e. arXiv: 1904.05765 [astro-ph.HE].

Rossi, Bruno Benedetto (1952). *High-energy particles*. Prentice-Hall physics series. New York, NY: Prentice-Hall. URL: https://cds.cern.ch/record/99081.

Roszkowski, Leszek, Enrico Maria Sessolo, and Sebastian Trojanowski (2018). "WIMP dark matter candidates and searches—current status and future prospects". In: *Reports on Progress in Physics* 81.6, 066201, p. 066201. DOI: 10.1088/1361-6633/aab913. arXiv: 1707.06277 [hep-ph].

Rubin, V. C. and Jr. Ford W. K. (1970). "A Comparison of Dynamical Models of the Andromeda Nebula and the Galaxy". In: *The Spiral Structure of our Galaxy*. Ed. by Wilhelm Becker and Georgios Ioannou Kontopoulos. Vol. 38, p. 61.

Saito, Takayuki (2011). "Study of the High Energy Gamma-ray Emission from the Crab Pulsar with the MAGIC telescope and Fermi-LAT". PhD thesis. -.

Sambruna, Rita M. et al. (1999). "ASCA and Contemporaneous Ground-based Observations of the BL Lacertae Objects 1749+096 and 2200+420 (BL Lac)". In: *ApJ* 515.1, pp. 140–152. DOI: 10.1086/307005. arXiv: astro-ph/9810319 [astro-ph].

Sanders, D. B., P. M. Solomon, and N. Z. Scoville (1984). "Giant molecular clouds in the Galaxy. I - The axisymmetric distribution of H2". In: *ApJ* 276, pp. 182–203. DOI: 10.1086/161602.

Sandrinelli, A. et al. (2017). "Gamma-ray and optical oscillations of 0716+714, MRK 421, and BL Lacertae". In: *A&A* 600, A132, A132. DOI: 10.1051/0004-6361/201630288. arXiv: 1701.04454 [astro-ph.HE].

Sawada, T. et al. (2004). "A molecular face-on view of the Galactic Centre region". In: *MNRAS* 349, pp. 1167–1178. DOI: 10.1111/j.1365-2966.2004.07603.x. eprint: astro-ph/0401286.

Sbarrato, T., P. Padovani, and G. Ghisellini (2014). "The jet-disc connection in AGN". In: *MNRAS* 445.1, pp. 81–92. DOI: 10.1093/mnras/stu1759. arXiv: 1405.4865 [astro-ph.HE].

Schlickeiser, R. (2002). *Cosmic Ray Astrophysics*.

Schödel, R. et al. (2002). "A star in a 15.2-year orbit around the supermassive black hole at the centre of the Milky Way". In: *Nature* 419.6908, pp. 694–696. DOI: 10.1038/nature01121. arXiv: astro-ph/0210426 [astro-ph].

Shayduk, M. et al. (2005). "A New Image Cleaning Method for the MAGIC Telescope". In: *29th International Cosmic Ray Conference (ICRC29), Volume 5*. Vol. 5. International Cosmic Ray Conference, p. 223.

Shukla, A. and K. Mannheim (2020). "Gamma-ray flares from relativistic magnetic reconnection in the jet of the quasar 3C 279". In: *Nature Communications* 11, 4176, p. 4176. DOI: 10.1038/s41467-020-17912-z.

Shukla, A. et al. (2015). "Multi-frequency, Multi-epoch Study of Mrk 501: Hints for a Two-component Nature of the Emission". In: *ApJ* 798.1, 2, p. 2. DOI: 10.1088/0004-637X/798/1/2. arXiv: 1503.02706 [astro-ph.HE].

Sikora, M. et al. (2002). "On the Nature of MeV Blazars". In: *ApJ* 577.1, pp. 78–84. DOI: 10.1086/342164. arXiv: astro-ph/0205527 [astro-ph].

Sikora, Marek (1997). "Radiation processes in blazars". In: *Proceedings of the Fourth Compton Symposium*. Ed. by Charles D. Dermer, Mark S. Strickman, and James D. Kurfess. Vol. 410. American Institute of Physics Conference Series, pp. 494–505. DOI: 10.1063/1.54010. arXiv: astro-ph/9708258 [astro-ph].

Sikora, Marek, Mitchell C. Begelman, and Martin J. Rees (1994). "Comptonization of Diffuse Ambient Radiation by a Relativistic Jet: The Source of Gamma Rays from Blazars?" In: *ApJ* 421, p. 153. DOI: 10.1086/173633.

Sikora, Marek, RafaŁ Moderski, and Greg M. Madejski (2008). "3C 454.3 Reveals the Structure and Physics of Its "Blazar Zone"". In: *ApJ* 675.1, pp. 71–78. DOI: 10.1086/526419. arXiv: 0711.3524 [astro-ph].

Silvestri, S. (2020). "Intergalactic magnetic field constraints through gamma-ray observations of the Extreme High Peaked BL Lac candidate HESS J1943+213". University of Pisa. eprint: etd-05312020-145512. URL: https://etd.adm.unipi.it/t/etd-05312020-145512/.

Sitarek, Julian et al. (2013). "Analysis techniques and performance of the Domino Ring Sampler version 4 based readout for the MAGIC telescopes". In: *Nuclear Instruments and Methods in Physics Research Section A: Accelerators, Spectrometers, Detectors and Associated Equipment* 723, pp. 109–120. ISSN: 0168-9002. DOI: https://doi.org/10.1016/j.nima.2013.05.014. URL: https://www.sciencedirect.com/science/article/pii/S0168900213005391.

Smirnov, Juri and John F. Beacom (2019). "Tev-scale thermal WIMPs: Unitarity and its consequences". In: *PhRvD* 100.4, 043029, p. 043029. DOI: 10.1103/PhysRevD.100.043029. arXiv: 1904.11503 [hep-ph].

Snowden, S. L. et al. (1997). "ROSAT Survey Diffuse X-Ray Background Maps. II." In: *ApJ* 485.1, pp. 125–135. DOI: 10.1086/304399.

Sormani, M. C. et al. (2018). "A theoretical explanation for the Central Molecular Zone asymmetry". In: *MNRAS* 475, pp. 2383–2402. DOI: 10.1093/mnras/stx3258. arXiv: 1707.03650.

Stecker, F. W. (1970). "The Cosmic γ-Ray Spectrum from Secondary Particle Production in Cosmic-Ray Interactions". In: *Ap&SS* 6, pp. 377–389. DOI: 10.1007/BF00653856.

– (1971). "Cosmic gamma rays". In: *NASA Special Publication* 249.

Stecker, F. W. et al. (1991). "High-energy neutrinos from active galactic nuclei". In: *PhRvL* 66.21, pp. 2697–2700. DOI: 10.1103/PhysRevLett.66.2697.

Stecker, Floyd W., Sean T. Scully, and Matthew A. Malkan (2016). "An Empirical Determination of the Intergalactic Background Light from UV to FIR Wavelengths Using FIR Deep Galaxy Surveys and the Gamma-Ray Opacity of the Universe". In: *ApJ* 827.1, 6, p. 6. DOI: 10.3847/0004-637X/827/1/6. arXiv: 1605.01382 [astro-ph.HE].

Steigman, Gary and Michael S. Turner (1985). "Cosmological constraints on the properties of weakly interacting massive particles". In: *Nuclear Physics B* 253, pp. 375–386. DOI: 10.1016/0550-3213(85)90537-1.

Stone, E. C. et al. (2013). "Voyager 1 Observes Low-Energy Galactic Cosmic Rays in a Region Depleted of Heliospheric Ions". In: *Science* 341.6142, pp. 150–153. DOI: 10.1126/science.1236408.

Strong, A. W. and I. V. Moskalenko (1998). "Propagation of Cosmic-Ray Nucleons in the Galaxy". In: *ApJ* 509, pp. 212–228. DOI: 10.1086/306470. eprint: astro-ph/9807150.

Strong, A. W., I. V. Moskalenko, and O. Reimer (2004). "Diffuse Galactic Continuum Gamma Rays: A Model Compatible with EGRET Data and Cosmic-Ray Measurements". In: *ApJ* 613, pp. 962–976. DOI: 10.1086/423193. eprint: astro-ph/0406254.

Strong, A. W. et al. (2004). "The distribution of cosmic-ray sources in the Galaxy, γ-rays and the gradient in the CO-to-H_2 relation". In: *A&A* 422, pp. L47–L50. DOI: 10.1051/0004-6361:20040172. eprint: astro-ph/0405275.

Su, M., T. R. Slatyer, and D. P. Finkbeiner (2010). "Giant Gamma-ray Bubbles from Fermi-LAT: Active Galactic Nucleus Activity or Bipolar Galactic Wind?" In: *ApJ* 724, pp. 1044–1082. DOI: 10.1088/0004-637X/724/2/1044. arXiv: 1005.5480 [astro-ph.HE].

Subramanian, Prasad, Amit Shukla, and Peter A. Becker (2012). "TeV blazar variability: the firehose instability?" In: *MNRAS* 423.2, pp. 1707–1710. DOI: 10.1111/j.1365-2966.2012.20991.x. arXiv: 1203.5727 [astro-ph.HE].

Sun, X. H. et al. (2008). "Radio observational constraints on Galactic 3D-emission models". In: *A&A* 477, pp. 573–592. DOI: 10.1051/0004-6361:20078671. arXiv: 0711.1572.

Svensson, Roland (1987). "Non-thermal pair production in compact X-ray sources : first-order Compton cascades in soft radiation fields." In: *MNRAS* 227, pp. 403–451. DOI: 10.1093/mnras/227.2.403.

Tavecchio, F. and G. Ghisellini (2016). "On the magnetization of BL Lac jets". In: *MNRAS* 456.3, pp. 2374–2382. DOI: 10.1093/mnras/stv2790. arXiv: 1509.08710 [astro-ph.HE].

Tavecchio, F. et al. (2009). "The hard TeV spectrum of 1ES 0229+200: new clues from Swift". In: *MNRAS* 399.1, pp. L59–L63. DOI: 10.1111/j.1745-3933.2009.00724.x. arXiv: 0905.0899 [astro-ph.CO].

Tavecchio, F. et al. (2011). "On the origin of the γ-ray emission from the flaring blazar PKS 1222+216". In: *A&A* 534, A86, A86. DOI: 10.1051/0004-6361/201117204. arXiv: 1104.0048 [astro-ph.HE].

Tavecchio, Fabrizio and Gabriele Ghisellini (2008). "Spine-sheath layer radiative interplay in subparsec-scale jets and the TeV emission from M87". In: *MNRAS* 385.1, pp. L98–L102. DOI: 10.1111/j.1745-3933.2008.00441.x. arXiv: 0801.0593 [astro-ph].

Tavecchio, Fabrizio, Laura Maraschi, and Gabriele Ghisellini (1998). "Constraints on the Physical Parameters of TeV Blazars". In: *ApJ* 509.2, pp. 608–619. DOI: 10.1086/306526. arXiv: astro-ph/9809051 [astro-ph].

Taylor, J. H. and J. M. Weisberg (1982). "A new test of general relativity - Gravitational radiation and the binary pulsar PSR 1913+16". In: *ApJ* 253, pp. 908–920. DOI: 10.1086/159690.

Tegmark, Max et al. (2004). "Cosmological parameters from SDSS and WMAP". In: *PhRvD* 69.10, 103501, p. 103501. DOI: 10.1103/PhysRevD.69.103501. arXiv: astro-ph/0310723 [astro-ph].

The LIGO Scientific Collaboration and the Virgo Collaboration and the KAGRA Collaboration, R. Abbott, et al. (2021). "GWTC-3: Compact Binary Coalescences Observed by LIGO and Virgo During the Second Part of the Third Observing Run". In: *arXiv e-prints*, arXiv:2111.03606, arXiv:2111.03606. DOI: 10.48550/arXiv.2111.03606. arXiv: 2111.03606 [gr-qc].

The Pierre Auger Collaboration et al. (2009). "Studies of Cosmic Ray Composition and Air Shower Structure with the Pierre Auger Observatory". In: *ArXiv e-prints*. arXiv: 0906.2319.

Tluczykont, M. et al. (2010). "Long-term lightcurves from combined unified very high energy γ-ray data". In: *A&A* 524, A48, A48. DOI: 10.1051/0004-6361/201015193. arXiv: 1010.5659 [astro-ph.HE].

Tsuboi, M., T. Handa, and N. Ukita (1999). "Dense Molecular Clouds in the Galactic Center Region. I. Observations and Data". In: *ApJS* 120, pp. 1–39. DOI: 10.1086/313165.

Unger, M. et al. (2007). "Study of the Cosmic Ray Composition above 0.4 EeV using the Longitudinal Profiles of Showers observed at the Pierre Auger Observatory". In: *Astronomische Nachrichten* 328, p. 614. arXiv: 0706.1495.

Urry, C. Megan and Paolo Padovani (1995). "Unified Schemes for Radio-Loud Active Galactic Nuclei". In: *PASP* 107, p. 803. DOI: 10.1086/133630. arXiv: astro-ph/9506063 [astro-ph].

Valverde, Janeth et al. (2020). "A Decade of Multiwavelength Observations of the TeV Blazar 1ES 1215+303: Extreme Shift of the Synchrotron Peak Frequency and Long-term Optical-Gamma-Ray Flux Increase". In: *ApJ* 891.2, 170, p. 170. DOI: 10.3847/1538-4357/ab765d. arXiv: 2002.04119 [astro-ph.HE].

van Eldik, Christopher (2015). "Gamma rays from the Galactic Centre region: A review". In: *Astroparticle Physics* 71, pp. 45–70. DOI: 10.1016/j.astropartphys.2015.05.002. arXiv: 1505.06055 [astro-ph.HE].

Vaughan, S. et al. (2003). "On characterizing the variability properties of X-ray light curves from active galaxies". In: *MNRAS* 345.4, pp. 1271–1284. DOI: 10.1046/j.1365-2966.2003.07042.x. arXiv: astro-ph/0307420 [astro-ph].

Čerenkov, P. A. (1937). "Visible Radiation Produced by Electrons Moving in a Medium with Velocities Exceeding that of Light". In: *Physical Review* 52.4, pp. 378–379. DOI: 10.1103/PhysRev.52.378.

Ventura, S. (2015). "Studio di Periodicità in Gamma-Ray Blazars". University of Siena.

– (2018). "Cosmic Rays Shining in the Galactic Center: A Study of Gamma-Ray Diffuse Emission of the Central Molecular Zone". University of Pisa. eprint: etd-03272018-145514. URL: https://etd.adm.unipi.it/theses/available/etd-03272018-145514/.

– (2022). "Untangling the Complexity in the Galactic Centre: a way to understand the origin of the gamma-ray emission from the inner Galaxy". In: *37th International*

Cosmic Ray Conference, p. 901. DOI: `10.22323/1.395.0901`. arXiv: `2107.13660 [astro-ph.HE]`.

Ventura, S., D. Grasso, and A. Marinelli (2019). "Shedding (Gamma) Light on the Cosmic Ray Population in the Galactic Center Region". In: *36th International Cosmic Ray Conference (ICRC2019)*. Vol. 36. International Cosmic Ray Conference, p. 816. DOI: `10.22323/1.358.0816`.

Ventura, S. et al. (2022). "Inter Galactic Magnetic field constraints through the gamma ray observations of the Extreme High-frequency-peaked BL Lac candidate HESS 1943+213". In: *37th International Cosmic Ray Conference*, p. 633. DOI: `10.22323/1.395.0633`.

Ventura, Sofia et al. (2021). "Very-High-Energy Detection of the Extreme Blazar 1RXS J081201.8+023735 with the MAGIC Telescopes". In: *43rd COSPAR Scientific Assembly. Held 28 January - 4 February*. Vol. 43, p. 1281.

Viana, A. et al. (2019). "The Cherenkov Telescope Array view of the Galactic Center region". In: *36th International Cosmic Ray Conference (ICRC2019)*. Vol. 36. International Cosmic Ray Conference, p. 817. DOI: `10.22323/1.358.0817`. arXiv: `1908.06162 [astro-ph.HE]`.

Vinogradov, S. and E. Popova (2020). "Status and perspectives of solid state photon detectors". In: *Nuclear Instruments and Methods in Physics Research Section A: Accelerators, Spectrometers, Detectors and Associated Equipment* 952. 10th International Workshop on Ring Imaging Cherenkov Detectors (RICH 2018), p. 161752. ISSN: 0168-9002. DOI: `https://doi.org/10.1016/j.nima.2018.12.067`. URL: `https://www.sciencedirect.com/science/article/pii/S0168900218318813`.

Vladimirov, A. E. et al. (2011). "GALPROP WebRun: An internet-based service for calculating galactic cosmic ray propagation and associated photon emissions". In: *Computer Physics Communications* 182, pp. 1156–1161. DOI: `10.1016/j.cpc.2011.01.017`. arXiv: `1008.3642 [astro-ph.HE]`.

Voges, W. et al. (1999). "The ROSAT all-sky survey bright source catalogue". In: *A&A* 349, pp. 389–405. DOI: `10.48550/arXiv.astro-ph/9909315`. arXiv: `astro-ph/9909315 [astro-ph]`.

Völk, H. J., F. A. Aharonian, and D. Breitschwerdt (1996). "The Nonthermal Energy Content and Gamma-Ray Emission of Starburst Galaxies and Clusters of Galaxies". In: *SSRv* 75.1-2, pp. 279–297. DOI: `10.1007/BF00195040`.

Völk, Heinrich J. and Konrad Bernlöhr (2009). "Imaging very high energy gamma-ray telescopes". In: *Experimental Astronomy* 25.1-3, pp. 173–191. DOI: `10.1007/s10686-009-9151-z`. arXiv: `0812.4198 [astro-ph]`.

von Kienlin, A. et al. (2020). "The Fourth Fermi-GBM Gamma-Ray Burst Catalog: A Decade of Data". In: *ApJ* 893.1, 46, p. 46. DOI: `10.3847/1538-4357/ab7a18`. arXiv: `2002.11460 [astro-ph.HE]`.

Wagner, S., B. Rani, and H. E. S. S. Collaboration (2021). "Enhanced HE and VHE gamma-ray activity from the FSRQ PKS 0346-27". In: *The Astronomer's Telegram* 15020, p. 1.

Wang, Q. D., F. J. Lu, and E. V. Gotthelf (2006). "G359.95-0.04: an energetic pulsar candidate near Sgr A*". In: *MNRAS* 367, pp. 937–944. DOI: 10.1111/j.1365-2966.2006.09998.x. eprint: astro-ph/0512643.

Wang, Ze-Rui and Rui Xue (2021). "Hadronuclear interpretation of the possible neutrino emission from PKS B1424-418, GB6 J1040+0617 and PKS 1502+106". In: *Research in Astronomy and Astrophysics* 21.12, 305, p. 305. DOI: 10.1088/1674-4527/21/12/305.

Watts, Anna L. and Tod E. Strohmayer (2007). "Neutron star oscillations and QPOs during magnetar flares". In: *Advances in Space Research* 40.10, pp. 1446–1452. DOI: 10.1016/j.asr.2006.12.021. arXiv: astro-ph/0612252 [astro-ph].

Watts, Anna L. et al. (2008). "Detecting gravitational wave emission from the known accreting neutron stars". In: *MNRAS* 389.2, pp. 839–868. DOI: 10.1111/j.1365-2966.2008.13594.x. arXiv: 0803.4097 [astro-ph].

Weekes, T. C. et al. (1989). "Observation of TeV Gamma Rays from the Crab Nebula Using the Atmospheric Cerenkov Imaging Technique". In: *ApJ* 342, p. 379. DOI: 10.1086/167599.

Weekes, Trevor C. (2003). *Very high energy gamma-ray astronomy*.

Wehrle, Ann E. et al. (2016). "Erratic Flaring of BL Lac in 2012-2013: Multiwavelength Observations". In: *ApJ* 816.2, 53, p. 53. DOI: 10.3847/0004-637X/816/2/53.

Weinstein, Amanda (2009). "The VERITAS Survey of the Cygnus Region of the Galactic Plane". In: *arXiv e-prints*, arXiv:0907.5435, arXiv:0907.5435. DOI: 10.48550/arXiv.0907.5435. arXiv: 0907.5435 [astro-ph.HE].

Wiedenbeck, M. E. et al. (2000). "Constraints on cosmic-ray acceleration and transport from isotope observations". In: *Acceleration and Transport of Energetic Particles Observed in the Heliosphere*. Ed. by R. A. Mewaldt et al. Vol. 528. American Institute of Physics Conference Series, pp. 363–370. DOI: 10.1063/1.1324340.

Workman, R. L. et al. (2022). "Review of Particle Physics". In: *PTEP* 2022, p. 083C01. DOI: 10.1093/ptep/ptac097.

Yamamoto, A. et al. (2008). "Search for primordial antiparticles with BESS". In: *Advances in Space Research* 42.3, pp. 442–449. DOI: 10.1016/j.asr.2007.04.069.

Yan, H. and A. Lazarian (2004). "Cosmic-Ray Scattering and Streaming in Compressible Magnetohydrodynamic Turbulence". In: *ApJ* 614, pp. 757–769. DOI: 10.1086/423733. eprint: astro-ph/0408172.

Yang, R., F. Aharonian, and C. Evoli (2016). "Radial distribution of the diffuse γ-ray emissivity in the Galactic disk". In: *PhRvD* 93.12, 123007, p. 123007. DOI: 10.1103/PhysRevD.93.123007. arXiv: 1602.04710 [astro-ph.HE].

Yang, R.-z., D. I. Jones, and F. Aharonian (2015). "Fermi-LAT observations of the Sagittarius B complex". In: *A&A* 580, A90, A90. DOI: 10.1051/0004-6361/201425233. arXiv: 1410.7639 [astro-ph.HE].

Zanin, Roberta et al. (2013). "MARS, The MAGIC Analysis and Reconstruction Software". In: *International Cosmic Ray Conference*. Vol. 33. International Cosmic Ray Conference, p. 2937.

Zatsepin, G. T. and V. A. Kuz'min (1966). "Upper Limit of the Spectrum of Cosmic Rays". In: *Soviet Journal of Experimental and Theoretical Physics Letters* 4, p. 78.

Zdziarski, A. A. and M. Bottcher (2015). "Hadronic models of blazars require a change of the accretion paradigm." In: *MNRAS* 450, pp. L21–L25. DOI: 10.1093/mnrasl/slv039. arXiv: 1501.06124 [astro-ph.HE].

Zhang, Bing (2019). "Extreme emission seen from γ-ray bursts". In: *Nature* 575.7783, pp. 448–449. DOI: 10.1038/d41586-019-03503-6. arXiv: 1911.09862 [astro-ph.HE].

Zwicky, F. (1933). "Die Rotverschiebung von extragalaktischen Nebeln". In: *Helvetica Physica Acta* 6, pp. 110–127.

– (1937). "On the Masses of Nebulae and of Clusters of Nebulae". In: *ApJ* 86, p. 217. DOI: 10.1086/143864.

Acknowledgements

The greatest thanks goes to my son Abram Giovanni who had the patience to wait for his mom, in the final months of thesis writing. All this would not have been possible without the help of my parents, especially my mom.

During the long nights of work it was invaluable support of Eugenio and discussions to make the work more usable.

In these years of work it was fundamental for me to help and collaborate with Paolo Da Vela, Daniel Morcuende, Elisa Prandini and Giovanni Morlino.

. . . to the Future what It wants to be . . .